"Discovery of new catalysts using supercritical CO_2"

Doctor of Philosophy

July 2012

Raimon Perea Marín

Thesis submitted in accordance with the requirement of Cardiff University for the degree of Doctor of Philosophy

DECLARATION

This work has not been submitted in substance for any other degree or award at this or any other university or place of learning, nor is being submitted concurrently in candidature for any degree or other award.

Signed …… (candidate) Date ……

STATEMENT 1

This thesis is being submitted in partial fulfillment of the requirements for the degree of PhD

Signed …… (candidate) Date ……

STATEMENT 2

This thesis is the result of my own independent work/investigation, except where otherwise stated.
Other sources are acknowledged by explicit references. The views expressed are my own.

Signed …… (candidate) Date ……

STATEMENT 3

I hereby give consent for my thesis, if accepted, to be available for photocopying and for inter-library loan, and for the title and summary to be made available to outside organisations.

Signed …… (candidate) Date ……

STATEMENT 4: PREVIOUSLY APPROVED BAR ON ACCESS

I hereby give consent for my thesis, if accepted, to be available for photocopying and for inter-library loans **after expiry of a bar on access previously approved by the Academic Standards & Quality Committee.**

Signed …… (candidate) Date ……

A Teresa, allà on sigues, pel viatge que emprenguérem junts i no poguérem acabar.

Ara de gran comprenc
Tot el que per tu sent
i et llence un homenatge
als quatre vents.

Com un record d'infantesa
sempre et recordaré a tu,
Teresa,
ballant el vals.

Ovidi Montllor, Homenatge a Teresa

Acknowledgements

I would like to acknowledge and thank my supervisor Professor Graham Hutchings for the giving me the opportunity to join Cardiff Catalysis Institute and his support during my PhD. Likewise, I would like to thank Dr. Jonathan Bartley, Dr. Stuart Taylor, Dr Albert Carley and Dr Gao Bin and specially Dr Simon Kondrat and Dr Thomas Davis for their support and help. I should especially thank the technical people at Cardiff University: John, Alun and my friend Steve. Also Professor Matt Roseinsky, Dr Paul Boldrin and James Gallagher at Liverpool University are acknowledged. I would like to thank the support from Johnson Matthey and Dr Gary Combes, Dr Matt Lunn, Dr Gordon Kelly, Dr Dan Enache and Sharon Bale.

Also I would like to thank Rebecca, who last year has been a special person for me, helping me with day by day things, many thanks.

I am especially pleased with all those people I have met and shared my lunch time at uni and Friday evenings at Pen&Wig: Vero & Nick, Gracia & Lino, Gabrielle, Sabrina, Marco; and Pili for all the walks through the British hills, we still miss Ben Nevis (pronto caera!). I should specially thank Annabel, who also helped a lot! Also, very pleased to have enjoyed having loads of beers with Oscar and Juan. To everybody I have met in Cardiff, many thanks for making this period a little bit warmer!

Per últim, voldria agrair tot el suport de la meva família durant aquestos tres anys, a ma mare i mon pare, la meva germana Irene i Pau (i Ainoa que acaba de vindre!) i la iaia també, sempre han estat amb mi, en els moments mes difícils. Per a tots ells, el meu reconeixement.

A la memòria de *Juan Marín*

i

Juan Miguel Marín,

treballadors incansables.

Index

List of figures

Chapter 1: Introduction.

Chapter 2: Experimental.

Chapter 3: Fundamental study of SAS process for catalysts synthesis.

Chapter 5: SAS co-precipitated catalysts for Fischer-Tropsch reaction

List of tables

Chapter 5: SAS co-precipitated catalysts for Fischer-Tropsch reaction.

List of equations

Chapter 4: Fundamental study of GAS process for catalyst synthesis.

List of symbols

Latin symbols:

C	Concentration
C_{WP}	Weisz-Prater criterion
d	Diameter
De	Diffusion coefficient
G	Gas phase
L	Liquid phase
Oh	Ohnesorge number
P	Pressure
-r	Reaction rate
Re	Reynolds number
S	Solid phase
T	Temperature
v	Velocity
w	Solute equilibrium solubility
We	Webber number
Z**	Reynolds to Webber coefficient

Greek symbols

α	Chain growth probability
χ	Molar ratio
μ	viscosity

ϕ	Thiele modulus
η	Effectiveness
λ	Wave length
ρ	Density
τ_{JB}	Jet break up time
τ_{ST}	Surface tension time

1

Introduction

1.1 Green Chemistry.

Sustainable Chemistry or Green Chemistry, comprises the design, manufacture and application of processes that reduce or eliminate hazardous chemicals [1]. Green Chemistry is a non-regulated, economically driven approach towards sustainable development that arose at the end of the 20th century [2]. The principle of this approach is to not generate waste, rather than disposing or treating it afterwards. Green Chemistry is cross-disciplinary, where different institutions are involved (such as academic, industrial and governmental institutions).

In the early 1990's, the US EPA's Office of Pollution Prevention and Toxics established the development of the Presidential Green Chemistry Challenge Award Program, after the passage of the first environmental law in 1990 which focused on preventing pollution at the source rather than abatement or capture of pollutants.

The efforts in the United Kingdom are coordinated by the academic community, where several researchers initiated research and education programs in Green

Chemistry. An example being The Royal Society of Chemistry's strong promotion of green chemistry by issuing a new journal: *Green Chemistry*.

The 12 Principles of Green Chemistry, a framework postulated by Paul Anastas and John C. Warner [3], sets out how to design chemical process that comply with Green Chemistry. These principles target the optimization of the use of raw materials to obtain the desired products, the design of safe and environmentally-benign process, energy efficiency and the better disposal of by-products.

The 12 principles of Green Chemistry can be described as follows:

1.- Prevention: It is better to prevent waste than treat it after been created.

2.- Atom Economy: Synthesis should economize the incorporation of all the materials used in the process into the final product.

3.- Less Hazardous Chemical Synthesis: Synthesis should be designed to generate products with little or non-toxicity.

4.- Designing Safer Chemicals: Chemicals should be designed to fit their purpose minimizing their toxicity.

5.- Safer Solvents and Auxiliaries: Auxiliary substances (*e.g.* solvents, separation agents, etc) should be made unnecessary wherever possible and non-hazardous when used.

6.- Design for Energy Efficiency: Energy requirements of chemical processes should be recognized for their environmental and economic impacts and should be minimized.

7.- Use of Renewals Feedstock: A raw material or feedstock should be renewable rather than depleting whenever practicable.

8.- Reduce Derivatives: Unnecessary derivatization (use of blocking groups, protection/deprotection, and temporary modification of physical/chemical

processes) should be minimized because such steps require additional reagents and can generate waste.

9.- Catalysis: Catalytic reagents are superior to stoichiometric reagents (as selective as possible)

10.- Design for Degradation: Products should be design so that at the end of their functional life they degrade to innocuous products.

11.- Real-Time analysis of Pollution Prevention: analytical methodologies should be implemented to in-process monitoring and control prior to the formation of hazardous substances.

12.- Inherently Safer Chemistry for Accident Prevention: Chemicals substances should be chosen to minimize the potential for chemical accidents.

In 2005 Ryoji Noyori (Nobel laureate in chemistry, 2001) identified three key points to be developed in Green Chemistry [4]: 1.- the use of supercritical carbon dioxide as green solvent; 2.- the use of aqueous hydrogen peroxide for clean oxidations and 3.- the use of hydrogen in asymmetric synthesis.

1.2 Green Chemistry and supercritical fluids.

In recent years several authors have remarked on the potential use of supercritical fluids for different applications. Specifically, supercritical fluids can be used as solvents for Green Chemistry to replace conventional hazardous organic solvents, such as perchloroethylene (fabrics cleaning) or perfluorooctane sulfonate (in polymer processing) [4-7]. Traditionally, supercritical CO_2 (SC-CO_2) and supercritical water have been used as solvent for organic reactions due to their benefits like non toxicity and low reactivity [8]. Despite CO_2 being identified as one of the main gases causing the green house effect, SC-CO_2 technology can

be considered as a green alternative as it is not generated for the process itself but recovered *ex situ* and used [5]. The reduction in waste, energy input, cost and safety advantages are normally pointed out as favourable properties in SC-CO_2 technology [5, 6].

1.3 Supercritical fluids.

1.3.1 Supercritical fluid definition.

A pure component at equilibrium can be represented on a three phase diagram where, normally, the following variables of state are represented: pressure (p), temperature (T) and elementary volume (1/ρ), as seen in Figure 1.1. The coexistence curves divide the usual state of matter: solid, liquid and gas. Two phases will coexist in equilibrium if conditions are placed below the coexistence curve. In Figure 1.1 it can be observed that the liquid-vapour coexistence curve shows a maximum, *i.e.* it is not infinite as for the liquid-solid line. This maximum is where the critical point (CP) lays [9].

The first observation of this continuum transition between liquid-vapour phases

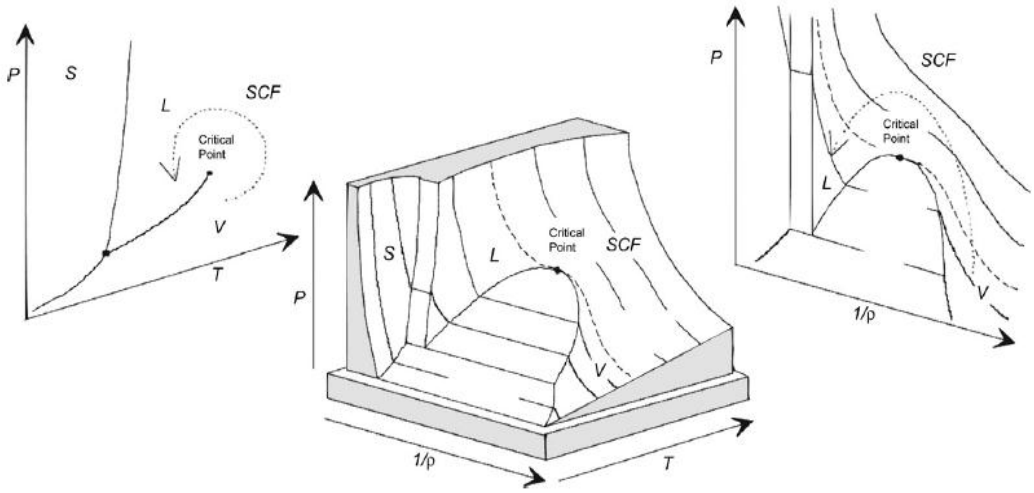

Figure 1.1. Phase diagram of a model compound. S stands for solid phase; L stands for liquid phase and V stands for vapour phase [12].

was made in the early 19th century by Baron Cagniard de la Tour [10]. Later on, Andrews [11] explained this transition and coined the top of the liquid-vapour coexistence curve as the *Critical Point*. A fluid with both pressure and temperature above the critical pressure and temperature is called a supercritical fluid (SCF). Actually, the term of supercritical fluid is normally used to address a fluid which sits at the vicinity of the CP [12].

1.3.2 Supercritical fluid properties.

A fluid above the CP presents different properties to those of gas and liquid (mainly related to density, diffusivity and viscosity), as seen in Figure 1.2 [13]. For instance, the compressibility of a fluid diverges in the vicinity of CP changing fluid density with pressure at constant temperature. The solvating capacity of a SCF is related to density at the critical point region. Therefore, the solubility of a compound can be tuned by adjusting either pressure or temperature [14]. It is worth noting that the large density values observed in SCF are equivalent to liquid-like properties in terms of solubility. The fluid viscosity gives an insight into the fluid *resistance* to flow, and this is close to the liquid values. Despite the similarities in

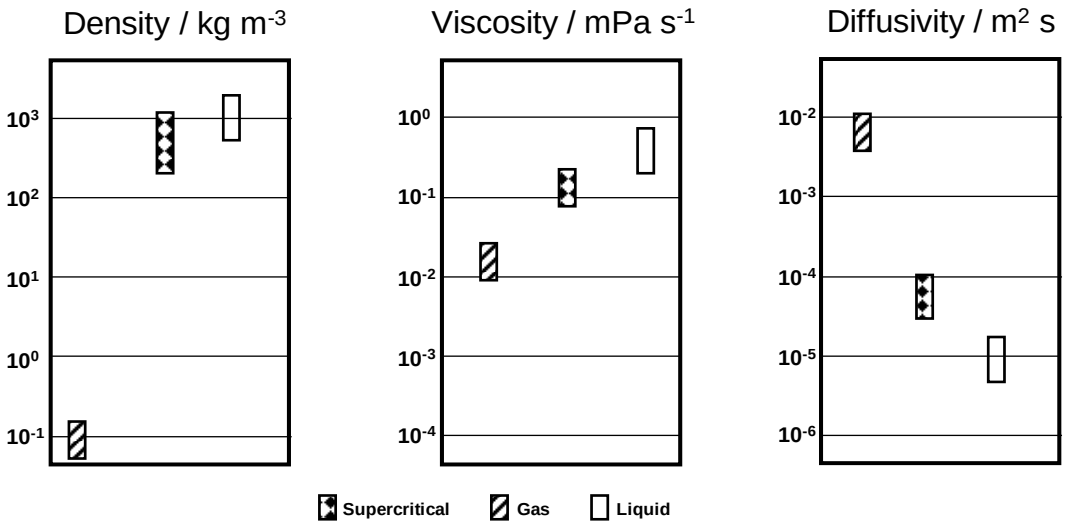

Figure 1.2. Sketch of supercritical properties of a model compound [16].

density and viscosity, diffusion rates remain close to gas-like values. Another interesting feature of SCFs is the negligible or even zero surface tension, this result in the fluid having good diffusion and wettability properties. The surface tension shrinkage at CP can be explained in terms of density variance. As the pressure increases, gas phase density rises due to compression effects, while liquid phase density drops due to volumetric expansion [15]. Eventually, densities equalize at CP and surface tension disappears.

The critical points of fluids typically used in supercritical applications are listed in Table 1.1. Some observations were pointed out by Rantakylä [16]:

- Small and light molecules tend to have lower critical temperatures and higher critical densities than heavier molecules.
- Critical pressures normally sit between 30 and 60 bar.
- Hydrogen bonds or molecular polarity tends to increase the critical point.

Among these fluids, CO_2 is widely used in supercritical technology due to its easy to handle properties, such as mild operating conditions (pressure and temperature), being environmentally friendly, low chemical reactivity and economic cost [5, 6].

Table 1.1. Critical properties of solvents commonly used.

Fluid	T_c / °C	p_c / bar	ρ_c / kg m^{-3}
Ammonia	132.6	112.8	240
Carbon dioxide	31.3	73.8	470
Dichlorodifluoromethane	111.8	39.9	560
Ethanol	243.5	63.8	280
Methanol	240.6	79.9	270
Water	374.5	221.0	340

1.3.3 Mixtures of supercritical CO_2/solvent.

The standard SC-CO_2 technology usually involves a second fluid, normally an organic solvent. The interaction between both, the SC-CO_2 and a solvent, are basically influenced by the reciprocal solubility. Langsfeld [17] described three kinds of interactions between SC-CO_2 and a solvent: immiscible, partial miscible and fully miscible conditions. A typical immiscible system is SC-CO_2/water, in this system SC-CO_2 and water are mainly in two different phases and the content of each into the other is very low. An example of a partially miscible system is SC-CO_2/1-octanol, in this case one of the fluids may ultimately diffuse into the other one. The last system described is the fully miscible, as SC-CO_2/methylene chloride where both components diffuses easily into the other.

In the particular case of a fully miscible mixture the phase state depends on the pressure, temperature and molar composition (χ) [18]. In this case, a critical curve exists between the lower and the upper critical point, as seen in Figure 1.3. The

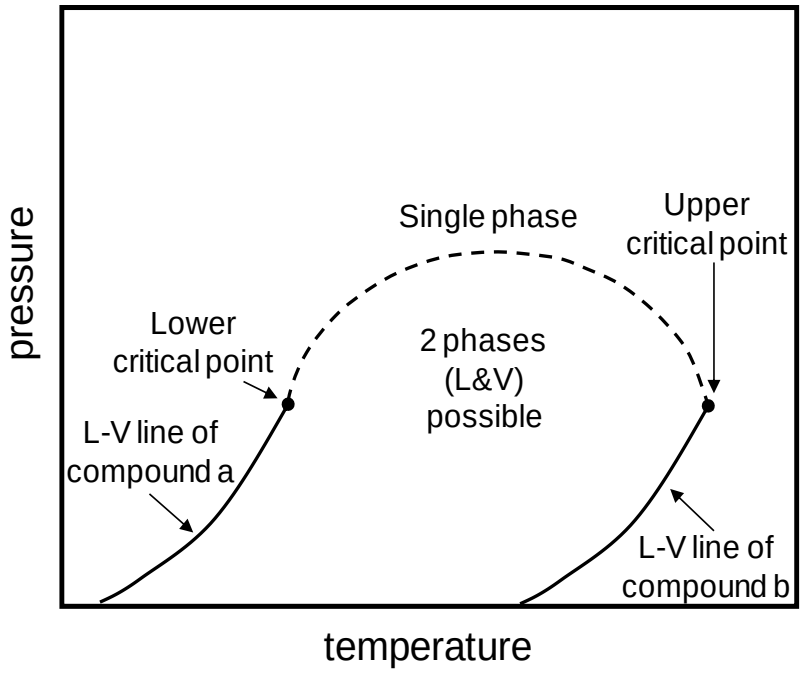

Figure 1.3. Phase diagram of a binary mixture. Critical points of compounds with low CP and high CP are sketched.

phase at which the experiment is being performed can be mapped on the T-p projection plane if during the course of a standard experiment the composition is fixed (*i.e.* SC-CO_2/solvent molar fraction), as seen in Figure 1.3. These curves have been reported for several SC-CO_2/solvent system, such as acetone, benzene, ethanol, hexane and methanol [19]. To fully characterize the phase behaviour of these binary systems a representation on three dimensions is required (temperature, pressure and molar composition) [20].

There are other properties that are less sensitive to system changes and can influence the fluid properties also. One of these properties is the dielectric constant which holds relatively low values for CO_2 but can be increased by a

Table 1.2. Vapour-liquid equilibria of CO_2 (χ_1)-Methanol (χ_2) system.

χ_1	χ_2	Temp./°C	Press./atm	SD	χ_1	χ_2	Temp./°C	Press./atm	SD
0.895	0.105	25.1	15.2	0.05	0.782	0.218	25.1	29.7	0.05
		30.5	16.4	0.05			30.6	32.1	0.1
		40.3	19.5	0.1			40.0	38.1	0.2
		50.0	22.7	0.2			50.1	44.8	0.1
		59.5	26.0	0.1			59.8	51.5	0.2
		69.3	29.7	0.05			69.4	58.4	0.3
		78.9	33.7	0.1			80.1	65.9	0.1
		89.4	37.6	0.2			90.0	72.79	0.32
		99.7	41.6	0.1			99.8	79.95	0.27
0.6412	0.3588	25.1	45.9	0.1	0.5114	0.4886	25.4	52.9	0.1
		31.0	49.7	0.4			30.5	58.1	0.2
		40.5	59.6	0.2			40.3	71.45	0.08
		49.0	69.03	0.28			50.0	84.61	0.26
		59.4	80.33	0.17			59.2	97.54	0.45
		69.8	91.11	0.12			69.7	112.4	0.4
		80.4	103.1	0.4			79.4	126.7	0.6
		89.0	112.0	0.7			89.2	137.6	1.9
		99.6	121.2	0.1			99.6	148.3	0.6
0.3613	0.6387	25.4	58.0	0.1	0.2900	0.7100	25.1	56.0	0.2
		31.2	64.0	0.2			30.5	62.6	0.1
		40.6	77.01	0.03			40.2	78.64	0.07
		49.6	90.13	0.09			49.4	93.66	0.40
		59.6	105.4	0.2			59.6	110.4	0.1
		69.5	120.7	0.5			69.4	125.7	0.1
		80.0	135.2	0.5			79.7	138.6	1.3
		89.4	144.1	0.3			89.3	152.0 [bp]	0.1
		99.2	152.7	0.4			99.3	153.5 [dp]	0.2
0.1792	0.8208	25.2	61.1	0.05	0.0883	0.9117	25.6	62.3	0.1
		30.6	66.5	0.1			30.5	68.06	0.07
		40.1	79.70	0.09			40.3	81.76 [bp]	0.14
		49.7	95.06 [bp]	0.95			49.4	94.60 [dp]	0.09
		60.1	110.4 [dp]	0.1			59.8	105.0	0.2
		69.8	122.1	0.3			69.6	116.4	0.2
		79.6	129.8	0.2			79.5	122.9	0.7
		89.9	133.3	0.1					
		99.0	129.9	0.6					

Note: SD is the standard deviation in four pressure measurement. Transition from bubble point (bp) to dew point (dp) is indicated and points the critical locus [23].

polar co-solvent, such as methanol [21]. The effect of the dielectric constant in supercritical fluids is not yet fully understood, although it has been suggested that it plays a role tuning the solvent properties [22]. There was also demonstrated a relationship between the dielectric constant and reaction rates and selectivity in chemical reactions conducted under SC-CO_2 environment.

The SC-CO_2-methanol system has been investigated by several authors [18, 20, 23-25]. The phase diagram of CO_2/methanol as a function of p-T-χ has been determined. Likewise, the mixture critical point (MCP) for different molar compositions were reported [20], as seen in Figure 1.4 and Table 1.2. Also, the authors suggested a type I phase behaviour (mixtures in which the critical point are connected by a line between the critical points of the gas and liquid, CO_2 an methanol in the present case) for the SC-CO_2/methanol system according to the van Konynenburg and Scott classification [26].

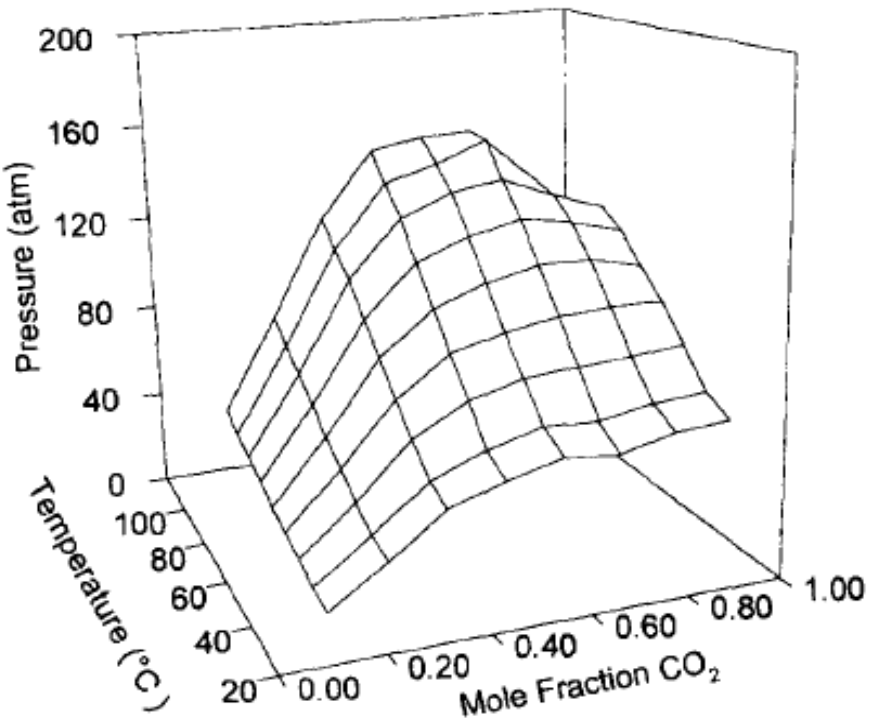

Figure 1.4. CO_2/methanol phase equilibria [23].

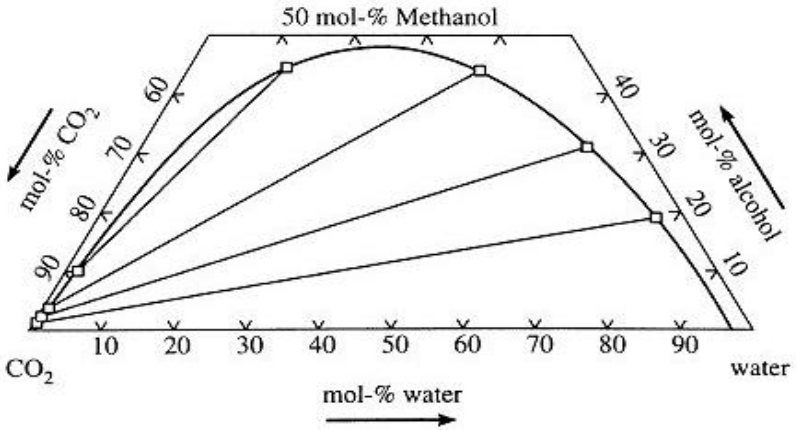

Figure 1.5. Gibbs diagram of CO_2/methanol/H_2O system at 40 °C and 100 bar [32].

In order to model the phase behaviour of CO_2/methanol and other systems, different equations of state (EOS) have been derived. Among them, Peng-Robinson-EOS (PR-EOS) [27] and Soave-Redlich-Kwong (SRK-EOS) [28] have shown good agreement with the experimental data.

The CO_2 ternary systems, such as CO_2/alcohol/H_2O, have been reviewed by Adrian and co-workers [29]. In this work, the coexistence of three phases, *i.e.* liquid-liquid-vapour (LL-V), were discussed. The formation of LL-V in a ternary system (*e.g.* CO_2/methanol/H_2O), where the rich H_2O liquid phase and the rich CO_2 liquid phase coexist with a vapour phase, as seen in Figure 1.5. This phenomenon could be explained using the CO_2/H_2O phase system: at certain pressure and temperature two liquid phases appear due to partial liquefaction of CO_2. Hence, the molar fraction of each compound inside the reciprocal phase is very poor due to solubility issues. Therefore, the partition of a third added compound occurs if this is soluble either in CO_2 and H_2O. Then a ternary LL-V system appears.

The authors also discussed the LL-V formation by a second approach. The superposition of a liquid-vapour (pressure dependent) on a liquid-liquid (almost pressure independent) is used to explain the LL-V formation. At low pressures liquid-vapour phase dominates concealing the liquid-liquid system. The

solubility of CO_2/H_2O shows small changes with pressure but in the case of solvent/H_2O solubility, it is largely affected. This implies that by increasing the pressure the ternary liquid-vapour phase diminishes leaving a ternary LL-V equilibrium.

1.3.4 Mass transfer between CO_2 and solvents.

Mass transfer is fundamental to the supercritical process and facilitates the control of the precipitation. When the antisolvent and solvent get into contact, mass transfer occurs either through gas-like mixing (single phase) or in some cases droplet formation (2-phases). The SC-CO_2 and solvent diffuse towards each other driven by concentration and temperature gradients.

The CO_2/solvent mass transfer was studied in miscible solvents scenarios below and above the MCP [30, 31]. It was suggested that far below the MCP droplets were formed and their lifetimes showed an inverse relationship to pressure and were independent of temperature. Also, it was suggested that mass transfer near the MCP was restricted. Whereas droplets were not expected above the MCP, density differences between the antisolvent and solvent were used as droplet definition and relatively short lifetimes were found [30].

1.4 Supercritical CO_2 applications.

SC-CO_2 has been used for several applications due to its versatile properties. For instance, SC-CO_2 has been implemented at industrial scale for caffeine extraction from coffee beans [32, 33], extraction of natural species, especially oils and dyes, have been studied extensively [34-37]. SC-CO_2 has been spotted as a suitable process to handle pharmaceutical drugs and proteins [38] and supercritical

chromatography is well known and has been used extensively during last two decades [37, 39, 40]. The supercritical chromatography research has brought not only improvements in analytical chemistry but also insights in phase behaviour of SC-CO_2/solvent [18, 37]. Also, the SC-CO_2 has been identified as a powerful tool for tailoring materials [41], such as catalysts [42-48], semiconductors [85] and pharmaceutical drugs [59].

1.4.1 Description of SC-CO_2 technology in material synthesis.

Research opportunities in material synthesis have pointed to SC-CO_2 as a potential tool for designing materials with added values [41, 44]. Normally, two approaches are considered: to use SC-CO_2 as solvent or to use SC-CO_2 as antisolvent.

In the former case, technological development has been scarcely developed. The rapid expansion of supercritical solutions (RESS) belongs to this approach and has been reported by various authors [49, 50].

The latter approach consists on using the SC-CO_2 as an antisolvent agent, reducing the solvating power of a solvent and ultimately precipitating out the solute. The following conditions must be matched for a successful precipitation: miscibility between antisolvent (SC-CO_2) and solvent (usually organic solvent), low solubility of the solute in the mixture SC-CO_2/solvent and relatively high solute solubility in the solvent [51]. The following methods are commonly reported as antisolvent processes: supercritical antisolvent (SAS) [52], gas antisolvent (GAS) [53], solution enhanced dispersion by supercritical fluids (SEDS) [54] and depressurization of an expanded liquid organic solution (DELOS) [55, 56].

1.4.1.1 Rapid expansion from a supercritical solution.

The rapid expansion of a supercritical solution (RESS) consists of dissolving a solute, where solute may refer to one or more compounds, in SC-CO_2 at controlled temperature and pressure. In this process, the solute is packed in a column and SC-CO_2 is delivered through. The solute is transferred to the supercritical fluid inside column and released into a low pressure chamber through a nozzle. The solvent solvating power decreases sharply due to the drop in pressure, hence solute precipitates. The temperature at nozzle exit should be controlled in order to avoid large temperature drops due to Joule-Thompson effect. A key factor in this process is the solute solubility in SC-CO_2 at work conditions (pressure and temperature). The absence of solvents during the process is an attractive feature due to the high purity of products [57]. However, low solubility of a wide variety of compounds in SC-CO_2 is a drawback.

Morphology and particle size depend on the nature of solute and the process parameters (mainly pressure, temperature drop at nozzle exit and nozzle geometry). Spherical particles and microencapsulation of pharmaceutical drugs have been reported using RESS [58].

1.4.1.2 Supercritical antisolvent precipitation.

The supercritical antisolvent precipitation (SAS), in general, is a process to introduce a solution into an antisolvent environment (supercritical antisolvent). The mechanism behind SAS is the dissolution of the antisolvent into the solution leading to solvent supersaturation and solute precipitation. Properties of the precipitate can be tuned by adjusting SAS process parameters such as temperature, pressure, hydrodynamics and nozzle geometry [55, 59, 60].

The phase where precipitation takes place is determined by the fluids pressure and temperature. There should be mentioned that two different fluids can have different critical temperature and pressure [18], as seen in Figure 1.3. Assuming that those fluids are fully miscible and one of those fluids is introduced below its CP and the other above the CP (*i.e.* SCF) ultimately both should mix intimately. Then, if the right conditions are achieved (pressure and temperature), the mixture will sit inside the supercritical region, once the MCP is overtaken. It was suggested that during the process, the MCP rises by 6 bar compared to static systems [61] and transient surface tension is formed between SC-CO_2 and solvent, which further shrinks to negligible value or even zero [17, 61].

Different nozzle configurations have been suggested for the SAS spraying. For example, two separate nozzles were used by Adami and co-workers [62] to precipitate polyvinyl alcohol. Reverchon *et al.* [48] used a similar device to form spherical particles. Falk [63] used a sonicated nozzle in order to improve the precipitation of pharmaceutical drugs. Also, Theodore [64] used a capillary nozzle obtaining sub-micrometer-sized particles. Nevertheless, the coaxial nozzle is suggested as the most suitable geometry to enhance the mass transfer during precipitation [65].

The coaxial nozzle consists of a tube distributed concentrically, as seen in Figure 1.6. Antisolvent and solvent are introduced simultaneously; normally the antisolvent is delivered through the outer tube and the solution through the inner tube. Recognizing the importance of the coaxial nozzle, Mawson [65] compared the performance of a coaxial nozzle and a standard nozzle in terms of control over particle morphology. The authors observed better control and particle size distribution in particles made using the coaxial nozzles.

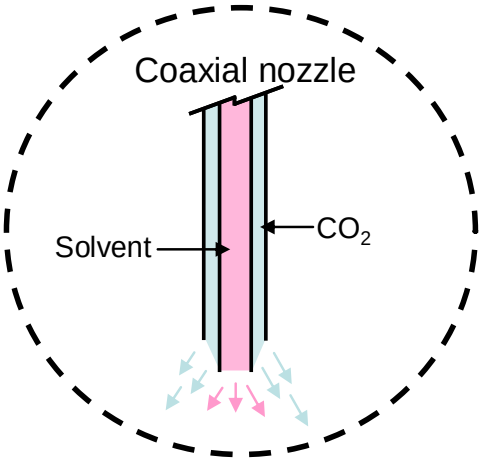

Figure 1.6. Sketch of a coaxial nozzle used in SAS process.

The hydrodynamic effects and jet break-up can be important phenomena during the course of SAS precipitation. Hydrodynamic dimensionless parameters can characterize the fluid behaviour, and moreover may help in further scale-up. Reynolds number ($Re = v \cdot d \cdot \rho / \mu$; where v is fluid velocity, d is nozzle diameter, ρ fluid density and μ is the dynamic viscosity) fully describes turbulence in a flow stream. The *Re* is the ratio between inertial forces to viscous forces, where for high values (*Re*>4000) inertial forces are predominant and the flow is turbulent [66]. The turbulent flow is randomly oriented in space and time and this disappears if an external energy source is not applied. Thus, turbulent flow is energy dissipative in nature [67]. If the viscous forces are predominant, (*Re*<2000) the fluid is laminar. Between those values (2000< and <4000) a transient regime can be considered. During the SAS process *Re* is usually settled inside the turbulent region (*i.e. Re*>4000), thus energy dissipation can be described through eddies disintegration. Rapid eddies disintegration should be preferred for rapid fluid mixing and fast surface tension elimination. Another dimensionless number considered is the Weber number ($We = \rho \cdot v^2 \cdot l / \sigma$; where v is fluid velocity, l is the characteristic length, ρ fluid density and σ is the fluid surface tension), this value correlates shear forces to surface tension. When the *We* number increases, the fluid jet does not tend to form droplets. In a stable mixed fluid, above the MCP

the *We* number tends to infinite due to the surface tension being reduced to zero or nearly zero value. However, during the transient time described in the preceding paragraph, surface tension may not be negligible and the *We* approach can be used. Other dimensionless number frequently used describing the jet break-up is the Ohnesorge number ($Oh = \sqrt{We/Re}$) which relates the viscous and the surface tension forces [68]. Czerwonatis *et al.* [69] mapped the jet break up relating *We* and *Oh* (compiled in the *Z*** factor, where $Z^{**} = Oh_{liquid} \cdot \sqrt{We_{gas}} \cdot \sqrt{(\mu_{liquid}/\mu_{gas})}$) to Re_{liquid}, as seen in Figure 1.7.

Reverchon [68] postulated a SAS precipitation mechanism where three scenarios were considered: spherical microparticle formation; liquid-like crystallization and gas-like mixing, as seen in Figure 1.8. The authors described the jet evolution as a competition between time for jet break-up (τ_{JB}) and time for surface tension shrinkage (τ_{ST}). Thus, if time for surface tension shrinkage is larger than for jet break-up, fluid atomization will occur, otherwise gas-like mixing will arise.

Micrometric spheres, as seen in Figure 1.9, were observed in a limited range of

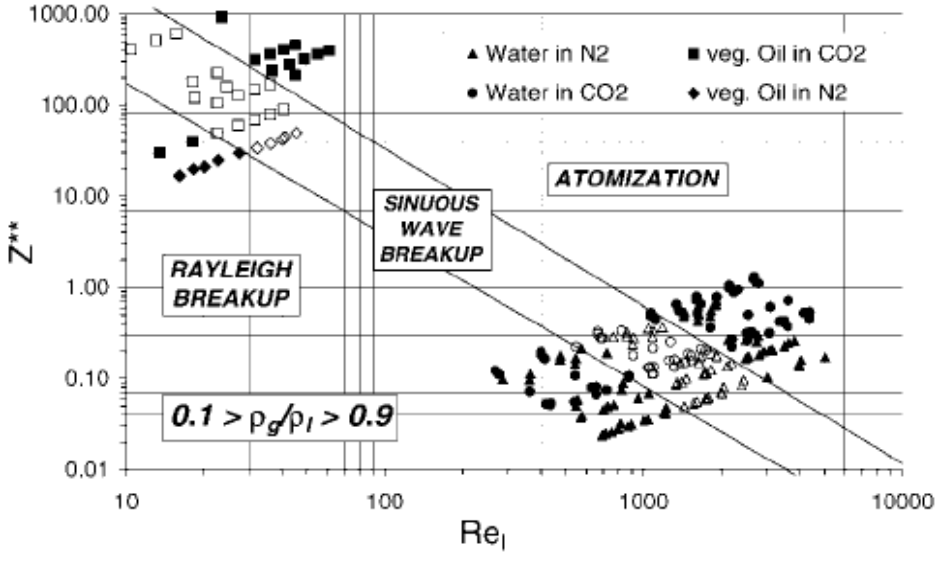

Figure 1.7. Jet break-up proposed by Czerwonatis and co-workers.

conditions above the MCP, where surface tension goes to zero at the end of the mixing [68]. Particles are formed inside the droplets at the nozzle exit (atomization), as conditions are not sufficient to reach the critical conditions. The droplet itself acts as a precipitation vessel, and then mainly the CO_2 diffuses into the droplet. Werling modelled the droplet formation and observed that droplets expand due to CO_2 inter-diffusion [30, 70], then the formation of hollow spheres are caused by the high CO_2 concentration at the droplet edge that causes solution supersaturation. At this point if the nucleation time is faster than diffusion, *i.e.* diffusion limited process, discontinuous structure are formed; whereas when the diffusion is fast uniform precipitation takes places leading continuous surfaces, *i.e.* micrometric spheres.

Crystals are likely formed during the diffusion of CO_2 into the droplet, due to a superimposition of crystallization on precipitation, *i.e.* growth time is long enough for material arrangement inside the liquid droplet (liquid-like crystallization). In the literature it has been shown that, depending on the solvent

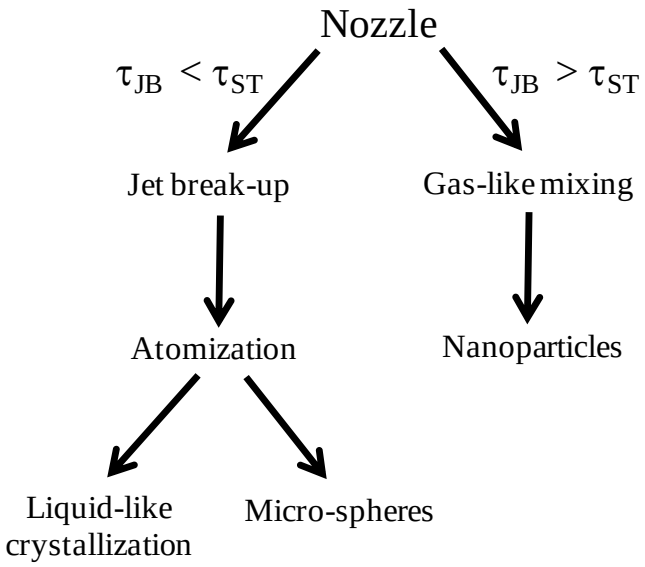

Figure 1.8. Sketch of mechanism described by Reverchon and co-workers [76].

used different crystal sizes and morphologies can be obtained [68]. Dowy [71] investigate the precipitation of paracetamol by SAS under *operando* conditions by Raman spectroscopy. It was found that the addition of the drug into the solution changed the precipitation environment from gas-like mixing to droplet formation ultimately producing crystalline paracetamol.

Nanoparticles, as seen in Figure 1.9, are formed at fully developed supercritical conditions [68]. At this state gas-like mixing is dominant and droplets are no longer formed as surface tension shrinks before jet break-up; the fluids mix and solids nucleate forming nanoparticulated aggregations.

Nevertheless, SAS is a complicated process and the mechanism of precipitation might vary dependant on the solute-solvent-antisolvent system.

Shekunov *et. al* [54] investigated the case of gas-like mixing for the paracetamol-

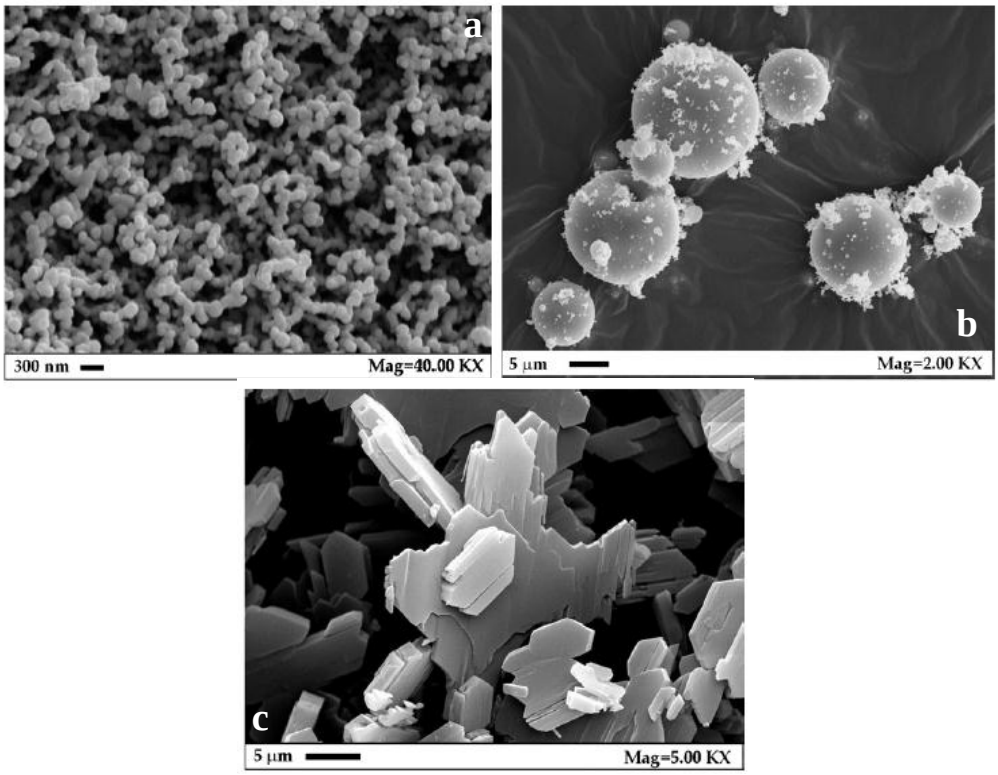

Figure 1.9. a) SAS nanoparticles of HPMA precipitated from DMSO; b) SAS micro-spherical particles of gandolinium acetate precipitated from DMSO. Both experiments at 150 bar, 40°C; c) SAS crystals of dexamethasone precipitated from acetone at 120 bar and 40 °C.

ethanol-CO_2 system. It was found that above the turbulent region the particle size became independent of the *Re* number, as seen in Figure 1.10. The authors suggested that eddies disintegration through a radial direction was the force driving mass-transfer and derived the turbulent diffusion time to evaluate the phenomena.

Several authors addressed the scale-up of the SAS process[72-74]. Reverchon [72] scaled-up the precipitation of Yttrium acetate from laboratory scale (precipitation vessel of 0.5 L) up to pilot scale (precipitation vessel of 5.2 L). Similar particle sizes and particle size distributions were obtained at conditions high above the MCP, the authors suggested that under these conditions scaling-up processes are easily performed due to the slight dependence of morphology and particle size on jet break-up. Perrut and Clavier [38] reported the successful development of several medium-sized plants for industrial applications showing the feasibility of the antisolvent process at industrial level. Boutin [74] and co-workers also developed a

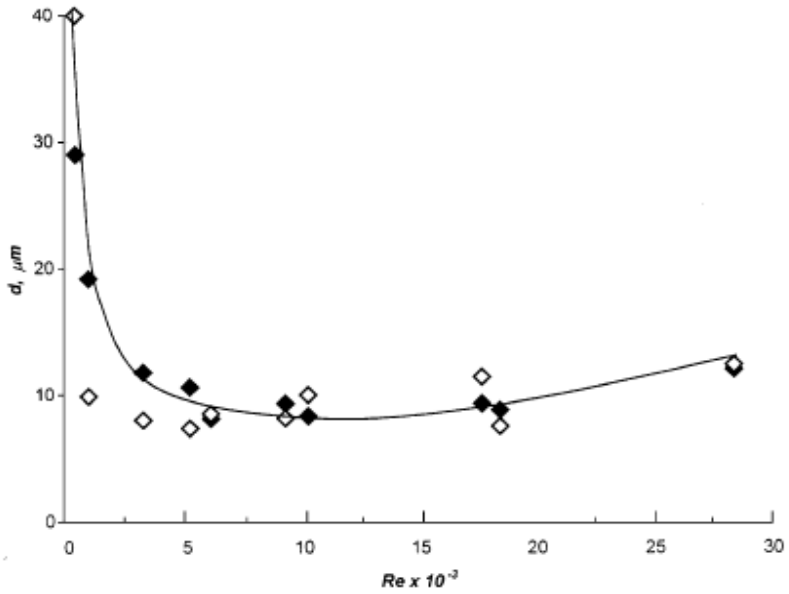

Figure 1.10. Relationship between *Re* and particle size of precipitates by SAS process under gas-like mixing. Solid symbols refer to experimental data, open symbols to modelled data [54].

SAS multi-tube device in which multiple small nozzles were fitted. Shekunov [75] successfully scaled-up supercritical precipitation at fully developed turbulent flows, *Re*>5000, correlating nozzle diameter and flow velocities, $(d_0/u_0)_1 = (d_0/u_0)_2$.

1.4.1.3 Solution enhanced dispersion by supercritical fluids.

The solution enhanced dispersion by supercritical fluids (SEDS) is considered to be a modification of the SAS process [54]. This consists of a coaxial nozzle leading into a pre-mixing chamber, placed just before the crystallization reactor. Inside this chamber the mixing of the fluids is enhanced by the increase of the mass transfer rates. Thereafter, the mixed fluid is delivered into the crystallization chamber where the solute is collected. In this method the supercritical fluid is used both as a mechanical mixer and as a precipitating agent [55].

1.4.1.4 Gas antisolvent.

Gas antisolvent (GAS) is a typical dense CO_2 gas technique. GAS normally refers to a physical process subject to solubility changes in different solvent environments. Being a handy tool for fine particle production, this technology has attracted significant attention in the recent decades [53, 76-78].

The GAS process involves the expansion of a solution by several times by the controlled addition of dense CO_2. The solvating strength is decreased as the solvent expands through the addition of CO_2; supersaturating the solution and eventually precipitating the solute [55]. The GAS process can be considered as a batch and transient process given that the particles are not continuously

precipitated and the pressure is increased during the process, ideally the temperature is kept constant.

With the addition of CO_2, the solubility of the solute in the system initially increases due to the increase in density [15]. However, once the pressure of nucleation is reached the solubility decreases gradually leading to precipitation. In line with this, the volumetric expansion of the system increases exponentially from the nucleation point as the pressure is further increased [53], as seen in Figure 1.11. Correspondingly, the nucleation and growth occur at the nucleation point and eventually cease once a new solubility balance is established. Therefore, the control of the expansion rate of the liquid phase is normally considered one of the key parameters affecting particle formation during GAS precipitation. The rapid expansion of the liquid phase promotes the supersaturation at the gas-liquid

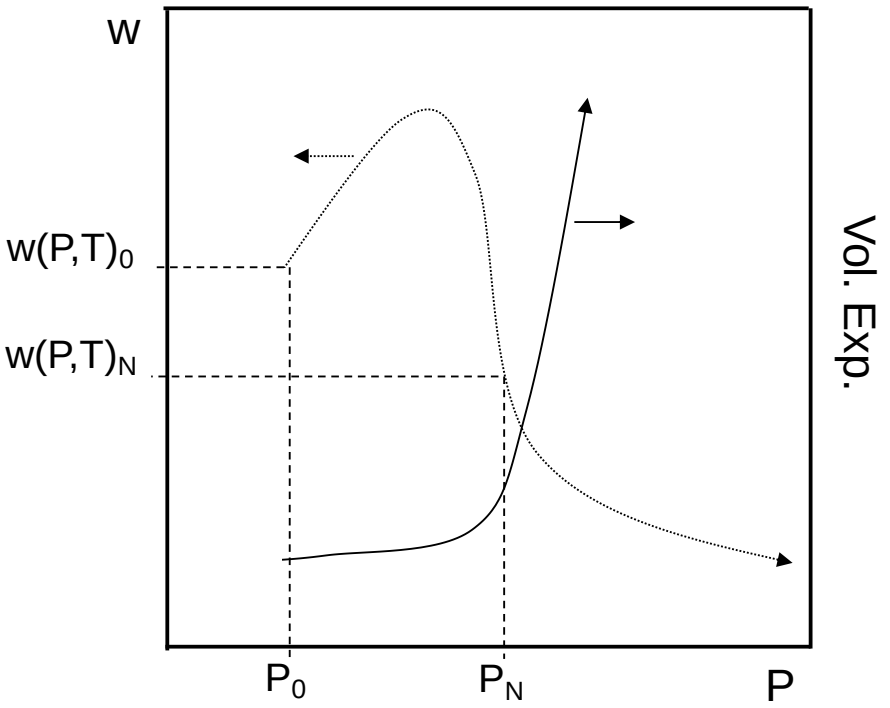

Figure 1.11 Schematic representation of solute equilibrium solubility (w) and volumetric expansion (Vol. Exp.) evolution at different pressures (P) at given temperature. Subindex N refers to nucleation (pressure and temperature). Subindex 0 refers to standard conditions (pressure and temperature).

boundary leading to nucleation of particles, as seen in Figure 1.12. Similar phenomenon was observed in liquid-liquid-vapour system by Warwick [78].

Kordikoswky [15] represented the volumetric expansion of a liquid phase against the CO_2 molar fraction for several solvents and a correlation was observed regardless of the temperature and nature of the organic solvent, as seen Figure in 1.13. The authors also suggested that the solubility of the solute in CO_2 is an important factor in GAS precipitation as the volumetric expansion is equivalent regardless of the nature of the organic solvent or the process temperature. Berends and co-workers [53] conveyed that solvent molar fraction, solute partial molar volume and expansion rate play a key role during the re-crystallization of phenanthrene dissolved in toluene by GAS process.

The particle size and morphology may also be correlated to other factors, such as the temperature, solute concentration or the solvent used [78]. For instance, the alteration of the operational temperature can influence the start of the nucleation point: the higher the temperature; the higher the pressure required for nucleation.

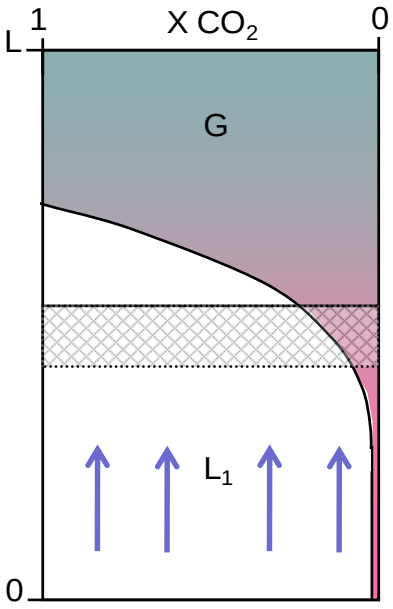

Figure 1.12. Sketch of GAS precipitation. Arrows indicate the direction of volumetric expansion. Dashed area indicates precipitation region. L1 stands for liquid phase and G for gas phase. On the top axis CO_2 molar fraction and on the left axis the precipitation chamber length.

A similar trend was found between the temperature and the expansion rate [76]. Hence, low temperatures may be preferred for GAS precipitation. Essentially, these effects reflect the shifts in solution supersaturation. Furthermore, since most of the GAS operations are approached from the sub-critical regime, the CO_2 mass diffusion from the gas phase into the liquid phase is undoubtedly an important aspect for the precipitation. Berends [53] experimented with stirring the expanded solution at two velocities, 900 and 300 r.p.m, and found that the particle size decreased at a high stirring velocity. In this work a seeded precipitation mechanism was performed, pulsing the pressure in the region of the precipitation pressure. It was found to increase the particles size but reduce the

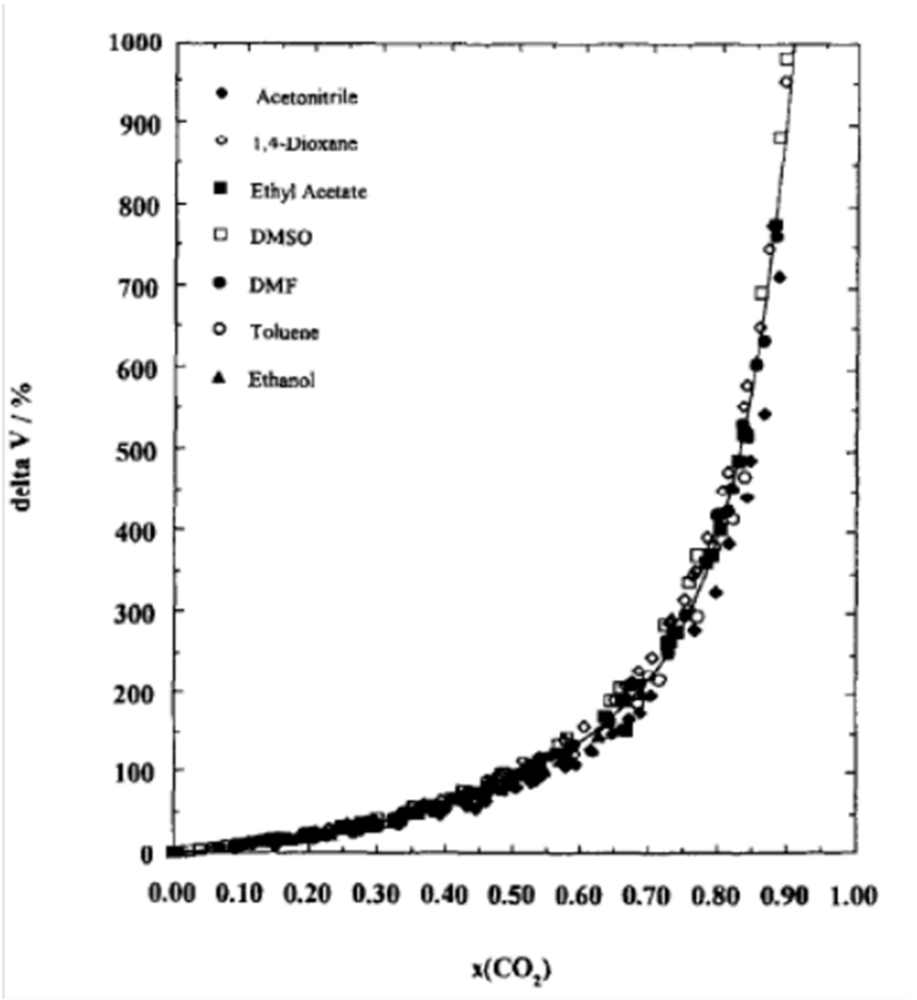

Figure 1.13. Relationship of CO_2 molar fraction and volumetric expansion of liquid phase [15].

particle size distribution.

Foster recognized the difficulties in scaling-up dense CO_2 processes, especially the GAS process. In this work the particle recovery and the lack of reliant models was addressed [79]. However, later on Mazzoti *et al.* derived a model, where different patterns of precipitation were observed depending upon relative the weight of the primary and secondary nucleation rates [73].

1.4.1.5 Depressurization of an expanded liquid organic solution.

Depressurization of an expanded liquid organic solution, normally referred to as DELOS generally includes the dissolution of a solute into an expanded organic solution by dense CO_2, where CO_2 plays the role of co-solvent. DELOS can be explained in three steps: 1.- solute dissolution in an organic solvent at ambient conditions. 2.- solution expansion by CO_2 addition below the precipitation pressure. 3.- rapid pressure reduction of expanded solution to ambient pressure by a nozzle. At the third step material precipitates due to CO_2 expansion [56, 80] .

1.4.2 Overview of patents in supercritical fluids applications.

Schütz [81] published an interesting patent survey in 2007. In this report can be seen an increasing interest of industrial research towards supercritical fluid technology. Among the world, Japan showed the largest amount of patents related to this technology last ten years, as seen if Figure 1.14, the United Kingdom hold a position on the *top-ten* countries; however, the volume of filed patents were one order of magnitude below Japan or the United States.

Extraction processes mainly with SC-CO_2 were the most claimed, as seen in Figure 1.15, although particle generation hold a strong point during 2004-2006.

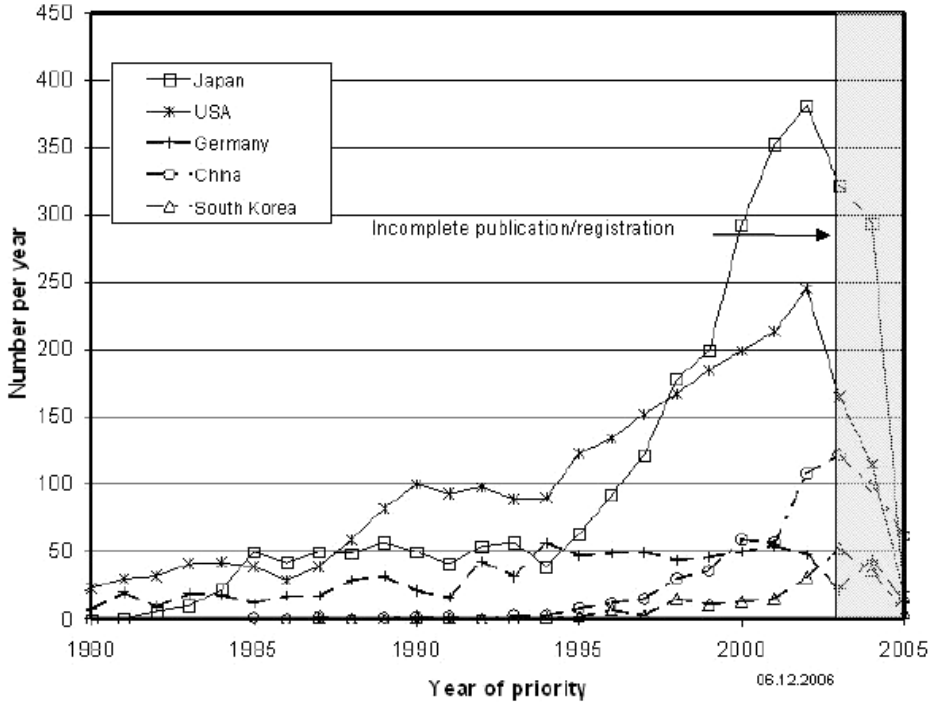

Figure 1.14. Regional number of patents applications per year [81].

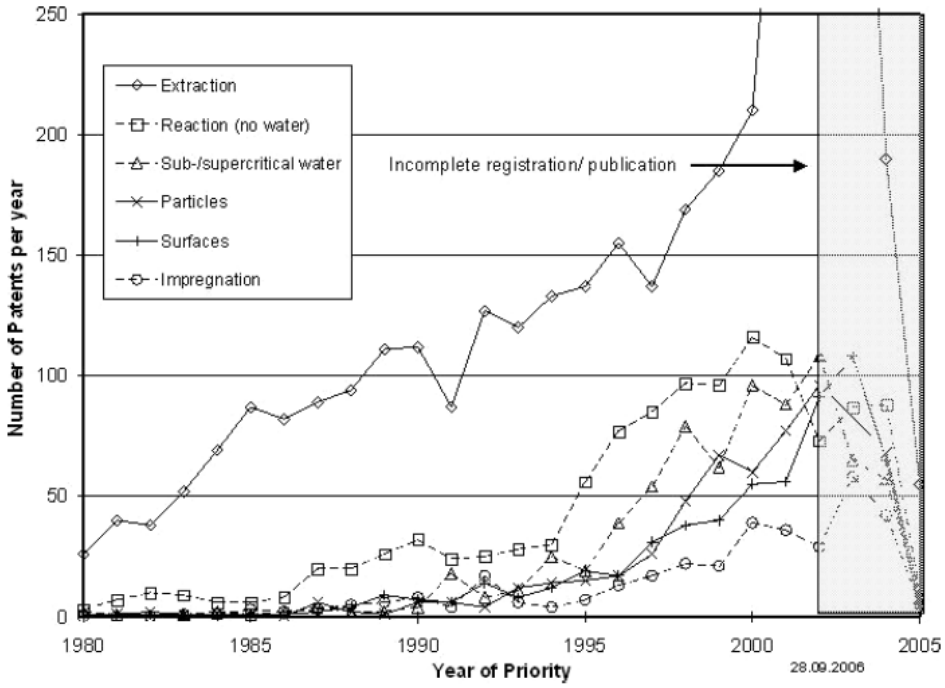

Figure 1.15. Fields related to the patents submitted per year [81].

1.5 Catalysis.

Catalysis is the acceleration of a chemical reaction by a substance called a catalyst. The catalyst interacts with the reactants, accelerating the kinetics of the reaction, without being consumed. Likewise, a catalyst can "choose" preferentially a certain range of products; it is named catalyst selectivity.

The term catalysis (from ancient Greek *katalusis*, which means *dissolution*) was first used by Berzelius [82] in 1836 to define a "new" force operating in chemical reactions. This force was the "catalytic force", a new concept besides the chemical affinity.

Catalytic processes have been used throughout history, for example sulphuric acid synthesis and fermentations were carried out during the Middle Ages. Later on, at the end of the 18th and beginning of the 19th century, the decomposition of reactants on metal oxides was studied by several scientists [82]. The idea of selectivity came up when different products were obtained using a reactant on different catalytic systems (*e.g.* decomposition of alcohols yielding different products whether it was decomposed over an iron or copper catalyst or when decomposed over pumice).

The dawn of industrial catalysis, that is, catalysts "designed" and fabricated by the human being, was set during the 19th century. The first catalysts were developed for oxidation reactions, such as HCl to Cl_2 (Deacon Process) or the sulphuric acid synthesis. However, until early the 20th century catalysis was not studied systematically under the scientific point of view. The first catalytic reactions studied, and then applied to the industry, were both the ammonia [83] and hydrocarbon [84] syntheses.

1.5.1 Heterogeneous catalysis.

During the course of a heterogeneous catalytic reaction, catalyst and reactants are in different phases. Thus, the chemical reaction takes place on the catalyst at certain places, the active sites.

A heterogeneous catalyst could present advantages compared to other catalytic processes, such as homogeneous catalysis, electro-catalysis or photo-catalysis. The advantages are that: the catalyst does not form inorganic salts; the products can be easily separated; catalysts may have a long life time and can be regenerated.

During the event of a heterogeneous catalytic reaction the following phenomena may take place:

- Transfer of reactants
- Adsorption of reactants
- Surface Reaction
- Desorption
- Removal of final products

1.6 Catalysts prepared by supercritical CO_2, an overview.

1.6.1 Vanadium phosphate catalyst for partial oxidation of butane.

Hutchings [46] group took early advantage of SCF for catalyst design making vanadium phosphate (VPO) for *n*-butane oxidation to maleic anhydride. The authors used supercritical CO_2 antisolvent precipitation (SAS process) to obtain amorphous VPO catalysts which turned out to be stable and highly active catalyst without the need for activation prior to reaction, as seen in Figure 1.16.

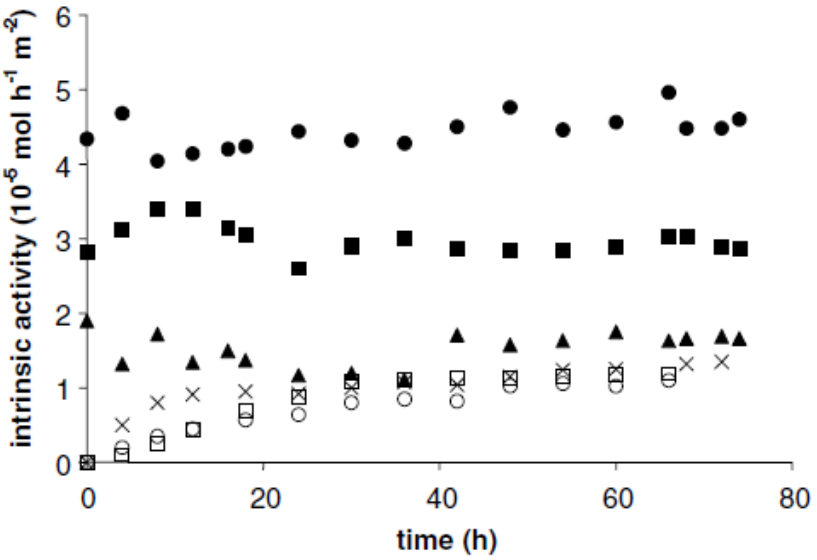

Figure 1.16. Intrinsic activity for maleic anhydride [48]. SAS-110 bar VPO; , SAS-60 bar VPO; 7 isopropanol evaporated VPO; □ refluxed H_2O-HCl VPO; – refluxed isopropanol-H_3PO_4 VPO; ∀ refluxed H_2O-H_3PO_4 VPO.

1.6.2 Hopcalite for CO oxidation.

Environmentally friendly methods of catalyst manufacture, *i.e.* nitrate free routes, have been used to co-precipitate Cu and Mn by SAS process (at 110 bar and 40ºC). The SAS processed catalysts yielded low surface area but highly active catalysts for CO oxidation, as seen in Figure 1.17. The relevant catalytic

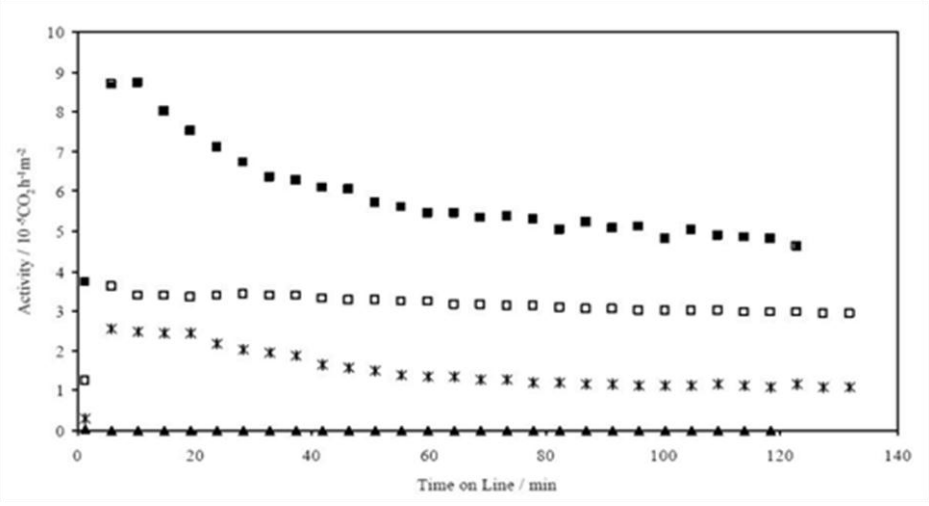

Figure 1.17. Specific activity of Cu/MnOx for CO oxidation. 7 Processed SAS Cu/MnOx; ! Calcined SAS Cu/MnOx; □ co-precipitated Cu/MnOx; ∀ commercial Cu/MnOx.

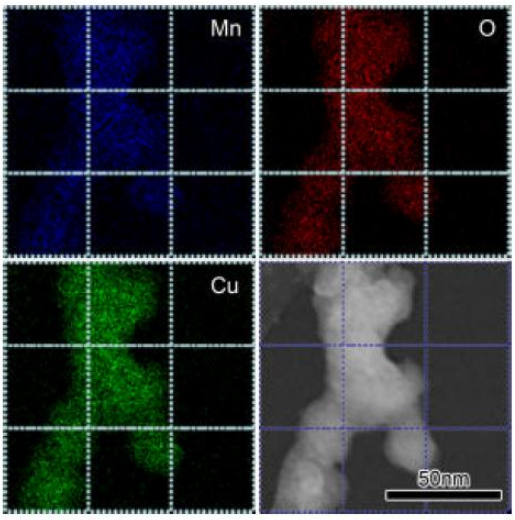

Figure 1.18. Elemental map of SAS Cu/MnOx.

activity was correlated to the high Cu and Mn homogeneity observed under STEM analysis, as seen in Figure 1.18.

Furthermore, water was introduced as co-solvent and high surface area catalyst stable under calcinations were obtained.

1.6.3 Ethane oxidative dehydrogenation.

Reverchon and co-workers [85] studied the precipitation of samarium acetate using the supercritical CO_2 antisolvent precipitation (SAS). The authors observed a highlighting catalytic activity of processed acetates compared to as-received acetates.

1.6.4 Supports for catalysts.

CeO_2 precursors were synthesized by SAS and then impregnated with gold-palladium and tested for benzyl alcohol oxidation. The catalytic activity and stability were the highest amongst the reported catalyst made by conventional routes [42], as seen in Figure 1.19. Hutchings *et al.* [44] also prepared CeO_2 by SAS for CO oxidation at ambient conditions, as seen in Figure 1.20. Again, the

catalyst showed a relevant performance and the authors pointed towards SAS technology as being a powerful tool tailoring supports for use in catalytic science.

Lu and co-workers [86] recognized the potential of SAS precipitation for nitrate free routes to catalyst supports and customized TiO_2 particle size by adjusting the flow rates, nozzle sizes and solvent concentrations. Tadros [87] also observed the potential of supercritical CO_2 in making TiO_2 using a batch process, similar to GAS, to obtain spherical TiO_2 using stabilized alkoxides in surfactant-dispersed water solutions. The authors also reported the solubility of several titanium alkoxides in SC-CO_2, as seen in Table 1.3. Reverchon [88] obtained spherical TiO_2 precursor dissolving Ti-isopropoxide in SC-CO_2 and then spraying together with water. Later on, Sui and co-workers [89, 90] reported the synthesis of TiO_2 polymerizing titanium isopropoxide and butoxide and acetic acid by SC-CO_2 in batch mode.

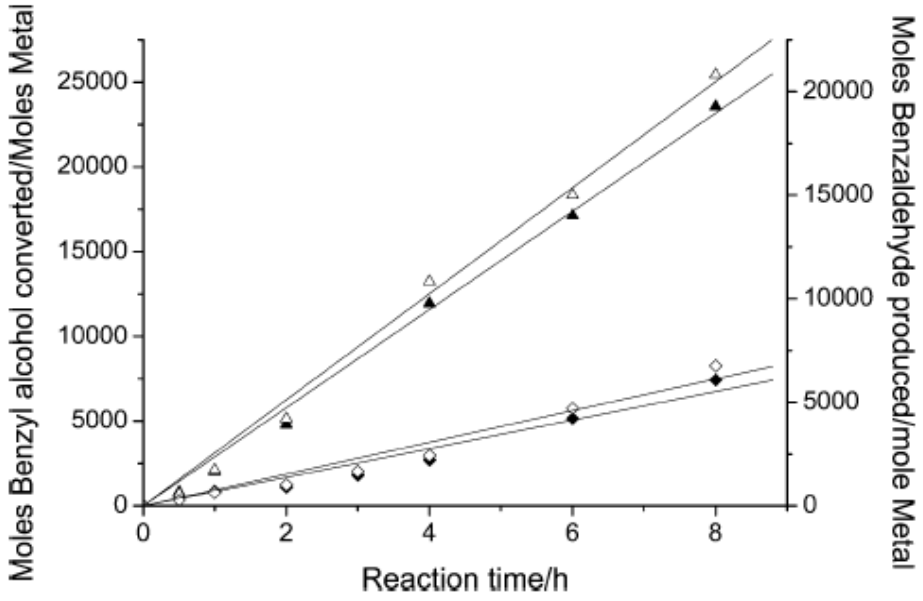

Figure 1.19. Benzyl alcohol oxidation by different Au supported CeO_2 catalysts. 8 SAS Au-Pd/CeO_2; M Un-processed Au-Pd/CeO_2. Full symbols refer to conversion, open symbols to benzaldehyde converted.

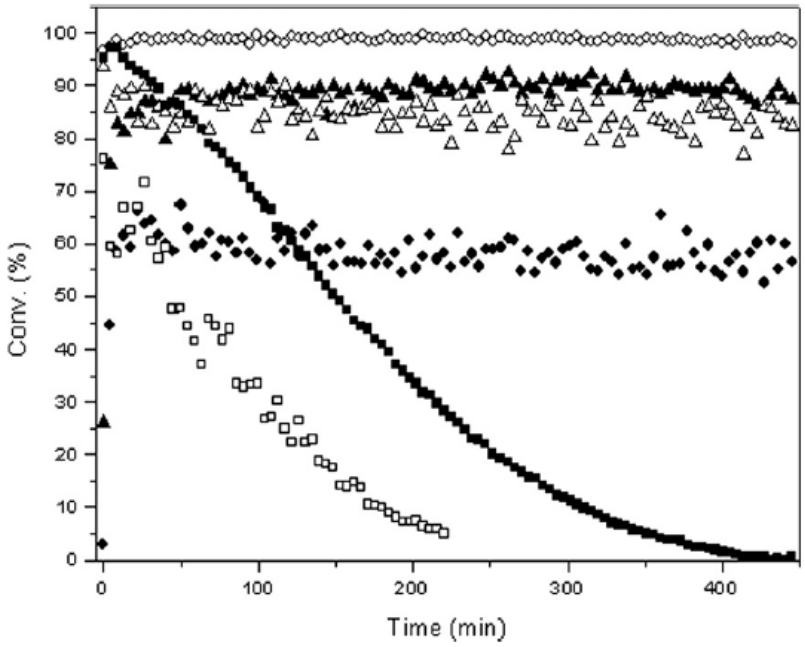

Figure 1.20. CO conversion at ambient conditions for several gold supported catalysts. Λ Un-processed Au/CeO_2; 7; M SAS Au/CeO_2-2; 8 SAS Au/CeO_2-3; ! World Gold Council provided Au/Fe_2O_3; ∀ SAS Au/CeO_2-1 at high GHSV (deactivated).

Table 1.3. Solubility (as %), dew point and boiling point of several Ti-alkoxides in SC-CO_2.

TABLE I

Alkoxide	Alkoxide Weight %	Dew Point, MPa	Boiling Point
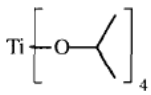	4.25	8.2	505 K/101.0 KPa
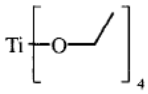	4.19	12.1	423 K/1.3 KPa
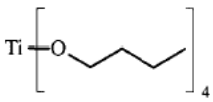	3.05	18.6	479 K/1.3 KPa
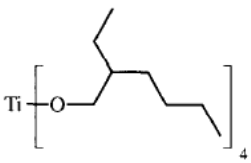	2.21	35.8	522 K/1.5 KPa
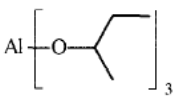	6.13	>62.0	473 K/30 mm

2.1 Aims of this project.

Recently, the development of chemical processes able to provide the increasing social requirements with the shortage of feedstock that currently the society is facing and, specially, those have been forecasted and fulfil the environmental friendly policy, *i.e. Green Chemistry*, are a challenge for both the academia and the industry.

Catalytic reactions can allow society to obtain products that normally are obtained from nature. Specifically, Fischer-Tropsch reaction is able to produce petroleum derivates such as platform chemicals and fuels avoiding the oil dependence. The Fischer-Tropsch catalyst preparation is one of key factors for an optimum Fischer-Tropsch performance and has been widely studied, topics as an adequate active phase and promoter effects are well described in the literature. Traditionally, the preparation of catalysts has been carried out impregnating nitrate salts, due to economical costs and significant solubility in aqueous solution, on solid supports (*e.g.* cobalt nitrate on alumina, silica or titania). Hence, streams generated, with a high concentration of nitrates, must be treated before they are disposed back into the nature, being a process with important economic costs.

Another problem that the actual society is currently facing is the elimination of volatile organic compounds from exhausts, generated in thermal engines. Normally, 3-way catalysts based on rhodium-platinum supported on oxides (generally but not only aluminium oxide) is used in the automotive industry, however, economically reasons encourages to survey for economic alternatives. The academia has sought substitutes for exhaust catalysts using transition metals oxides (normally cobalt oxide), preparing this catalyst by different methods,

including wet chemistry and mechanochemical routes [91, 92]. The propane deep oxidation is normally used as a model reaction to test the performance of catalysts eliminating volatile organic compounds from exhaust.

Supercritical CO_2 has been identified as a green solvent in material science, has been implement in industrial processes, such as caffeine extraction, and has been widely investigated and reported at academic level. Specifically, important improvements have been accomplished using supercritical CO_2 as solvent in catalysts synthesis. It has been observed that the formation of metal carbonates, starting from metal acetates, yields very active catalysts for different reactions, such as CO or alcohol oxidations.

In the present work supercritical CO_2 technology (SAS and GAS precipitation) have been studied as alternative routes preparing catalysts for Fischer-Tropsch synthesis and propane total oxidation. The project has been approached as follows:

1. An investigation of the formation of cobalt carbonates by the SAS process to obtain catalyst for propane total oxidation.
2. An investigation of GAS process impregnating TiO_2 with cobalt acetate and promoters (barium and ruthenium) that potentially may provide catalysts with comparable activity to the state of the art catalysts for Fisher-Tropsch synthesis.
3. An investigation of SAS co-precipitation preparing catalysts (cobalt-zinc based catalysts) active for Fischer-Tropsch synthesis.

3.1 References.

1. Anastas, P. T.; Williamson, L. G., *Green chemical syntheses and Processes*. American Chemical Society: Washington, DC,, 2000.

2. Ritter, S. K., *Chemical Engineering News* **2001,** (79), 27-29.

3. Anastas, P. T.; Warner, J. C., *Green Chemistry: Theory and Practice*. Oxford University Press: New York, 1998.

4. Noyori, R., *Chemical Communications* **2005,** (14), 1807-1811.

5. Beckman, E. J., *Industrial & Engineering Chemistry Research* **2003,** *42* (8), 1598-1602.

6. Beckman, E. J., *The Journal of Supercritical Fluids* **2004,** *28* (2-3), 121-191.

7. Leiter, W.; Poliakoff, M., *Green Chemistry* **2008,** *10* (4), 730-730.

8. Teja, A. S.; Eckert, C. A., *Industrial & Engineering Chemistry Research* **2000,** *39* (12), 4442-4444.

9. Carlès, P., *The Journal of Supercritical Fluids 53* (1-3), 2-11.

10. Cagniard de la Tour, C., *Annales de Chemie Physique* **1822,** *21*, 127.

11. Andrews, T., *Philosophical Transactions of the Royal Society of London* **1869,** *159*, 575-590.

12. Tom, J. W.; Debenedetti, P. G., *Journal of Aerosol Science* **1991,** *22* (5), 555-584.

13. Schneider, G.; Egon S.; Günther W., *Extraction with Supercritical Gases*. Verlag Chemie: Weinheim, 1980.

14. Schneider, G., *Extraction with Supercritical Gases*. Verlag Chemie: Weinheim, 1980.

15. Kordikoswki, A.; Schenk, A. P.; van Nielen, R. M.; Peters, C. J., *The Journal of Supercritical Fluids* **1995,** *8*, 205-216.

16. Rantakylä, M. Particle production by supercritical antisolvent processing techniques. Helsinki University of Technology, Helsinki, 2004.

17. Lengsfeld, C. S.; Delplanque, J. P.; Barocas, V. H.; Randolph, T. W., *The Journal of Physical Chemistry B* **2000,** *104* (12), 2725-2735.

18. Ziegler, J. W.; Dorsey, J. G., *Analytical Chemistry* **1995,** *67* (2), 456-461.

19. Page, S. H.; Sumpter, S. R.; Lee, M. L., *Journal of Microcolumn Separations* **1992,** *4* (2), 91-122.

20. Reighard, T. S.; Lee, S. T.; Olesik, S. V., *Fluid Phase Equilibria* **1996,** *123* (1-2), 215-230.

21. Roskar, V.; Dombro, R. A.; Prentice, G. A.; Westgate, C. R.; McHugh, M. A., *Fluid Phase Equilibria* **1992,** *77*, 241-259.

22. Combes, G. B. University of New South Wales, Sidney, 2002.

23. Abdulagatov, I.; Polikhronidi, N.; Abdurashidova, A.; Kiselev, S.; Ely, J., *International Journal of Thermophysics* **2005,** *26* (5), 1327-1368.

24. Yoon, J.-H.; Lee, H.-S.; Lee, H., *Journal Chemical Engineering Data* **1993,** *38* (1), 53-55.

25. Secuianu, C.; Feroiu, V.; Geană, D., *Cententral European Journal of Chemistry* **2009,** *7* (1), 1-7.

26. Konynenburg, P. H. V.; Scott, R. L., *Philosophical Transactions of the Royal Society of London. Series A, Mathematical and Physical Sciences* **1980,** *298* (1442), 495-540.

27. Peng, D. Y.; Robinson, D. B., *Industrial & Engineering Chemistry Fundamentals* **1976,** *15* (1), 59-64.

28. Soave, G., *Chemical Engineering Science* **1972,** *27* (6), 1197-1203.

29. Adrian, T.; Wendland, M.; Hasse, H.; Maurer, G., *The Journal of Supercritical Fluids* **1998,** *12* (3), 185-221.

30. Werling, J. O.; Debenedetti, P. G., *The Journal of Supercritical Fluids* **2000,** *18* (1), 11-24.

31. Reverchon, E.; Torino, E.; Dowy, S.; Braeuer, A.; Leipertz, A., *Chemical Engineering Journal* **2010,** *156* (2), 446-458.

32. Zosel, K. Decaffeinizing coffee. 1972.

33. Hubert, P.; Vitzthum, O. Separation of caffeine from supercritical solutions. 1978.

34. Cocero, M. J.; García, J., *The Journal of Supercritical Fluids* **2001,** *20* (3), 229-243.

35. Danh, L. T.; Truong, P.; Mammucari, R.; Foster, N., *Chemical Engineering Journal* **2010,** *165* (1), 26-34.

36. Chen, C.-H.; Chen, W.-H.; Chang, C.-M. J.; Lai, S.-M.; Tu, C.-H., *The Journal of Supercritical Fluids* **2010,** *52* (2), 228-234.

37. Kong, C. Y.; Gu, Y. Y.; Nakamura, M.; Funazukuri, T.; Kagei, S., *Fluid Phase Equilibria* **2010,** *297* (2), 162-167.

38. Perrut, M.; Clavier, J.-Y., *Industrial & Engineering Chemistry Research* **2003,** *42* (25), 6375-6383.

39. Robert, H. R.; Ronald, R. Method for the purification of prostaglandins using supercritical fluid chromatography. 2010.

40. Klejdus, B.; Lojková, L.; Plaza, M.; Snóblová, M.; Sterbová, D., *Journal of Chromatography A* **2010,** *1217* (51), 7956-7965.

41. Aymonier, C.; Loppinet-Serani, A.; Reverón, H.; Garrabos, Y.; Cansell, F., *The Journal of Supercritical Fluids* **2006,** *38* (2), 242-251.

42. Miedziak, P. J.; Tang, Z.; Davies, T. E.; Enache, D. I.; Bartley, J. K.; Carley, A. F.; Herzing, A. A.; Kiely, C. J.; Taylor, S. H.; Hutchings, G. J., *Journal of Materials Chemistry* **2009,** *19* (45), 8619-8627.

43. Tang, Z.-R.; Jones, C.; Aldridge, J. W.; Davies, T. E.; Bartley, J. K.; Carley, A. F.; Taylor, S. H.; Allix, M.; Dickinson, C.; Rosseinsky, M. J.; Claridge, J. B.; Xu, Z.; Crudace, M. J.; Hutchings, G. J., *ChemCatChem* **2009,** *1* (2), 247-251.

44. Tang, Z.-R.; Edwards, J. K.; Bartley, J. K.; Taylor, S. H.; Carley, A. F.; Herzing, A. A.; Kiely, C. J.; Hutchings, G. J., *Journal of Catalysis* **2007,** *249* (2), 208-219.

45. Lopez-Sanchez, J. A.; Bartley, J. K.; Burrows, A.; Kiely, C. J.; Havecker, M.; Schlogl, R.; Volta, J. C.; Poliakoff, M.; Hutchings, G. J., *New Journal of Chemistry* **2002,** *26* (12), 1811-1816.

46. Hutchings, G. J.; Lopez-Sanchez, J. A.; Bartley, J. K.; Webster, J. M.; Burrows, A.; Kiely, C. J.; Carley, A. F.; Rhodes, C.; Hävecker, M.; Knop-Gericke, A.; Mayer, R. W.; Schlögl, R.; Volta, J. C.; Poliakoff, M., *Journal of Catalysis* **2002,** *208* (1), 197-210.

47. Hutchings, G. J.; Bartley, J. K.; Webster, J. M.; Lopez-Sanchez, J. A.; Gilbert, D. J.; Kiely, C. J.; Carley, A. F.; Howdle, S. M.; Sajip, S.; Caldarelli, S.; Rhodes, C.; Volta, J. C.; Poliakoff, M., *Journal of Catalysis* **2001,** *197* (2), 232-235.

48. Reverchon, E., Adami, R., Caputo, G., De Marco, I., *The Journal of Supercritical Fluids* **2008,** *47* (1), 70-84.

49. Oum, K.; Harrison, J. J.; Lee, C.; Wild, D. A.; Luther, K.; Lenzer, T., *Physical Chemistry Chemical Physics* **2003,** *5* (24), 5467-5471.

50. Chingunpitak, J.; Puttipipatkhachorn, S.; Tozuka, Y.; Moribe, K.; Yamamoto, K., *Drug Development & Industrial Pharmacy* **2008,** *34* (6), 609-617.

51. Reverchon, E.; Cardea, S.; Rapuano, C., *Journal Applied Polymer Science* **2007,** *104* (5), 3151-3160.

52. Reverchon, E.; De Marco, I.; Torino, E., *The Journal of Supercritical Fluids* **2007,** *43* (1), 126-138.

53. Berends, M. E.; Bruinsma, S. L.; de Graauw, J.; van Rosmalen, M. G., *AIChE* **1996,** *42* (2), 431-439.

54. Shekunov, Y. B.; Baldyga, J.; York, P., *Chemical Engineering Science* **2001,** *56* (7), 2421-2433.

55. Jung, J.; Perrut, M., *The Journal of Supercritical Fluids* **2001,** *20* (1), 179-219.

56. Ventosa, N.; Sala, S.; Veciana, J., *The Journal of Supercritical Fluids* **2003,** *26* (1), 33-45.

57. Jean, T. W.; Debenedetti, P. G., *Journal Aerosol Science* **1991,** *22* (5), 555-584.

58. Debenedetti, P. G.; Tom, J. W.; Sang-Do, Y.; Gio-Bin, L., *Journal of Controlled Release* **1993,** *24* (1-3), 27-44.

59. Bristow, S.; Shekunov, T.; Shekunov, B. Y.; York, P., *The Journal of Supercritical Fluids* **2001,** *21* (2), 257-271.

60. Marr, R.; Gamse, T., *Chemical Engineering and Processing* **2000,** *39* (1), 19-28.

61. Cardoso, M. A. T.; Cabral, J. M. S.; Palavra, A. M. F.; Geraldes, V., *The Journal of Supercritical Fluids* **2008,** *47* (2), 247-258.

62. Adami, R.; Osséo, L. S.; Huopalahti, R.; Reverchon, E., *The Journal of Supercritical Fluids* **2007,** *42* (2), 288-298.

63. Falk, R.; Randolph, T. W.; Meyer, J. D.; Kelly, R. M.; Manning, M. C., *Journal of Controlled Release* **1997,** *44* (1), 77-85.

64. Baumann, T. F.; Gash, A. E.; Chinn, S. C.; Sawvel, A. M.; Maxwell, R. S.; Satcher, J. H., *Chemistry of Materials* **2004,** *17* (2), 395.

65. Simon, M.; Sanjay, K. K.; Johnston, P., *Journal of Applied Polymer Science* **1997,** *64* (11), 2105-2118.

66. Perry, R. H.; Green, W. D., *Perry's Chemical Engineers' Handbook*. 7th ed.; McGraw-Hill Professional: New York, 1997.

67. Hinze, J. O., *Turbulence*. 1st ed.; Mc-Graw Hill: New York, 1975.

68. Reverchon, E.; De Marco, I., *Chemical Engineering Journal* **2011,** *169* (1-3), 358-370.

69. Czerwonatis, N.; Eggers, R., *Chemical Engineering & Technology* **2001,** *24* (6), 619-624.

70. Werling, J. O.; Debenedetti, P. G., *The Journal of Supercritical Fluids* **1999,** *16* (2), 167-181.

71. Dowy, S.; Braeuer, A.; Reinhold-López, K.; Leipertz, A., *The Journal of Supercritical Fluids* **2009,** *50* (3), 265-275.

72. Reverchon, E.; Caputo, G.; De Marco, I., *Industrial & Engineering Chemistry Research* **2003,** *42* (25), 6406-6414.

73. Muhrer, G.; Lin, C.; Mazzotti, M., *Industrial & Engineering Chemistry Research* **2002,** *41* (15), 3566-3579.

74. Boutin, O.; Maruejouls, C.; Charbit, G., *The Journal of Supercritical Fluids* **2007,** *40* (3), 443-451.

75. Baldyga, J.; Czarnocki, R.; Shekunov, B. Y.; Smith, K. B., *Chemical Engineering Research and Design* **2010,** *88* (3), 331-341.

76. Park, S.; Yeo, S., *The Journal of Supercritical Fluids* **2008,** *47* (1), 85-92.

77. Park, Y. J.; Nam, K. H.; Ha, S. J.; Pai, C. M.; Chung, C. P.; Lee, S. J., *Journal of Controlled Release* **1997,** *43* (2-3), 151-160.

78. Warwick, B.; Dehghani, F.; Foster, N. R.; Biffin, J. R.; Regtop, H. L., *Industrial & Engineering Chemistry Research* **2002,** *41* (8), 1993-2004.

79. Thiering, R.; Dehghani, F.; Foster, N. R., *The Journal of Supercritical Fluids* **2001,** *21* (2), 159-177.

80. Ventosa, N.; Sala, S.; Veciana, J.; Torres, J.; Llibre, J., *Crystal Growth & Design* **2001,** *1* (4), 299-303.

81. Schütz, E., *Chemical Engineering & Technology* **2007,** *30* (6), 685-688.

82. Averill, B. A.; Moulijn, J. A.; van Leeuwen, P. W. N. M.; van Santen, R. A., *Catalysis: An Integrated Approach (Studies in Surface Science and Catalysis)*. 2nd ed.; Elsevier Science: Amsterdam 2000.

83. Haber, F.; van Oordt, G., *Zeitschrift für anorganische und allgemeine Chemie* **1905,** *44*, 341-378.

84. Sabatier, P.; Senderens, J. B., *Compte Rendus Hebd.* **1902,** *134*, 514.

85. Reverchon, E.; Porta, G. D.; Sannino, D.; Lisi, L.; Ciambelli, P., *Supercritical AntiSolvent precipitation: a novel technique to produce catalyst precursors*. Elsevier: Amsterdam, 1998.

86. Lu, T.; Blackburn, S.; Kickinson, C.; Rosseinsky, J. M. H., G.; Axon, S.; Leeke, A. G., *Powder Technology* **2009,** *188* (3), 264-271.

87. Tadros, M. E.; Adkins, C. L. J.; Russick, E. M.; Youngman, M. P., *The Journal of Supercritical Fluids* **1996,** *9* (3), 172-176.

88. Reverchon, E.; Caputo, G.; Correra, S.; Cesti, P., *The Journal of Supercritical Fluids* **2003,** *26* (3), 253-261.

89. Sui, R.; Rizkalla, A. S.; Charpentier, P., *Langmuir* **2005,** *21* (14), 6150-6153.

90. Sui, R.; Rizkalla, S. A.; Charpentier, A. P., *Journal Physical Chemistry B* **2006,** *110* (33), 16212-16218.

91. Davies, T. E.; Garcia, T.; Solsona, B.; Taylor, S.H., *Chemical Communications* **2006**, *32*, 3417-3419.

92. Solsona, B.; Davies, T. E.; Garcia, T.; Vazquez, I.; Dejoz, A.; Taylor S.H., *Applied Catalysis B: Environmental* **2008**, *84* (1-2),176–184.

2

Experimental

The target of this work has been to produce catalysts using a process that is complicit with Green Chemistry principles. SC-CO_2 has been suggested as a suitable solvent for green processes. Hence, CO_2 (in dense or supercritical state) has been systematically used as anti-solvent agent in order to precipitate desired catalysts. The processes used for precipitation of catalysts are further explained.

2.1 Precipitation equipment.

2.1.1 Jerguson equipment.

The apparatus referred to as the *Jerguson* equipment (Figure 2.1) has been developed and built at Cardiff Catalysis Institute, Cardiff University. The equipment is made of stainless steel tubing 1/4" and 1/8", as required. The CO_2 is delivered in the liquid phase from a cylinder and then chilled to -7 °C in a cooling bath. The CO_2 is subsequently pressurised by pumping it with an air-driven pump (Haskel MS-71). The pressure is adjusted using a back pressure regulator. A surge tank avoids fluctuations in CO_2 flow. Thereafter, the fluid is heated inside the thermal bath up to working temperature, before being injected through a coaxial nozzle. The external nozzle (equivalent diameter 736 μm) is used to deliver CO_2 into the precipitation chamber. In parallel, a solution is

pumped using a HPLC pump (Agilent Technologies series 1200) through the internal nozzle, see inset Figure 2.1. Three internal nozzles were used (i.d. = 50, 120 and 250 μm), whereas the external nozzle was kept constant. The coaxial nozzle protrudes 5 cm inside the precipitation chamber. The precipitation chamber (length/diameter = 12) is made with stainless steel (*Jerguson* gauge 13-R-32) with an internal volume of 100 ml and equipped with a borosilicate window to allow internal observations. A stainless steel frit is placed on the bottom of the chamber (porous 0.5 μm and 15 mm diameter). The frit facilitates the collection of the precipitate while the fluid passes through. The CO_2 flow rate is adjusted using the needle valve placed after precipitation chamber (see Figure 2.1). Afterwards, the fluid is then separated in two consecutive separation vessels (at 20 bar and room temperature). The CO_2 is vented in gas phase and the effluent solution is recovered inside the separation vessel. The back pressure

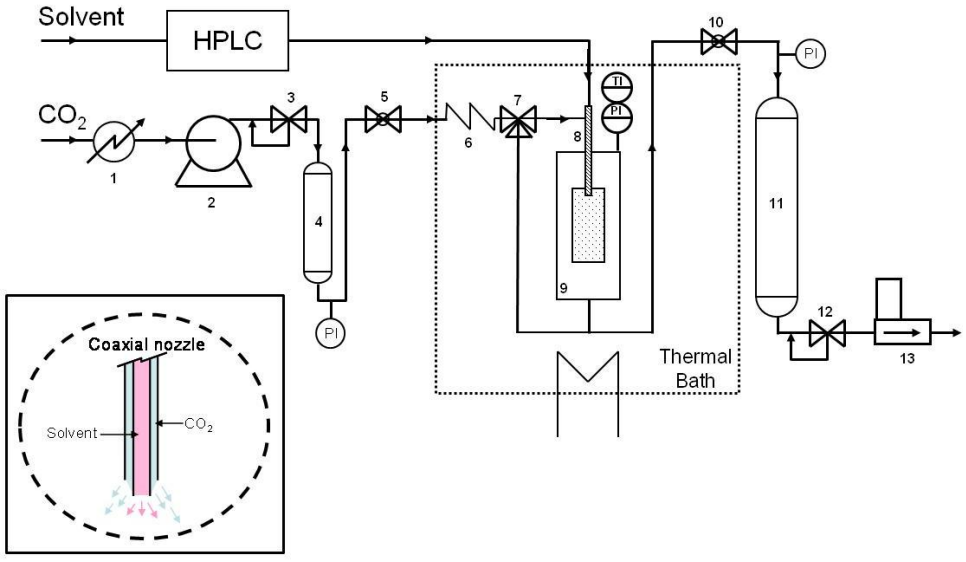

Figure 2.1. Jerguson layout. 1.- cooling bath, 2.- air driven pump, 3.- back pressure regulator, 4.- surge tank, 5.- needle valve (GAS mode), 6.- coil, 7- three-way valve (downwards for GAS mode, straight to the top of the chamber for SAS), 8.- coaxial nozzle, 9.- precipitation vessel (windowed *Jerguson* vessel), 10.- needle valve (SAS mode), 11.- expansion chamber, 12.- back pressure regulator, 13.- mass flow meter, TI.- temperature indicator, PI.- pressure indicator Inset nozzle sketch.

regulator placed downstream of the separation vessels finally expands the CO_2 to 1 bar. There, the CO_2 flow rate is monitored using an in-line flow meter (Alborg GFM 37).

To monitor the temperature, an in-line thermocouple (T-type model) is placed before the coaxial nozzle. Likewise, a pressure transducer (Druck PTX 610) is placed in-line before the precipitation chamber to measure the pressure, as can be seen on Figure 2.1.

For GAS experiments an alternative CO_2 route is used. The three-way valve placed before the coaxial nozzle is switched to GAS mode. Then, the dense CO_2 goes straight to the bottom of the precipitation chamber. Then, it is introduced into the chamber by passing upwards through the frit. Once expansion is completed, the abovementioned valve is switched back to SAS mode allowing dense CO_2 downwards through the chamber.

2.1.2 Separex equipment.

The *Separex* equipment was designed and commissioned by *Separex S.A.* –France- (see Figure 2.2). The main feature of the equipment is the large scale when compared to the *Jerguson* equipment. The solvent is delivered using a HPLC pump (Series III pump). The liquid CO_2 is provided by a cylinder and chilled down to -4 °C. Then, the dense CO_2 is pumped by means of diaphragm pump. The CO_2 flow rate is adjusted by altering the pump frequency. The fluid temperature is stabilized by an electrical heat exchanger (25-150 °C). Once the CO_2 working temperature is reached, it is introduced into the precipitation chamber. Three different options for CO_2 delivery were considered: 1.- SAS mode: using a coaxial nozzle. 2.- GAS mode: an auxiliary line is used to deliver

dense CO_2 upwards from the bottom, the flow is controlled by means of needle valve placed before precipitation chamber. 3.- direct delivery: CO_2 is delivered straight into the precipitation vessel controlled by an on/off valve. The precipitation chamber (Length/Diameter = 2.75) consists on a 1.0 litre cylindrical chamber placed inside a secondary chamber heated by an electrical resistance. A stainless steel frit (porous 0.5 μm and 80 mm diameter) is placed on the bottom of the precipitation chamber. The as-precipitated material is recovered on the frit whilst the fluids leave the chamber through an outlet placed on the bottom of the secondary chamber. Fluids are then conducted to the expansion chamber after depressurization at the back pressure regulator. The expansion chamber is heated in order to avoid blockage due to CO_2 condensation.

2.1.3 High pressure injection equipment.

The high pressure injection (HiPI) was developed at Cardiff Catalysis Institute,

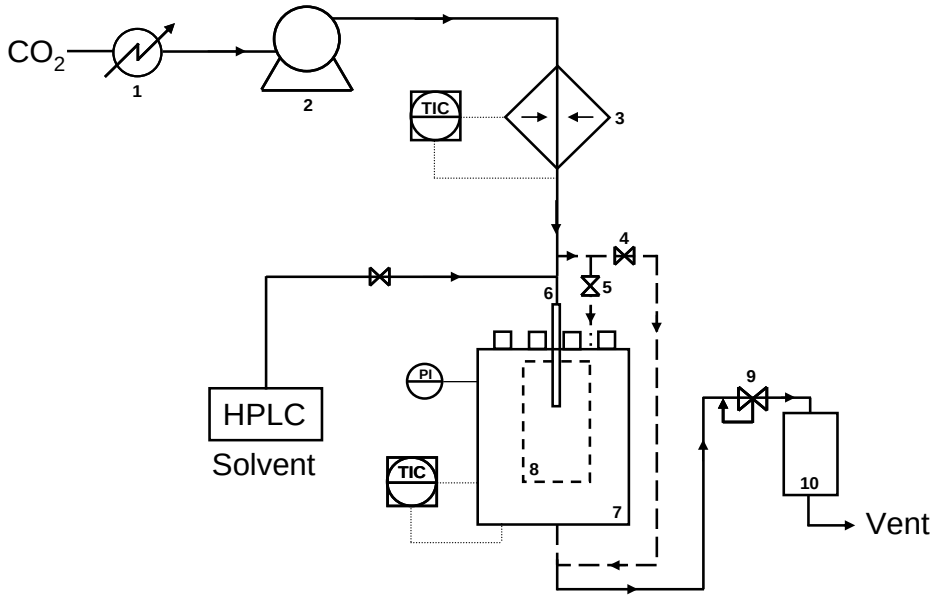

Figure 2.2. Separex layout. 1.- cooling bath, 2.- diaphragm pump, 3.- CO_2 heater, 4.- GAS mode valve, 5.- straight feed valve, 6- SAS mode inlet and coaxial nozzle, 7.- secondary chamber, 8.- precipitation chamber, 9.- back pressure regulator, 10.- expansion chamber, TIC.- temperature controller, PI.- pressure indicator

Cardiff University during this research project. The HiPI injection process was developed to allow a slurry solution to be injected into a pressurized chamber. Normally SC-CO_2 is continuously delivered whilst the slurry is injected. Therefore HiPI experiments could be considered as heterogeneous SAS process. After injection, CO_2 is flushed to remove the remaining solvent.

The HiPI unit is a modification made on the *Separex* equipment, as can be seen in Figure 2.3. The device consists of a high pressure vessel placed above the *Separex* precipitation chamber. It is connected to the *Separex* using a 1/8" tube. In order to control the injection an on/off valve is placed in the connecting tube between the HiPI vessel and the precipitation vessel. The tube protrudes 1 cm inside the precipitation vessel. The HiPI and the *Separex* are connected by a tube fitted with a nozzle; then the nozzle can be changed as desired. The HiPI vessel is equipped with a heating jacked tuned by means of a PID (Calcom 3300) fed by a thermocouple (T-type) placed just below the HiPI vessel. The pressure is

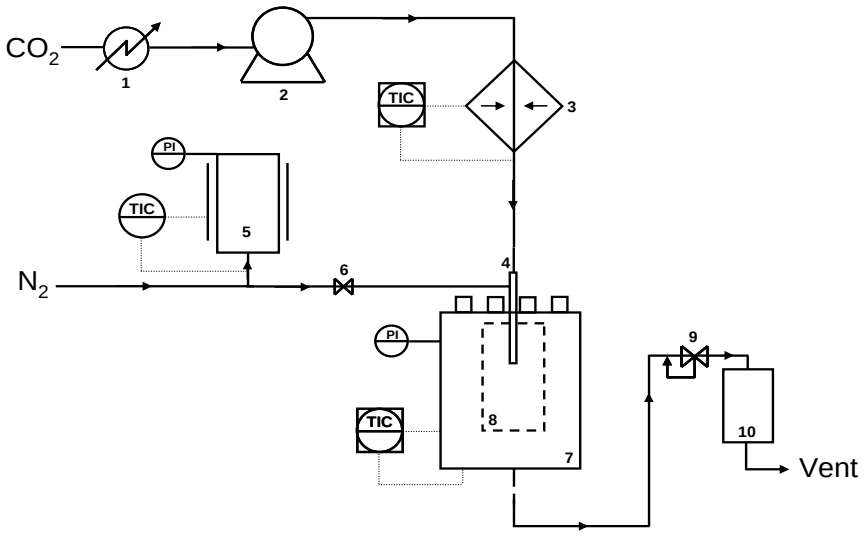

Figure 2.3 HiPI layout. 1.- cooling bath, 2.- diaphragm pump, 3.- CO_2 heater, 4.- Nozzle, 5.- HiPI vessel, 6- isolating valve, 7.- secondary chamber, 8.- precipitation chamber, 9.- back pressure regulator, 10.- expansion chamber, TIC.- temperature controller, PI.- pressure indicator

monitored by a pressure transducer (PTX 600 series) placed on the top of the equipment.

2.2 Experimental process description.

2.2.1 SAS experiments.

The SAS experiments were started when both pressure and temperature were reached and stabilized. The pressure was stabilized by pumping CO_2 through the reactor chamber with a continuous flow, while the system temperature was maintained by the heating system. Before injecting any solution for precipitation, the system was firstly purged with a CO_2/solvent mixture for 30 minutes, in order to reach a quasi-steady state equilibrium of antisolvent/solvent. The metal salt solution and CO_2 were then pumped coaxially into the chamber for the required time followed by another 30 minutes of pure CO_2 to remove residual solvent. The system was then depressurized in a stepwise manner to ambient pressure. The as-precipitated products were recovered inside reactor chamber afterwards. Details of preparation of metal salt solution are given elsewhere.

The operation of small scale *Jerguson* equipment comprises the regulation of pressure and CO_2 flow rate by the needle valve and the solution flow rate delivered within the system. The solvent flow rate did not present major issues since this is governed by the HPLC pump and typically the nozzle does not block. The CO_2 pressure and flow rate may present some issues because the needle valve can freeze due to the Joule-Thompson effect. The choice of a valve with an adequate valve coefficient (*Cv*) value helps to improve the valve handling. The fine particles normally produced during the experiments may block both the frit inside precipitation chamber and the in-line filter placed

before needle valve. A good practice was cleaning the frit after every experiment using an acidic solution inside an ultrasonic bath.

The *Separex* unit was easily operated and pressure and flow rates, both solution and CO_2, were stable during the experiments. Depending on the material produced, particles may pass around the frit. These particles were eventually trapped in the in-line filter placed before the back pressure regulator. When the filter was blocked the line below this point freezes down due to the filter behaving as an expansion valve. After depressurization system, the frit can be washed using acidic solution inside an ultrasonic bath. In order to recover all the effluent the temperature inside the expansion chamber was always set below the boiling point of the solvent used.

2.2.2 GAS experiments.

The GAS experiment starts by setting the working temperature of the precipitation vessel. Then the precursor solution was injected from the top into the chamber. The precipitation chamber was then isolated and the solution is ready for expansion. The solution expansion was carried out by adding CO_2 from the bottom. The desired pressurization rate was controlled using the needle valve placed before the precipitation chamber. Once expansion was completed, the as-precipitated catalyst is dried using a continuous CO_2 flow, as described in *Section 2.2.1*.

2.2.3 HiPI experiments.

The HiPI equipment was operated by two persons. One individual is in charge of the *Separex* equipment, and the second manages the N_2 cylinder and the HiPI

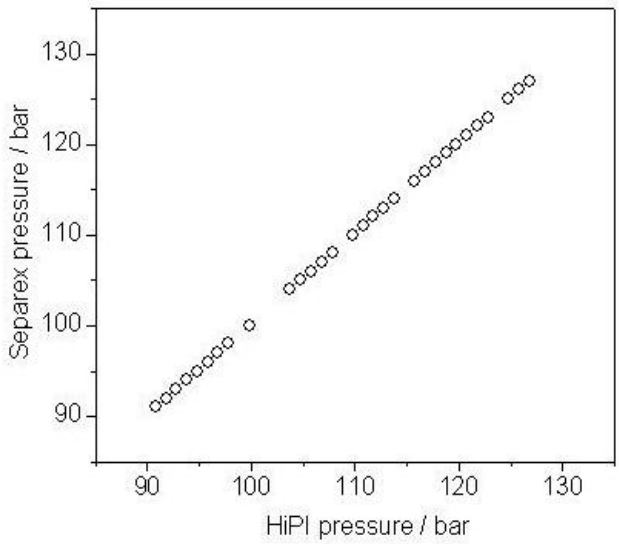

Figure 2.4 Calibration curve between HiPI unit and *Separex* equipment.

equipment. Once both sets of equipment were connected by the valve described in *Section 2.1.3*, the HiPI vessel was loaded with the slurry solution, isolated and gently pressurized up. The N_2 was used to pressurize the vessel and as a mechanical mixer since the bubbling maintained the homogeneity of the slurry. The pressure inside the vessel was monitored by the pressure transducer and the pressure gauge. Then the second operator started pressurizing up the *Separex* unit and once the pressure was close but below the HiPI pressure the valve was opened and the slurry was injected.

After the slurry injection, CO_2 was flushed to remove solvent that could be trapped in the precipitated material.

The pressure in both units was calibrated and good agreement was observed (see Figure 2.4). The pressure changes are used to control the slurry flow rate during the injection (see Figure 2.5). The authors interpreted the pressure instabilities as a consequence of slurry injection, region A on Figure 2.5. Once the injection was finished, pressure variations were less significant, as can be seen on region B on Figure 2.5.

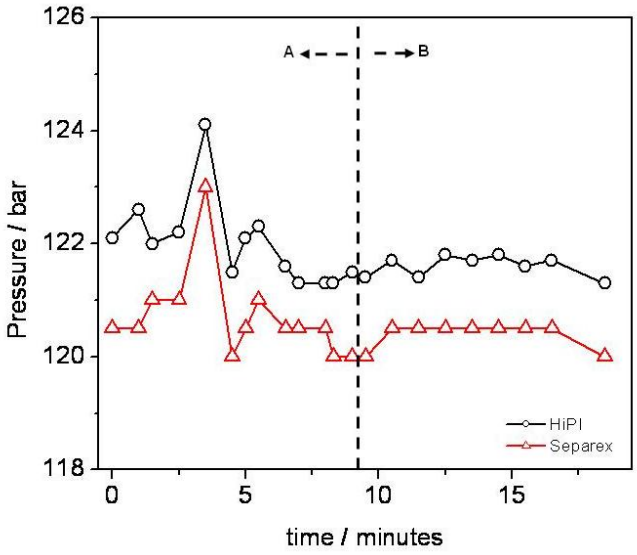

Figure 2.5 Example of HiPI injection using 500 μm nozzle.In region A one can observe pressure changes, in region B the pressure is relatively stable.

2.2.4 Solubility measurements in supercritical carbon dioxide.

The solubility of $Co(CH_3COO)_2 \cdot 4\,H_2O$ was measured using CO_2 as a solvent in a dynamic extraction system [1]. The CO_2 is pumped up by means of a CO_2 pump (Jasco PU-1580-CO_2) into stainless steel tube 1/4" (Length/Diameter = 30) and packed with sieved cobalt salt (fraction 250-500 μm). A back pressure regulator (Jasco, BP-1580-81) maintains pressure in the system. The temperature of the system is maintained by means of an air circulating oven. Solubility experiments are conducted at constant pressure, temperature and flow rate over 20 hours. The effluent is collected in a container; after the back pressure regulator, downstream. After the measurement the system is flushed with water in order to remove the salt that may precipitate during depressurization. The washing process is performed at 1 ml min^{-1} for 15 minutes using the HPLC pump. Subsequently the solution is analyzed off-line by atomic absorption spectroscopy.

2.3 Catalyst testing.

2.3.1 Propane total oxidation.

Catalysts were tested for propane total oxidation at ambient pressure and steady state conditions at different temperatures. The catalysts were packed inside a ¼ stainless steel tube (i.d. = 6.2 mm) and placed inside a tubular furnace. Temperature was monitored by means of a thermocouple placed inside the reactor just above the catalytic bed. A reaction gas mixture consisting of 0.5% propane balanced with synthetic air (O_2/He 20%) was flowed over the catalyst bed. The flow rates were controlled by means of mass flow controllers (MKS). The product stream was analyzed in an on-line gas chromatograph (Varian 3800 equipped with thermal conductivity and flame ionisation detector). A sketch of the experimental equipment is presented on Figure 2.6.

The gas chromatograph was calibrated for analysis by injecting known amounts of reactants and products (propane, CO_2 and propene). The peak areas corresponded to a specific concentration determined by multiplying the raw counts by the response factor (RF). The response factor (RF) is taken from the gradient of the calibration curve.

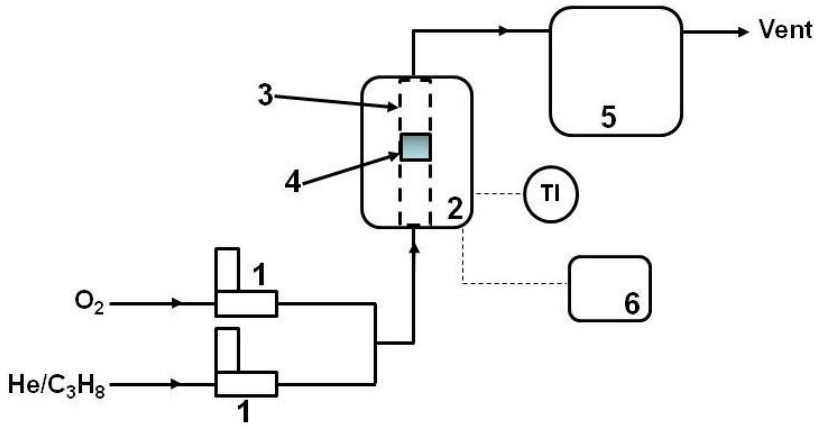

Figure 2.6 Schematic of the equipment used to test propane total combustion. 1.- mass flow controllers, 2.- furnace, 3.- stainless steel reactor tube, 4.- catalyst bed, 5.- gas chromatograph (including FID and TCD), 6.- thermostat.

Propane conversion is calculated as follow:

$$Conversion\% = [(C_{in} - C_{out})/C_{in}] \times 100 \qquad Equation\ 2.1.$$

Where: C_{in} stands for propane inlet concentration, measured at the beginning of run at room temperature, and C_{out} propane concentration measured in the gas chromatograph.

Each data point at a given temperature is the average of three injections. The reaction data in the work were reproducible with a relative error of 7%.

2.3.2 Fischer-Tropsch reaction.

The catalysts were tested for Fischer-Tropsch reaction at *Johnson Matthey* facilities. The equipment consists of six in line reactors (i.d. = 4 mm) placed inside forced N_2 circulating furnace. The catalysts were tested under isothermal conditions over the range of 210-245 °C and 20 bar, the syn-gas mixture used was $Ar:CO:H_2 = 0.1:2:1$. The catalyst was packed inside the reactors preceded by alumina spheres, these spheres worked as heat diluting. The reactors were fed by syn-gas flow controlled by mass flow controllers. In order to trap water, alcohols and waxes two traps were placed downstream of the reactors. The first trap was set at 90 °C, there water and alcohols were trapped and the second was kept at 1.5 °C where waxes were retained. The gas products were conducted and analyzed in on-line gas chromatograph. A sketch of the experimental equipment is showed on Figure 2.7.

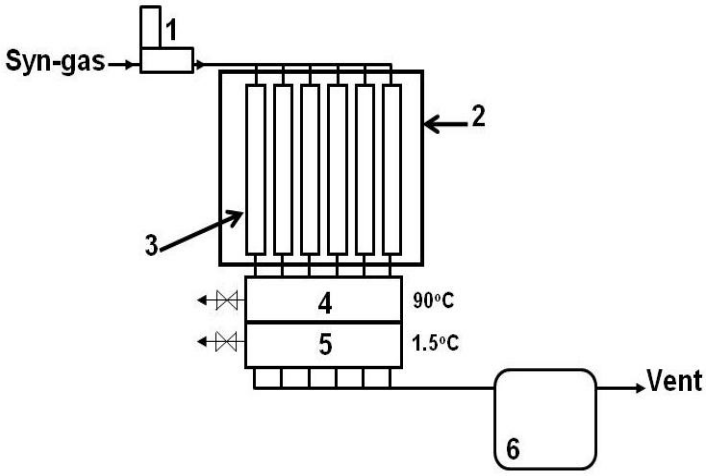

Figure 2.7 Sketch of the equipment used to test catalyst for Fischer-Tropsch synthesis. 1.- mass flow controller, 2.- furnace, 3.- stainless steel tube reactor, 4.- hot trap, 5.- cold trap, 6.- gas chromatograph.

2.4 Characterization techniques.

2.4.1 Powder X-ray diffraction.

Powder X-ray diffraction (XRD) is a technique widely used in catalyst identification [2]. It is used to identify the crystallographic phases present in the catalyst and to calculate average crystallite sizes.

X-ray diffraction is reliant on the scattering of photons by atoms arranged in a periodic lattice. The scattered X-rays that are in phase produce constructive interference. By measuring the angles of constructive interferences leaving the sample characteristic lattice spacing can be obtained (see Figure 2.8).

The X-rays are produced through the bombarding of a copper target with high-energy electrons from a tungsten source. X-rays are emitted by two processes: electrons slowed down by Bremsstralung (background); and a radiation that emerges due to a primary beam that creates a hole in the K-shell. The hole is filled by an electron from L-shell emitting X-ray radiation. This effect is called fluorescence and it is the basis of XRD technique [2]. An X-ray source (usually Cu

$K\alpha_1$) and rotating detector are used to measure the difference between incoming and diffracted beam (2θ angle). In order to obtain a representative pattern, the sample grains (or crystallites) should be randomly orientated; the random orientation allows all lattice planes to be hit at all required angles. Grains with 50 μm diameter inside a 10 mm diameter *x* 0.1 mm deep holder can be considered as a random orientated sample.

It is important to highlight that this technique has an important limitation. Diffraction peaks are only present when crystallites are ordered in a relatively large range. Thus, when diffraction peaks do not appear, it may be indicative either of amorphous or small crystallite domains.

The theoretical basis behind XRD analysis is based on Bragg's Law. According to this law when X-rays are diffracted from a sample the distances between atoms (d-spacing) forming the sample can be measured if 2θ angles are known [2]. Therefore, a set of d-spacing generated during XRD analysis can be compared against a reference pattern, since each crystalline system has a unique X-ray diffraction pattern. By comparing the experimental XRD pattern with a reference pattern, crystalline phases in a catalyst can be identified.

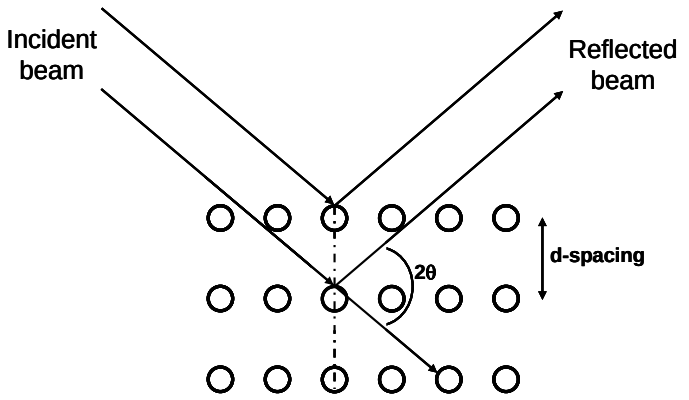

Bragg's Law: $n \cdot \lambda = 2 \cdot d \cdot \sin\theta$

Figure 2.8 Schematic picture of XRD analysis

The crystallite size (n) can be estimated using the Scherer correlation (Equation 2.2). The equation correlates the shape factor (K), the Bragg angle (2θ angle) and the characteristic wavelength (λ) with the full width at half maximum (b) of the diffracted peaks.

$$n=(K\cdot\lambda)/(b\cdot\cos\theta) \quad \text{Equation 2.2}$$

In this work, XRD diffraction patterns were collected in an X'Pert Pro diffractometer with a monochromatic Cu Kα source (λ = 0.154 nm) operated at 40 kV and 40 mA. The scans were recorded in the 2θ range between 10 ^{o} and 80 ^{o} using a step size of 0.016 ^{o} and scan step time of 55 seconds.

2.4.2 Fourier transform infra-red spectroscopy.

Fourier transform infra-red spectroscopy is a useful technique for identifying the type of bonds of chemical species [3]. Infra-red is a particular method measuring infrared spectra (IR) using the transmission pathway. Transmission IR can be used when bulk catalyst absorbs the IR beam weakly. The catalyst is typically compressed in a self-supporting disk of 1 cm^2 and few tenth of mm deep.

The infra-red spectrometer works on the principle of a Michelson interferometer. The major advantage is that a full spectrum can be obtained for each scan, drastically reducing the analysis time [2]. The optical devices can be made with NaCl (within the range 650 cm^{-1} to 4000 cm^{-1}), KBr (with a cut-off at 400 cm^{-1}) or CsI (with the most favourable cut-off at 250 cm^{-1}).

IR techniques work due to the fact that chemical bonds have specific vibration frequencies. The main types of vibrations are: stretch, bending in one plane, bending in 3 planes and torsion [2]. As different functional groups absorbs at different wavelengths, IR spectra provides characteristic information of functional groups presents in the catalyst.

In the current work, the catalyst was supported using dehydrated KBr. Thereafter, infra-red was carried out on a Jasco FT/IR 660 plus spectrometer in transmission mode in the 400-4000 cm^{-1} wave range.

2.4.3 Scanning electron microscopy.

Scanning electron microscopy (SEM) is a versatile tool for the examination and analysis of solid microstructures. It provides high resolution and good depth of field imaging compared to microscopy using visible light [4].

The basic components of SEM are the lens system, electron gun, the electron collector, the visual and photorecording equipment and the associated electronics [4].

SEM microscopy is performed by impacting a narrow electron beam over the sample surface (see Figure 2.9). When the electron beam interacts with the surface of the sample, two sorts of electrons are evolved: secondary and backscattered. The secondary electrons have mostly low energies, 5-50 eV, and originate from the sample surface. Whereas, backscattered electrons come from deep regions and carry information about sample composition. Therefore, an image can be produced. Image resolution in standard instruments is below micrometer scale, although resolution in more advanced instruments can be about 5 nm [2].

In the present work, SEM was used to observe particle morphologies. The fresh catalyst was dispersed on to an adhesive carbon disc and mounted on a 12.5 mm aluminium Stub. Analysis was performed using a Carl Zeiss Evo 40 model, normally operated between 5-20 kV and 50-2000 pA.

2.4.4 Energy dispersive X-ray spectroscopy.

Energy Dispersive X-ray analysis (EDX) uses the X-rays emitted from an excited sample to identify the sample composition. When a flat and polished sample surface is used, a quantitative analysis can be carried out within a precision close to 1-2% [4].

In the particular case of rough surfaces special care should be taken into account. As a consequence of geometrical effects, alterations in the absorption of scattered electrons appear. The arbitrary orientated surface can decrease X-ray production and vary the path causing re-absorption, as can be seen on Figure 2.10. Therefore, surface sample should be correctly orientated in order to avoid the problems described above [4].

In the present thesis, the EDX analysis was performed to examine the

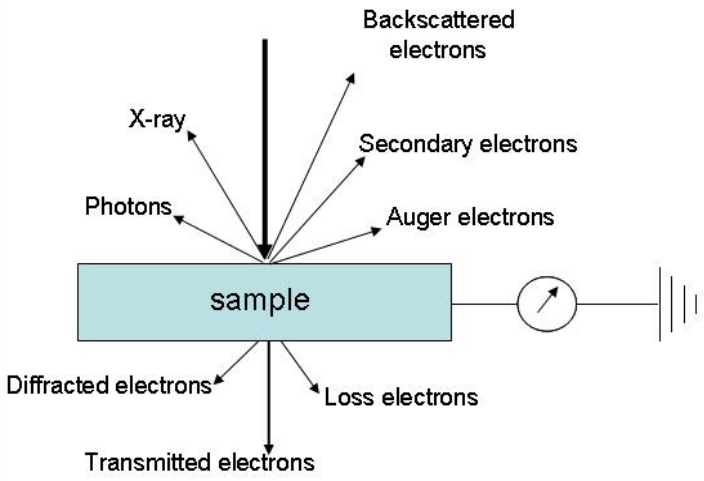

Figure 2.9 Schematic representation of electronic microscopy analysis [4].

composition of metal loadings. The analysis was carried out at 25 kV and 25 nA, and calibrated against cobalt standard.

2.4.5 X-ray photoelectron spectroscopy.

X-ray photoelectron spectroscopy (XPS) is a technique commonly used in catalyst characterization. It yields information at surface level about elemental composition, oxidation state and dispersion of catalyst components [2].

XPS is based on the photoelectric effect, in which an atom absorbs a photon of energy *hv*, and consequently a core or valence electron with binding energy E_b is ejected with a characteristic kinetic energy [2].

Usual XPS instruments are composed of an X-ray source Mg Kα (1253.6 eV) and Al Kα (1486.3 eV) and a hemispherical analyzer. Electrons pass through a filter and interact with the sample. Thereafter, electrons are recorded at the detector, which consists on an electron multiplier or a channeltron.

During the course of an XPS experiment intensity of photoelectron N(E) is recorded and plotted versus kinetic (E_k) or binding (E_b) energy as a function of E_k. The E_k or E_b contains particular information of each single element present in the catalyst. Therefore, one can use this information to identify the material.

In this work a Kratos Axis Ultra DLD spectrometer was used with a

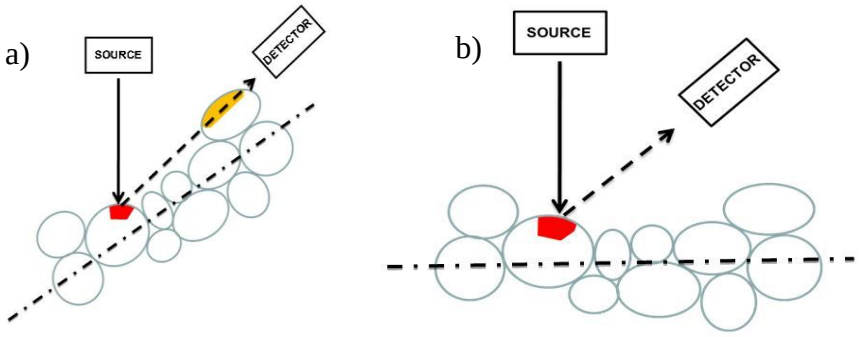

Figure 2.10 EDX analysis with (a) and without (b) interferences [4].

monochromatic Al-K_α X-ray source (75 W) and an analyser pass energy of 40 eV. Samples were mounted using double-sided adhesive tape, and binding energies are referenced to the C(1s) binding energy of adventitious carbon contamination taken to be 284.7 eV.

2.4.6 Thermogravimetic analysis.

Thermogravimetic analysis (TGA) is typically used to obtain information about sample composition, thermal stability and thermal decomposition of a sample. The analysis involves measuring mass change as a function of temperature. Different atmospheres can be used in order to observe material evolution under different conditions (air, inert and reducing atmospheres). TGA equipment is normally composed of a sensitive balance placed in a gas flowing furnace.

The physical and chemical properties of a sample can affect mass loss profiles in TGA. An example is the effect of particle size on the reaction temperature, due to mass transfer effects. Thermal conductivity of material can increase or decrease the temperature lag between the furnace and sample.

Differential thermal analysis (DTA) was also performed in the same equipment to observe the heat exchanged during decomposition. The principals of this analysis are the simultaneous monitoring of temperature in the crucible and in the oven by two thermocouples. The difference of temperature as consequence of phase transition or exothermic/endothermic reaction is expressed as potential difference between thermocouples measured by a voltammeter (mV) per unit of mass.

In this work TGA and DTA analysis are mainly applied to determine temperature, weight change and exothermic/endothermic nature of

decomposition reactions. All of the TGA analyses in the current work were carried out on a SETARAM Labsys thermogravimetric analyzer using 100 µl alumina crucible.

2.4.7 Atomic absorption spectroscopy.

Atomic absorption spectroscopy (AAS) is used to determine the metal content within a sample. A metallic atom is able to absorb light if it is excited by heat. The UV/VIS wavelength that is absorbed by the atom can be used as a fingerprint of this element. The process consists of spraying a solution into a flame, in order to atomise the metal. Meanwhile, a beam of light, with a particular wavelength, passes through the flame towards a detector. The detector measures changes in intensity of the beam. The intensity is related to the absorbance by the Beer Lamber Law and consequently the concentration of metal in solution.

In order to measure the concentration in a solution a calibration curve is required using standards with known concentration During the AAS analysis, successful operation of AAS often depends on the correct choice of flame, suitable preparation of samples and standards, careful optical alignment of the lamp with the monochromator and alignment of the burner with the light path.

In the current work, AAS is used to measure the sample metal content. All the analysis carried out with a Varian 22B Atomic Absorption spectrometer using an air-acetylene flame.

2.4.8 N_2 physisorption.

N_2 physisorption can be used to determine the surface area of a sample. The most widely used method is that reported by Brunauer, Emmet and Teller [5] (BET analysis). The BET method relies on the principle that gas molecules physically adsorb on a solid in layers infinitely. The BET assumes that there are no lateral interactions between adsorbed molecules and the surface comprises energetically equal surface adsorption sites. Hence, BET is able to determine surface area by measuring the amount of absorbed gas at low temperature and fixed pressure. Then using the BET approach, one can calculate the required amount of gas needed to cover a monolayer on the surface. In this work N_2 physisorption data was treated according to the BET method at constant temperature. The BET equation reads as follow:

$$\frac{P}{v\left(P/P_o\right)} = \frac{c-1}{v_m \cdot c}\left(\frac{P}{P_o}\right) + \frac{1}{v_m \cdot c} \quad \text{Equation 2.3}$$

Where v is the amount of gas adsorbed, usually N_2, P and P_o refer to equilibrium pressure and saturation pressure, v_m is the monolayer of adsorbed gas quantity. The c value refers to the BET constant. This equation is valid within the interval $0.05<P/P_o<0.35$. The intercept and the tangent of BET equation permit the calculation of v_m and c. The n_m, number of moles of adsorbate per gram of sample in the monolayer, is found from v_m. Finally the surface area can be calculated using:

$$A = n_m \cdot a_m \cdot L \quad \text{Equation 2.4}$$

Where a_m is the average area occupied by a molecule of adsorbate in the complete monolayer and L is the Avogadro constant, $6.023 \cdot 10^{23}$ mol^{-1}. As the N_2 is measure at the boiling temperature, 77.4 K, a_m may be estimated using a suggestion made by Emmett, Brunauer and Teller [5]:

$$a_m = k\left(\frac{M}{\rho_L \cdot L}\right)^{2/3} \quad \text{Equation 2.5}$$

Being M the N_2 molecular mass and ρ_L the density of liquid N_2 at 77.4 K and k a packing factor, k = 1.091.

For the BET surface area analysis, powder samples are first degassed at 120 °C to remove surface adsorbates. The analysis begins with evacuation of the chamber in order to remove adsorbed molecules from the surface followed by the N_2 deposition step at 77.4 K. The measurements were performed using Autosorb AS-1 (Quantachrome).

2.4.9 Temperature programmed reduction.

Temperature programmed reduction (TPR) is a characterization technique in which the chemical reduction of the bulk catalyst is monitored while temperature is increased [6].

The basic TPR experimental set up consists of a reactor, where catalyst is packed inside an electric heater. A thermal conductivity detector (TCD)

measures differences in thermal conductivity at the in/out flow. The variation in hydrogen can be measured by this difference.

As the sample reduces with respect to temperature, a TPR pattern is produced (normally TCD signal *vs.* temperature). The pattern shows temperatures where the catalyst reduces. Likewise, the area under the reduction peaks is proportional to the hydrogen consumed.

In this work, TPR has been used to follow the catalyst reducibility from 50 °C up to 900 °C and a ramp rate of 5 °C min^{-1} unless otherwise specified. The reducing gas used was H_2/Ar 10%.

2.4.10 H_2 chemisorption.

H_2 chemisorption describes the process in which a strong chemical bond is formed between the surface (catalysts) and an adsorbate (H_2) and furthermore presents high degree of specificity. This reaction involves the exchange of electrons between the atoms on the surface and adsorbate. It has been observed that chemisorbed species are stable at high temperatures and the adsorbtion enthalpies are within the range 40 to 1000 kJ mol^{-1}. The bonds formed can be ionic or covalent or a mixture. The formation of a chemical bond can be termed as non-dissociative or dissociative chemisorptions. There are two forms of dissociative chemisorptions: activated requiring additional energy and non-activated chemisorptions [7]. The case of H_2 chemisorption is dissociative and follows:

$$2\ M + H_2 \rightleftharpoons 2\ M\text{-}H \quad \text{Equation 2.6}$$

To perform the analysis 0.5 g of catalyst was reduced with 200 ml min^{-1} of 100% H_2 flow at 3 °C up to 425 °C and then held for 6 hours. After reduction the H_2 is removed by evacuation at 450 °C for 2 h after achieving vacuum of <10 μmHg. Then, the temperature is lowered to the analysis temperature of 150 °C. During the analysis 100% H_2 is dosed over a range of pressures between 100 and 760 mmHg. At each pressure is allowed to equilibrate and H_2 uptake is measured by volume difference.

In this work hydrogen chemisorption was performed to elucidate the total cobalt metal surface area. The equipment used was Micromeritics ASAP 2020 and analyses were performed at *Johnson Matthey* facilities.

2.4.11 Raman spectroscopy.

Irradiating a molecule with an incident beam of radiation gives rise to scattering, absorption or transmission. Such conditions give rise to Raleigh scattering where the scattered energy consists almost entirely of radiation of the incident frequency. In Raman spectroscopy the incident beam of radiation ($h\upsilon$) interacts with the molecule and the scattered beams consist of energies above and below that of the incident beam of radiation. The gain or loss of energy from the beam corresponds to the energy differences in the vibrational and rotational energy levels of the molecule. The quantum theory behind the Raman effect is as follows: radiation of frequency υ is treated as a stream of photons of energy $h\upsilon$. The photons can undergo inelastic or elastic collisions with the irradiated molecule. In the case of Raleigh scattering the collision is elastic and there is a known energy change. With an inelastic collision the molecule can gain or lose energy ΔE. If the molecule gains energy there is a loss of energy from the photon

as in hυ-ΔE and if the molecule loses energy there is a gain of energy in the photon as in hυ+ΔE. These two forms are referred to as stokes and anti-stokes radiation respectively [8].

In this work, Raman analysis was performed using a Renishaw inVia Raman Microscope fitted with a green Ar+ laser (λ = 514.532 nm).

2.4.12 Syn-gas stability test.

The stability of catalysts towards sintering under syn-gas conditions were studied at Liverpool University. The samples were first reduced under H_2, 50 ml min^{-1}, at 500 °C and ramp rate of 5 °C min^{-1} for 12 h. Then, catalysts were passivated under 1% O_2 in Ar, 50 ml min^{-1}, for 2 h at room temperature. At this point, XRD was performed to analyze the cobalt metal particles, range 38-57 2θ degree. Thereafter, syn-gas tests were performed using a CO:H_2 molar ratio of 1:4, 50 ml min^{-1}, at 230 °C for 100 h (before being passivated again under same conditions). Afterwards, cobalt metal particles were examined by XRD.

2.5 References.

1. Pourmortazavi, S. M.; Hajimirsadeghi, S. S., *Journal of Chromatography A* **2007,** *1163* (1-2), 2-24.

2. Niemantsverdriet, J. W., *Spectroscopy in Catalysis*. Wiley-VCH: Weinheim, 2007.

3. Schrader, B., *Infrared and Raman Spectroscopy*. VCH Publishers Inc: New York, 1995.

4. Goldstein, J.; Newbury, D.; Joy, D.; Lyman, C.; Echlin, P.; Lifshin, E.; Sawyer, L.; Michael, J., *Scanning Electron Microscopy and X-Ray Microanalysis*. 3rd ed.; Springer Science: New York, 2003.

5. Brunauer, S.; Emmett, P. H.; Teller, E., *Journal of the American Chemical Society* **1938,** *60*, 309-319.

6. Averill, B. A.; Moulijn, J. A.; van Leeuwen, P. W. N. M.; van Santen, R. A., *Catalysis: An Integrated Approach (Studies in Surface Science and Catalysis)*. 2nd ed.; Elsevier Science: Amsterdam 2000.

7. Elaine, M. C. M., *Surface Chemistry*. 1st ed.; Oxford University Press: Oxford, 2001.

8. Nakamoto, K., *Infrared and Raman Spectra of Inorganic and Coordination Compounds*. 5th ed.; New York, 1997.

3

Study into the effect of water during SAS precipitation

In this chapter a study into the effect of water in the SAS process on the performance of catalysts for propane total oxidation has been carried out. Propane total oxidation was chosen as a model reaction as the catalyst performance could be influenced by properties such as physical surface area and crystallite size.

3.1 Introduction.

Volatile organic compounds (VOCs) are continuously emitted into the atmosphere by industrial and automotive engines. These compounds are involved in ground level ozone formation[1], ozone depletion [2] and the greenhouse effect [3]. Amongst VOCs, short chain compounds are the most difficult to eliminate. The emission of alkanes, such as propane, has increased since the use of liquefied

petroleum gas (LPG), based on propane and butane, as fuel for engines has increased [4].

The development of a catalyst able to remove propane from these emissions is highly desirable. In Table 3.1 precious metal and non-precious metal based catalysts for propane combustion are compared [5]. So far, nanocrystalline Co_3O_4 and platinum supported systems are the most active with economic reasons encouraging research into precious metal substitution.

Watters *et al.* [6] studied the catalytic methane decomposition by 5% Au/MO, where MO = Co_3O_4, CeO_2, Fe_2O_3, NiO and MnOx. The authors reported low temperature activity of Au/Co_3O_4, between 200-225 °C for 1.48 vol% CH_4 and 21 vol% O_2 at 61 ml min^{-1}. Grisel and co-workers [7] increased the activity of 5% Au/Al_2O_3 for CH_4 oxidation by adding transition metal oxides to the catalyst, such as Zn, Co, Cr, Mn and Ni. The $Au/CuOx/Al_2O_3$ and $Au/MnOx/Al_2O_3$ were the most active catalysts at low temperatures, 350-400 °C, 0.8 vol% CH_4 and 3.2

Table 3.1 Catalysts used for propane total oxidation [5].

Catalyst	GHSV/s^{-1}	Reaction conditions	T_{10} /°C	T_{50}/°C
Nanocrystalline Co_3O_4	13	0.5% C_3 20% O_2	145	165
Co_3O_4–Avocado 4 m^2 g^{-1}	13	0.5% C_3 20% O_2	275	340
Co_3O_4 (15 m^2 g^{-1})	26	2% C_3, 10% O_2	250	290
Co_3O_4/CuO/Ni	6	0.5% C_3, 10% O_2	315	380
Perovskite LaCaCoO	5	2% C_3, 10% O_2	205	267
Au/Co_3O_4–Al_2O_3	2	1% C_3, 16% O_2	275	325
Co_3O_4–Al_2O_3	2	1% C_3, 16% O_2	305	355
Pt/Al_2O_3	2	1% C_3, 16% O_2	215	265
5% Pd/SiO_2–ZrO_2	260	0.25% C_3, 3% O_2	300	350
0.02% Pd/ZrO_2	19		340	510
0.33% Pt/Beta	17	0.8% C_3, 10% O_2	200	212
0.36% Pt/ZSM-5	17	0.8% C_3, 10% O_2	210	227
Perovskite LaSrMnNiO	10	1% C_3, 20% O_2	277	336
Perovskite LaSrCuFeO	10	1% C_3, 20% O_2	300	370
Rh/Al_2O_3	7	5% C_3, 25% O_2	360	380
Rh/Al_2O_3–SO_4	7	5% C_3, 25% O_2	320	330
1% Pt/Al_2O_3	45	0.4% C_3, 4% O_2	270	310
SO_2–1% Pt/Al_2O_3	45	0.4% C_3, 4% O_2	175	185
Sulphated 1% Pt/Al_2O_3	7	2.5% C_3, 15% O_2	150–200	210
1% Pt/TiO_2	4	0.4% C_3, 12% O_2	180–190	260
SO_2–1% Pt/TiO_2	4	0.4%C_3, 12% O_2		

T_X is the temperature required to achieve the specified conversion.

vol% O_2 at 30 ml min^{-1}. Morales *et al.* [8] co-precipitated a range of transition metal nitrates (Fe, Mn and Ni) as precursor catalysts for propane abatement (300 mg of catalyst with 50 ml min^{-1} of C_3H_8:O_2:He = 2:20:78). The authors observed lower temperature activity for co-precipitated NiMnOx (mixture of $NiMnO_3$ and Ni_6MnO_8) and FeMnOx (Mn_2O_3-Fe_2O_3 solid solution), 227-327 °C, than for the single oxides, NiO and Fe_2O_3, 250-350 °C and 300-500 °C, respectively. The relevant activity of NiMnOx was attributed to the high concentration of α-oxygen (surface O_2^- species). The enhancement of the activity by bimetallic oxides was also observed by Cadus *et al.* [8] where $Cu_{1.5}Mn_{1.5}O_4$ oxides presented better activity than the single CuO or Mn_2O_3, 200-342 °C, 277-427 °C and 200-425 °C respectively, in propane total oxidation (300 mg of catalyst with 50 ml min^{-1} of C_3H_8:O_2:He = 2:20:78).

Solsona *et al.* [4] compared the activity of supported and unsupported cobalt catalysts for propane deep oxidation (the reaction of propane and air to form CO_2 and H_2O) and found that the unsupported Co_3O_4 catalysts were more active than the alumina supported Co_3O_4 showing total combustion at 200-250 °C and 250-400 °C, respectively, using 250 mg of catalyst and 0.8 vol% of C_3H_8 in air at 50 ml min^{-1}. The authors observed that the catalyst activity decreased with decreasing surface area and increasing crystallite size. On the other hand, co-precipitated CuMnOx was found to be more active than palladium supported catalysts using 50 mg of catalyst and 0.5 vol% of C_3H_8 in air at 50 ml min^{-1}. This was further improved with gold additions, increasing the conversion from 60% up to 90% at 250 ºC. Moreover, these catalysts were stable over 24 hours at 250 °C (250 mg of catalyst and 0.8 vol% of C_3H_8 in synthetic air at 50 ml min^{-1}) [9]. Nanocrystalline Co_3O_4 was found to be a very active catalyst at low temperatures

(250 °C) for total propane combustion using flows of 0.5 vol% of C_3H_8 in air at 50 ml min^{-1} with 50 mg of catalyst [10]. Ordered Co_3O_4 with high surface area (177 m^2 g^{-1}) was synthesized showing high activity oxidizing 0.8 vol% of C_3H_8 in air at 50 ml min^{-1} with 250 mg of catalyst. However, Co_3O_4 with a surface area of 99 m^2 g^{-1} was found to be more active than the ordered Co_3O_4, and this was attributed to the oxygen defects observed in the latter metal oxide. This catalyst was further improved with the addition of gold as the activity increased from 40 % conversion up to *ca.* 100% conversion at 200 °C [11].

The mechanism of propane deep oxidation has been studied by several authors. For example, Solsona *et al.* [12] pointed to a Mars-van Krevelen mechanism driving the reaction on nanocrystalline Co_3O_4 at temperatures close to 200 °C. Liu [13] and co-workers correlated surface O_2^- species with highly active Co_3O_4 nanocrystalline at temperatures below 200 °C [14]. Likewise, Finocchio suggested the implication of surface O_2^- species in propane oxidation at low temperatures.

In this *Chapter*, the SAS precipitation was firstly used to screen different metal oxides as bulk catalysts for propane total oxidation. After identifying the most active metal oxide, different calcinations treatments were surveyed to obtain a very active nanocrystalline Co_3O_4 catalyst for propane total oxidation.

3.2 Screening of metal bulk catalysts.

3.2.1 Preparation.

Cobalt, copper, iron, manganese and nickel acetate salts were used to synthesize the catalysts listed in Table 3.2. Solutions of 7 mg ml^{-1} were prepared in 300 ml of methanol and stirred for 30 minutes. Then, syntheses were carried out under SAS conditions (see *Section 2.2.1*) in the *Separex* equipment (see *Section 2.1.2*). The SAS conditions are listed in Table 3.3.

Table 3.2. Chemicals used for catalysts synthesis.

Chemical	Company	Grade / purity
$Co(CH_3COO)_2 \cdot 4\,H_2O$	Sigma Aldrich	ACS reagent, ≥ 98.0%
$Co(CH_3COO)_2$	Sigma Aldrich	99.995% trace metals basis
$Cu(CH_3COO)_2 \cdot x\,H_2O$	Sigma Aldrich	ACS reagent, ≥ 98%
$Fe(CH_3COO)_2$	Sigma Aldrich	≥ 99.99% trace metals basis
$Mn(CH_3COO)_2 \cdot 4\,H_2O$	Sigma Aldrich	≥ 99%
$Ni(CH_3COO)_2 \cdot 4\,H_2O$	Sigma Aldrich	98%
$CoCO_3$	Sigma Aldrich	99.998% trace metals basis
Cobalt Oxide (II) (III)	Sigma Aldrich	99.995% trace metals basis
Methanol	Fisher-Scientific	Laboratory reagent grade
Methanol	Sigma Aldrich	Anhydrous 99.8%

Table 3.3. Experimental conditions for catalysts screening.

Pressure / bar	120
Temperature / °C	40
Inner nozzle diameter / µm	120
CO_2 flow rate / kg h^{-1}	9
Solution flow rate / ml min^{-1}	3.75
CO_2:methanol molar ratio	40:1

3.2.2 Results and discussion.

3.2.2.1 Fourier transform infra-red spectroscopy.

The infra-red spectra of the precipitated metal acetates are depicted in Figure 3.1. The bands at 1420 and 1568 cm^{-1} are assigned to COO^- symmetric and asymmetric stretching, respectively [15]. The bands at 665 and 618 cm^{-1} are indicative of COO^- bending and rocking frequencies [16]. The manganese and nickel precipitates showed strong bands at 1500 cm^{-1} that can be attributed to CO_3^{2-}, which is seen as a weak band in the cobalt precipitate. Likewise, bands attributed to CO_3^{2-} are visible at 840 cm^{-1} in all cases except iron. Copper precipitate shows the band at 840 cm^{-1} but as there was no observable band at

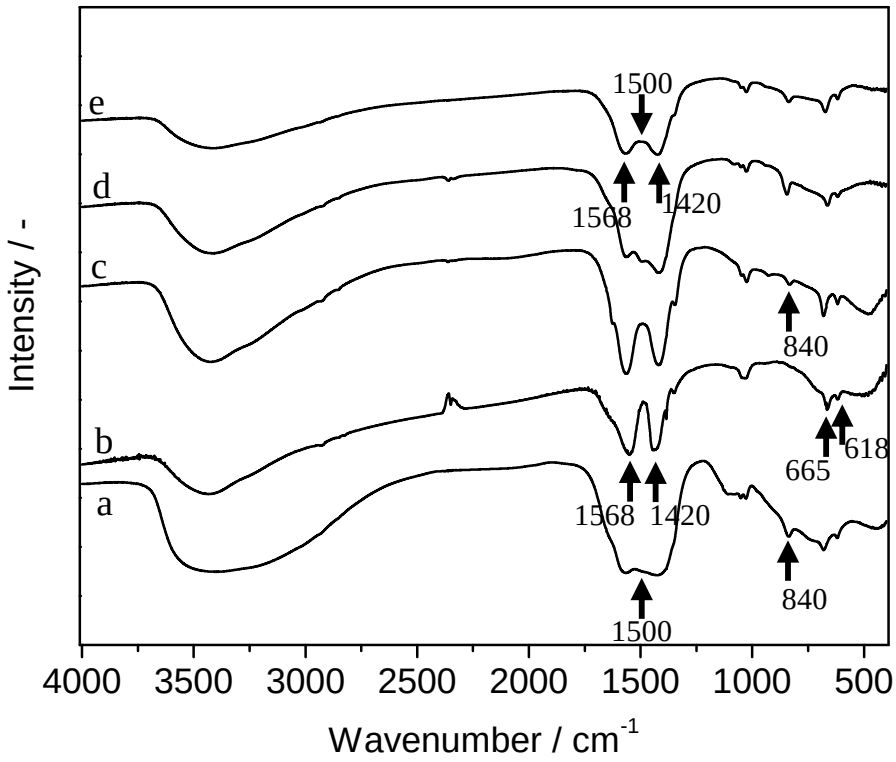

Figure 3.1 Infra-red spectra of metal precipitates: a) nickel precipitate; b) iron precipitate; c) copper precipitate; d) manganese precipitate; e) cobalt precipitate. Arrows indicate reference bands.

1500 cm^{-1} the presence of carbonate species is not clear. The bands at 1029 and 1051 cm^{-1} can be assigned to OH deformation modes, which can be due to adsorbed water or hydroxy compounds [17]. Likewise, the large shoulder around 3500 cm^{-1} can be assigned to hydroxy species or adsorbed water. Therefore, acetate and OH are present in all precipitated materials. Moreover, carbonate/hydroxycarbonate bands are present in cobalt, manganese and nickel precipitates, whilst in copper this is not clear.

Thus, the precipitated precursor catalysts are acetate based materials, which contain carbonate/hydroxycarbonate species in cobalt, manganese and nickel precipitates. The reaction of CO_2 with the coordinated water to form CO_3^{2-} may have permitted the formation of the carbonates/hydroxycarbonates.

3.2.2.2 Thermogravimetric analysis.

Thermogravimetic analysis was performed to study the decomposition of the precipitated metal acetates and is depicted in Figure 3.2.

The experimental weight losses from the iron and copper precipitates, 47% and 48% respectively, are close to the theoretical weight loss for metal acetates, 55% and 56% respectively, considering ±6% absolute error, as explained in *Appendix I*. Therefore, thermogravimetric observations suggest that, in this case, the SAS process produced acetate based materials and this agrees with bands observed in the infra-red analysis. The iron precipitate showed three exothermic decomposition steps (189, 221 and 259 °C, respectively) as for precipitated copper compound (199 °C, 239 °C and 261 °C), as seen in Figure 3.4. Pol *et al.* [18] observed the formation of Fe_3O_4 during the decomposition of iron acetate

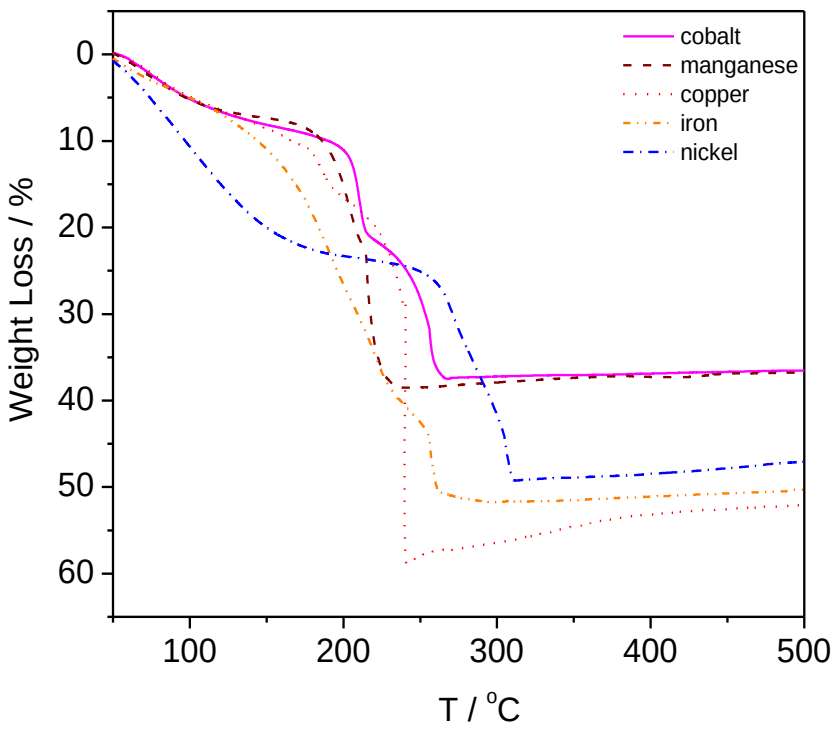

Figure 3.2. TGA of precipitated metal precursors. Experimental absolute error of ±6% calculated upon 4

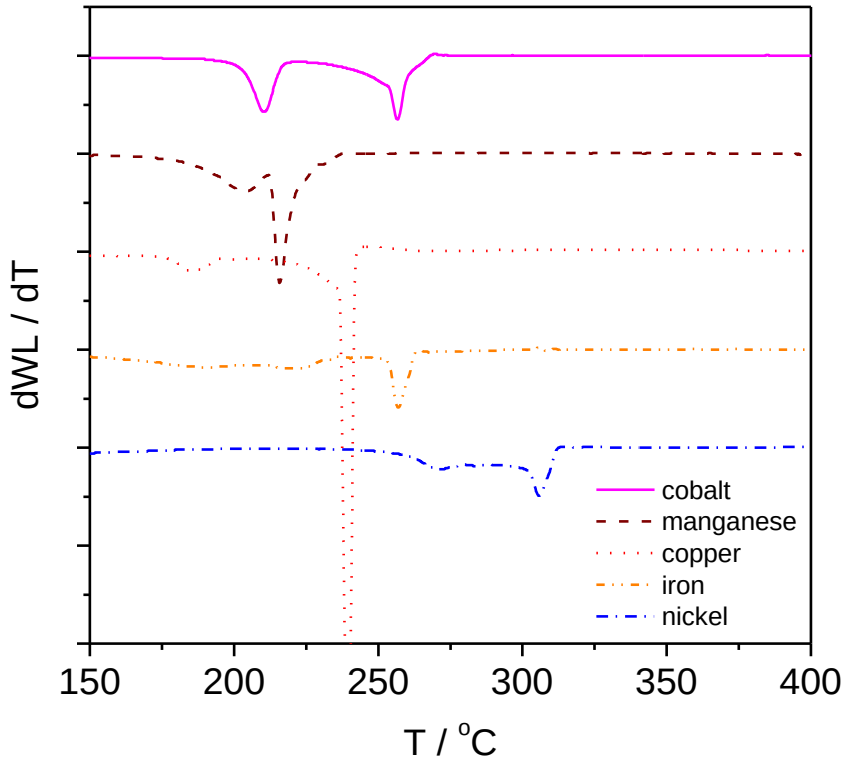

Figure 3.3. Differential thermal analysis (DTA) of metal precursors.

under N_2 *via* $FeCO_3$ formation, and it was observed that the acetates were completely decomposed at 400 °C. In the current work, the iron precipitate most likely decomposed in a different way as three decomposition steps were observed, which could be due to the formation of intermediates such as acetylacetates, as seen for cobalt acetate in Equation 3.1. Kondrat *et al.* [19] observed during the copper acetate decomposition, under static air, a weight loss at 250 °C accompanied by several exothermic steps, between 250-350 °C, that were assigned to the oxidation of Cu^+ or Cu. They also observed the auto-reduction of copper acetate to copper during decomposition. In the present work, most likely the precipitated copper acetate decomposed in the same way as that observed by Kondrat, as several exothermic peaks were also observed.

With regard to cobalt, manganese and nickel precipitates, the experimental weight losses of 28%, 25% and 29%, respectively, are below the theoretical

weight losses for acetates of 53%, 64% and 55%, to the correspondent metal oxide. The mismatch between the theoretical and the observed weight losses might arise from the precipitation of either non-stoichiometric metal acetates or the carbonate/hydroxycarbonates species observed in infra-red analysis. The cobalt, nickel and manganese precipitates decomposed in two steps: an endothermic decomposition at 210°C and an exothermic decomposition at 256 °C in the cobalt precipitate; two exothermic steps at 270 °C and 305 °C in the nickel precipitate and two exothermic decompositions at 203 °C and 215 °C in the manganese precipitate, as observed in Figures 3.3 and 3.4. It was suggested that $Co(CH_3COO)_2 \cdot 4\,H_2O$ decomposes *via* acetyl acetate (exothermic reaction), then the decomposition to acetate hydroxide (endothermic reaction) and finally complete oxidation to form Co_3O_4 under air (exothermic reaction) [15, 20], as follows:

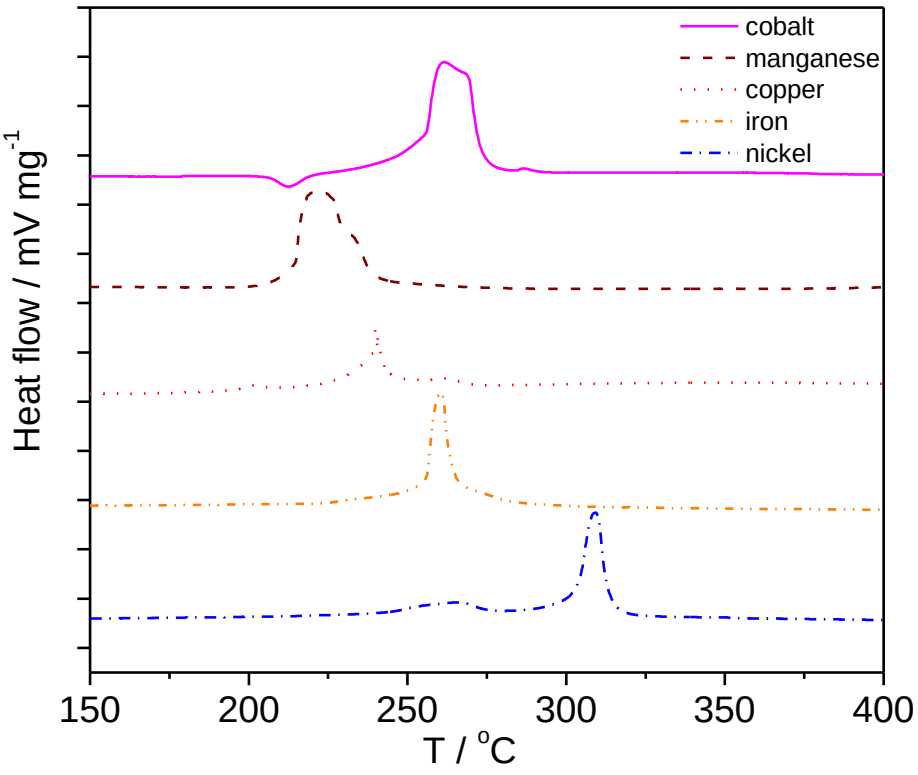

Figure 3.4. Differential thermal analysis (DTA) of metal precursors.

$$Co(CH_3COO)_2 \rightarrow Co(CH_3COO)COCH_3[+H_2O] \rightarrow Co(CH_3COO)OH \rightarrow Co_3O_4$$

Equation 3.1

The two decomposition steps in manganese and nickel may be assigned to the acetate decomposition *via* $M(CH_3COO)COCH_3$ and a final decomposition to form metal oxides as those were exothermic decompositions. The precipitated cobalt acetate showed an endothermic peak which is likely to be due to the decomposition of $Co(CH_3COO)_2$ to $Co(CH_3COO)OH$ (endothermic reaction) and subsequent exothermic decomposition to Co_3O_4. Overall, TGA suggests that SAS precipitates were metal acetates and according to the weight losses observed in cobalt, manganese and nickel, non-stoichiometric metal acetates. The presence of carbonate/hydroxycarbonates in cobalt, manganese and nickel precipitates cannot be ruled out as simultaneous acetate combustion and carbonate/hydroxycarbonate decomposition can take place [21].

The catalyst precursors were calcined at 400 °C to ensure complete acetate or carbonate/hydroxycarbonate elimination to form the metal oxides.

3.2.2.3 Powder X-ray diffraction.

The XRD patterns of the precipitated materials indicated that they are amorphous, as seen in Figure 3.5. The formation of amorphous precursors can be attributed to the faster nucleation time compared to time for crystal growth during the SAS precipitation, which yielded amorphous materials, and agrees with previous findings [22, 23].

The XRD patterns of the calcined samples showed oxide species, as can be seen in Figure 3.6 (Miller indices in brackets).

It should be noted that metal acetates have been shown to auto-reduce during activation under air [19]. In the particular case of copper acetate, Kondrat *et al.* [19] demonstrated that the oxidation state of copper can be tailored by adjusting the

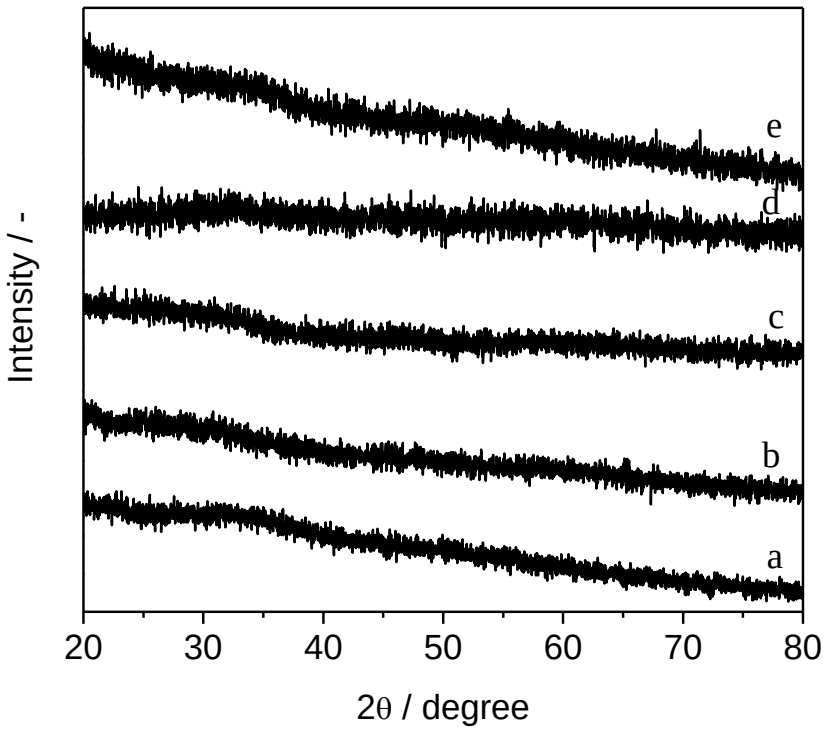

Figure 3.5. XRD diffractions of SAS precipitates: a) nickel precipitate; b) iron precipitate; c) copper precipitate; d) manganese precipitate; e) cobalt precipitate.

thermal treatment (time and O_2 concentration in the atmosphere). However, in the present work, the calcination time was fixed at 5 h, so the complete oxidation of precipitated copper to CuO was allowed, as seen in Figure 3.6. Even under N_2 atmospheres iron acetate can easily form Fe_3O_4 [18]; hence, the iron precipitated easily formed Fe_3O_4 during calcination. De Jesus [24] observed the decomposition of nickel acetate to NiO under air at temperatures close to 400 °C, and in the present work NiO was also obtained after the nickel precipitate was activated under static air. The cobalt precipitate formed Co_3O_4 after calcination, as previously observed by Wajun and Mohamed when decomposing cobalt acetate under air [20, 25]. MnO has been observed as the product from manganese acetate decomposition under air at 350 °C, which was further oxidised to Mn_2O_3 at 500

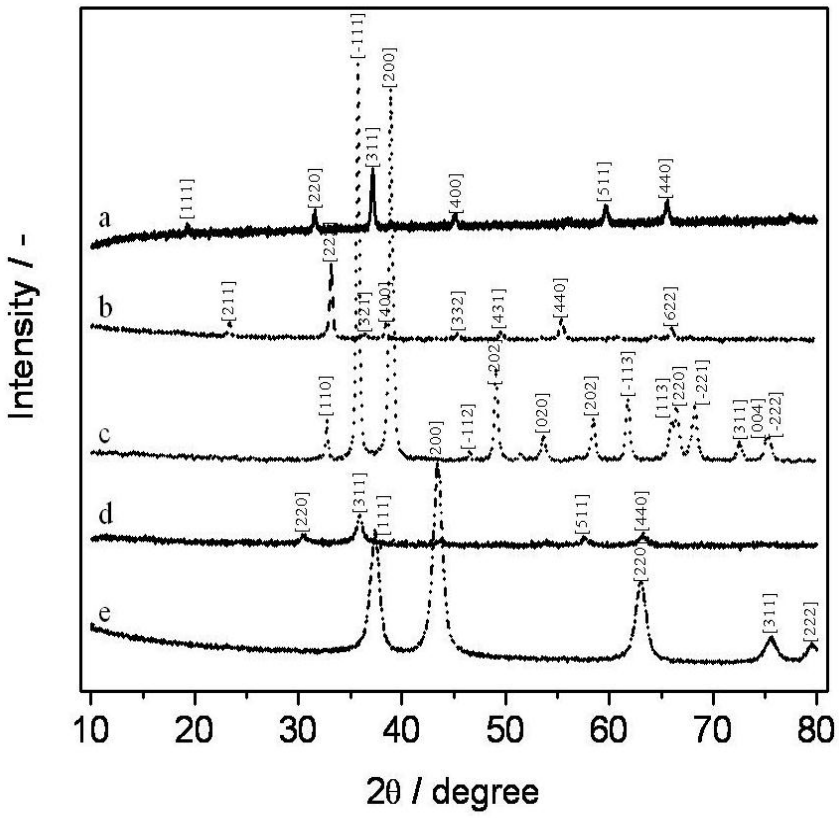

Figure 3.6. XRD diffraction of SAS precipitated materials calcined at 400°C. Miller indices in brackets. a) Co_3O_4, b) Mn_2O_3, c) CuO, d) Fe_3O_4, e) NiO.

Table 3.4. B.E.T. surface area, crystallite size and solution pH of metal screening experiments.

Material	Surface area / $m^2 g^{-1}$		Crystallite size	Solution pH
	Precipitated	After calcination at 400°C	nm	
cobalt	119	16	43	7.63
copper	72	2	49	6.75
iron	105	71	9	5.84
manganese	74	25	33	7.84
nickel	16	26	10	7.62

°C [15]. However, in the present work Mn_2O_3 was observed, most likely due to the relatively long calcination time (5 h) at 400 °C.

The crystallite sizes of the materials were obtained using the Scherrer equation, see *Section 2.4.1*, and results are shown in Table 3.4. The crystallite size ranges from 9 nm up to 49 nm depending on the nature of the metal oxide.

3.2.2.4 N_2 physisorption.

N_2 physisorption analysis was performed on both precipitated and calcined materials to obtain the physical surface area using the B.E.T method (Table 3.4).

As has previously been observed [26], the surface area of many SAS precipitated materials drops after calcination (Table 3.4). The surface area of the nickel material slightly increased after calcination, however this was not further investigated. The decrease in surface area can be attributed to the exothermic

decomposition of the acetates that may enhance particle aggregation and sintering.

3.3.2.5 Temperature programmed reduction.

The TPR profiles of calcined metal bulk catalysts are shown in Figure 3.7. For cobalt oxide, the standard reduction profile reported in the literature was observed: Co_3O_4 to CoO and CoO to Co [27]. The three reduction steps observed in NiO were previously reported and attributed to both loss of non-stoichiometric oxygen (low temperature peak), the medium temperature peak is contributed by the reduction of small particles, whereas the highest temperature peak was assigned to the largest particles [28]. Mn_2O_3 showed the reduction steps from Mn_2O_3 to Mn_3O_4 and the high temperature peak was attributed to reduction of Mn_3O_4 to MnO [29]. The Fe_3O_4 bulk catalyst presented a typical reduction profile

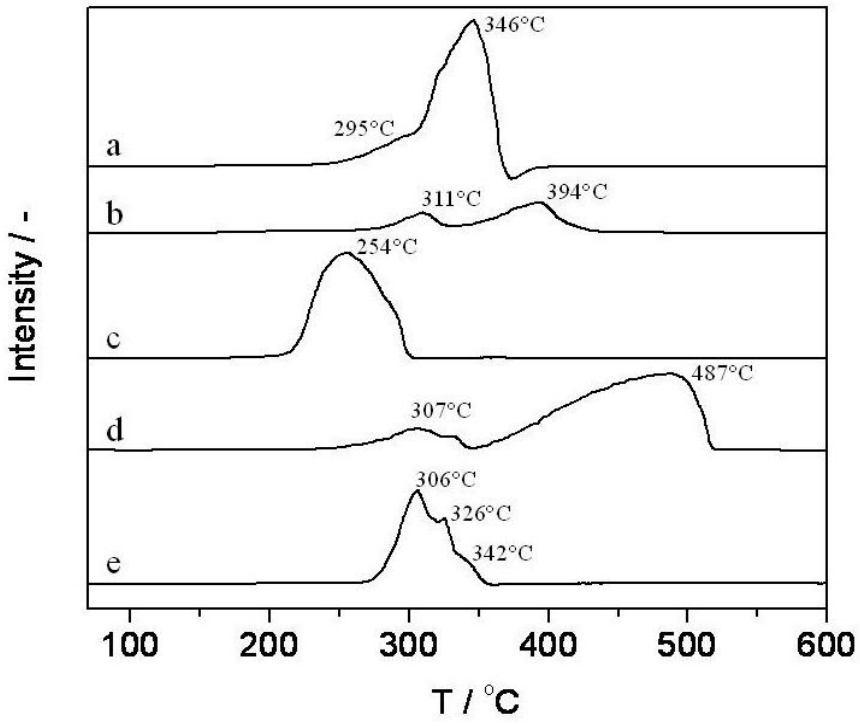

Figure 3.7. TPR profile of the metal oxide catalysts. a) Co_3O_4, b) Mn_2O_3, c) CuO, d) Fe_3O_4, e) NiO.

in two steps, Fe_3O_4 to FeO and further reduction to Fe [30]. The CuO bulk catalyst presents one peak (CuO to Cu) as the favourable kinetic reduction conditions avoided the Cu_2O formation, as reported by Kim *et al.* [29, 31, 32].

3.2.2.6 Propane total oxidation.

The precipitated materials were tested, after calcination at 400 °C, for propane total oxidation as described in *Section 2.3.1*. The light-off profiles and selectivities towards CO_2 and propene are plotted in Figures 3.8 and 3.9, respectively, with each data point the average of 3 injections. The data were reproducible within 7% relative error.

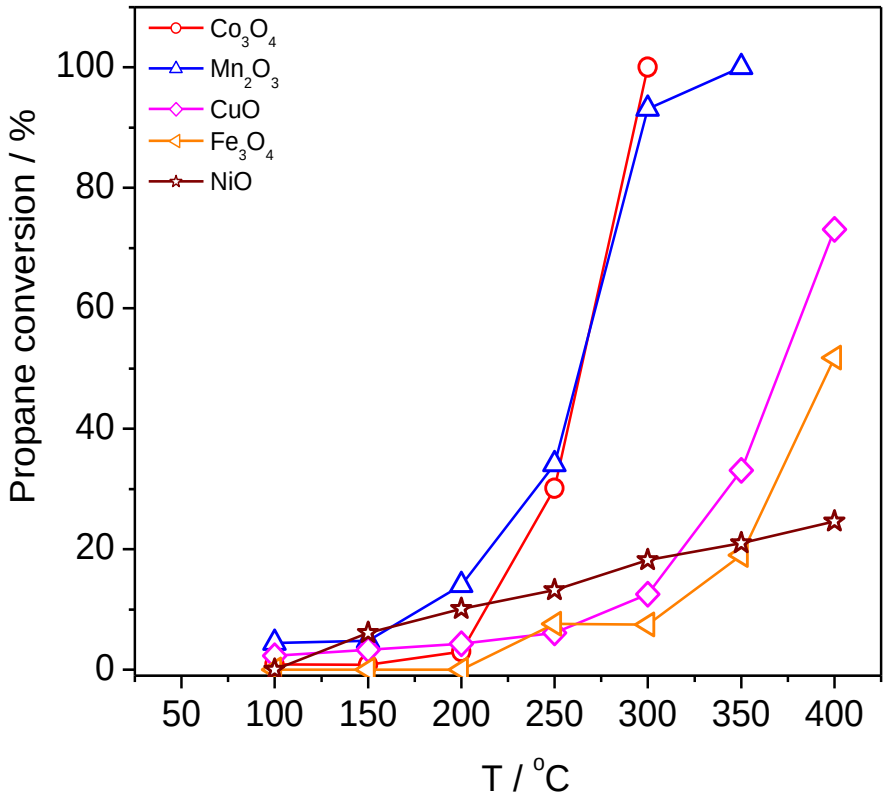

Figure 3.8. Catalytic performance of SAS precipitated metal oxides for propane total oxidation. Reaction conditions: 0.1 g of catalyst, 50 ml min^{-1} of synthetic air (O_2 20 vol% in He) and propane (0.4 vol%).

The light-off for the cobalt and manganese oxides was observed at 225-250 °C with a slightly higher temperature of 300 °C for the iron and copper oxides. The iron and copper oxide catalysts needed high thermal energy to be activated. Nickel did not show light-off and conversion increased steadily with temperature. In terms of low temperature propane conversion, cobalt and manganese oxides were the most attractive catalysts.

The CO_2 yield over the catalysts is depicted in Figure 3.10. This yield increases with propane conversion and is also dependent on temperature.

Propene was the predominant product below 250 °C in all cases, except for iron oxide where neither propene nor any other organic compounds were detected. It should be mentioned that the manganese oxide catalyst also converted propane to

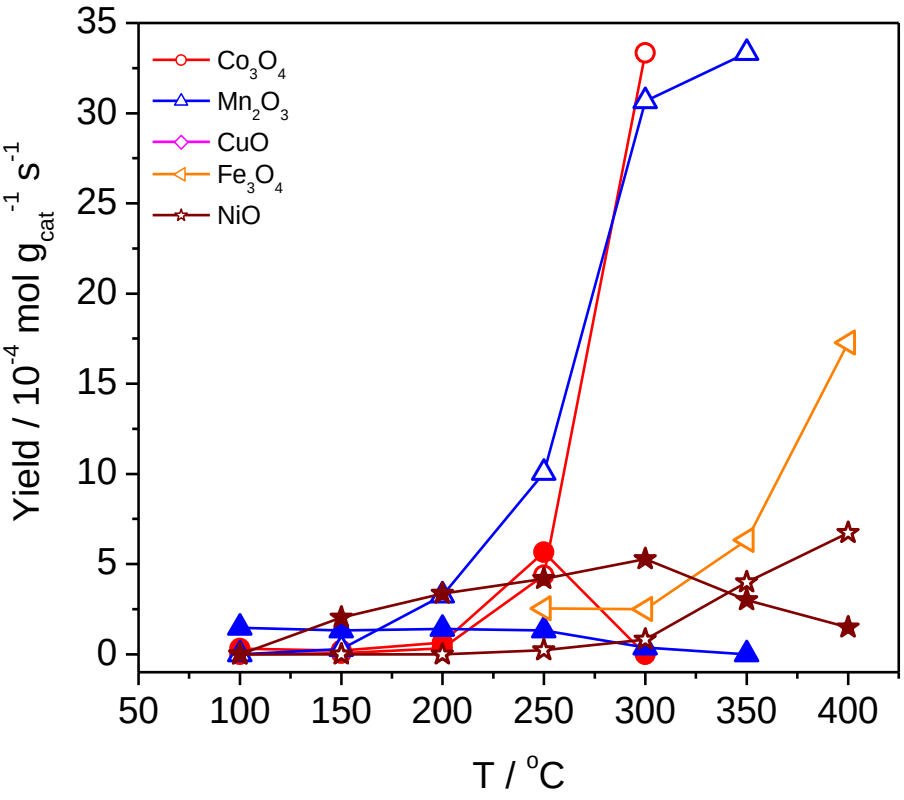

Figure 3.9. Yields of products of propane oxidation. Solid figures CO_2 yield, open figures propene yield.

small amounts of an unknown organic compound at temperatures above 300 °C, however this compound was not identified.

The SAS prepared Mn_2O_3 and Co_3O_4 showed similar or even better performance than other metal oxides used as catalysts for propane total oxidation under similar conditions. For instance, Solsona *et al.* [8] observed total propane combustion at 250-300 °C over nanocrystalline Co_3O_4 and Morales [8] and collaborators reported complete oxidation of propane over Mn_2O_3 above 300 °C.

3.2.2.7 Conclusions.

SAS precipitated materials predominantly comprised acetates with some materials containing carbonates/hydroxycarbonates. The formation of these carbonate/hydroxycarbonate precursors can be correlated to the coordinated water. Interestingly, the solution pH may also be important for carbonate/hydroxycarbonate formation, with more acidic starting solutions less likely to form carbonate/hydroxycarbonate.

Calcination of the precipitated materials at 400 °C produced metal oxides with a reduced surface area compared to the uncalcined material which could be as a consequence of particle sintering promoted by the exothermic acetate decomposition, with the nickel catalyst being an exception.

Following the propane test reaction, the metal oxide catalysts could be divided in to three main groups:

1. Low temperature activity, below 250 °C: Cobalt and manganese oxides are noteworthy for low temperature reaction.

2. High temperature activity, above 250 °C: Iron and copper. The case of iron could be interesting due to 100% selectivity towards CO_2.
3. Non activation temperature: the activity of nickel oxide was very poor and increased steadily without light-off temperature within the studied range.

In the present study, the Co_3O_4 and Mn_2O_3 were found as the most active phases for low temperature propane total oxidation amongst the studied transition metals and showed similar or even better catalytic performance than reported catalysts.

3.3 Carbonate formation under SAS conditions.

Previous studies on copper manganese oxides showed that if carbonate species were formed during the SAS process, the surface area of the material after calcination remained constant or even increased leading to CuMnOx with CO activity higher than commercial catalysts [26]. Thus, in this work the formation of carbonates under SAS conditions was studied and three hypothesis were suggested: 1.- carbonaceous species are formed as the material is precipitated; 2.- carbonaceous species are formed after precipitation by an aging process; 3.- carbonaceous species are formed both during precipitation and aging.

3.3.1 The CO_2/methanol/water system at working conditions.

It is thought that carbonates are formed during the SAS process due to the presence of water [26]. The CO_2 dissolves in water as follows:

$CO_2 + H_2O \rightleftharpoons H_2CO_3$ Equation. 3.2

The formed carbonic acid dissociates as follows:

$H_2CO_3 + H_2O \rightleftharpoons H_3O^+ + HCO_3^-$ Ka_1 Equation 3.3

$HCO_3^- + H_2 \rightleftharpoons H_3O^+ + CO_3^{2-}$ Ka_2 Equation 3.4

The dissociation constants (Ka_1 and Ka_2) associated with these equilibrium are temperature and pressure dependent; hence, the rate of carbonate formation should also be temperature and pressure dependent.

The pH of CO_2/H_2O between 25 °C and 70 °C and pressures between 70 bar and 200 bar were estimated to be 2-4 [34]. Normally the pH of methanol is not equivalent to the hydrogen ion activity ($pH = -log(a_H)$) but to the methanol autoprotolysis ($CH_3OH\text{-}H^+$) giving a pH of 8.2. It is worth noting that in the presence of water the following equilibrium can be depicted:

$CH_3OH\text{-}H^+ + H_2O \rightleftharpoons CH_3OH + H_3O^+$ Equation 3.5

The pKa of H_3O^+ and $CH_3OH\text{-}H^+$ are -1.7 and -2.2, respectively, and in a system with both species, the equilibrium will be further displaced towards right. Thus, in methanol/H_2O solutions, the acidity predominantly will come from H_3O^+, whereas in anhydrous solutions acidity will come from $CH_3OH\text{-}H^+$. Hence, in methanolic $Co(CH_3COO)_2 \cdot 4\,H_2O$ solutions the acidity most likely will be equivalent to the hydrogen ion activity, with more acidic starting solutions being less likely to form carbonates, as the presence of H_3O^+ will displace Equations 3.3 and 3.4 to the left, ultimately hampering the formation of CO_3^{2-}. However, in this study, for the sake of simplicity, temperature and pressure were kept constant and the pH of the solution was not adjusted.

Table 3.5. Henry's constant, k_H in molality scale for different methanol/H_2O molar fractions (CO_2 free basis) at 40 °C. CO_2 molality in methanol/H_2O calculated using equation 3.6.

Methanol molar fraction	$Ln[k_H^{(m)}/MPa]$	k_H	kg CO_2 / kg solvent
1.000	-0.496	7.308	1.642
0.952	-0.410	7.964	1.507
0.901	-0.310	8.801	1.363
0.750	0.084	13.052	0.919

Xia *et al.* [35] reported solubilities of CO_2 in methanol/H_2O for different methanol molar fractions in the temperature range of 40-122 °C. An increase in solvation power was observed at high pressures and high methanol molar fractions. In this work, the solubility of CO_2 in methanol/H_2O at different methanol molar

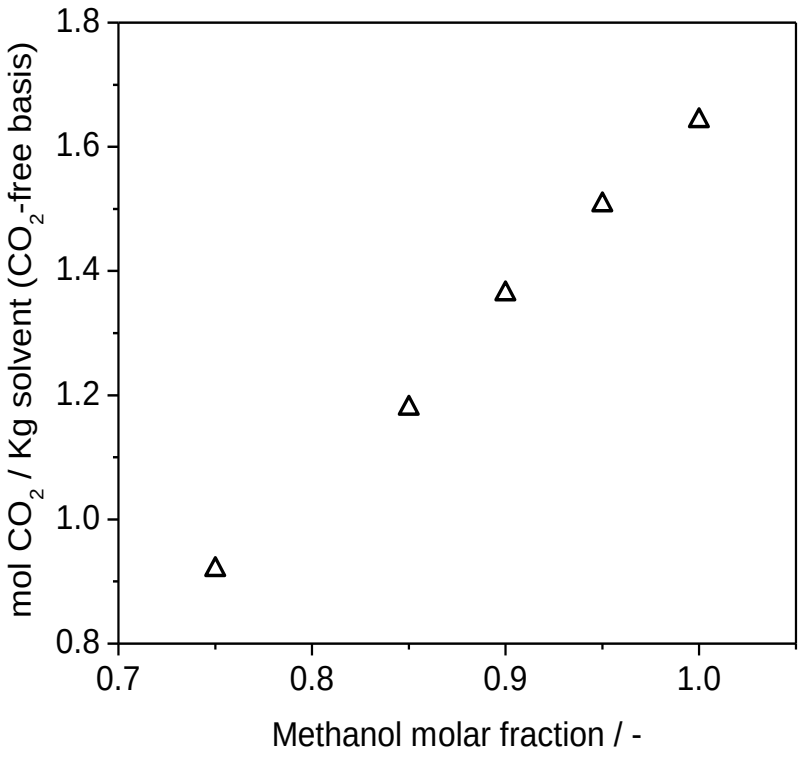

Figure 3.10. Solubility of CO_2 in methanol/H_2O for different methanol molar fractions at 40°C and 120 bar. Solubility expressed as mol of CO_2 per Kg of solvent (methanol + H_2O).

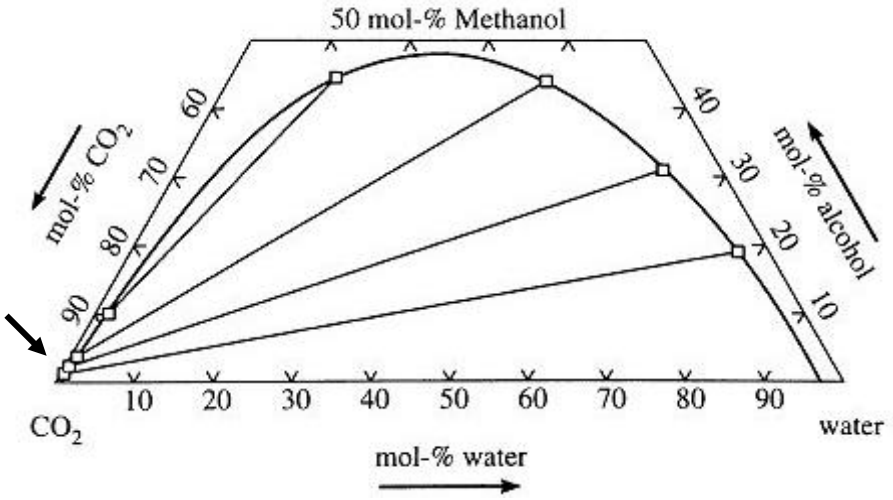

Figure 3.11. Phase diagram of CO_2/methanol/H_2O at 40 °C and 100 bar. Arrow indicates the region where experiments with $Co(CH_3COO)_2 \cdot 4\,H_2O$ in methanol was performed.

fractions at working temperature and pressures were estimated using Henry's law, as seen in Equation 3.6, using the parameters listed in Table 3.5 [35], results are shown in Figure 3.10.

$$p = k_H \cdot C \qquad \text{Equation 3.6}$$

where p refers to the partial pressure of solute, k_H to Henry's constant and C to the concentration of solute.

The solubility of CO_2 decreases as the H_2O molar fraction increases; therefore, as precipitation is based on the antisolvent effect of CO_2, large amounts of water may hamper the CO_2 dissolution and ultimately the precipitation.

The phase behaviour of CO_2/methanol/H_2O has been reviewed by Adrian [36]. For low H_2O molar fractions at 100 bar and 40 °C the system lays on the boundary between a single phase and a 2-phase system, as seen in Figure 3.11. Therefore,

precipitations carried out at 120 bar and 40 °C are on the boundary of the 2-phase system, as the boundary between single phase and 2-phases shrinks with pressure and increases in dynamic systems, *i.e.* under SAS conditions [37].

3.3.2 Preparation.

Experiments were carried out in the *Jerguson* equipment (see *Section 2.1.1*) following the experimental procedure described in *Section 2.2.1*. Experimental conditions are summarized in Table 3.6. Solutions were prepared using anhydrous cobalt acetate (7 mg ml^{-1}) in anhydrous methanol, referred to as *water-free* experiments. Additionally, 5 vol% H_2O in anhydrous methanol solutions were prepared to probe the effect of water.

Table 3.6. Experimental list of catalysts made to study carbonate formation under SAS conditions.

Sample name	Process	Solvent	Aging solution	Aging time
S-Aged-H_2O	SAS	methanol	5% methanol/H_2O	1.5 h
S-Aged-MeOH	SAS	methanol	methanol	1.5 h
S-Non-aged	SAS	methanol	-	-
S-Non-aged-H_2O	SAS	5% methanol/H_2O	-	-
A-Aged-H_2O-1.5	SC-Aging	-	5% methanol/H_2O	1.5 h
A-Aged-MeOH-1.5	SC-Aging	-	methanol	1.5 h

Note: prefix S- stands for anhydrous cobalt acetate precipitated by SAS, i.e. first dissolved in a solvent and then precipitated by SAS; whereas A- prefix stands for as-received anhydrous cobalt acetate aged by different solutions.

3.3.3 Results and discussion.

3.3.3.1 Fourier transform infra-red spectroscopy.

Infra-red analysis was performed to elucidate the nature of aged and non-aged materials, as can be seen in Figure 3.12. The materials formed during the process could be classified as either carbonate or acetate based materials.

The acetate based materials showed bands at 1558-1564 and 1411-1423 cm^{-1} assigned to COO^- asymmetric and symmetric stretching bands, respectively. Additionally, the COO^- rocking band at 618 cm^{-1} was observed. The bands at 1344, 1050 and 1026 cm^{-1} were assigned to CH_3 bending and rocking modes [16]. The band at 1342 cm^{-1} assigned to CH_3 symmetric bending [16] was much stronger in the commercial cobalt acetate than the S-Aged-MeOH-1.5 where it appeared as a shoulder. The band at 838 cm^{-1} (assigned to CO_3) and the weak band at 1500 cm^{-1} (assigned to CO_3^{2-}) were visible in S-Aged-MeOH-1.5 and S-Non-aged-MeOH [17, 38]. This indicates that traces of carbonates were formed during the SAS process, even if experiments were done under *water-free* conditions. Therefore, it

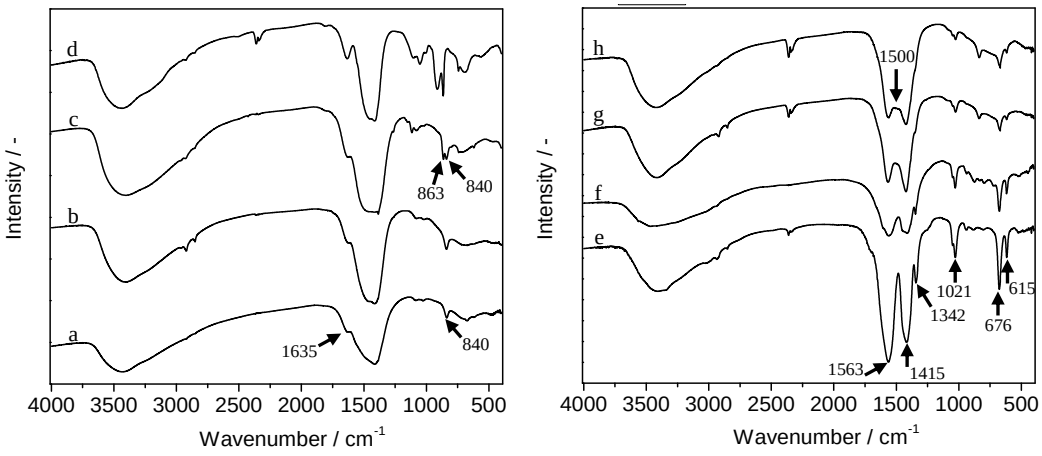

Figure 3.12. Infrared spectra of carbonate base materials, a) A-Aged-H_2O, b) S-Aged-H_2O,c) S-Non-Aged-H_2O, d) commercial $CoCO_3$; and acetate based materials, e) commercial $Co(ac)_2$, f) A-Aged-MeOH, g) S-Non-Aged-MeOH, h) S-Aged-MeOH.

can be concluded that SAS precipitation under *water-free* conditions yields cobalt acetate containing small amounts of cobalt carbonate that are formed if traces of H_2O are present (*e.g.* the CO_2 cylinder and anhydrous methanol may contain traces of H_2O).

The carbonate materials showed typical OH stretching vibrations, associated with adsorbed H_2O or OH species. The shoulder observed in commercial $CoCO_3$ was assigned to H_2O interacting with carbonate anions [21]. The band at 1635 cm^{-1} (assigned to the OH bending mode) [39] is more intense than in the commercial sample, suggesting a higher degree of hydration. The plateau at 1500cm^{-1} and bands at 865 and 840 cm^{-1} are all assigned to CO_3^{2-} stretching vibrations, albeit the band at 840 cm^{-1} is only present in precipitated materials and was attributed to the presence of hydroxycarbonates [21, 39]. The Co-OH bending mode (913 cm^{-1}) is only observed in commercial $CoCO_3$.

In summary, infra-red analysis suggests that the addition of water leads to the formation of carbonates and/or hydroxycarbonates that have a higher degree of hydration than commercial $CoCO_3$.

3.3.3.2 Thermogravimetric analysis.

The unprocessed anhydrous $Co(CH_3COO)_2$ showed a large weight loss in three steps, as can be seen in Figure 3.13-a. The first step, from 70-150 °C, was assigned to the removal of adsorbed water (4% weight loss). The second decomposition step (11% weight loss) was assigned to the formation of intermediate compounds (*i.e.* $Co(CH_3COO)COCH_3$ and $Co(CH_3COO)OH$) formed during decomposition [20] and the final weight loss (31%) corresponds to Co_3O_4 formation. The SAS precipitated materials A-Aged-MeOH, S-Aged-MeOH and S-Non-aged-MeOH also presented three decomposition steps that were assigned to the cobalt acetate decomposition pathway. In the particular case of S-Aged-MeOH, the total weight loss is significantly lower than other samples, 32% compared to *ca.* 40% excluding the weight loss attributed to the water or methanol desorption. This observation can be attributed to the aging time under SAS conditions that may cause modifications in the cobalt acetate coordination (*e.g.* formation of non-stoichiometric cobalt acetate). It is worth noting that precipitated materials present weight changes at lower temperatures than commercial material, which may be attributed to differences in particle size [40].

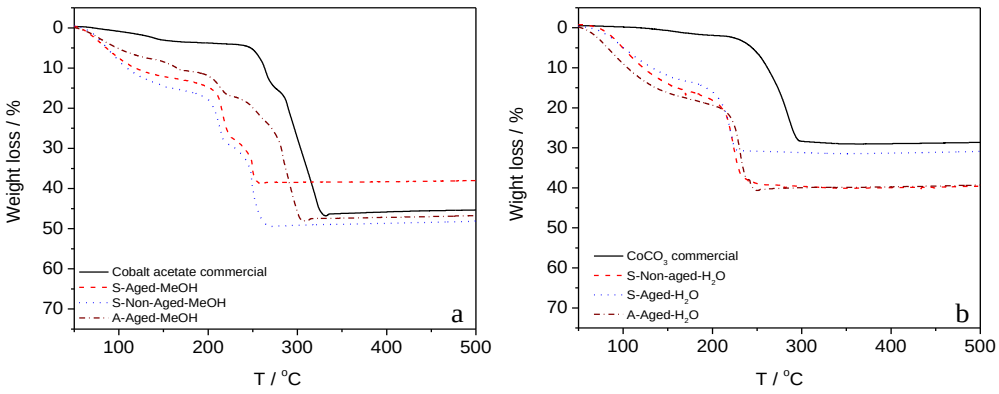

Figure 3.13. TGA of acetate based materials a) and carbonate based materials b). Absolute error in weight loss (±6%) has been estimated over repetitions.

As seen in Figure 3.13-b, the commercial cobalt carbonate presents one decomposition step with a total weight loss of 29%, close to the theoretical weight loss of 32% for $CoCO_3$ decomposition to Co_3O_4. The SAS precipitated carbonate based materials lost weight during an initial step, between 70 and 150 °C, possibly due to the loss of either water or methanol that could be trapped in the structure during the precipitation process. Total weight losses (excluding solvent desorption) were 24%, 19% and 22% for S-Non-Aged-H_2O, S-Aged-H_2O and A-Aged-H_2O, respectively. These weight losses were far from the theoretical weight loss for $CoCO_3$ decomposition to Co_3O_4 and close to the value expected for decomposition of $Co(OH)_2CO_3$ or $Co(OH)_{1.42}(CO_3)_{0.29}\cdot 0.04\,H_2O$, as seen in Equation 3.7 and 3.8 (theoretical weight loss of 24.2% and 25.5% respectively) [21, 39]. Consequently, it can be concluded that water promotes the formation of cobalt carbonate/hydroxycarbonate, when it is either in the starting solution or in the solution used to age the materials after precipitation.

$$Co(OH)_2CO_3 \rightarrow Co_3O_4 + H_2O \quad \text{Equation 3.7}$$

$$Co(OH)_{1.42}(CO_3)_{0.29}\cdot 0.04\,H_2O \rightarrow Co_3O_4 + H_2O \quad \text{Equation 3.8}$$

3.3.4 Conclusions of carbonate investigations.

Experiments suggested that $CoCO_3$ or $Co(OH)_{1.42}(CO_3)_{0.29}\cdot 0.04\,H_2O$ are formed in the SAS precipitated materials in the presence of water, both in starting and aging solutions. Likewise, carbonate/hydroxycarbonate traces were observed in *water free* experiments. Herein, it has been demonstrated that carbonates can be formed aging cobalt SAS precipitates, however at this point is still not clear

whether this carbonaceous species were also formed during the precipitation step.

3.4 Synthesis of cobalt catalysts for propane oxidation.

3.4.1 Preparation.

To prepare cobalt catalysts, $Co(CH_3COO)_2 \cdot 4\ H_2O$ was dissolved in H_2O/methanol solutions (7 mg ml^{-1}) with four different water additions: 0, 5, 10 and 15 vol%. The precipitates were labelled as: Co-0-P, Co-5-P, Co-10-P and Co-15-P, respectively. The precursors were precipitated using the SAS process described in *Section 2.1.2* using the experimental parameters listed in Table 3.3. The catalyst precursor, Co-A-P, was precipitated from a solution of 0% H_2O/methanol and then aged after precipitation by a solution of 5% H_2O/methanol under SC-CO_2 at 120 bar and 40 °C for 1.5 h.

The precipitated materials were calcined at 400 °C for 5 h under static air (labelled as Co-0-C, Co-5-C, Co-10-C, Co-15-C and Co-A-C) and tested for propane total oxidation using 0.1 g catalyst with 0.4 vol% C_3H_8 in synthetic air (20 vol% O_2 in He) at 50 ml min^{-1}. As a comparison, $Co(CH_3COO)_2 \cdot 4\ H_2O$ and $CoCO_3$ were calcined at 400 °C (labelled as Co(ac)-C and $CoCO_3$-C) and tested for propane oxidation. Also, commercial Co_3O_4 (labelled as Co_3O_4) was tested without further treatment.

3.4.2 Results and discussion.

3.4.2.1 Fourier transform infra-red spectroscopy.

The infra-red analyses of precipitated materials are illustrated in Figure 3.14. The Co-0-P showed the characteristic COO^- bands at 1566 and 1425 and 618 cm^{-1}, which represent asymmetric, symmetric and rocking modes, respectively. A weak band can be seen in the 1500 cm^{-1} region suggesting CO_3^{2-}, with the band at 630 cm^{-1} suggesting CO_3^{2-} in Co-0. The Co-5-P, Co-10-P, Co-15-P and Co-A-P showed characteristic CO_3^{2-} bands in the 1500 cm^{-1} region. The band at 1635 cm^{-1}, associated with -OH bending grew in intensity upon water addition suggesting an increase in the degree of hydration. It is worth noting that the band at 830 cm^{-1} in Co-15 shifts towards 839 cm^{-1} in Co-0-P, Co-5-P, Co-10-P and Co-A indicating differences in CO_3^-. A sharp band at 863 cm^{-1} was visible only

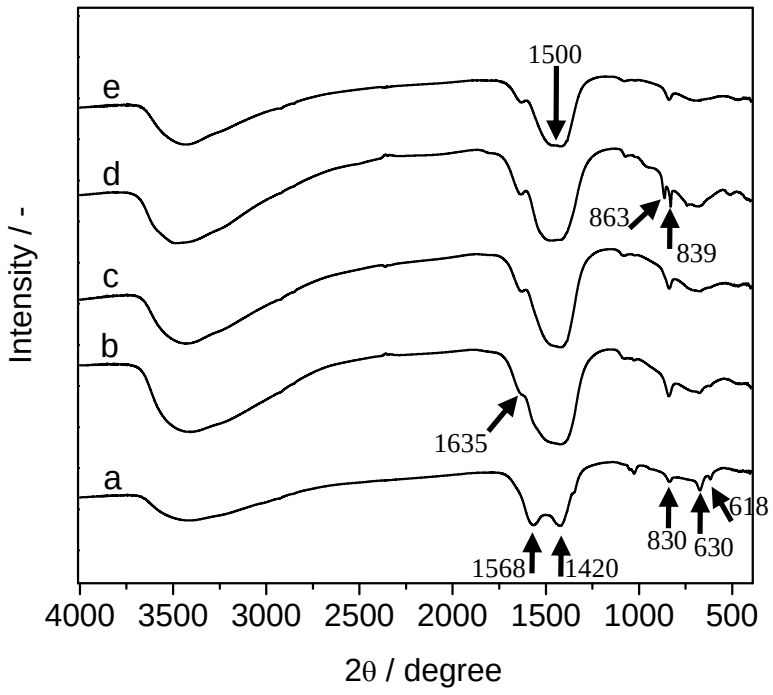

Figure 3.14. Infra-red analysis of the precipitated cobalt precursors. a) Co-0-P, b) Co-5-P, c) Co-10-P, d) Co-15-P and e) Co-A-P. Arrows indicates referred bands.

in Co-15-P, suggesting the presence of crystalline carbonate, although this was not detected by XRD. These features indicate differences in the materials and can be attributed to the presence of hydroxycarbonate in Co-0-P, Co-5-P, Co-10-P and Co-A-P [41]. In the case of Co-0-P peaks assigned to acetate were also observed, see *Section 3.3.3.1*.

3.4.2.2 Thermogravimetric analysis.

TGA of the precipitated materials are shown in Figure 3.15. These materials followed the same trend as seen previously, with a cobalt acetate precursor formed in the absence of water (Co-0-P) and cobalt carbonate/hydroxycarbonate precursors formed when water is added to the precipitated solution (Co-15-P, Co-10-P, Co-5-P and Co-A-P). The Co-15-P precursor showed a large weight loss at low temperature, <150 °C, indicating the sample retained a large amount of

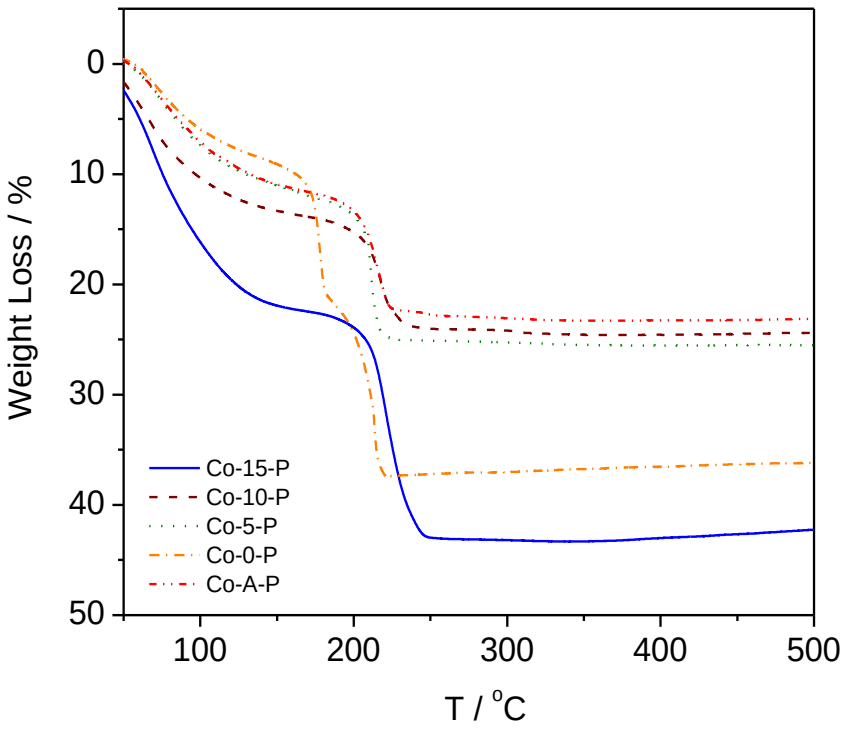

Figure 3.15. TGA of precursors prepared using different amounts of water in the precipitated solution.

solvent. This could be due to the additional water being more difficult to remove due to its low solubility in CO_2. With regards to the total weight loss, excluding solvent desorption at temperatures below 150 °C, the values for Co-5-P, Co-10-P, Co-15-P and Co-A-P were 18%, 16%, 21% and 17%, respectively. These were closer to the theoretical weight loss in decomposing $Co(OH)_{1.42}(CO_3)_{0.29}{\cdot}0.04\ H_2O$ to Co_3O_4. Therefore, TGA is in agreement with the infra-red analysis, with cobalt carbonate/hydroxycarbonate compounds for Co-5-P, Co-10-P, Co-15-P and Co-A-P, whereas a cobalt acetate decomposition profile was observed for Co-0-P, as seen in Figures 3.16 and 3.17 (*i.e.* the decomposition of $Co(CH_3OO)_2$ to $Co(CH_3COO)OH$ is endothermic at 212 °C, and finally to Co_3O_4 is exothermic at 258 °C). It should be mentioned that the total weight loss of Co-0-P (29%) was far from the theoretical weight loss expected for the decomposition of $Co(CH_3COO)_2$ to Co_3O_4 (54%), that also suggests the precipitation of either non-

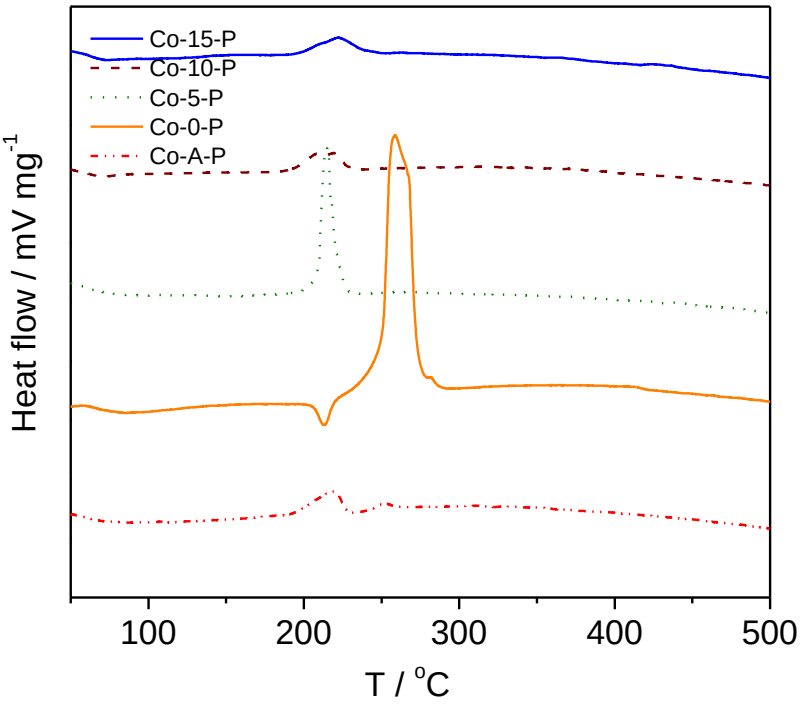

Figure 3.16. Differential thermal analysis of precipitated materials.

stoichiometric acetates or acetates containing carbonate/hydroxycarbonates.

The differential thermal analysis, as seen in Figure 3.17, showed that Co-0-P had two endothermic peaks, one at 235 °C, attributed to the decomposition of $Co(CH_3COO)_2$ to $Co(CH_3COO)OH$, and the other at 261 °C that was assigned to the formation of Co_3O_4. The Co-5-P showed only one exothermic peak at 215 °C assigned to the simultaneous decomposition of carbonate/hydroxycarbonates and residual acetates to Co_3O_4, as suggested by Xu *et al.* [21]. The Co-10-P and Co-15-P showed small exothermic decomposition peaks at 219 °C also assigned to the simultaneous decomposition of residual acetates and carbonates/hydroxycarbonates, however, in those cases the low exothermicity suggested a lesser degree of residual acetates. The Co-A showed the same exothermic peak at 219 °C, *i.e.* simultaneous decomposition of residual acetates and carbonate/hydroxycarbonates, but also a small peak at 253 °C. The two

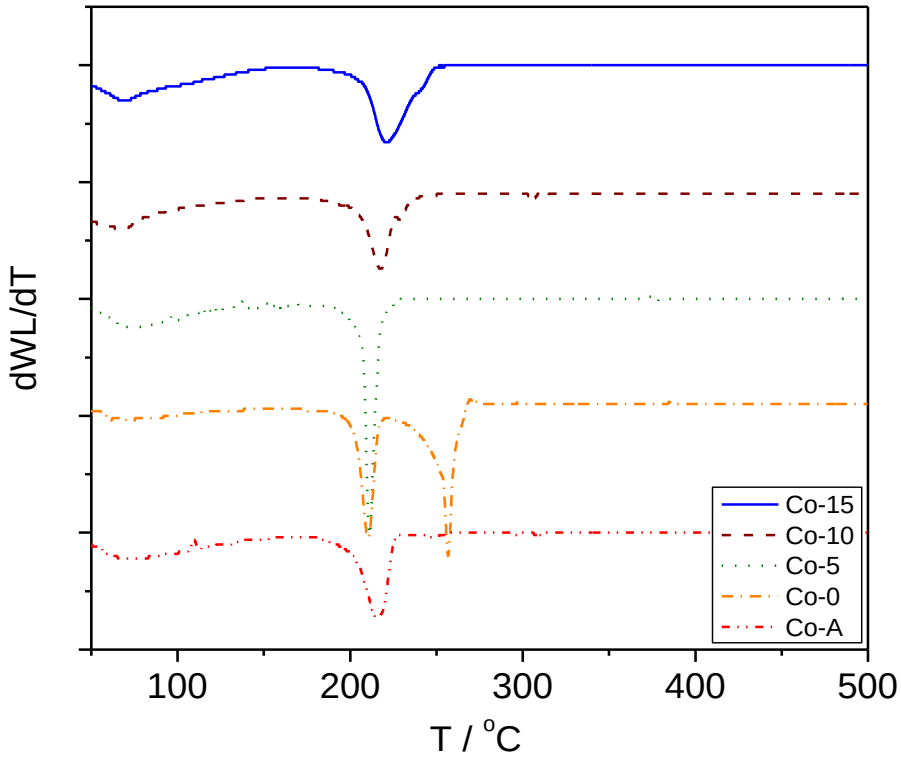

Figure 3.17. Derivative of weight loss of precipitated materials.

exothermic peaks suggest two kinds of cobalt acetate, *i.e.* acetates associated to carbonate/hydroxycarbonates that decomposed at low temperatures (215-219 °C) and non-associated acetates decomposing at high temperatures (235-262 °C) as in Co-0-P.

3.4.2.3 Powder X-ray diffraction.

XRD analysis was performed on the precursors and calcined materials. The precipitated materials did not show any reflections indicating amorphous materials, as seen in Figure 3.18-a. This was attributed to the fast nucleation rate that did not allow the crystal growth. The materials calcined at 400 °C showed spinel Co_3O_4 diffractions. In Figure 3.18-b Co-0-C, Co-5-C, Co-A-C and Co(ac)-C showed highly crystalline patterns which are probably a consequence of the highly exothermic acetate combustion conveying residual acetates in Co-10-0-C, Co-5-P and Co-A-P.

Crystallite size was obtained using the Scherrer equation and values are summarized in Table 3.7.

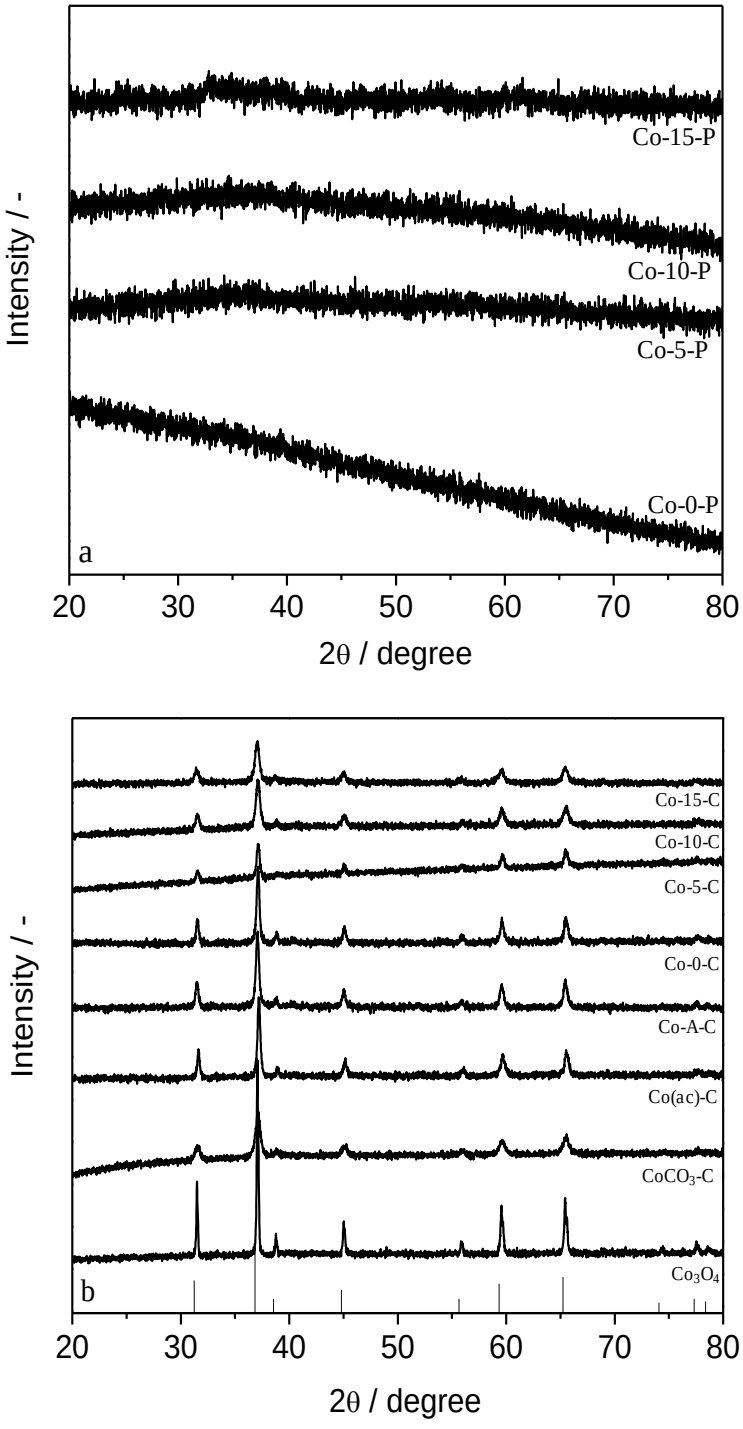

Figure 3.18. XRD patterns of precipitated and calcined cobalt catalysts.

Bars indicate reflections of spinel Co_3O_4.

3.4.2.4 N_2 physisorption.

The surface area of the materials was measured before and after calcination and values are given in Table 3.7.

There was a small increase in surface area when a small amount of water was added to the precursor solution, Co-5-P. As the water content in the starting solution increased from 5% to 10% and 15% the surface area decreased. After calcination at 400 °C the surface area of all the materials reduced significantly,

Table 3.7. BET surface area, crystallite size, solution and effluent pH of materials synthesised with different amounts of water in the precursor solution.

Catalyst	Surface area		ΔSA[a]	Crystallite	Solution	Effluent
	Precipitated $m^2 g^{-1}$	Calcined $m^2 g^{-1}$	%	size[b] nm	pH[c]	pH[c]
Co-15	54	35	35	24	7.7	5.3
Co-10	81	32	60	26	7.6	4.2
Co-5	131	15	89	41	7.6	4.1
Co-0	119	16	87	43	7.6	6.2
Co-A	74	40	75	37	-	-
Co(ac)	8	2	75	45	-	-
$CoCO_3$	78	20	46	21	-	-
Co_3O_4	1	-	-	190	-	-

[a] *ΔSA is defined as the difference between precipitated and calcined divided by precipitated surface area.*

[b] *Crystallite size obtained using Scherrer equation.*

[c] *pH was measured using a pH-meter, methanol pH = 8.3.*

although to a lesser degree for Co-10-C and Co-15-C (see ΔSA in Table 3.7). These results suggested that the formed carbonate/hydroxycarbonate maintain surface area after calcination in Co-10 and Co-15, however the exothermic combustion of residual acetates may have sintered the Co-5 bringing the surface area close to Co-0.

3.4.2.5 Temperature programmed reduction.

TPR was conducted to estimate the reducibility of the bulk catalysts (see *Section 2.5.8*) and the results are shown in Figure 3.19.

The commercial Co_3O_4 reduced at higher temperature (386 °C) than the SAS prepared cobalt oxide. Also, the commercial cobalt oxide showed asymmetry

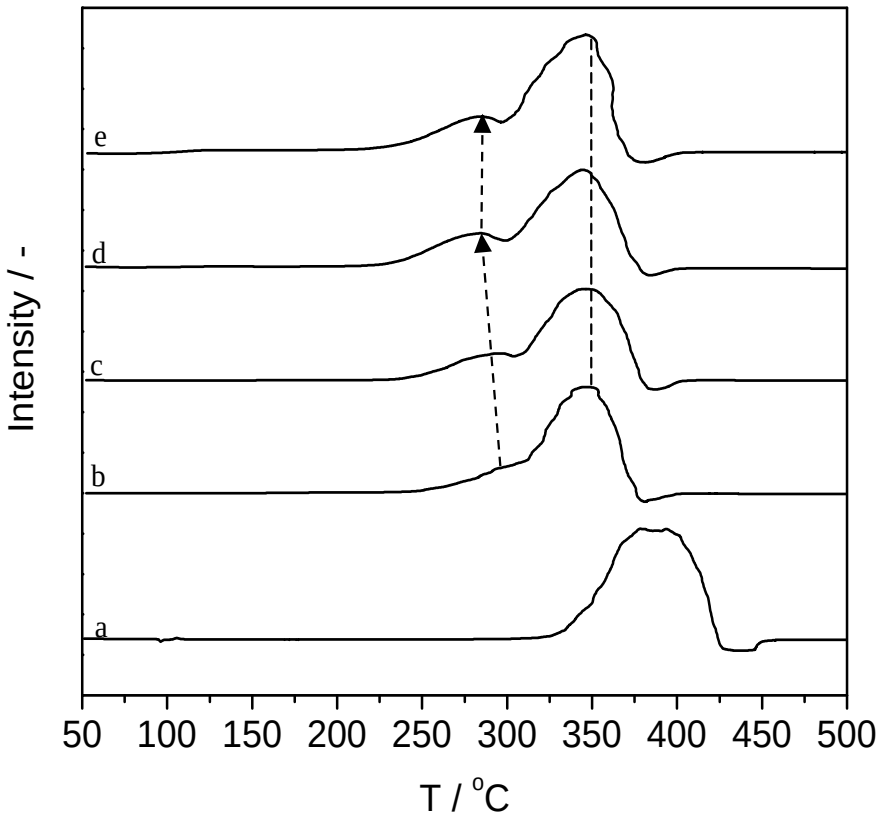

Figure 3.19. TPR of cobalt oxide catalysts. a) Co_3O_4 commercial, b) Co-0-C, c) Co-5-C, d) Co-10-C and e) Co-15-C. Lines for visual guidance.

conveying a peak at *ca.* 354 °C suggesting that the reduction proceeded *via* reduction of Co_3O_4 to CoO and finally to Co. The SAS prepared catalysts showed two reduction steps, Co_3O_4 to CoO and CoO to Co [42]. The first reduction step slightly shifts towards lower temperature from Co-0-C to Co-10-C and then slightly shifted towards high temperatures in Co-15-C. This may indicate higher oxygen lattice mobility in Co-10-C that may play an important role for propane total oxidation as the Mars-van Krevelen mechanism has been suggested [4]. The second reduction peak did not show any significant trend.

3.4.2.6 Scanning electron microscopy.

Representative SEM images of the precursors and Co_3O_4 catalysts can be seen in Figures 3.20 to 3.23.

The Co-0-P precursor comprised agglomerated spherical nanoparticles and is indicative of precipitation under supercritical conditions, *i.e.* single phase precipitation [23, 43]. In Co-5-P, Co-10-P and Co-15-P spherical microparticles together with agglomerated spherical nanoparticles were observed, indicating 2-phases were present during precipitation and the subsequent droplet formation [23, 43, 44]. The droplet could work as a precipitator container giving the spherical shape to the particles and permitting the precipitate to grow, as proposed by Reverchon *et al.* [43, 45]. Thermal treatment modified the particle morphology. In the case of Co-0-C, large particles were abundant, indicating that thermal treatment might sinter the particles, which is the cause of the large drop in surface area. Nevertheless, some nanoparticulate material was still present. In Co-5-C sharp geometries were observed indicating particle sintering and

coalescence. In Co-10-C spherical microparticles were still present suggesting that the main morphology was kept during calcinations and agrees with the small decrease in surface area. Rocky material was also observed in Co-15-C which might suggest that crystals grew during calcination.

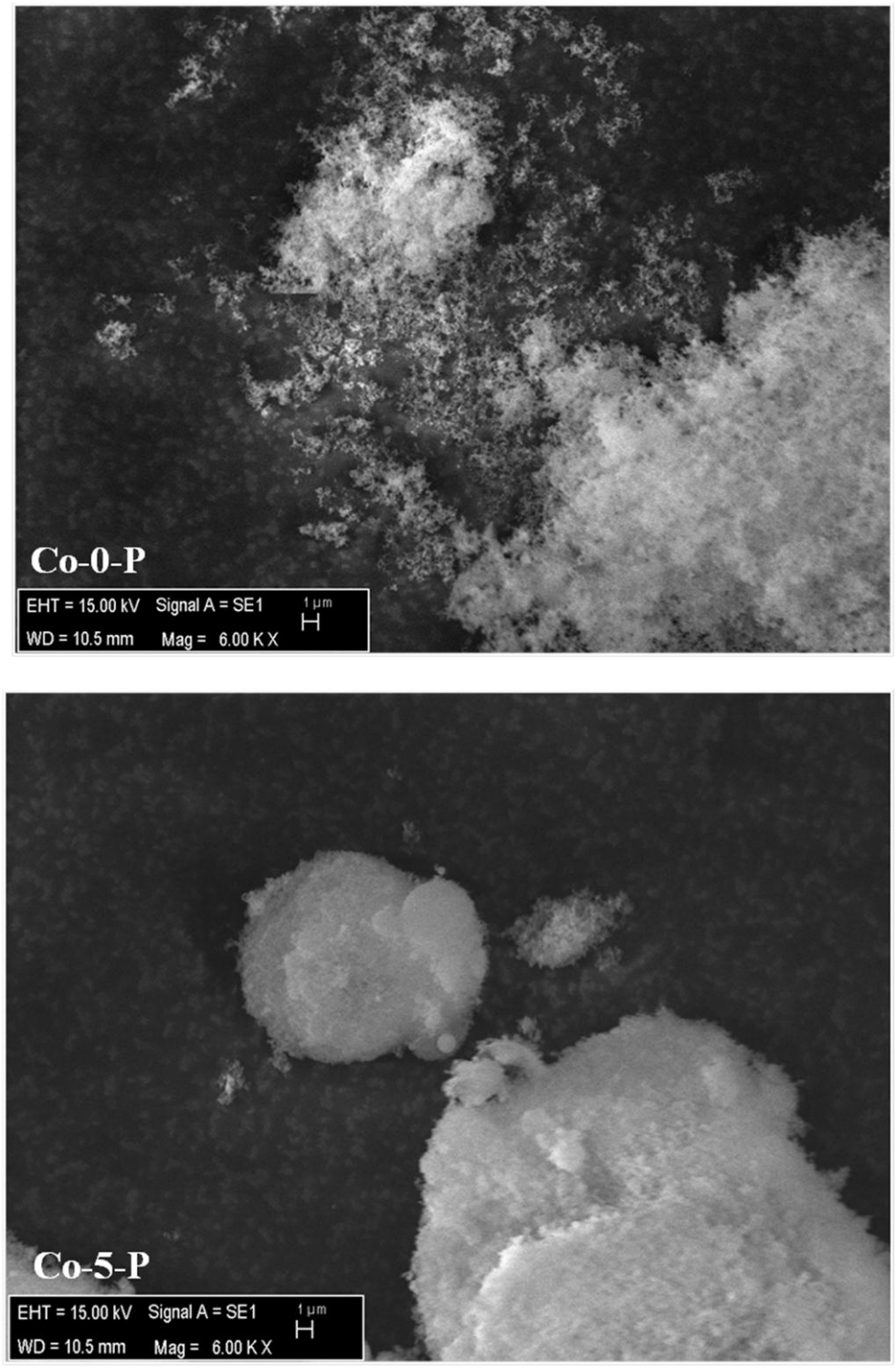

Figure 3.20. SEM images of SAS precipitates.

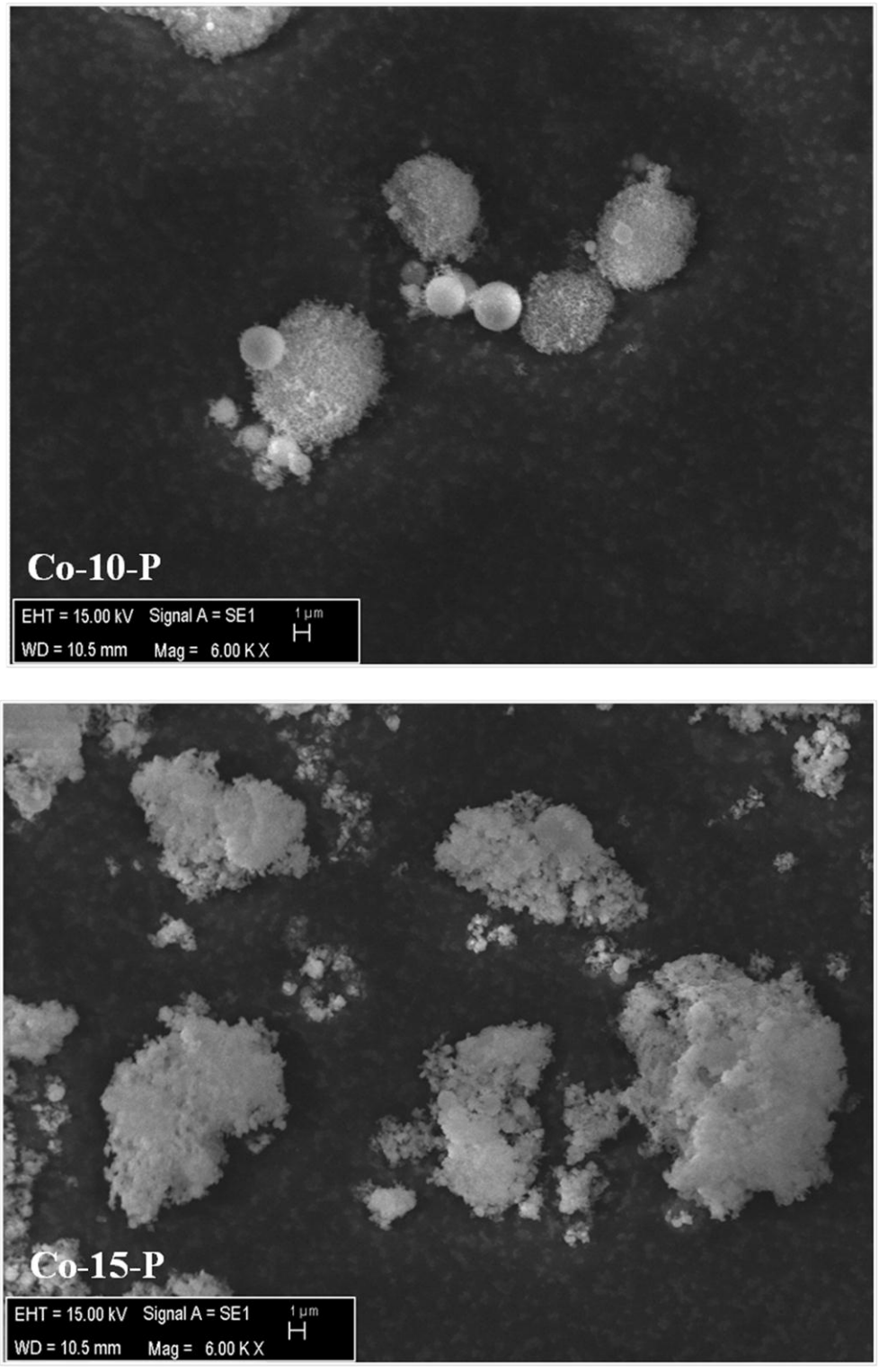

Figure 3.21. SEM images of SAS precipitates.

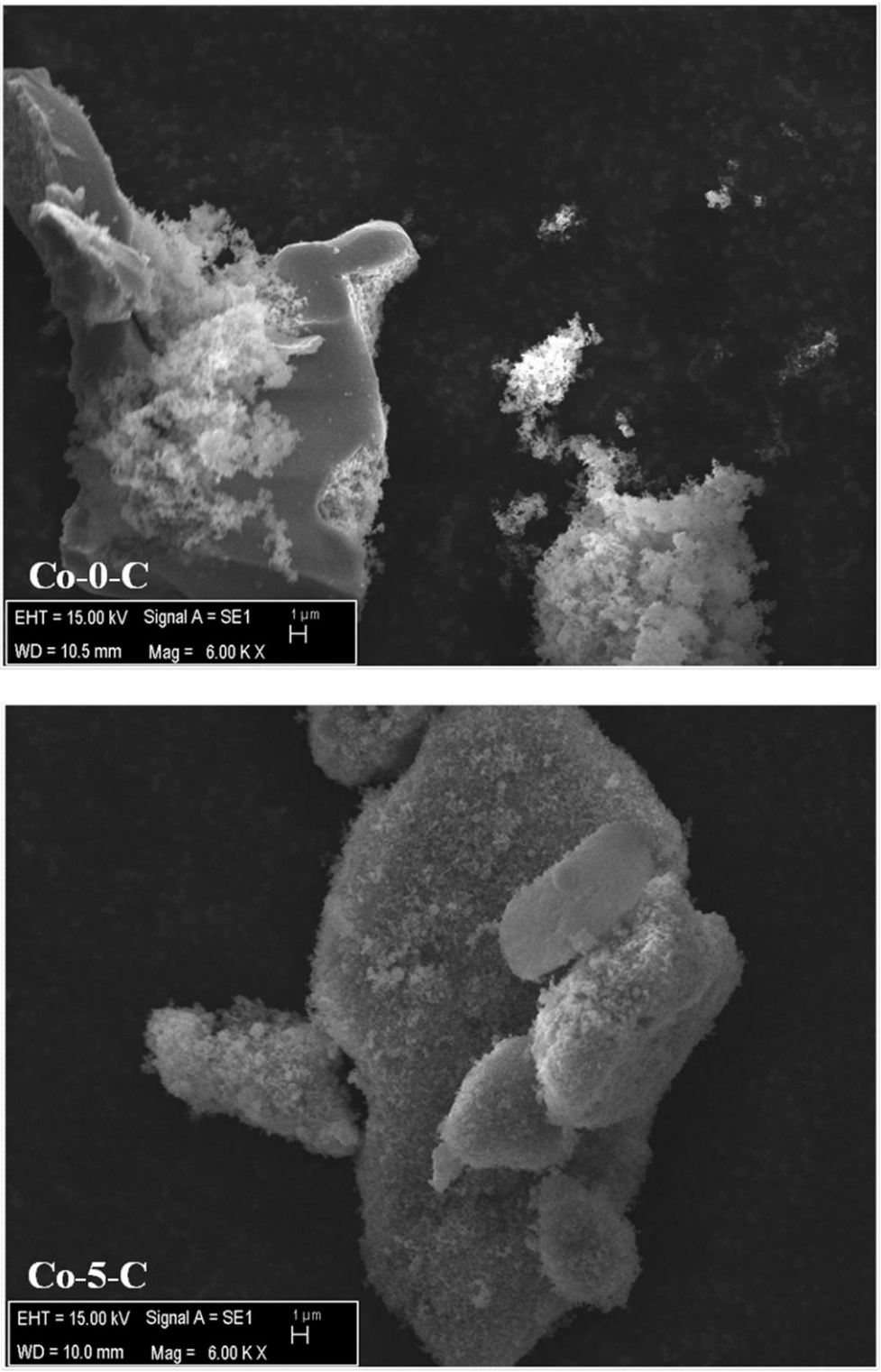

Figure 3.22. SEM images of SAS precipitates.

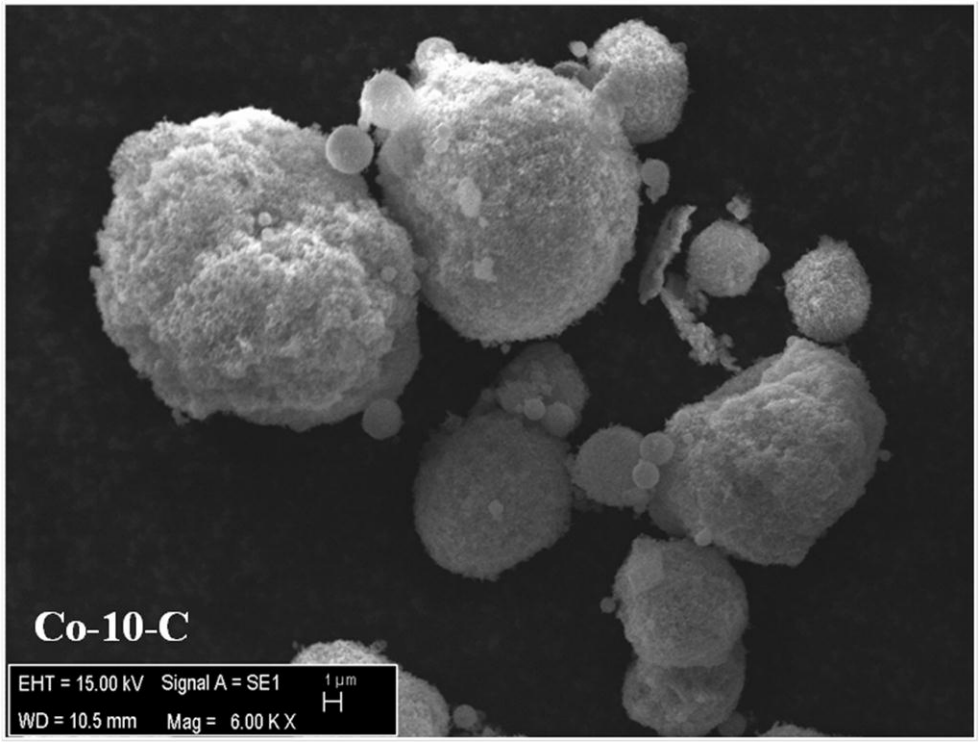

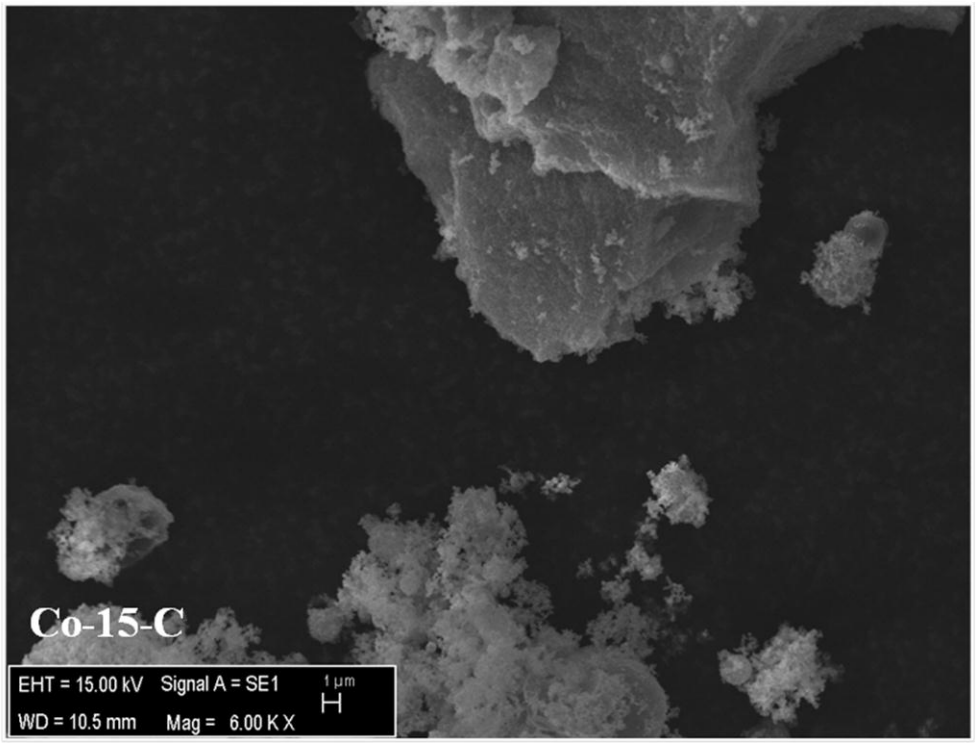

Figure 3.23. SEM images of SAS precipitates.

3.4.2.7 Effluent analysis.

The process effluent was collected and the pH and the total cobalt content was measured by atomic absorption analysis, see *Section 2.5.6*.

As can be seen in Figure 3.24, the minimum cobalt concentration in the effluent and the maximum cobalt acetate yield was obtained for Co-5-P. The amount of cobalt detected in the effluent increased as water concentration increased, but were all much lower than for the experiment without water in the solution (Co-0-P).

The fluid density may drive the solute solubility, and hence the precipitation. The density-solubility relationship in SC-CO_2 could arise from the close interaction between molecules at high densities promoting the solute salvation. Fluid densities in these experiments, considering CO_2/methanol/H_2O, slightly increase with water addition, from 651.3 kg m^{-3} up to 653.4 kg m^{-3} for

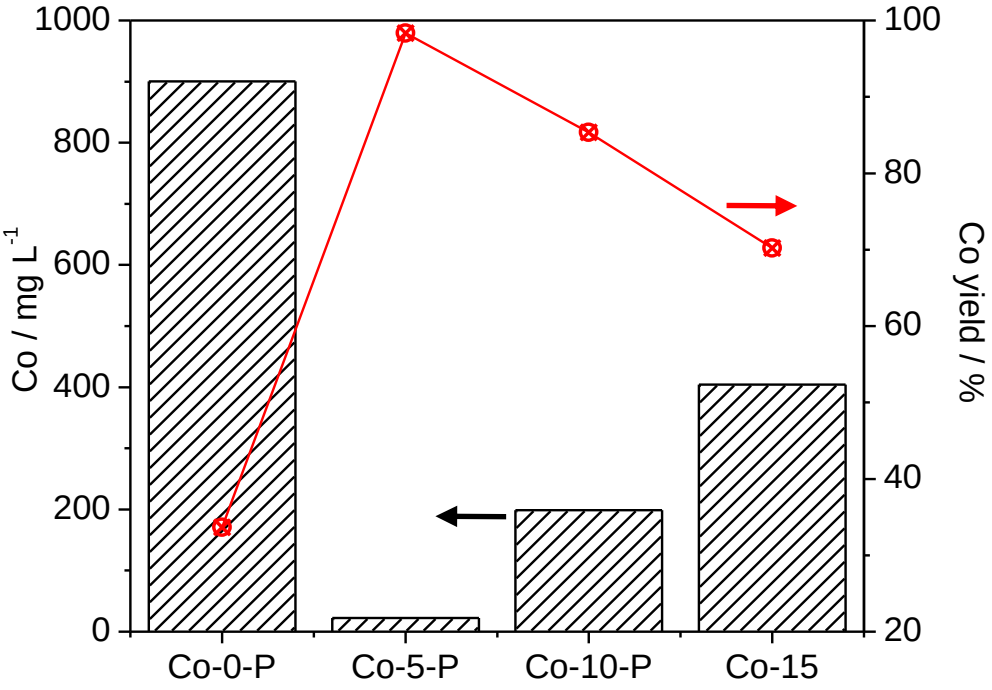

Figure 3.24. Effluent analysis of experiments described in Table 4.10. On the left axis cobalt effluent concentration; on the right axis cobalt precipitation yield.

experiments performed to precipitate Co-0-P to Co-15-P. However, the cobalt concentration in the effluent suggested that not only density, and solubility by extension [46], drives the precipitation but other factors also play a paramount role during the precipitation.

The experiments Co-5-P, Co-10-P and Co-15-P may occur on the boundary of or inside the 2-phases [36], allowing droplets to form [47], as suggested by SEM images; whereas the Co-0-P experiment may occur in a single phase [43, 47, 48].

Debendetti [49] suggested relatively low mass transfer between SC-CO_2 and solvents at values close to the critical point. Considering the CO_2/methanol critical point (82 bar, 40 °C and CO_2 molar fraction = 0.968) [48] and that electrolytes and a dynamic system (*e.g.* SAS precipitation) may increase the critical point [37, 50], the Co-0-P could be formed in the vicinity of the critical point inside the single phase [42]. The precipitation likely performed close to the critical point (with low mass transfer between SC-CO_2 and solvent) and the solubility enhancement by methanol (co-solvent effect) may explain the high cobalt concentration observed in the effluent of Co-0-P.

If droplets are formed (*i.e.* 2-phases), a CO_2 rich phase and a H_2O rich phase may exist [36], as seen in Figure 3.25, and then as methanol is soluble in both phases, methanol partition will occur. The methanol H_2O/SC-CO_2 partition coefficient indicates that methanol will tend to stay in the polar phase (see *Appendix I* for the calculations of the partition coefficient) decreasing the co-solvent effect which decreases the cobalt acetate solubility in SC-CO_2, enhancing the precipitation, as seen in Figure 3.25. Furthermore, both CO_2 solubility in methanol/H_2O and the SC-CO_2/solvent mass transfer decreases as H_2O increases,

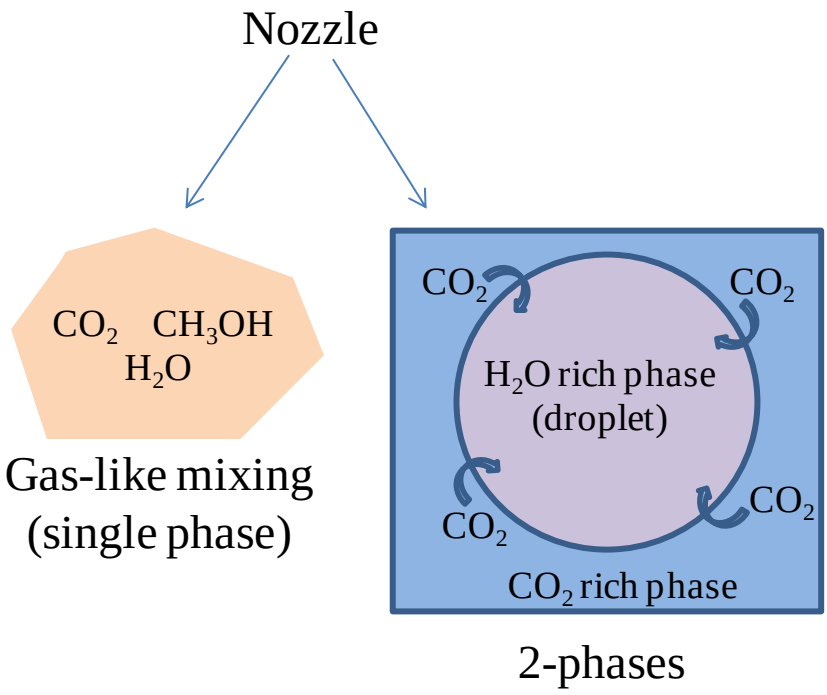

Figure 3.25. Proposed mechanisms for cobalt catalysts precipitation.

as calculated in *Appendix I*. These two factors could be the reasons behind the initial decrease and further increase in cobalt effluent concentration when water is added.

The effluent pHs are given in Table 3.7 which shows that after the process the pH decreases and it is dependent on the water incorporation. This decrease can be attributed to the formation of acetic acid, as previously observed [51] and can be written as follows::

$$Co(CH_3COO)_2 \rightleftharpoons Co^{2+} + 2\ CH_3COO^- \quad \text{Equation 3.9}$$

$$CH_3COO^- + H_2O \rightleftharpoons CH_3COOH + OH^- \quad \text{Equation 3.10}$$

$$CH_3COOH + H_2O \rightleftharpoons CH_3COO^- + H_3O^+ \quad \text{Equation 3.11}$$

The postulated OH^- in this mechanism could be consumed either by the formation of hydroxycarbonates, as suggested by TGA and infra-red analysis, or

by the H_3O^+ proposed in Equations 3.3 and 3.4. The acid pH observed in the effluent indicates that all the OH^- that could form, as seen in Equations 3.8 and 3.9, was consumed leaving the acid solution due to the Equation 3.10 or the dissolution of CO_2 in the effluent (methanol/H_2O).

3.4.2.8 Propane total oxidation.

The materials listed in Table 3.7 were tested for propane total oxidation, as described in *Section 2.3.1*. The catalytic performance is shown in Figure 3.26.

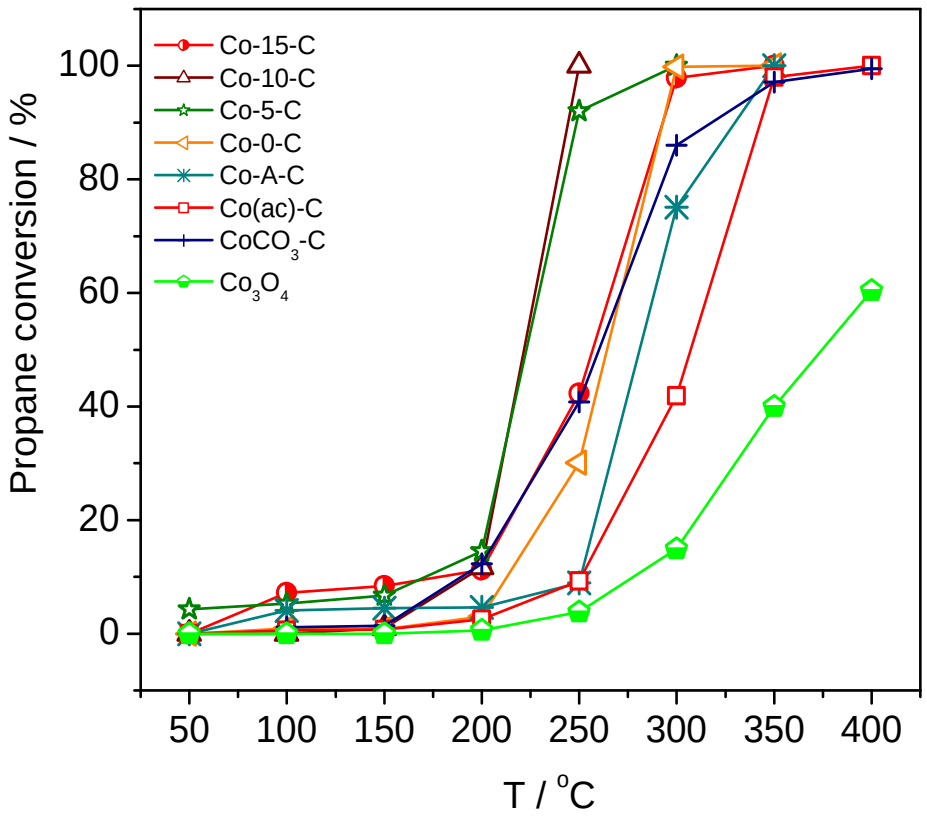

Figure 3.26. Catalyst performance of precipitated and unprocessed materials. Reaction conditions: 0.1 g of catalyst, 50 ml min^{-1} of synthetic air (O_2 20 vol% in He) and propane 0.4 vol%.

Three groups were observed according to the temperature required for 10% conversion of propane. The low temperature group, which includes SAS

precipitated catalysts with water incorporated, Co-5-C, Co-10-C, Co-15-C, and the calcined $CoCO_3$, combusted 10% of propane at temperatures between 173-194 °C. The second group that includes Co-A-C and Co(ac)-C combusted 10% of the propane at 250 °C. Finally, the commercial Co_3O_4 needed the highest temperature (280 °C) to combust 10% of propane. The experiments suggested that large Co_3O_4 crystallites are not active enough to fully oxidise propane at low temperatures, as seen in commercial Co_3O_4 (crystallites of 190 nm required the highest temperatures at 10% conversion). The activity did not show any relation to surface area, as catalysts with low surface area (Co(ac)-C with 2 m^2 g^{-1}) required similar temperatures at 10% conversion to catalysts with relatively high surface area (Co-A-C with 40 m^2 g^{-1}).

For combustion of 50% propane, Co-5-C and Co-10-C required lower temperatures (220 °C) compared to the other SAS made catalysts (Co-0-C, Co-15-C and Co-A-C) and $CoCO_3$ (temperatures between 256-277 °C). The catalyst Co(ac)-C needed a relatively high temperature (307 °C) to achieve 50% conversion. The commercial Co_3O_4 also showed the highest temperature (374 °C) at 50% conversion. At 50% conversion, nanocrystalline Co_3O_4 (15-40 nm) showed better activity than large crystallites (190 nm), as observed at 10% conversion, and temperatures required to achieve the 50% propane did not show any trend with surface area, as suggested previously [4]. Hence, it is suggested that catalyst characteristics other than surface area such as the oxygen on the surface, catalyst pore volume and pore size distribution, affinity of the propane for the catalyst or mass transfer limitations during catalytic reaction could be more indicative of catalytic activity at low temperatures for propane total oxidation.

The total combustion of propane was achieved at relatively low temperatures (250-300 °C) in SAS precipitated catalysts with water incorporated (Co-5-C, Co-10-C and Co-15-C). The Co-0-C and Co-A-C required relatively high temperatures (350 °C) to fully combust the propane. The $CoCO_3$, Co(ac)-C and Co_3O_4 catalysts required the highest temperature (400 °C).

In general, the SAS precipitated cobalt carbonate/hydroxycarbonate catalyst precursors required lower temperatures to combust propane (at 10%, 50% and 100% conversion) than other SAS made catalysts, Co-0-C and Co-A-C, or commercial samples ($CoCO_3$, Co(ac)-C or Co_3O_4).

In order to assess the reaction limitations due to internal diffusion limitations, the Weisz-Prater criterion (C_{WP}) can be used [63, 64]. This parameter weights the ratio between the observed reaction rate and the diffusion rate and reads as follow:

$$C_{WP} = \frac{observed\ reaction\ rate}{reaction\ rate\ at\ C_{As}} \cdot \frac{reaction\ rate\ at\ C_{As}}{diffusion\ rate} \quad \text{Equation 3.12}$$
$$C_{WP} = \eta \cdot \phi^2 = 3 \cdot (\phi \cdot \coth\phi - 1)$$

where η is the effectiveness factor and ϕ the Thiele modulus:

$$\phi = \frac{reaction\ rateat\ at\ C_{As}}{diffusion\ rate} = \frac{-r_{As} \cdot \rho_{cat} \cdot R^2}{De \cdot C_{As}} \quad \text{Equation 3.13}$$

$$\eta = \frac{-r_{observed}}{-r_{As}} \quad \text{Equation 3.14}$$

Combining Equation 3.12 and 3.13 C_{WP} can be expressed as follow:

$$C_{WP} = \frac{-r_{observed}}{-r_{As}} \cdot \frac{-r_{As} \cdot \rho_{cat} \cdot R^2}{De \cdot C_{As}}$$ Equation 3.15

where $-r_{observed}$ is the reaction rate calculated experimentally, ρ_{cat} is the density of catalyst, R the catalyst particle radius, C_{As} is the propane concentration on the catalyst surface and De the reactants diffusion rate.

To evaluate the limitations of reaction due to reactants/products, the C_{WP} is assessed as follows:

$C_{WP}<1$ there are no diffusion limitations

$C_{WP}>1$ the internal diffusion of products/reactants limit the reaction

In this work, the observed reaction rate was evaluated for catalysts listed in Table 3.8 at 200 °C and particle size was estimated using SEM microscopy, as seen in Table 3.8. For the sake of simplicity in calculus, density of catalyst has been considered constant through all samples (Co-0, Co-5, Co-10 and Co-15), and as a consequence of equal reaction conditions diffusion rate (*De*) and C_{As}, which depends on diffusion rate, are assumed constant, too. Hence, taking the ration of C_{WP} for Co-0 to Co-5:

$$\frac{C_{WP0}}{C_{WP5}} = \frac{\dfrac{-r_{observed0} \cdot \rho_{cat} \cdot {R_0}^2}{De \cdot C_{As}}}{\dfrac{-r_{observed5} \cdot \rho_{cat} \cdot {R_5}^2}{De \cdot C_{As}}} = \frac{3 \cdot (\phi_0 \cdot \coth \phi_0 - 1)}{3 \cdot (\phi_5 \cdot \coth \phi_5 - 1)}$$ Equation 3.16

$$\frac{C_{WP0}}{C_{WP5}} = \frac{-r_{observed0} \cdot {R_0}^2}{-r_{observed5} \cdot {R_5}^2} = \frac{(\phi_0 \cdot \coth \phi_0 - 1)}{(\phi_5 \cdot \coth \phi_5 - 1)}$$

Note subindex 0 stands for sample Co-0, and 5 for Co-5.

and using the definition of Thiele modulus, Equation 3.12:

$$\frac{\phi_0}{\phi_5} = \frac{{R_0}^2}{{R_5}^2}$$
$$\phi_0 = \frac{{R_0}^2}{{R_5}^2} \cdot \phi_5$$

Equation 3.17

Hence, combining Equation 3.15 and 3.16 the Equation 3.17 is obtained:.

$$\frac{-r_{observed0} \cdot {R_0}^2}{-r_{observed5} \cdot {R_5}^2} = \frac{\left(\phi_0 \cdot \coth\phi_0 - 1\right)}{\left(\phi_0 \cdot {R_5}^2 \Big/ {R_0}^2 \cdot \coth\left(\phi_0 \cdot {R_5}^2 \Big/ {R_0}^2\right) - 1\right)}$$

Equation 3.18

In Equation 3.17, all values are known and are listed in Table 3.8. Then, ϕ_0 can be calculated by iterative calculus and ϕ_5 by substituting ϕ_0 in Equation 3.16.

The Thiele modulus, and then the C_{WP}, for catalysts Co-10 and Co-15 can be calculated following the same sequence as per Co-0 and Co-5.

The C_{WP}, as seen in Table 3.8, indicates propane oxidation on SAS prepared catalysts were not diffusion limited, as all of them show $C_{WP}<1$. Although, a detailed examination suggests there may exist better diffusion properties in Co-5 and Co-10 as the C_{WP} in this catalysts were smaller than in Co-0 and Co-15. This could be further correlated with relevant catalyst activity observed in Co-5 and Co-10. The results also convey that small catalyst particles are preferred to minimize the internal diffusion problems.

Table 3.8. Experimental parameters used to calculate C_{WP}. Note: Particle radii have been estimated by SEM microscopy.

	Aggregated particle radius	$-r_{observed}$	C_{WP}
	μm	$mol_{C3H6} \cdot g_{cat}^{-1} \cdot s^{-1}$	
Co-0	50	$3.27\ 10^{-7}$	0.0077
Co-5	10	$3.22\ 10^{-7}$	0.0011
Co-10	11	$5.47\ 10^{-7}$	0.0024
Co-15	16	$2.05\ 10^{-6}$	0.0105

3.4.3 Conclusions on the effect of water.

The results suggest two precipitation scenarios depending on the presence of water. These scenarios are: single phase (water not incorporated) with precipitation of nanoparticles and 2-phases (water incorporation) with the formation of droplets and precipitation of microspheres, as observed under SEM. The initial introduction of water (5%) to the solutions increased the precipitated surface area; however, the addition of large volumes of water (10% and 15% water) decreased the surface area of the precipitates. This was attributed to an initial decrease in the co-solvent effect by water introduction and the restriction of mass transfer (CO_2/solvent). After calcination the surface area of cobalt carbonate/hydroxycarbonates precursors was slightly higher than the acetate precursors. It is worth noting that for Co-5-C, where carbonate/hydroxycarbonates were observed in infra-red analysis, the surface

area was similar to Co-0-C, which could be due to the combustion of residual acetates. Overall, Co_3O_4 was observed under XRD after calcination with the large crystallites observed in Co-0-C and Co-5-C attributed to the exothermic combustion of acetates that could sinter the crystallites. TPR showed similar reduction patterns in SAS made catalysts.

Different materials were formed depending on the presence of water in the solution and were also further observed during the catalytic combustion of propane. Results suggested that carbonate/hydroxycarbonate precursors yielded very active catalysts.

With regard to the catalyst performance, water added SAS precipitation produced catalysts more active than non water added or commercial processed cobalt oxide catalysts. The trend between catalysts activity and catalysts properties was not clearly elucidated by comparison with physical properties such as surface area, crystallite size or catalyst reducibility, C_{WP} suggested better internal diffusion in Co-5 and Co-10 than in Co-0 and Co-15.

3.5 Study of the effect of heat treatment.

An investigation of the calcination conditions was carried out using Co-5-P and Co-10-P, the most promising catalysts from the previous study. The activation atmosphere was also modified to see how this influenced the final catalysts.

3.5.1 Preparation.

The modified activation treatments applied to the precursors Co-5-P and Co-10-P are depicted in Table 3.9. The thermal treatment labelled as Co-10-C6 was carried out as follows: after introducing the precipitated material into a tubular furnace N_2 was allowed to flow. The temperature was increased up to 250 ºC at 5 ºC per minute and kept for 2.5 h. Then, without decreasing the temperature, N_2 flow was stopped and air was allowed to flow for a further 2.5 h. The thermal treatment terminated and the calcined sample was allowed to cool down whilst air was flowing.

Table 3.9. Modified calcination conditions applied to Co-5-P and Co-10-P.

Catalyst	Conditions
Co-5-C1	Static air at 250°C, 5°C min^{-1}, 5 h
Co-10-C1	Static air at 250°C, 5°C min^{-1}, 5 h
Co-10-C2	Static air at 250°C, 1°C min^{-1}, 5 h
Co-10-C3	Static air at 250°C, 5°C min^{-1}, 2.5 h
Co-10-C4	Flowing air, at 250°C, 5°C min^{-1}, 5 h
Co-10-C5	Flowing N_2, 250°C, 5°C min^{-1}, 5 h
Co-10-C6	Flowing N_2 to flowing air 250°C, 5°C min^{-1}, 5 h

3.5.2 Results and discussion.

3.5.2.1 Powder X-ray diffraction.

Powder XRD showed spinel Co_3O_4 following calcinations and CoO following the thermal treatment under N_2, as seen in Figure 3.27-a and 3.27-b. The

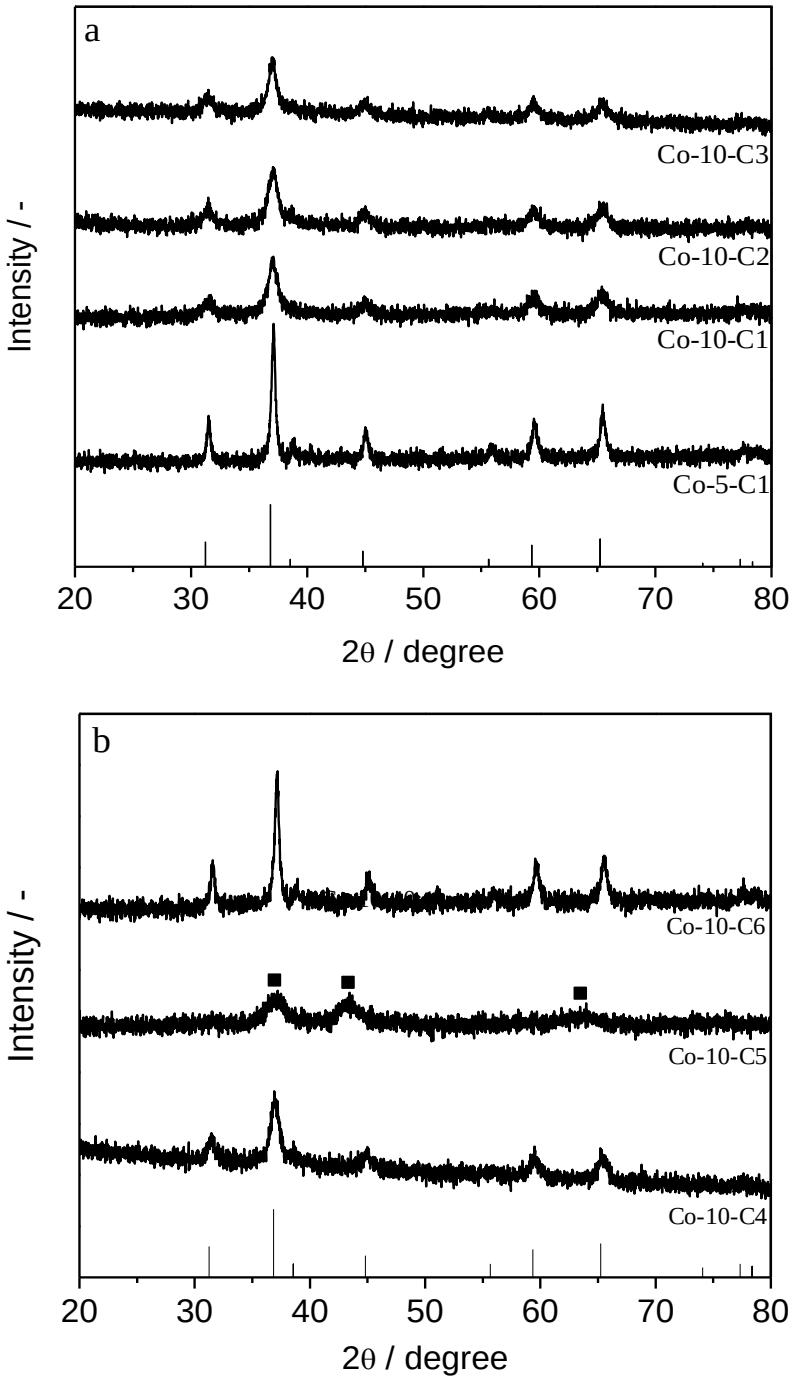

Figure 3.27. XRD of heat treatment study. Columns: spinel Co_3O_4; solid squares: CoO.

crystallite sizes were obtained by the Scherrer equation (see *Section 2.4.1*) and values are illustrated in Table 3.10. The experiment Co-10-C6 showed Co_3O_4 reflections indicating that the CoO formed during the thermal treatment under N_2 was oxidized to Co_3O_4 as the flow was changed to air.

The crystallite size was much larger in Co-5-C1 than in Co-10-C1 as a consequence of the high exothermic combustion of residual acetates observed in the differential thermal analysis, as seen in Figure 3.16, and agrees with surface area values. The mild calcination conditions for Co-10-C2 and Co-10-C3 did not significantly change the crystallite size, which suggests that crystallites did not sinter due to either the 5 h calcinations or the ramp rate of 5 °C min^{-1}. However, the cobalt oxide crystallites became larger when flowing air was used instead of static air. The use of flowing air, Co-10-C4, contributing to a relatively high O_2 concentration, compared to the static air, may promote the exothermic combustion of residual acetates, and hence, the crystallite growth. The flowing N_2 heat treatment, Co-10-C5, yielded a relatively small crystallite size (6 nm), which was attributed to the formation of poorly crystalline CoO species, as observed in Figure 3.27-b. The calcination procedure Co-10-C6 increased the crystallinity of Co_3O_4 as the most probable CoO phase formed during the initial thermal activation under N_2, was oxidized to Co_3O_4. The oxidation of CoO to Co_3O_4 is exothermic (ΔH = -178 kJ mol^{-1}); hence, the heat released could sinter the crystallites during the formation of Co_3O_4.

3.5.2.2 N_2 physisorption.

The surface areas of the catalysts are shown in Table 3.10. As can be observed, calcination at low temperature, 250 °C, yielded higher surface area catalysts

compared to those calcined at 400 °C. Using a slower temperature ramp rate, Co-10-C2, also slightly increased the surface area (from 96 m^2 g^{-1} in 5 °C min^{-1} to 106 m^2 g^{-1} in 1 °C min^{-1}). Similar surface areas were obtained on reducing the calcination time from 5 h to 2.5 h (Co-10-C1 96 m^2 g^{-1} and Co-10-C3 91 m^2 g^{-1}, respectively). Calcination under flowing air, Co-10-C4, decreased the surface area with respect to the materials calcined in static air, which has been previously observed for nanocrystalline Co_3O_4 [52].

Activation under N_2, Co-10-C5, was performed to reduce the exothermic combustion of acetates that may be the cause of sintering. However, this process gave a low surface area material compared to calcination in static air. Activation of Co-10-C6 was performed to avoid the exothermic combustion of the precursor and then oxidize cobalt species formed during heat treatment under N_2. However, the surface area of this catalyst was found to be the lowest. It is suggested that

Table. 3.10. BET surface area and crystallite size of catalysts calcined using the procedures detailed in Table 3.7.

Experiment	Surface area / m^2 g^{-1}	Crystallite size / nm
Co-5-C1	36 (15)[a]	28 (41)[b]
Co-10-C1	96 (32)[a]	8 (26)[b]
Co-10-C2	106	8
Co-10-C3	91	10
Co-10-C4	78	12
Co-10-C5	76	6
Co-10-C6	51	21

[a]in brackets surface area of catalysts calcined at 400 ºC.

the introduction of oxygen in the activation treatment at high temperature may increase the sintering of particles.

3.5.2.3 Propane total oxidation.

The catalysts described in Table 3.9 were tested for propane total oxidation and the results are shown in Figure 3.28.

All the catalysts fully decomposed the propane at 225-250 °C except the Co-10-C4, which only showed 80% conversion at 250 °C. It is worth noting that the reduction of the calcination temperature from 400 °C down to 250 °C improved the catalytic activity.

A detailed examination of the temperatures for propane 10% conversion allows the catalysts to be classified in two groups: low temperature activity (109-129 °C), catalysts Co-10-C1 and Co-10-C2, and medium temperature activity (177-207 °C), catalysts Co-10-C3, Co-10-C4, Co-10-C5, Co-10-C6 and Co-5-C1. The temperatures required by the catalysts to achieve 50% propane conversion reduced the temperature differences, and all the catalysts combusted 50% of propane within the range 177-207 °C excluding the Co-10-C4, which showed the

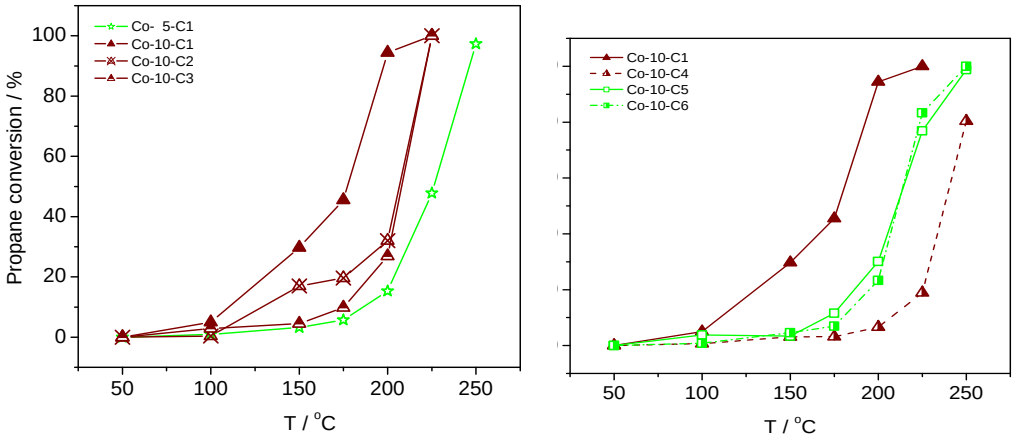

Figure 3.28 Catalytic performance of catalysts described in Table 3.8. Reaction conditions: 0.1 g of catalyst, 50 ml min^{-1} of synthetic air (O_2 20 vol% in He) and propane 0.4 vol%.

highest temperature for both 10% and 50% conversion (207 °C and 237 °C, respectively). The similarity in catalytic behaviour at 50% conversion may arise from mass transport limitations (reactants-products). Regarding the Co-10-C1 and Co-10-C2 similar activity was observed at 10% conversion suggesting that the reduction of ramp rate during the calcination from 5 °C min^{-1} to 1 °C min^{-1} did not significantly change the catalytic properties of Co_3O_4. The reduction in calcination time from 5 h to 2.5 h increased the temperature needed to achieve 10% conversion, which could be due to incomplete cobalt precursor decomposition, although only Co_3O_4 phases were observed under XRD. The catalyst calcined under flowing air showed the worst performance, as previously observed [33]. This can be attributed to the formation of highly ordered Co_3O_4, which is less active than poorly ordered Co_3O_4 due to a lack of defects where the oxidation reaction can take place [10]. Thus, it is suggested that under flowing air, relatively ordered Co_3O_4 was formed yielding lower activity than catalysts activated under static air. The precursor activated under N_2, which showed CoO in the XRD pattern, required similar temperatures to decompose 10% and 50% of propane as Co_3O_4 catalysts. It has been suggested that tetrahedral Co^{2+} and octahedral Co^{3+} are active centres for hydrocarbon combustion, due to these species increasing electron transfer during the catalytic combustion [53]. However, it should be noted that CoO is an unstable phase and reoxidises to Co_3O_4. Thus, a fraction of CoO formed during the activation under N_2 could reoxidise forming Co_3O_4 (most likely during the test as the reactant flow was mainly synthetic air: 20 vol% O_2 with only 0.4 vol% of C_3H_8), hence explaining the similar activity to Co_3O_4 catalyst. The Co-10-C6, activated first under N_2 and then under air, achieved 10% and 50% conversion at lower temperature than Co-10-C4. This

may suggest that the Co_3O_4 was less ordered than the Co-10-C4 which is probably due to the initial decomposition under N_2 or to the short oxidation step under flowing air (2.5 h). The Co-5-P calcined at 250 °C, Co-5-C1, required high temperatures to achieve 10% and 50% propane conversion (188 °C and 225 °C, respectively), similar to Co-10-C6; however, the surface area was lower and crystallite size larger (36 m^2 g^{-1} and 28 nm) than Co-10-C6 (51 m^2 g^{-1} and 21 nm).

It is worth noting that the catalytic oxidation of propane showed a poor correlation to surface area, as catalysts with high surface area, such as Co-10-C3 with 91 m^2 g^{-1}, required similar temperatures to combust 10% of propane than catalysts with low surface area, such as Co-10-C6 with 51 m^2 g^{-1}. In terms of the crystallite size of Co_3O_4, or CoO, correlation was not found between temperatures required to combust either 10% or 50% of propane. This conveys that the catalytic propane combustion is not only dependent upon surface area, but other catalyst properties, as discussed in *Section 3.4.2.8*, can play an important role during the catalytic combustion of propane.

In general, very active nanocrystalline Co_3O_4 catalysts were obtained; however, the activity was not clearly correlated to the crystallite size. An example of this is that Co-10-C6 had crystallites of 21 nm and a similar activity to Co-10-C3 with crystallite size of 10 nm. Thus, Co_3O_4 nanocrystallites could be indicative of low temperature propane combustion, but do not necessarily imply that the smaller the crystallite, the lower the temperature activity.

3.5.3 Conclusions on the effect of heat treatment study.

The calcinations under static air, in general, yielded Co_3O_4 with higher surface area than the precursor calcined under flowing air. Likewise, Co_3O_4 crystallite sizes were slightly larger in the catalyst calcined under flowing air than the catalysts activated under static air. The thermal activation under N_2 produced CoO with relative high surface area and small crystallite sizes. However, Co-10-C6 showed Co_3O_4 even though it was initially activated under N_2, with the formation of Co_3O_4 attributed to the later activation step under air that could promote the particle aggregation, then the decrease in surface area.

In general, the catalysts fully combusted propane between 225 and 250 °C. The results showed that Co-10-C1 and Co-10-C2 had the best activity in terms of low temperature propane total combustion (at conversions of 10% propane). Highly active Co_3O_4 nanocrystalline catalysts were obtained; however, activity was not correlated to crystallite size. The results suggested that other catalysts characteristics rather than surface area and crystallite size can be indicative of low temperature propane oxidation as no clear trend was found between activity and surface area. Catalysts characteristics like catalyst porosity, propane-catalyst affinity or oxygen activation on the surface catalysts could be indicative of low temperature propane total oxidation activity.

3.6 Study of catalyst stability.

The promising Co-10-C1 catalyst was tested for a longer time to probe the catalyst's stability after several hours of reaction. After the reaction the catalyst was left to cool down inside the reactor overnight, and tested again under the same conditions. This experiment is relevant as Co_3O_4 is targeted as a substitute

for conventional PGM based catalysts for exhaust aftertreatment. The engine with which the exhaust catalysts are associated will be started and stopped a large number of times during the catalyst cycle of life, hence the importance of catalyst stability under such conditions.

3.6.1 Catalyst testing.

Stability testing was performed on the Co-10-C1 catalyst to probe the performance. Fresh catalyst was loaded into the reactor and tested for approximately 5 h at 200 °C (0.4 vol% C_3H_8 in synthetic air: 20 vol% O_2 in He); then the gas flow and reactor furnace were switched off, and catalyst was left to cool down inside the reactor. After 19 h the reactants were allowed to flow and the temperature was increased back to 200 °C and the catalyst tested for 5 h under the same conditions.

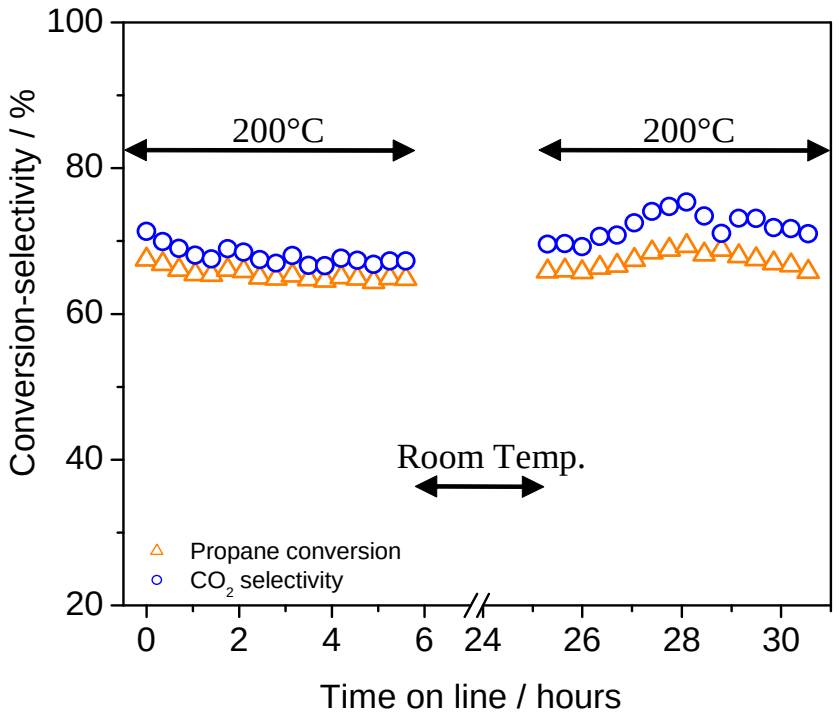

Figure 3.29. Stability test conducted on Co-10-1C at 200 °C. Reaction conditions: 0.1 g of catalyst, 50 ml min^{-1} of synthetic air (O_2 20 vol% in He) and propane 0.4 vol%.

3.6.2 Results and discussion

The stability test was conducted at 200 °C, which was chosen due to the high activity of the catalyst at this temperature (Figure 3.29). During the first hour, the catalyst slightly deactivated and conversion dropped by 2-3%. The propane conversion and selectivity towards CO_2 then stabilized at 67% and 69%, respectively. After the reaction was switched off and restarted, propane conversion remained fairly stable at 69%. It is worth noting that Co-10-C1 activity in the light-off experiment at 200 °C, as seen in Figure 3.28, was significantly higher than in the stability test (*ca.* 100% and 69%, respectively). This was attributed to the experimental conditions. During the light-off experiment the temperature was increased stepwise 50 °C approximately every hour up to 150 °C, and then 25 °C every hour up to 225 °C, whereas in the stability test the temperature was increased directly up to 200 °C (50 °C min^{-1}). Thus, the catalyst suffered different thermal activation that most likely changed the activity at the same temperature.

Hence, Co-10-1C did not show any deactivation over the time scale tested, therefore nanocrystalline Co_3O_4 produced by SAS process was as stable as the previously reported nanocrystalline Co_3O_4 [4, 33].

3.6.3 Conclusion on catalyst stability.

The Co-10-C1 was stable a Co_3O_4 catalyst under laboratory conditions over a relative large period of time, 5 h. After cooling down the catalyst and ramping the temperature back to 200 °C the catalyst showed similar activity and CO_2 selectivity, *i.e.* it did not deactivate. This encourages further testing under

realistic conditions, such as reactions at high space velocities and at conversions close to 100%.

3.7 Comparison of SAS and commercial catalysts.

The activity of Co-10-C1 Co_3O_4 catalyst was compared against a 5 wt% Pt/Al_2O_3 catalyst. This catalyst was chosen as a model of PGM catalysts, which are normally used for exhaust aftertreatment (the 3-way catalyst normally contains 1-2 wt% platinum and rhodium supported on a washcoat of 70-80% Al_2O_3 containing other oxides such as CeO_2 and BaO [54]). The catalysts were tested as described in *Section 2.3.1*.

3.7.1 Comments and conclusion.

The light-off curve for a 5 wt% Pt/Al_2O_3 catalyst and Co-10-C1 is plotted in Figure 3.30. The figure clearly shows that SAS prepared Co_3O_4 were far more

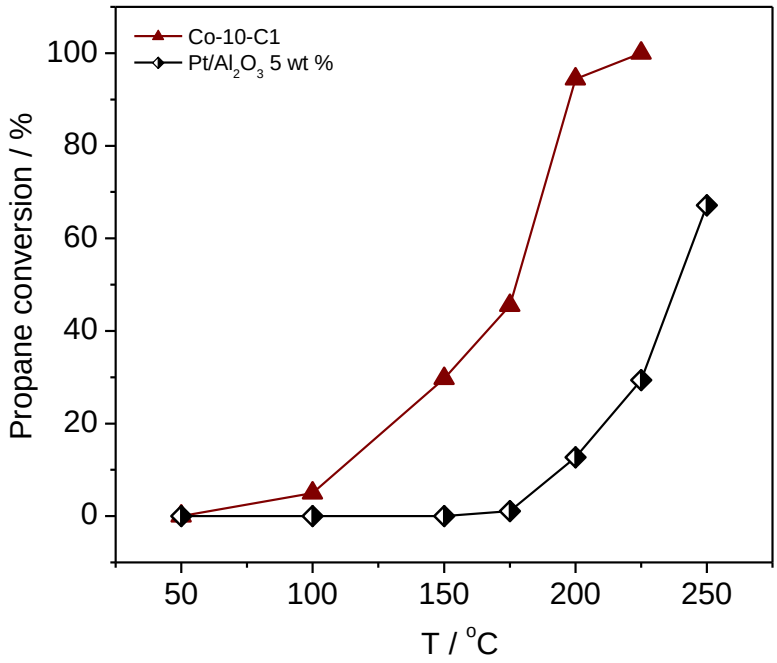

Figure 3.30. Catalytic activity of 5 wt% Pt/Al_2O_3 and SAS prepared nanocrystalline Co_3O_4. Reaction conditions: 0.1 g of catalyst, 50 ml min^{-1} of synthetic air (O_2 20 vol% in He) and propane 0.4 vol%.

active at lower temperatures than supported platinum. This could be attributed to the relative amount of active catalyst (Co_3O_4:C_3H_8 = 2.07 and Pt:C_3H_8 = 0.12) that indicates that there was more active phase per mol of propane in the case of cobalt oxide than in the platinum supported catalyst. The low temperature propane combustion indicates that nanocrystalline Co_3O_4 could be a possible substitute for precious metal catalysts for low temperature VOCs deep oxidation.

3.9 References.

1. Finlayson-Pitts, B. J.; Pitts, J. N., *Science* **1997,** *276* (5315), 1045-1051.

2. Molina, M. J.; Rowland, F. S., *Nature* **1974,** *249* (5460), 810-812.

3. Rodhe, H., *Science* **1990,** *248* (4960), 1217-1219.

4. Solsona, B.; Davies, T. E.; Garcia, T.; Vázquez, I.; Dejoz, A.; Taylor, S. H., *Applied Catalysis B: Environmental* **2008,** *84* (1-2), 176-184.

5. Solsona, B.; Vazquez, I.; Garcia, T.; Davies, T. E.; Taylor, S. H., *Catalysis Letters* **2007,** *116* (3-4), 116-121.

6. Waters, R. D.; Weimer, J. J.; Smith, J. E., *Catalysis Letters* **1994,** *30* (1), 181-188.

7. Grisel, R. J. H.; Nieuwenhuys, B. E., *Catalysis Today* **2001,** *64* (1-2), 69-81.

8. Morales, M. R.; Barbero, B. P.; Cadús, L. E., *Applied Catalysis B: Environmental* **2006,** *67* (3-4), 229-236.

9. Solsona, B.; Garcia, T.; Agouram, S.; Hutchings, G. J.; Taylor, S. H., *Applied Catalysis B: Environmental* **2011,** *101* (3-4), 388-396.

10. Solsona, B.; Vázquez, I.; Garcia, T.; Davies, T.; Taylor, S., *Catalysis Letters* **2007,** *116* (3), 116-121.

11. Solsona, B.; Aylón, E.; Murillo, R.; Mastral, A. M.; Monzonís, A.; Agouram, S.; Davies, T. E.; Taylor, S. H.; Garcia, T., *Journal of Hazardous Materials* **2011,** *187* (1-3), 544-552.

12. Solsona, B.; García, T.; Hutchings, G. J.; Taylor, S. H.; Makkee, M., *Applied Catalysis A: General* **2009,** *365* (2), 222-230.

13. Finocchio, E.; Busca, G.; Lorenzelli, V.; Escribano, V. S., *Faraday Transactions* **1996,** *92* (9), 1587-1593.

14. Liu, Q.; Wang, L.-C.; Chen, M.; Cao, Y.; He, H.-Y.; Fan, K.-N., *Journal of Catalysis* **2009,** *263* (1), 104-113.

15. Edwards, D. A.; Hayward, R. N., *Canadian Journal of Chemistry* **1968,** *46*, 3443-3446.

16. Nickolov, Z.; Georgiev, G.; Stoilova, D.; Ivanov, I., *Journal of Molecular Structure* **1995,** *354* (2), 119-125.

17. Yang, J.; Cheng, H.; Frost, R. L., *Spectrochimica Acta Part A: Molecular and Biomolecular Spectroscopy* **2011,** *78* (1), 420-428.

18. Pol, S. V.; Pol, V. G.; Felner, I.; Gedanken, A., *European Journal of Inorganic Chemistry* **2007,** *2007* (14), 2089-2096.

19. Kondrat, S. A.; Davies, T. E.; Zu, Z.; Boldrin, P.; Bartley, J. K.; Carley, A. F.; Taylor, S. H.; Rosseinsky, M. J.; Hutchings, G. J., *Journal of Catalysis* **2011,** *281* (2), 279-289.

20. Mohamed, M.; Halawy, S.; Ebrahim, M., *Journal of Thermal Analysis and Calorimetry* **1994,** *41* (2), 387-404.

21. Xu, R.; Zeng, H. C., *The Journal of Physical Chemistry B* **2003,** *107* (46), 12643-12649.

22. Adami, R.; Reverchon, E.; Järvenpää, E.; Huopalahti, R., *Powder Technology* **2008,** *182* (1), 105-112.

23. Reverchon, E.; De Marco, I.; Torino, E., *The Journal of Supercritical Fluids* **2007,** *43* (1), 126-138.

24. De Jesus, J. C.; González, I.; Quevedo, A.; Puerta, T., *Journal of Molecular Catalysis A: Chemical* **2005,** *228* (1-2), 283-291.

25. Wanjun, T.; Donghua, C., *Chemical Papers* **2007,** *61* (4), 329-332.

26. Tang, Z.-R. Green catalysts preparation using supercritical CO2 as an antisolvent. Cardiff University, Cardiff, 2003.

27. Belambe, A. R.; Oukaci, R.; Goodwin, J. J. G., *Journal of Catalysis* **1997,** *166* (1), 8-15.

28. Christel, L.; Pierre, A.; Abel, D. A. R., *Thermochimica Acta* **1997,** *306* (1-2), 51-59.

29. Kim, S. C.; Shim, W. G., *Applied Catalysis B: Environmental* **2010,** *98* (3-4), 180-185.

30. Liang, M.; Kang, W.; Xie, K., *Journal of Natural Gas Chemistry* **2009,** *18* (1), 110-113.

31. Jae, Y. K.; Jonathan, C. H.; Anatoly, I. F.; Peter, L. L.; José, A. R., *Journal of Physics: Condensed Matter* **2004,** *16* (33), S3479.

32. Hosseinpour, M.; Ahmadi, S. J.; Mousavand, T.; Outokesh, M., *Journal of Materials Research* **2010,** *25* (10), 2025-2034.

33. Davies, T.; Garcia, T.; Solsona, B.; Taylor, S. H., *Chemical Communications* **2006,** *32*, 3417-3419.

34. Toews, L. K.; Wai, C. M., *Analytical Chemistry* **1995,** *67*, 4040-4043.

35. Xia, J.; Jödecke, M.; Pérez-Salado Kamps, Á.; Maurer, G., *Journal of Chemical & Engineering Data* **2004,** *49* (6), 1756-1759.

36. Adrian, T.; Wendland, M.; Hasse, H.; Maurer, G., *The Journal of Supercritical Fluids* **1998,** *12* (3), 185-221.

37. Dowy, S.; Braeuer, A.; Reinhold-López, K.; Leipertz, A., *The Journal of Supercritical Fluids* **2009,** *50* (3), 265-275.

38. Xing, W.; Zhuo, S.; Cui, H.; Zhou, H.; Si, W.; Yuan, X.; Gao, X.; Yan, Z., *Materials Letters* **2008,** *62* (8-9), 1396-1399.

39. Wang, S. L.; Qian, L. Q.; Xu, H.; Lü, G. L.; Dong, W. J.; Tang, W. H., *Journal of Alloys and Compounds* **2009,** *476* (1-2), 739-743.

40. Blažek, A., *Thermal analysis* 1st ed.; van Nostrand Reinhold: London, 1973.

41. Xie, X.; Shang, P.; Liu, Z.; Lv, Y.; Li, Y.; Shen, W., *The Journal of Physical Chemistry C* **2010,** *114* (5), 2116-2123.

42. Shekunov, Y. B.; Baldyga, J.; York, P., *Chemical Engineering Science* **2001,** *56* (7), 2421-2433.

43. Reverchon, E.; De Marco, I., *Chemical Engineering Journal* **2011,** *169* (1-3), 358-370.

44. Reverchon, E., Adami, R., Caputo, G., De Marco, I., *The Journal of Supercritical Fluids* **2008,** *47* (1), 70-84.

45. Reverchon, E.; Cardea, S.; Schiavo Rappo, E., *The Journal of Supercritical Fluids* **2008,** *45*, 356.

46. Schneider, G.; Egon S.; Günther W., *Extraction with Supercritical Gases*. Verlag Chemie: Weinheim, 1980.

47. Reverchon, E.; Torino, E.; Dowy, S.; Braeuer, A.; Leipertz, A., *Chemical Engineering Journal* **2010,** *156* (2), 446-458.

48. Ziegler, J. W.; Dorsey, J. G., *Analytical Chemistry* **1995,** *67* (2), 456-461.

49. Werling, J. O.; Debenedetti, P. G., *The Journal of Supercritical Fluids* **2000,** *18* (1), 11-24.

50. Reverchon, E., *The Journal of Supercritical Fluids* **2007,** *43* (1), 126-138.

51. Kondrat, S. A. W. Nitrate Free Synthesis of Catalysts Using Supercritical CO2 Anti-Solvent Precipitation. Cardiff University, Cardiff, 2010.

52. Davies, T. E. Metal Oxide Catalysis for the Low Temperature Selective Oxidation of Propane to Iso-propanol. Cardiff University, Cardiff, 2006.

53. Łojewska, J.; Kołodziej, A.; Żak, J.; Stoch, J., *Catalysis Today* **2005,** *105* (3-4), 655-661.

54. Stone, R., *Introduction to Internal Combustion Engines*. 3 ed.; Palgrave Macmillan: London, 1999.

55. Lagalante, A. F.; Bruno, T. J., *The Journal of Physical Chemistry B* **1998,** *102* (6), 907-909.

56. Abraham, M. H.; Chadha, H. S.; Whiting, G. S.; Mitchell, R. C., *Journal of Pharmaceutical Sciences* **1994,** *83* (8), 1085-1100.

57. Frank, M. J. W.; Kuipers, J. A. M.; van Swaaij, W. P. M., *Journal of Chemical & Engineering Data* **1996,** *41* (2), 297-302.

58. Kong, C. Y.; Funazukuri, T.; Kagei, S., *The Journal of Supercritical Fluids* **2006,** *37* (3), 359-366.

59. Lucien, F. P.; Foster, N. R., *Journal of Chemical & Engineering Data* **1998,** *43* (5), 726-731.

60. Ting, S. S. T.; Tomasko, D. L.; Foster, N. R.; Macnaughton, S. J., *Industrial & Engineering Chemistry Research* **1993,** *32* (7), 1471-1481.

61. Song, Q.; Zhu, J.; Wan, J.; Cao, X., *Journal of Chemical & Engineering Data* **2010,** *55* (9), 3946-3951.

62. Pourmortazavi, S. M.; Hajimirsadeghi, S. S., *Journal of Chromatography A* **2007,** *1163* (1-2), 2-24.

63. Perry, R. H.; Green, W. D., *Perry's Chemical Engineers' Handbook*. 7th ed.; McGraw-Hill Professional: New York, 1997.

64. Fogler, H. S., Elements of chemical reaction engineering. 2nd ed.; Prentice-Hall International: New Jersey 1992.

Appendix I.

3.I.1 Methanol partition coefficient in H_2O/SC-CO_2.

In the case of a two phase system, the partition coefficient indicates the affinity of a solute towards one phase. This can be defined as the ratio between solute molar fraction in both phases and reads as follow:

$$K_{\frac{I}{II}} = \frac{\aleph^{I}_{solute}}{\aleph^{II}_{solute}} \qquad \text{Equation 3.I.1}$$

Where $\aleph^{I}_{solute}$ refers to solute molar fraction in phase I and $\aleph^{II}_{solute}$ to solute molar fraction in the phase II.

In the particular case of H_2O/SC-CO_2, the solubility of CO_2 in H_2O is very poor and the system can split into two phases. If a third compound, soluble in both

phases is present in the system (*e.g.* methanol), this will distribute in both phases depending on the affinity towards the phases. Therefore one can define the partition coefficient of methanol in H_2O/SC-CO_2 as follows:

$$K_{\frac{H_2O}{SC}-CO_2} = \frac{\aleph_{MeOH}^{H_2O}}{\aleph_{MeOH}^{SC-CO_2}}$$ Equation 3.I.2

Table 3.I.1 Values from Abraham [56].

Methanol excess index of refraction (R_2)	Methanol effective hydrogen bond acidity (α_2^H)	Methanol dipolarity/polarizability (π_2^H)	SC-CO_2 dipolarity/polarizability (π_1)
0.278	0.430	0.440	-0.139

Langalate [55] and co-workers modelled partition coefficients of several organic compounds in the H_2O/SC-CO_2 system with a 22% error. The authors reported equation 3.I.3 to calculate the *log* $K_{H2O/SC\text{-}CO2}$:

$$logK_{H2O/SC\text{-}CO2} = 2.436 - 1.914 \cdot R_2 - 1.224 \cdot \alpha_2^H + 2.499 \cdot \pi_1 \cdot \pi_2^H$$

Equation 3.I.3

The descriptors used in Equation 3.I.3 are detailed in Table 3.I.1 from Abraham [56].

Taking into account Equation 3.I.3 and values reported in Table 3.I.1, the following $logK_{H2O/SC\text{-}CO2}$ was obtained when methanol was considered as solute:

$$logK_{H2O/SC\text{-}CO2} = 1.22$$

This value suggests methanol stays preferentially in the H_2O rich phase.

3.I.2 Diffusion coefficients.

Due to the lack of diffusion coefficients values for the SC-CO_2/H_2O/methanol system in the literature, these were calculated using the following assumptions:

- Diffusion coefficients were taken as proportional to molar fractions.
- SC-CO_2 was assumed to diffuse into either the H_2O or methanol phase.

Diffusion coefficients of SC-CO_2 into both phases were weighted in function of the molar fraction, and then merged in one parameter. The SC-CO_2/H_2O and SC-CO_2/methanol diffusion coefficients were taken from the literature.

Then:

$$D_{\frac{H2O}{\frac{MeOH}{SC}-CO2}} = \aleph_{H2O}\ x\ D_{\frac{H2O}{SC}-CO2} + \aleph_{MeOH}\ x\ D_{\frac{MeOH}{SC}-CO2}$$

Equation 3.I.4

where $D_{SC\text{-}CO2/H2O/MeOH}$ refers to the diffusion coefficient of SC-CO_2 into H_2O/methanol, $D_{SC\text{-}CO2/H2O}$ to the diffusion coefficient of SC-CO_2 into H_2O and $D_{SC\text{-}CO2/MeOH}$ to the diffusion coefficient of SC-CO_2 into methanol. Molar fractions are referred as $\aleph_{H2O}$ molar fraction of H_2O (CO_2 free) and $\aleph_{MeOH}$ molar fraction of methanol (CO_2 free).

At 120 bar and 40 °C:

$D_{SC\text{-}CO2/H2O}$ [57] = 3.07 10^{-9} m^2 s^{-1}

$D_{SC\text{-}CO2/MeOH}$ [58] = 3.24 10^{-8} m^2 s^{-1}

Thus, applying Equation 3.I.4 and the molar fractions listed in Table 3.I.3 the diffusion coefficients reported in Table 3.I.2 were obtained.

Table 3.I.2. Estimated diffusion coefficients ($D_{SC\text{-}CO2/H2O/MeOH}$), water and methanol molar fractions used in the calculations.

Sample	χ_{H2O}	χ_{MeOH}	$D_{SC\text{-}CO2/H2O/MeOH}$
Co-5	$1.12 \cdot 10^{-1}$	$8.88 \cdot 10^{-1}$	$2.12 \cdot 10^{-8}$
Co-10	$2.06 \cdot 10^{-1}$	$7.94 \cdot 10^{-1}$	$1.93 \cdot 10^{-8}$
Co-15	$2.90 \cdot 10^{-1}$	$7.10 \cdot 10^{-1}$	$1.76 \cdot 10^{-8}$

3.I.4 Cobalt acetate tetrahydrate solubility in SC-CO_2.

3.I.4.1 Experimental.

Solubility of $Co(CH_3COO)_2 \cdot 4\ H_2O$ in SC-CO_2 was measured at different pressures (from 90 to 180 bar) and temperatures (from 35 °C to 50 °C) following the methodology described in *Section 2.2.4*.

3.I.4.2 Results and discussion.

The solubility of $Co(CH_3COO)_2 \cdot 4\ H_2O$ is shown in Figure 3.I.1. The molar fraction of $Co(CH_3COO)_2 \cdot 4\ H_2O$ dissolved in neat SC-CO_2 is below 10^{-7}; this value is lower than previously reported low solubility compounds [59], indicating

that $Co(CH_3COO)_2 \cdot 4\,H_2O$ presents a very low solubility in SC-CO_2. It is worth noting that solubility is dependent on both pressure and temperature. However, temperature is more relevant than pressure as previously observed [60]. Hence, the supersaturation of $Co(CH_3COO)_2 \cdot 4\,H_2O$ will strongly depend on the temperature and in lesser degree on the pressure at constant working concentration.

The addition of a polar co-solvent can increase the solubility by several orders of magnitude due to the hydrogen bonding between the polar solvent and the solute [61]. This enhancement can be further promoted if the salt is very soluble in the co-solvent [62]. Therefore, the solubility of $Co(CH_3COO)_2 \cdot 4\,H_2O$ during the experiments described in this work is expected to be greatly increased by methanol. It has been suggested, however that water additions, as a co-solvent, may not change the solubility as it is poorly soluble in SC-CO_2 [62]. The fluid supersaturation is an indicator of the nucleation rate (the higher the

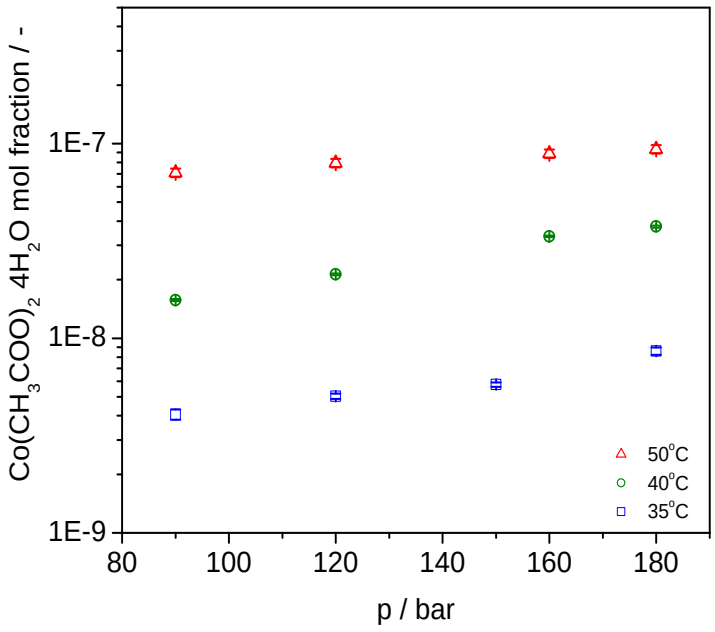

Figure 3.I.1. $Co(CH_3COO)_2 \cdot 4\,H_2O$ solubility in SC-CO_2 at different pressures and temperatures. Solubility expressed as $Co(CH_3COO)_2 \cdot 4\,H_2O$ molar fraction.

supersaturation, the higher the nucleation rate) and can be reduced to the following equation [42]:

$$Sc = \frac{c}{c'_o}$$ Equation 3.I.5

where *Sc* refers to supersaturation, *c* to solute concentration in the solvent and c'_o to equilibrium solubility of solute in the fluid (considering the fluid to be the solvent and SC-CO_2).

3.I.5 Error in thermogravimetric analysis.

In order to evaluate the error in TGA analysis, commercial $Co(CH_3COO)_2 \cdot 4\ H_2O$ was analysed four times and the maximum deviation of measurements at

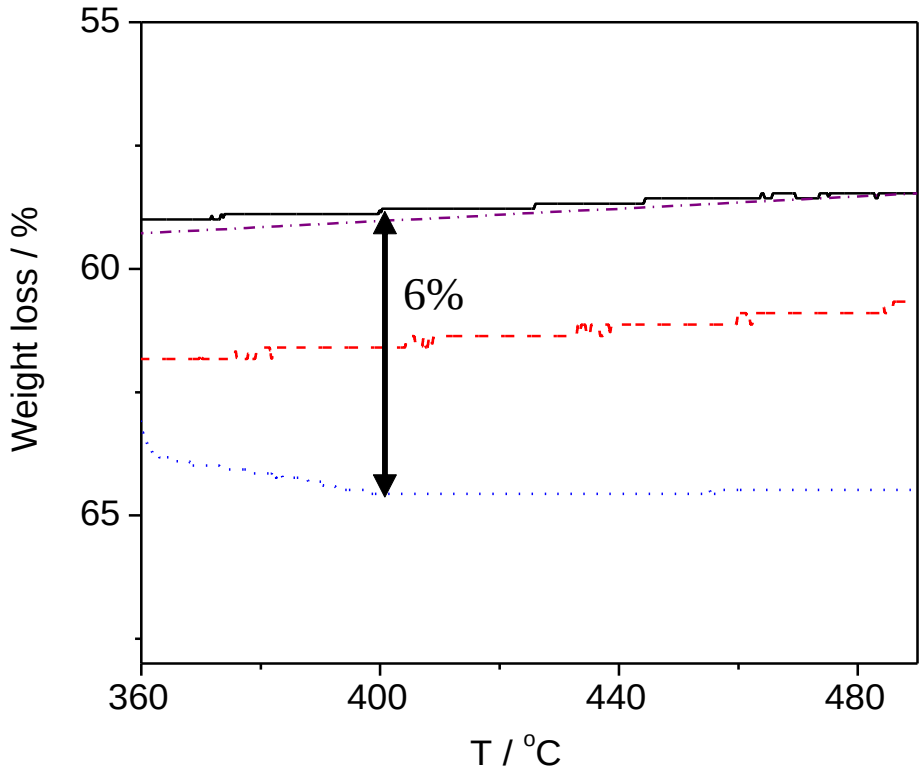

Figure 3.I.2. TGA analysis of $Co(CH_3COO)_2 \cdot 4\ H_2O$, each line represents one of the four analysis performed.

400 °C was established as analytical absolute error, as seen in Figure 3.I.2. The error was set as ±6% of weight loss.

4

Fundamental study of GAS process for catalyst synthesis

The GAS process has been extensively used to precipitate solids from homogeneous solutions. In this chapter, a comprehensive study on synthesising catalyst for the Fisher-Tropsch reaction by impregnating cobalt onto supports (heterogeneous solutions) using GAS technology has been performed.

4.1 Introduction.

The Fischer-Tropsch (FT) process was first investigated by Sabatier and Senderens in the early 20th century. They patented a cobalt-nickel based catalyst for methane production, feeding synthesis gas (syn-gas) at atmospheric pressure and mild temperatures (200-300 °C). At the beginning of 1923, Franz Fischer and Hans Tropsch reported the production of oily mixtures (composed of oxygenated compounds) using an alkalized iron catalyst at high pressure and relatively high temperatures (100-150 bar and 400-450 °C, respectively) [1]. It was also observed that the same catalyst could produce linear hydrocarbons at low pressures. However, it was found that the catalyst deactivated rapidly [2]. This

milestone work began a race to find out a suitable metal for a commercial FT catalyst. Early results showed nickel to be unsuitable, due to rapid deactivation, while iron was shown to have poor performance at low pressures. Therefore, cobalt based catalysts became the focus of attention during World War II, with Germany commissioning several plants to supply fuel using a cobalt thorium oxide catalyst.

Later, several companies developed fixed and fluidized bed reactors for the FT process. However, the discovery of large amount of crude oil in Middle East in the late 1940s and 1950s was an inflection point for FT development, as the economic costs of petroleum resources were more attractive compared to the FT process [3].

The FT technology was improved drastically by South African Coal, Oil and Gas Corporation (Sasol) in 1955 when a commercial plant based on fixed and fluidized bed reactors using a promoted iron based catalyst was commissioned.

The capability of FT to produce fuels and chemicals from coal and so avoiding petroleum dependence attracted attention due to petroleum crisis in 1973. In spite of the petroleum crisis, investment in FT research began to decline in the early 1980s. However, there has been a renewal of interest in the FT reaction since the Gulf oil crisis in the 1990s.

It has been estimated that around 80% of the global energy has a fossil fuel dependence (which includes oil, natural gas and coal). The forecasting of available fuel is: 40 years for oil, 65 years for natural gas and 155 years for coal and worldwide fuel demand are increasing sharply. Hence, an alternative method of producing fuels is highly desired. Due to the high quality of products obtained

using syn-gas, FT should play an important role in the world wide fuel supply [4] and the synthesis of platform chemicals.

Syn-gas corresponds to a mixture of a carbon monoxide and hydrogen. Syn-gas can be prepared using coal gasification which involves an endothermic reaction of carbon with steam, as seen in Table 4.1. Several other methods can also be used for the synthesis of syn-gas as detailed in Table 4.1.

The FT reaction is limited by low selectivity, yielding a wide range of products. The product distribution from CO hydrogenation has been explained using different theoretical models [5, 6]. The following assumptions have been made to derive these models:

1.- Chain growth proceeds *via* polymerization process predominantly by single-carbon increments.

2.- The probability of chain growth and termination are independent of oligomer length attached on the surface.

The FT reaction is based on the growth of hydrocarbons and oxygenates from CO and H_2. The constant contact of monomers with oligomeric species on the surface allows chain growth. The final products result from desorption of species. The FT reaction mechanism is very complex because of the wide range of

Table 4.1. Reactions to obtain syn-gas.

Coal gasification	$C + H_2O \leftrightarrow CO + H_2$
Steam reforming of methane	$CH_4 + H_2O \leftrightarrow CO + 3\,H_2$
CO_2 reforming of methane	$CH_4 + CO_2 \leftrightarrow CO + 2\,H_2$
Methane partial oxidation	$2\,CH_4 + O_2 \leftrightarrow 2\,CO + 2\,H_2$
Autothermal reforming	$4\,CH_4 + O_2 + 2\,H_2O \leftrightarrow 4\,CO + 10\,H_2$

products [7]. Three mechanisms are commonly proposed which either compete with each other or run in parallel. These mechanisms are the carbide, hydroxycarbide and CO insertion mechanisms.

In the carbide mechanism, methylene groups are formed by hydrogenation of metal carbides. These groups can be polymerized to yield a wide range of hydrocarbons. The C-O bond is activated on the metal site prior reaction with H_2. Then a CH_x group of one M-CH_x is inserted into the M-C bond of another M-CH_x species:

$$CO \rightarrow M\text{-}CO \rightarrow M\text{-}C \rightarrow M\text{-}CH_x \rightarrow \text{polymerization} \quad \text{Equation 4.1}$$

However, the carbide mechanism cannot explain the formation of oxygenated products and so does not fully explain the total product stream.

In the hydroxycarbene mechanism, CO is initially chemisorbed on the active site without dissociation. Then, the hydroxycarbene is formed due to reaction of non-dissociated, adsorbed CO with H_2. The hydroxycarbene intermediate formed, M-CHOH, promotes the C-C formation and hence, the chain growth. Chain termination and desorption of products takes place by hydrogenation of an intermediate to an alcohol. This mechanism successfully explains how oxygenated and branched products are obtained during the course of FT reaction [3].

In the CO insertion mechanism it is postulated the pristine metal carbonyl intermediate is hydrogenated. This is followed by the insertion of a carbonyl group into the M-H bond and the consequent hydrogenation [8], as follows:

$$MH\text{-}(CO)_x \rightarrow M\text{-}CHO(CO)_{x-1} \rightarrow M\text{-}CH_3(CO)_{x-1} \rightarrow M\text{-}CH_3(CO)_x \quad \text{Equation 4.2}$$

The chain growth is achieved by insertion of a CO molecule into the metal alkyl bond and subsequent reduction to an acyl species [5], as follows:

$$M\text{-}CH_3 + CO \rightarrow M\text{-}COCH_3 + H_2 \rightarrow M\text{-}CH_2CH_3 \rightarrow CH_2{=}CH_2 \quad \text{Equation 4.3}$$

FT is a complex reaction and although the mechanisms above may explain the product formation others routes are still possible.

In order to classify product distribution Anderson *et. a.l.* [9] modified the distribution function postulated by Schulz and Flory. They used in this definition the chain growth probability, α, and read as follow:

$$\alpha = \frac{r_g}{r_g + r_t} \quad \text{Equation 4.4}$$

where r_g is chain growth rate and r_t the chain termination. Therefore, the higher the α value, the longer the chain length.

Due to economic considerations, high selectivity and a narrow product distribution is desired which has led to considerable research into FT catalysts, reactor operation and optimization [10].

The FT reaction initially involves the chemisorption of CO and H_2. A suitable metal catalyst for these processes are iron group metals (group 8 metals of the periodic table) [11].

Fe, Co, Ni and Ru are found to be suitable for the production of hydrocarbons. The ultimate activity and selectivity of group 8 metals depends on the choice of promoters and the support in addition to suitable catalyst synthesis and reaction conditions [12, 13]. Generally, Ni presents high selectivity to methane making it an unsuitable metal for FT reaction. Ruthenium presents good selectivity to paraffinic waxes, although the economic cost and small ruthenium mineral

reserves are prohibitive to the use of this metal for commercial plants. Iron tends to form more carbon on the surface yielding fast catalyst deactivation. Hence, cobalt appears as a suitable catalyst for FT reaction.

Cobalt based FT catalysts have been continuously improved since they were discovered (1902-1928) and Germany developed a commercial cobalt-iron based catalyst in 1928-1929. After this period, the "iron age" started in South Africa and cobalt lost momentum (1950-1975). The more recent development of Gas-to-Liquid technology, *i.e.* the conversion of natural gas or syn-gas to other hydrocarbons, has increased the development of cobalt catalysts (1990-present). Early catalysts contained cobalt oxide as the active phase. However, experience has shown that Co metal is more active, especially if it is combined with promoters.

Iglesias and co-workers [14, 15] carried out a basic study into cobalt performance in the FT reaction, reporting the effect of metal dispersion, cobalt reduction enhancement by promoters (especially precious metals such as ruthenium or rhenium) and the impact of metal promoters on the selectivity towards C_{5+}. It was suggested that catalyst activity is a function of these factors [16]. Iglesia further investigated the effect of ruthenium addition to Co/TiO_2 (Ru 0.13 wt% and Co 20 wt%). It was observed that calcining the $Ru\text{-}Co/TiO_2$ before the reduction step, improved the catalyst activity without increasing cobalt dispersion. This was attributed to an intimate contact between Ru-Co that reduced the cobalt reoxidation and the carbon formation on the cobalt surface, commonly proposed to be the factors causing catalyst deactivation [17]. Luo [18] promoted iron based catalysts with group 2 alkali-earth metals (Mg, Ca, Ba and Be) and compared the results with a potassium doped catalyst. It was found that alkali-earth doped iron

catalysts yielded lower FT activity than potassium doped catalysts but that potassium promoted catalysts deactivate rapidly compared to alkali-earth catalysts at 270 °C and 13 bar. The Ba promoted catalyst showed higher activity and stability than the other alkali-earth doped catalysts [18]. Bao *et al.* impregnated Al_2O_3 with $Ba(NO_3)_2$ and after calcining added 15 wt% Co. It was found that small amounts of barium (2 wt%) restricted the cobalt support interaction improving the Co_3O_4 reducibility [19].

The standard method of preparing cobalt based catalysts is by the impregnation of a porous support, such as titania, silica, alumina or carbon, with a solution of cobalt salt such as $Co(NO_3)_2 \cdot 6\,H_2O$ [15]. It has been found that different supports and preparation methods yield a wide range of cobalt crystallite sizes, from 6 up to 25 nm [20-22]. The size of the supported Co particles has an important role in the FT activity. Bezemer *et al.* [20] and Borg *et. al.* [22] suggested that small crystallites, <4 nm were more sensitive to oxidation, whereas crystallites <6 nm did not have stable domains where the FT reaction steps take place and the ratio between the different reaction sites may not be the optimum. Therefore, the authors suggested a 6-8 nm Co crystals supported on carbon nanotubes gave the optimum activity and C_{5+} selectivity for reactions between 1 to 35 bar. Borg *et al.* [22] observed a volcano plot for C_{5+} selectivity and cobalt crystallite size and suggested that different volcano curves exits depending on the nature of the support.

In this *Chapter* a new process for impregnating FT catalysts *via* dense CO_2 (GAS process) will be described. Initially, GAS experimental parameters were surveyed to obtain the desired cobalt properties and then the catalyst was promoted to improve the performance under realistic FT conditions. A new methodology developed at Liverpool University by Professor Rosseinsky's group

was used to probe the catalysts under severe FT conditions. Thereafter, the suitable catalysts were scaled up and FT testing carried out at *Johnson Matthey*.

4.2 Preliminary study of GAS process.

4.2.1 Preparation.

The GAS experiments were performed as described in *Section 2.2.2* using the *Jerguson* equipment (see *Section 2.1.1*). The chemicals used are described in Table 4.2. Experiments performed are detailed in Table 4.3.

$Co(CH_3COO)_2 \cdot 4\,H_2O$ and $Co(NO_3)_2 \cdot 6\,H_2O$ were tested as cobalt precursors both at 25 °C and 40 °C. The pressure was increased until the solution volume had expanded by 900%, which was *ca.* 80 bar for experiments carried out at 25 °C and 40 °C. The initial study of the effect of the different cobalt precursors used a fixed concentration of salt in the solution. However, due to the variable solubility of the different salts in methanol, a fixed ratio of salt concentration to the equilibrium concentration was also probed. Slurries were prepared with the Co salt solutions and TiO_2 to give 20 wt% Co/TiO_2, unless otherwise specified, with the concentration ratios detailed in Table 4.3. Cobalt loadings of 10, 20 and 30 wt% were investigated using $Co(CH_3COO)_2 \cdot 4\,H_2O$.

Table 4.2. Chemicals used preparing GAS catalysts.

Chemicals	Company	Grade / purity
$Co(CH_3COO)_2 \cdot 4\,H_2O$	Sigma Aldrich	ACS reagent, ≥98.0%
$Co(NO_3)_2 \cdot 6\,H_2O$	Sigma Aldrich	ACS reagent, ≥98%
TiO_2-P25	Evonik-Degussa	75% Anatase – 25 Rutile
$Ru(NO)(NO_3)_2$	Sigma Aldrich	1.5% Ru in nitric acid
$Ru(C_5H_7O_2)_3$	Sigma Aldrich	purum, ≥97.0%
$Ba(NO_3)_2$	Sigma Aldrich	ACS reagent, ≥99%
Ba-isopropoxide	Sigma Aldrich	Powder, 99.9% trace metals basis
Methanol	Fisher-Scientific	Laboratory reagent grade
Ethanol	Fisher-Scientific	Laboratory reagent grade

In Table 4.3 the samples were labelled using the following system based on the preparation methodology. The catalysts were given a label, *e.g.* Co/Ti-C25, where C stands for acetate precursor and in the case of Co/Ti-N25, N for nitrate precursor. The number refers to the reaction temperature, either 25 or 40 for an operating temperature of 25 °C or 40 °C. The samples prepared to investigate the cobalt loading were labelled according to the wt% of Co added, *e.g.* Co/Ti-10L for 10 wt% or Co/Ti-20L for 20 wt% and Co/Ti-30L for 30 wt%. The sample labelled as Co/Ti-N25-c was performed using the same working concentration (c) to equilibrium concentration (c_o) ratio (c/c_o).

4.2.2 Cobalt precursors: acetate and nitrate salts.

4.2.2.1 Energy dispersive X-ray spectroscopy.

EDX was performed to analyze the cobalt loadings. Analysis was carried out on three spots and values were averaged with the relative error being within 7%.

Cobalt acetate yielded loadings close to targeted values, whereas the nitrate salt gave low loadings of cobalt at both at 25 °C and 40 °C, as seen in Table 4.4. This trend was also observed when the nitrate salt experiments performed under the same c/c_o ratio, Co/Ti-N25-c.

Table 4.4. Cobalt loading and effluent analysis of GAS experiments.

Catalyst precursors	c/c_o [a]	Co loading wt%	Effluent Co mg ml^{-1}	Yield %
Co/Ti-C25	0.35	29.6	1.54	98
Co/Ti-C40	0.35	28.3	83.5	96
Co/Ti-N25	0.09	5.4	77.07	18
Co/Ti-N40	0.09	8.3	87.73	7
Co/Ti-N25-c	0.35	10.9	367.45	27

[a]ratio of cobalt concentration in the solution (c) to the equilibrium concentration in methanol (c_0). Suffix -C25 and -C40 stand for samples synthesized using cobalt acetate precursor at either 25 °C or 40 °C. Suffix -N25 and –N40 stand for experiments using nitrate salts instead at temperatures of 25 °C or 40 °C. Cobalt loading aimed was 30 wt%.

The results suggest acetate was a more suitable salt for the GAS impregnation process, with the poor loadings found with the nitrate salt likely attributed either to high salt solubility in dense CO_2 or to the high coordinated water contribution. The large water content could have altered the CO_2/methanol phase system leading to a large water rich phase with hampered CO_2 diffusion, as discussed in *Chapter 3*. It should also be noted that the solubility of nitrates in dense CO_2 was not found in the literature.

4.2.2.2 Effluent analysis.

The effluent from the GAS experiments were analysed by atomic absorption spectroscopy and showed a low cobalt concentration for acetate salts and a high cobalt concentration for nitrate experiments (Table 4.4), relative error of 10% was observed upon 3 repetitions. The yields calculated from the atomic absorption spectroscopy show high precipitation efficiency for cobalt acetate but poor yields for nitrate salts. These observations agree with both the high cobalt yield and low cobalt acetate solubility in CO_2, as seen in *Chapter 3*.

4.2.3 Cobalt loadings on TiO_2: results and discussion.

In this section experiments were carried out to investigate the feasibility of GAS precipitation to load different amounts of cobalt on TiO_2, as described in Table 4.2. The loadings aimed were 10, 20 and 30 wt% Co/TiO_2, labelled as Co/Ti-L10, Co/Ti-L20 and Co/Ti-L30, respectively.

4.2.3.1 Energy dispersive X-ray spectroscopy.

EDX mapping of samples was performed to probe the loading and distribution of precipitated cobalt on the support (Table 4.5). As can be seen in Figure 4.1, cobalt was mainly precipitated on the support, although some regions of non supported cobalt was observed as seen in Figure 4.1. The initial hypothesis was that during the volumetric expansion the turbulence induced by dense CO_2 addition kept the slurry homogeneous, precipitating the cobalt precursor on the support.

Good agreement was found between targeted and measured loadings, as seen in Table 4.4. It suggests that the TiO_2 did not have an entrainer effect, *i.e.* decrease

or increase the solubility of a compound in CO_2 as a consequence of the introduction of a second compound [23].

4.2.3.2 Effluent analysis.

The cobalt content of the effluent was measured by atomic absorption and the observed concentrations and yields were similar to previous experiments, see *Section 4.2.2.1*, Co/Ti- C25 in Table 4.4. It is worth noting that cobalt acetate solubility in dense CO_2 was still very low, as yields were close to 100%. This suggested that TiO_2 did not modify the cobalt acetate solubility in dense CO_2 due to the introduction of a second solute [23].

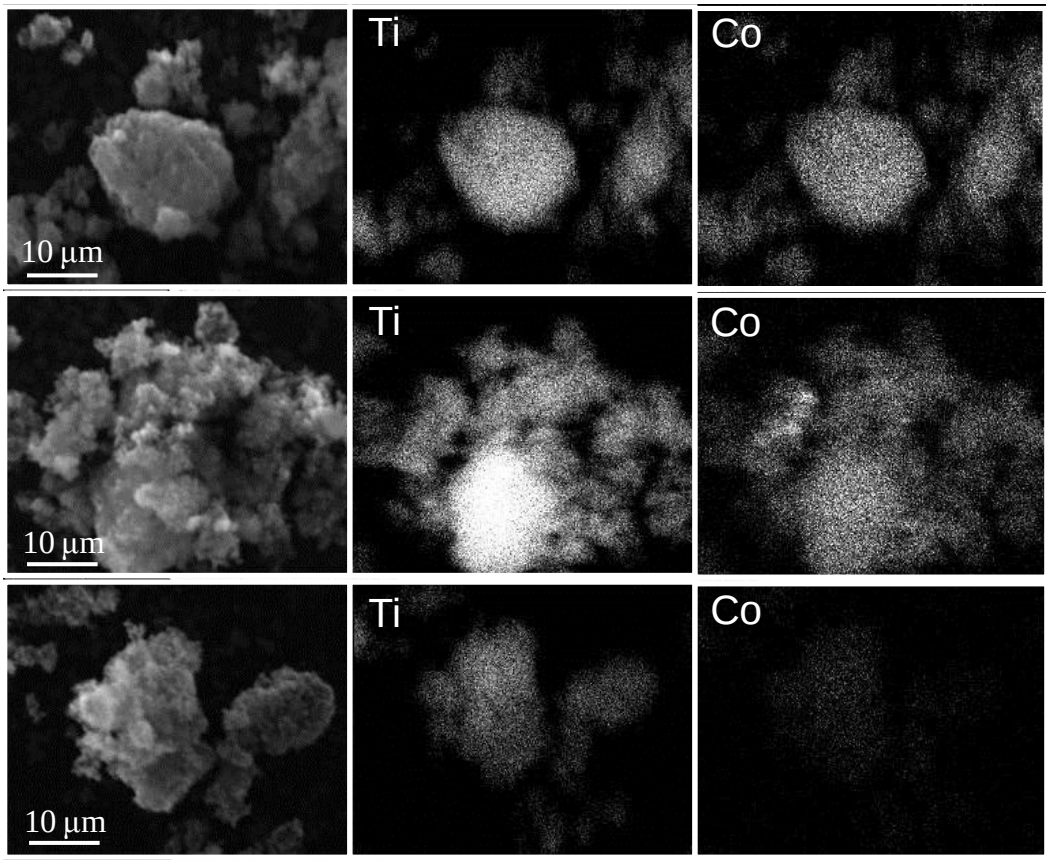

Figure 4.1. EDX mapping of Co/TiO_2 catalysts. Top row: 30 wt%, middle row: 20 wt% and bottom row: 10 wt%. On the left column SEM images, central column titanium mapping and right column cobalt mapping. Circle shows non supported cobalt.

Table 4.4. Cobalt loading and effluent analysis of loading study.

Catalyst precursors	Co loading wt %	Effluent Co mg ml^{-1}	Yield %
Co/Ti-L10	10.8	1.27	94
Co/Ti-L20	18.3	1.07	98
Co/Ti-L30	29.6	1.54	98

4.2.4 Solvent removal during the GAS synthesis.

The complete elimination of solvent from the precipitate is a key step in GAS precipitation, as residual solvent can cause re-dissolution as the pressure decreases at the end of the experiment, or may influence further thermal treatments such as calcination. The removal of the solvent at different CO_2 flow rates and process times was investigated, as described in Table 4.5.

4.2.4.1 Preparation.

Slurries of Co/Ti-C25, see Table 4.2, were stirred for 30 minutes and placed into the *Jerguson* precipitation vessel. The solutions were expanded at 25 °C up

Table 4.5. Weight loss of drying study.

Catalysts precursor	Time min	Flow rate L min^{-1} (STP)	CO_2 velocity cm s^{-1}	Weight loss at 110°C %	CO_2 used kg_{CO2} $g_{precursor}^{-1}$
Co/Ti-10m	10	12	6.8	10.0 ± 0.6	1.20
Co/Ti-30m	30	12	6.8	5.0 ± 0.3	3.55
Co/Ti-90m	90	12	6.8	5.0 ± 0.3	10.70
Co/Ti-4L	30	4	2.3	7.0 ± 0.4	1.20
Co/Ti-12L	30	12	6.8	5.0 ± 0.3	3.55
Co/Ti-20L	30	20	11.3	4.0 ± 0.2	6.00

Weight loss error estimated as 6% upon 4 repetitions. STP = standard temperature and pressure.

to 900% volumetric expansion. The elimination of the solvent from the precipitate was investigated by applying different time process and CO_2 flow rates. Initially three time intervals were surveyed: 10, 30 and 90 minutes (samples labelled: Co/Ti-10m, Co/Ti-10m, Co/Ti-10m respectively), by pumping 12 L min^{-1} (STP) of CO_2 at 80 bar and 25 °C through the precipitation vessel. CO_2 flow rates were also investigated, 4, 12 and 20 L min^{-1} (STP), samples labelled: Co/Ti-4L, Co/Ti-12L, Co/Ti-20L respectively, during 30 minutes at 80 bar and 25 °C.

4.2.4.2 Thermogravimetric analysis.

The weight loss between 50 °C and 150 °C is normally attributed to water and/or solvent trapped within or physisorbed on the catalysts. In this work the weight loss at 110 °C was taken as an indicator of how much solvent remained after the solvent removal.

After 10 minutes, the weight loss at 110 °C was double that seen after 30 or 90 minutes (Table 4.5), 10.0 ± 0.6% and 5.0 ± 0.3% respectively, showing that relatively long CO_2 purging time is needed to remove solvent. The 20 L min^{-1} CO_2 flow rate slightly decreased the weight loss compared to 12 L min^{-1}, 5.0 ± 0.3% and 4.0 ± 0.2% respectively. The experimental results suggest that long process time did not change the weight loss (5.0 ± 0.3% for both Co-Ti-30m and Co/Ti-90m), but the increase in CO_2 flow velocity slightly decreased the weight loss from 5.0 ± 0.3% to 4.0 ± 0.2% in Co-Ti-12L and Co/Ti-20L. It conveys that CO_2 velocity has a greater impact on solvent removal than the process time. The reason the solvent removal did not increase with time could be due to the TiO_2 porosity, 0.25 cm^3 g^{-1}, which retained solvent or water inside the pores. However,

the presence of coordination water in the cobalt acetate or water traces in the methanol or CO_2, which has a low solubility in CO_2, could also be responsible for the residual mass loss observed in the TGA.

4.2.5 Conclusions of preliminary study of GAS process.

It can be concluded that $Co(CH_3COO)_2 \cdot 4\,H_2O$ was the preferred salt for the GAS processes as it gave a high precipitation yield. The poor performance of cobalt nitrate was attributed to either high cobalt precursor solubility in dense CO_2 or to the large amount of coordinated water present in this precursor decreasing the CO_2 diffusion into the solvent in the system and ultimately restricting the solvent removal.

With the cobalt acetate salt, it has been demonstrated that metal loadings normally used for these catalysts can be achieved.

The removal of residual solvent by flushing CO_2 over the sample was investigated with the varying of flow rate and the residence time. It was concluded that flushing CO_2 for 30 minutes at 12 L min^{-1} (STP) was the most efficient drying process which was then used for future experiments.

4.3 Impact of GAS parameters in cobalt crystallite size under syn-gas conditions.

In this study several GAS parameters, see Table 4.6, were surveyed to determine the optimum settings required to obtain relatively small and stable cobalt particles, >6 nm, under syn-gas conditions, see *Section 2.4.12*, as this is an indicator of good Fisher-Tropsch performance, low methane and high C_{5+} selectivity [20]. Samples were labelled as follow: Co/Ti-WI sample wet impregnated with methanol, Co/Ti-SE sample expanded by GAS by slow

expansion rate, Co/Ti-FE sample expanded by GAS by fast expansion rate, Co/Ti-40 sample expanded by GAS by slow expansion rate at 40 °C, Co/Ti-C sample expanded by GAS by slow expansion rate but using half of the cobalt acetate concentration used in Co/Ti-SE and Co/Ti-EtOH sample expanded by GAS by slow expansion rate using ethanol as solvent.

4.3.1 Preparation.

The slurries were prepared as described in *Section 4.2.1* and the GAS impregnation experiments performed using the parameters described in Table 4.6. After synthesis, the samples were calcined at 350 °C for 5 h under static air to fully decompose the cobalt precursor and the syn-gas stability tests were then carried out, see *Section 2.4.12*.

Table 4.6. Experimental list of the GAS parameter studied for catalysts synthesis.

Catalysts precursors	Solvent	Volumetric expansion	Cobalt acetate mg ml^{-1}	Temperature °C	Studied variable
Co/Ti-WI	methanol	-	7	25	Wet impregnation
Co/Ti-SE	methanol	Slow (~5 bar min^{-1})	7	25	Volumetric expansion
Co/Ti-FE	methanol	Fast (~10 bar min^{-1})	7	25	Volumetric expansion
Co/Ti-40	methanol	Slow	7	40	Temperature
Co/Ti-C	methanol	Slow	3.5	25	Cobalt concentration
Co/Ti-EtOH	ethanol	Slow	7	25	Solvent

4.3.1.1 Powder X-ray diffraction.

XRD analysis was performed on the calcined catalysts and typical TiO_2-P25 (rutile-anatase mixture) and spinel Co_3O_4 reflections were observed (Figure 4.2). The intensity of the Co_3O_4 diffraction lines was not intense enough to use the Scherrer equation to calculate crystallite sizes. However, a relationship between Co_3O_4 and Co metal crystallite size has been reported as follows:

$$d_{Co} = 0.75 \cdot d_{Co3O4} \quad \text{Equation 4.5}$$

where d_{Co} = cobalt metal crystallite size and d_{Co3O4} = cobalt oxide crystallite size [24]. It is therefore possible for the cobalt oxide size to be estimated using values obtained in *Section 4.3.1.3*.

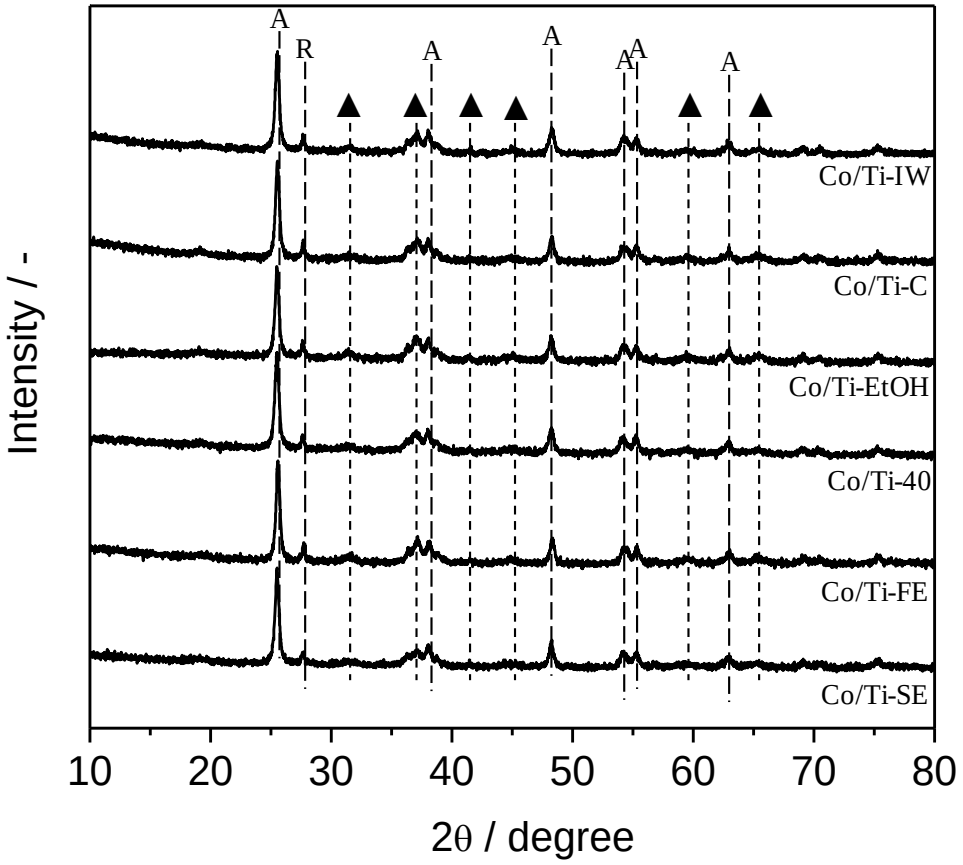

Figure 4.2. XRD analysis of Co/TiO_2 GAS catalysts. A indicates the anatase TiO_2 phase, R indicates the rutile TiO_2 phase and ▲ indicates the to spinel Co_3O_4 phase.

4.3.1.2 Temperature programmed reduction.

The cobalt reduction was analyzed by TPR and the results are shown in Table 4.7. Three reduction peaks were observed in all samples, except the Co/Ti-WI where only two were detected. The peak at low temperature, T_{R1}, was assigned to reduction of non-supported Co_3O_4 to CoO. The second reduction peak, T_{R2}, was attributed to the reduction of the supported Co_3O_4 to CoO and the third reduction peak, T_{R3}, was attributed to reduction of CoO to Co [15, 25]. It is suggested that during the GAS experiment, as the liquid phase was expanding cobalt acetate was precipitated in the liquid-gas boundary. Hence, some segregated cobalt precursor could be formed which was not observed under EDX mapping. This suggests that the mixing provided by the addition of CO_2 was not sufficient to ensure good contact and a mechanical mixer is needed to ensure good contact between the cobalt acetate and the support during the GAS precipitation.

The two reduction steps observed in Co/Ti-WI were attributed to the reduction of Co_3O_4 supported particles on TiO_2, Co_3O_4 to CoO (T_{R2}) and CoO to Co (T_{R3}), as observed by several authors [15]. It should be noted that Co/Ti-WI T_{R2} was very close to T_{R1} of GAS precipitated materials. This was likely to be due to the better contact between the cobalt precursor and TiO_2 during the GAS precipitation

Table 4.7. TPR results of the study of GAS parameters for catalysts synthesis.

Catalyst	T_{R1} °C	T_{R2} °C	T_{R3} °C
Co/Ti-WI	-	268	421
Co/Ti-SE	290	324	430
Co/Ti-FE	283	341	420
Co/Ti-40	286	335	431
Co/Ti-*C*	270	322	432
Co/Ti-EtOH	294	327	438

compared to the wet impregnation as a consequence of the low surface tension of CO_2 at 25 °C (1 mN m^{-1}) compared to methanol (22.5 mN m^{-1}), solvent used in Co/Ti-WI. The intimate contact between cobalt precursor and TiO_2 could yield strong Co_3O_4 interaction with TiO_2 after calcination; hence high reduction temperature.

4.3.1.3 Syn-gas stability test.

The stability of cobalt metal crystallites under severe Fischer-Tropsch conditions was studied. The catalysts were reduced under H_2 at 500 °C, and analysed by XRD. The catalysts were then exposed to syn-gas (50 ml min^{-1}, 230 °C and $CO:H_2$ = 1:4) for 100 h before post reaction XRD analysis was carried out (see *Section 2.4.12*). The results for the GAS catalysts are depicted in Figure 4.3, which shows the crystallite size and the relative content of Co before and after being subjected to syn-gas treatment. The cobalt crystallites were estimated using the Scherrer approach on the cobalt metal reflection located

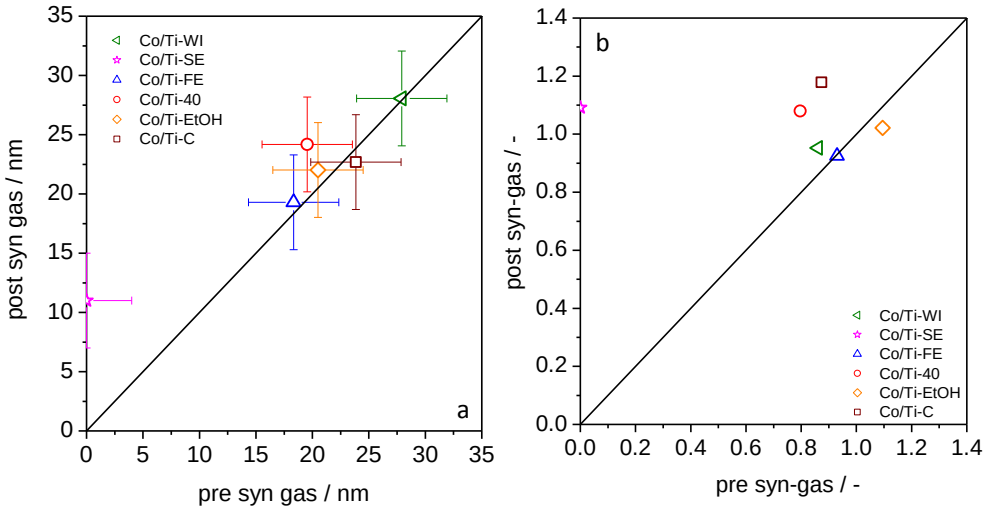

Figure 4.3 a) cobalt metal crystallite size and b) reducibility of catalysts synthesised under different GAS conditions, reducibility was calculated as the ratio between the area below the cobalt metal peak, 38-57 2θ degrees, and the TiO_2 peak, 56.2-56.3 2θ degrees. Absolute error 4 nm were measured upon repetition.

between 51.7-51.9 2θ degrees. The cobalt reducibility was estimated by dividing the area below the cobalt metal reflection by that of the area below the TiO_2 peak, between 56.2-56.3 2θ degrees.

Comparison between the GAS and wet impregnation preparation methods shows larger crystallites in the latter which is attributed to the longer time available for crystallite growth during the wet impregnation.

The study of the volumetric expansion rate, Co/Ti-SE and Co/Ti-FE, showed small cobalt metal crystallites of *ca.* 12 nm in Co/Ti-SE after syn-gas treatment and crystallites of *ca.* 22 nm in Co/Ti-FE. It is worth noting that the Co/Ti-SE catalyst did not show cobalt metal reflections before the syn-gas treatment. This fact was attributed either to the formation of a stable and non-reducible Co species (*i.e.* $CoTiO_3$) or to incomplete cobalt reduction and was investigated further, see *Section 4.3.2*. However, it is clear that the slow expansion method provided the smaller cobalt metal crystallites under the reaction conditions. Small particles have been observed previously when slow GAS expansions were used [26]. The precipitation during a GAS experiment takes place at the liquid-gas interface as a consequence of CO_2 diffusion into the liquid phase. The time available for this process in a fast expansion is shorter than in a slow expansion. Thus, the slow expansion facilitates the diffusion of CO_2 into the liquid phase promoting the supersaturation [26-28].

The cobalt concentration was reduced to half of the initial concentration, Co/Ti-*C*. Following the syn-gas treatment particles were stable but large, *ca.* 25 nm. Co/Ti-*C* showed larger cobalt particles than for Co/Ti-SE that can be attributed to the decrease in supersaturation (*Sc*) ($Sc = c/c'_0$, where c = concentration of

solute in the solvent and c'_0 = equilibrium concentration of solute in CO_2) that decreases the nucleation time increasing the time available for particle to grow [29].

The catalyst synthesized at 40 °C, Co/Ti-40, showed relatively large cobalt crystallites compared to Co/Ti-SE. The increase in process temperature yields large particles as the salt solubility in CO_2 increases, lowering the supersaturation degree and the nucleation rate, yielding larger particles [26]. These large crystallites sintered slightly during the syn-gas treatment.

The solvent impact on the precipitation was investigated by preparing a precursor solution with ethanol, Co/Ti-EtOH. The syn-gas treatment showed stable cobalt metal particles, albeit with a larger particle size than catalysts made using methanol, Co/Ti-SE. The increase in particle size was attributed to the difference in solvent viscosity (ethanol = 1.04 mPa·s and methanol = 0.59 mPa·s). The high viscosity hampers the mass transport, *i.e.* diffusion of CO_2 into the solution, decreasing the nucleation rate and increasing the particle growth time.

The reducibility of the catalysts is shown in Figure 4.3-b. A shift towards the left indicates that the area below the cobalt reflection increases in relation to the TiO_2 reflections. Generally cobalt reduced during the syn-gas treatment and points moved towards the left side of the centre line. This might suggest that catalysts were not fully reduced during the heat treatment under H_2 as a consequence of small Co_3O_4 particles or the strong interaction between Co_3O_4 particles and TiO_2 that limited the reducibility. It is worth noting Co/Ti-SE had cobalt metal present after the syn-gas treatment but not before, suggesting that the catalyst was poorly reduced after thermal treatment in H_2 prior to the XRD measurement.

4.3.2 Investigation of $CoTiO_3$ formation in the Co/Ti-SE catalyst.

The Co/Ti-SE catalyst showed small cobalt metal particles after the syn-gas treatment, but not before. Stable Co-Ti species (*i.e.* $CoTiO_3$) can be formed during calcination and could be responsible for the lack of observable cobalt metal crystallites [30]. These stable Co-Ti species reduce at high temperatures, and ultimately decrease the catalyst activity and increase the CH_4 selectivity during the FT reaction [30]. Hence, *in situ* XRD and TPR analysis were performed to investigate the formation of $CoTiO_3$.

4.3.2.1 In situ powder X-ray diffraction.

In situ XRD (Figure 4.4) was performed as described in *Section 2.4.1*. The sample was placed inside a high temperature cell fed with air at 50 ml min^{-1}. The temperature was steadily increased from room temperature up to 650 °C at a rate of 5 °C min.

The analysis did not show any $CoTiO_3$ at the calcination temperature (350 °C). At 550 °C the spinel Co_3O_4 was visible but $CoTiO_3$ reflections were only observed at 650 °C. Therefore, *in situ* XRD analysis suggests there was not bulk $CoTiO_3$ formation at 350 °C.

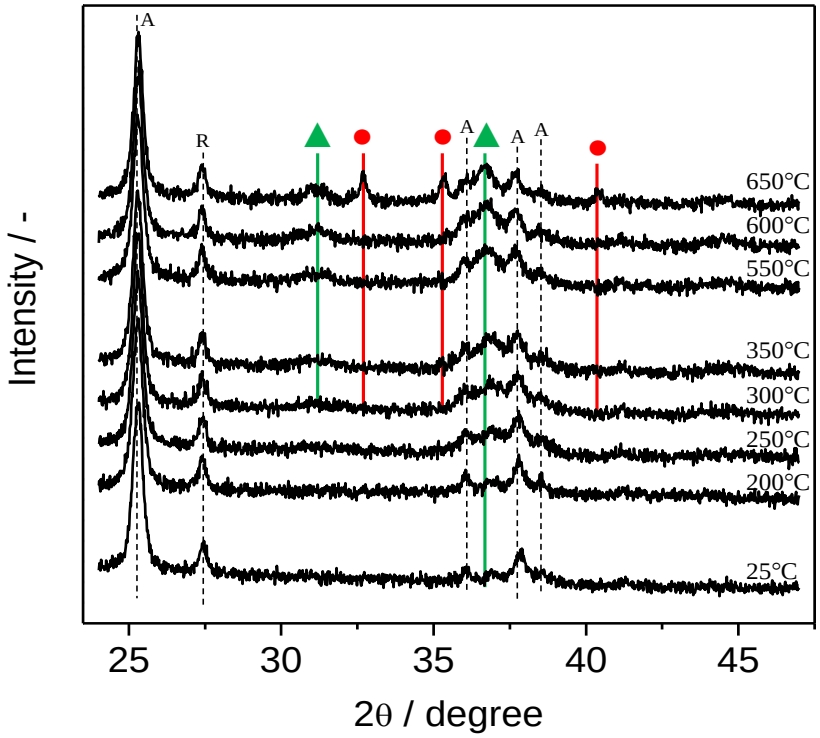

Figure 4.4. In situ XRD of Co/Ti-SE, analysis temperature at right side. A = anatase TiO_2 phase; R = rutile TiO_2 phase; ▲ spinel Co_3O_4; ● $CoTiO_3$.

4.3.2.2 Temperature programmed reduction.

The presence of high-temperature reducible species was investigated by TPR (Figure 4.5). A typical Co_3O_4 reduction profile was observed with a first reduction of unsupported Co_3O_4 to CoO, the second peak supported Co_3O_4 to CoO and the third reduction step of CoO to cobalt metal [15]. High temperature H_2 consumption was not observed, with all cobalt oxide species reduced below 450 °C. The reported reduction temperature of $CoTiO_3$ is between 700-800 °C [30], which is clearly not present.

Hence, the absence of cobalt metal diffraction peaks in Co/Ti-SE before the syn-gas treatment was likely due to an insufficient reduction treatment under H_2 prior to XRD measurement.

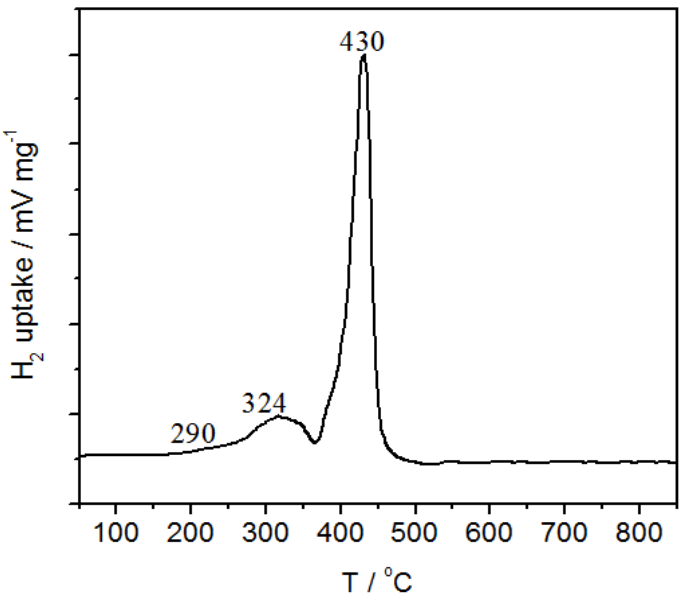

Figure 4.5. TPR of Co/Ti-SE.

4.3.3 Conclusions.

In general the cobalt crystallites produced in the GAS catalysts were stable during syn-gas treatment, with a degree of sintering only observed for Co/Ti-40. It was found that the Co/Ti-SE catalyst was not completely reduced before the syn-gas treatment and cobalt metal was only observed after the syn-gas treatment. The reason for this is unclear. XRD and TPR experiments did not find indications of $CoTiO_3$ in the catalyst. Hence, the absence of cobalt metal particles before the syn-gas treatment was attributed to an incomplete catalyst reduction step and not to the formation of $CoTiO_3$. For the other catalysts, stable cobalt particles were observed. The stability of the cobalt crystallites can be correlated to their relative large size, as sintering of cobalt crystallites is normally observed for small particles in the range of 6-15 nm [31-33].

XRD also gave information on the relative content of Co before and after the syn-gas treatment. It was clear by the shift towards higher cobalt content after syn-gas treatment, that unreduced cobalt species were present following H_2 reduction and these were reduced by syn-gas treatment.

4.4 Stabilization of cobalt metal crystallites via catalyst modification.

The previous study pointed Co/Ti-SE process as producing the smallest cobalt metal crystallites. This provides evidence for it being the most successful candidate for an active FT catalyst. However, the crystallites were not visible before the syn-gas treatment indicating either non-reduced cobalt species, which are barely active for FT, or very small cobalt crystallites that eventually can increase the methanation. Hence, research underwent at Liverpool University by Professor Rosseinskys's group was incorporated into the GAS process to improve Co/Ti-SE catalyst. This work involved the addition of promoters such as ruthenium and barium to improve the stability of catalysts under FT reaction.

4.4.1 Preparation.

The GAS synthesis was conducted using the same preparation parameters as used for Co/Ti-SE, as seen in Table 4.6 and the catalysts prepared are detailed in Table 4.8. Co/Ti-S was made using the same Co/Ti-SE parameters to assess the process reproducibility. To prepare modified support, barium nitrate was impregnated on TiO_2 and then calcined at 350 °C under static air for 5 h. Thereafter, the Ba-TiO_2 support was used to prepare the slurry for GAS synthesis, with the Co impregnated material denoted Co/Ti-Ba-N. Ruthenium was

Table 4.8. Metal loadings, chemical precursors and targets to stabilize GAS catalysts.

Catalyst	Ru wt%	Ba wt%	Co wt%	H_2O vol%	Chemical modification	Parameter under investigation
Co/Ti-Ba-N	-	1	20	-	$Ba(NO_3)_2$	Co reducibility
Co/Ti-Ru	0.1	-	20	-	$Ru(NO)(NO_3)_2$	Co reducibility
Co/Ti-5	-	-	20	5	H_2O	Co stability
Co/Ti-S	-	-	20	-	-	Reproducibility

introduced after calcination of the Co/Ti-S by catalyst impregnation with $Ru(NO)(NO_3)_2$ and then calcining at 350 °C for 5 h, with the material denoted Co/Ti-Ru. Water was introduced in the initial slurry as it had been observed that the water addition promotes stability of nanocrystalline Co_3O_4 (*Chapter 3*), with the material denoted Co/Ti-5.

The processed cobalt based catalysts were calcined at 350 °C, with a heating rate of 5 °C min^{-1}, for 5 h under static air.

4.4.2 Results and discussion.

4.4.2.1 Powder X-ray diffraction.

The XRD showed typical TiO_2-P25 (rutile-anatase) and spinel Co_3O_4 reflections, as seen in Figure 4.6. Reflections of either Ru or Ba oxides or to Co-Ru or Ba-Ti were not observed in the modified catalysts due to low amount of Ru and Ba added. The $Ba(NO_3)_2$ has been reported to form highly dispersed BaO

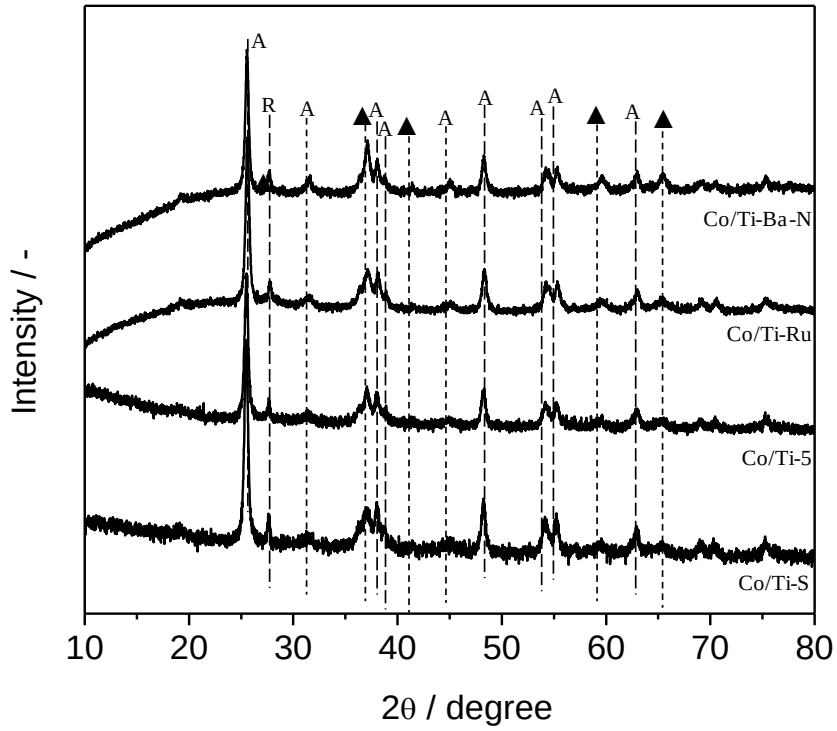

Figure 4.6. XRD patterns of catalysts described in Table 4.8. A = anatase TiO_2 phase; R = rutile TiO_2 phase; ▲ spinel Co_3O_4 phase.

after calcination, but this is not observable by XRD [19]. The $Ru(NO)(NO_3)_2$ decomposes to RuO_2 under calcination but the small proportion of this phase made difficult the observation in the XRD.

4.4.2.2 Temperature programmed reduction.

The reduction peaks of the catalysts prepared are listed in Table 4.9. Most of the catalysts reduced in three steps, as seen for the undoped Co/TiO_2 in *Section 4.3.1.2*, suggesting small amounts of non-supported cobalt. The Co/Ti-Ru catalyst was observed to have a lower reduction temperature, 157 °C and 280 °C, which is in agreement with Co-Ru catalysts described in the literature [13, 17]. The low temperature reduction was attributed to the rapid H_2 activation in presence of ruthenium and then the spillover which facilitates the reduction of Co_3O_4 to CoO and the CoO to Co [15, 17]. In the present work, it is suggested that ruthenium, as it was impregnated after calcination, covered all the Co_3O_4, regardless of whether it was supported or non-supported cobalt oxide. Therefore, only two reduction peaks were observed. The Co/Ti-S presented discrepancies with Co/Ti-SE, despite being synthesised using the same process parameters. This was attributed to the difficulties keeping the expansion rate constant as a consequence of the equipment limitations.

Table 4.9. EDX loadings and TPR results of GAS stabilized catalysts.

Catalyst	Ru wt%	Ba wt%	Co wt%	T_{R1}	T_{R2}	T_{R3}
Co/Ti-Ba-N	-	0.6	25.1	292	316	419
Co/Ti-Ru	0.08	-	22.4	-	157	280
Co/Ti-5	-	-	19.3	280	349	446
Co/Ti-S	-	-	21.3	267	329	411

Co/Ti-5 reduced at the highest temperature which may be attributed to small particles being formed after calcination due to the presence of water in the initial solution (see *Chapter 3*) which ultimately evolved in strong cobalt-support interactions hampering cobalt reduction. The barium promoted catalyst, Co/Ti-Ba-N, had a lower temperature assigned to the reduction of Co_3O_4 to CoO than Co/Ti-S, suggesting that barium promotes cobalt reducibility, as it may intercalate between Co_3O_4 and TiO_2 reducing the cobalt support interaction, as suggested previously [18].

4.4.2.3 Energy dispersive X-ray spectroscopy.

EDX analysis was performed to determine the catalysts chemical composition. The analysis was performed on three spots and values were averaged. The maximum error was found to be within 7%, as seen in Table 4.9. Mapping was performed to estimate metal distribution of relevant GAS processed catalysts, as shown in Figures 4.7 to 4.9.

Figure 4.8 shows the EDX of Co/Ti-S, within the scanned region. In general, good agreement was found between the Ti and Co signals; although, cobalt and magnesium/titanium mismatch was observed in Figure 4.8. With reference to Co/Ti-Ba-N, shown in Figure 4.8, the barium signal overlapped the titanium signal showing good contact between Ba and Ti. The ruthenium promoted catalyst, shown in Figure 4.9, presented good match between ruthenium, cobalt and titanium signals which is expected as the ruthenium precursor was impregnated on the calcined catalyst. Hence, the process studied achieved the loadings target demonstrating the viability of the process incorporating different promoters.

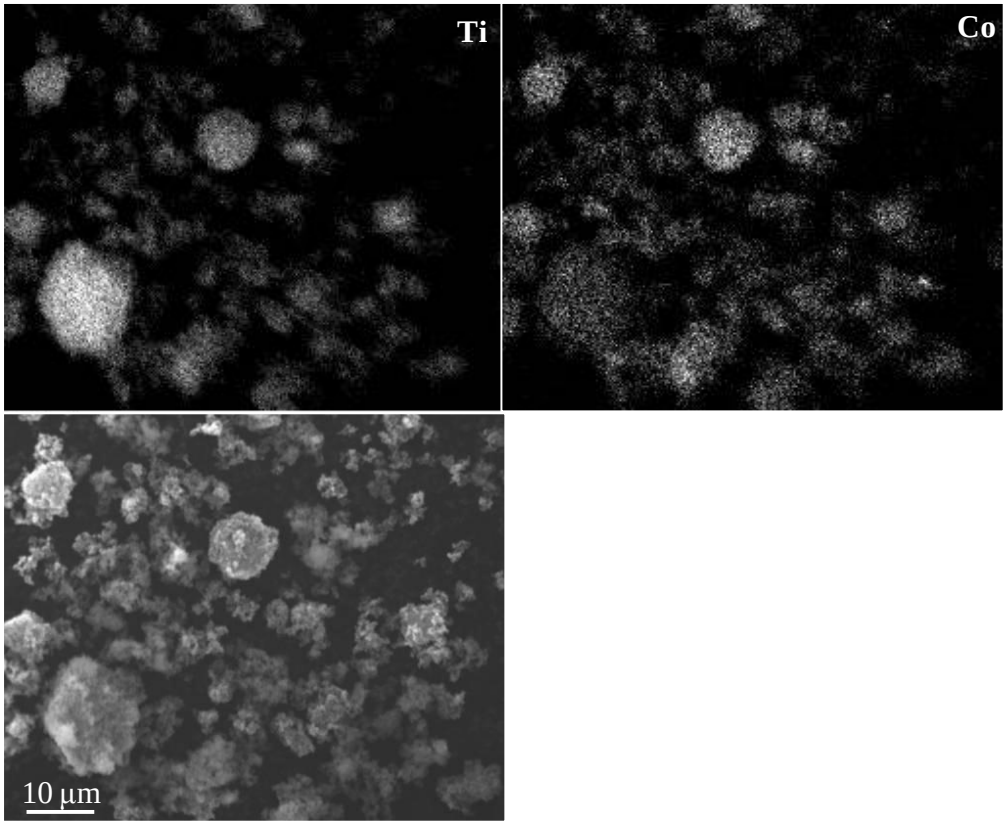

Figure 4.7. EDX mapping of Co/Ti-S. Top left picture elemental Ti distribution. Top right elemental Co distribution. Bottom left picture SEM image.

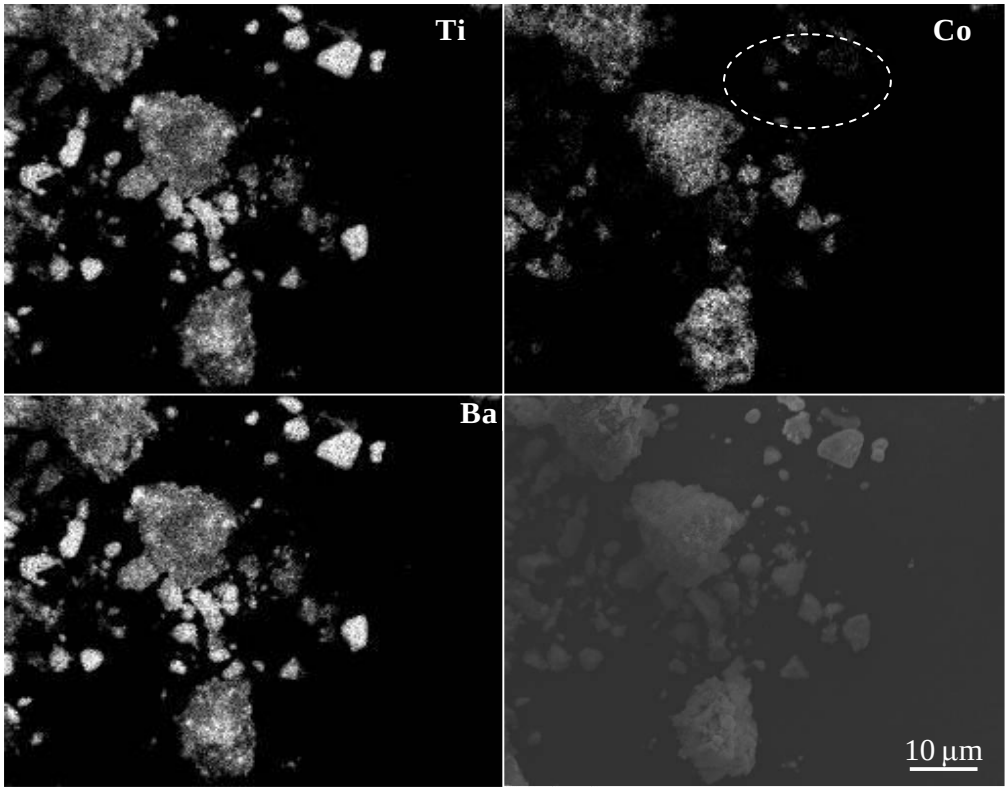

Figure 4.8. EDX mapping of Co/Ti-Ba-N. Top left elemental Ti distribution. Top right elemental Co distribution. Bottom left elemental Ba distribution. Bottom right SEM image. Circle indicates mismatch between cobalt and titanium signal.

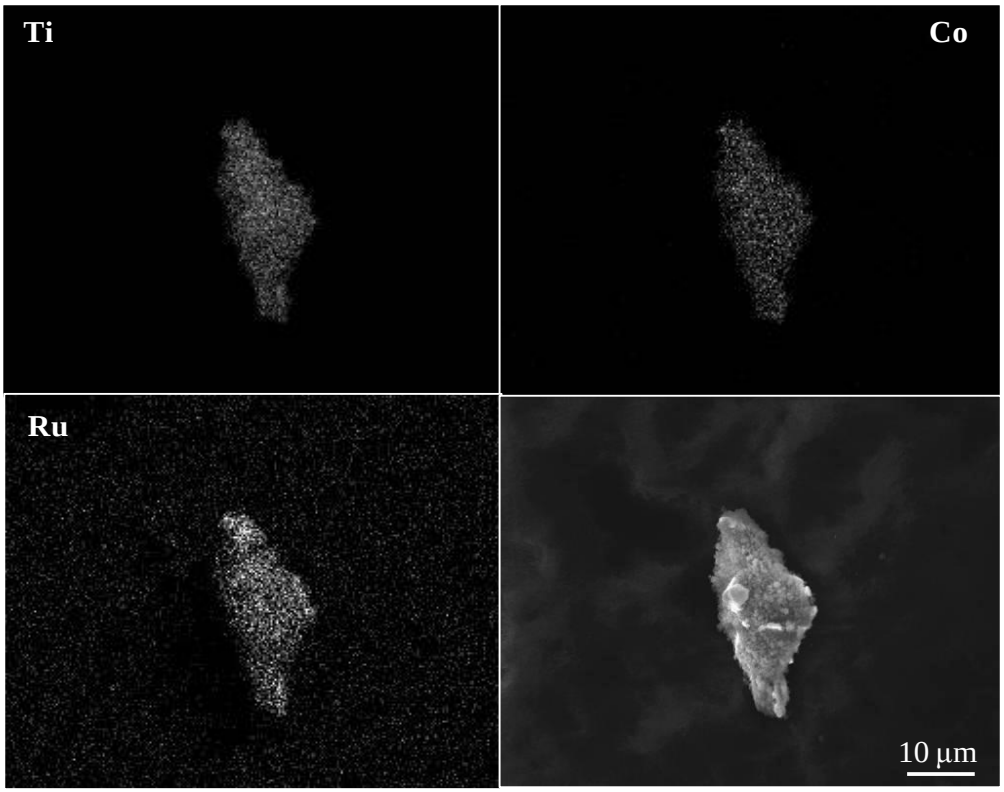

Figure 4.9. EDX mapping of Co/Ti-Ru catalyst. Top left elemental Ti distribution. Top right elemental Co distribution. Bottom left elemental Ru distribution. Bottom right SEM image

4.4.2.4 Syn-gas stability tests.

The catalysts detailed in Table 4.8 were then subjected to the syn-gas treatment, as described in *Section 2.4.12*, and the results are shown in Figure 4.10. The cobalt particle size observed in Co/Ti-S were *ca.* 12 nm, the same as previously observed for Co/Ti-SE after the syn-gas treatment. However, in this case cobalt particles were observed before syn-gas treatment. This fact along with the lack of evidence of $CoTiO_3$, *Section 4.3.2*, strongly suggests that species difficult to reduce (*e.g.* $CoTiO_3$) were not formed during calcination of Co/Ti-SE or Co/Ti-S. It is worth noting that after syn-gas treatment the cobalt crystallites remained close to the centre line (within the error) indicating certain cobalt stability.

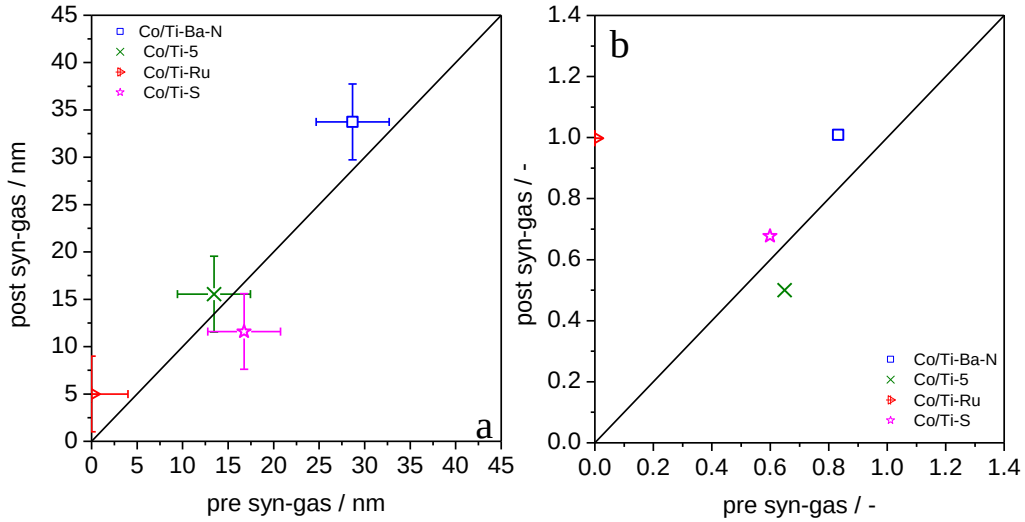

Figure 4.10. a) cobalt metal crystallite size. b) cobalt reducibility. Error bars ±4 nm.

The addition of ruthenium, Co/Ti-Ru, clearly reduced the cobalt crystallite size, as seen in Figure 4.10, although the crystallites were only visible after syn-gas treatment. It is conveyed that particles before the syn-gas treatment were too small to be detected under XRD. The formation of small particles was likely to be promoted by the addition of ruthenium as it facilitates a nucleation site to form the cobalt metal [13, 34].

The barium modified supports did not give any improvement in terms of cobalt metal crystallite size with the particles even larger than the non-doped cobalt catalyst.

The addition of water to the precipitation process (Co/Ti-5) likely formed small Co_3O_4 particles, as observed in *Chapter 3*, that reduced to relative small and stable cobalt particles (15 nm).

The cobalt reducibility was also investigated and results are shown in Figure 4.10. Overall, modified catalysts, both with barium and ruthenium, improved the cobalt reduction which agrees with TPR analysis.

4.4.3 Conclusions.

The size and stability of the cobalt metal crystallites were improved by the addition of ruthenium to the catalysts prepared by GAS. The addition of barium to the support prior to GAS impregnation improved the cobalt reducibility; however, it also increased the crystallite size. Hence, the ruthenium doped catalyst, Co/Ti-Ru, and the catalyst impregnated onto the barium doped support, Co/Ti-Ba-N, were chosen to scale-up and further test under FT conditions.

It is worth noting that TPR showed differences in reduction temperatures for Co-Ti-SE and Co-Ti-S. However, the cobalt crystallites were of similar size (11-12 nm) and the cobalt loading agreed in both cases. This provided confidence in the process to carry out further experiments. The inconsistencies in the materials might arise from the difficulties of managing the *Jerguson* equipment to run the GAS experiments (*i.e.* difficulties managing the expansion rate as a consequence of the volumetric exponential growth) or to a lack of contact between cobalt precursor and TiO_2 during precipitation.

4.5 Scale-up GAS catalysts.

Selected catalysts were scaled-up using the larger scale *Separex* unit, to produce the required amount of catalyst precursors to allow testing under FT conditions and cobalt surface area to be analyzed.

4.5.1 Preparation.

The GAS experiments were carried out using the *Separex* unit, see *Section 2.1.2*, and the experimental process described in *Section 2.2.2*. As mentioned in *Section 4.4*, slight inconstancies were seen in materials prepared under the same

Table 4.10 Experimental conditions in scaled-up experiments.

Pressure rate / bar min^{-1}	*ca.* 5 (Slow)
Temperature / °C	25
Slurry volume / ml	100
Stirring velocity / r.p.m.	600
Volumetric expansion / %	900

conditions (*i.e.* cobalt metal was observed in Co/Ti-S after reduction with H_2 and prior to syn-gas treatment but it was not seen in Co/Ti-SE under same treatments), which was attributed to poor mixing and/or difficulties handling in-house made equipment. Consequently, a stirrer shaft was used to avoid the TiO_2 settling on the bottom of the pressure vessel. Also, baffler units were introduced to avoid vortex formation and improve slurry homogeneity. The experimental parameters are shown in Table 4.10, the metal loadings aimed in Table 4.11 and the chemical reagents used in Table 4.1. The S-Co/Ti-S was made reproducing conditions for Co/Ti-S. Barium and ruthenium salts were introduced as described in *Section 4.4.1*, with the catalysts denoted S-Co/Ti-Ba and S-Co/Ti-Ru-WI respectively. The S-Co/Ti-Ru-OP catalyst was prepared in a one-step process by dissolving both $Ru(C_5H_7O_2)_3$ and $Co(CH_3COO)_2{\cdot}4\,H_2O$ in the TiO_2 methanol slurry which was then expanded using the GAS process. This process can

Table 4.11. Loading aimed in scaled-up catalysts.

Catalysts	Ba wt%	Ru wt%	Co wt%	Variable studied
S-Co/Ti-S	-	-	20	Standard GAS synthesis
S-Co/Ti-Ru-WI	-	0.1	20	Ru wet impregnation
S-Co/Ti-Ba	1	-	20	TiO_2 support modified with Ba
S-Co/Ti-OP	-	0.1	20	GAS co-precipitation of Co-Ru on TiO_2
S-Co/Ti-HiPI	-	-	20	HiPI process

provide good mixing of Co and Ru in the material, as observed in the precipitation of CuMnOx [35]. It has been shown that solubility of metal salts in dense CO_2 change depending on the environment (*i.e.* presence of co-solvents, second solute, etc.). Poor solubility of $Co(CH_3COO)_2 \cdot 4\,H_2O$ in CO_2 was found in *Chapter 3* and the solubility did not change significantly with TiO_2 addition, as observed in *Section 4.2.3.2*. Yoda and co-workers experimentally obtained the $Ru(C_5H_7O_2)_3$ molar fraction solubility to be $170 \cdot 10^{-7}$ in CO_2, at 100 bar and 40 °C [36]. It is known that metal salt solubility increases with pressure and temperature. Therefore, as normal GAS experiments are performed at 25 °C and pressures up to *ca.* 80 bar, $Ru(C_5H_7O_2)_3$ solubility might decrease. Likewise, solubility of one salt may enhance or decrease due to the presence of a second solute in the system [23]. Furthermore, with the addition of methanol the co-solvent effect generally increases salt solubility by more than one order of magnitude [37, 38]. Therefore, the solubility of $Ru(C_5H_7O_2)_3$ under working conditions may differ substantially from values reported by Yoda [36]. Hence, for this study the value reported was increase by one order of magnitude due to the co-solvent effect, *i.e.* methanol presence, and for the sake of simplicity, factors such as the presence of other solutes, pressure and temperature were initially ignored. Based on these assumptions, the amount of ruthenium was adjusted to 0.1 wt%. The S-Co/Ti-HiPI was made using the semi-continuous, high pressure impregnation methodology, as described in *Section 2.2.3* using the equipment described in *Section 2.1.3*. A semi-continuous precipitation of slurry may improve particle size dispersion as time for nucleation and growth is more homogeneous than in the batch GAS process.

It is worth noting that after the drying step, see *Section 2.2.2*, and the subsequent depressurization, the processed catalysts were frozen due to the formation of dry ice. In order to avoid this, the system was slowly depressurized to 12 bar and the CO_2 was allowed to flow at 40 °C for 1 h, before depressurizing fully.

Processed catalysts were calcined at 350 °C, with a ramp rate of 5 °C min^{-1}, for 5 h under static air and sent to *Johnson Matthey* for FT testing and cobalt surface area analysis.

4.5.2 Results and discussion.

4.5.2.1 Powder X-ray diffraction.

The XRD analysis was performed on the calcined catalysts, as seen in Figure 4.11. As observed previously for the catalysts prepared on a smaller scale, traces of neither Ba nor Ru were observed and only TiO_2 diffractions (anatase and rutile

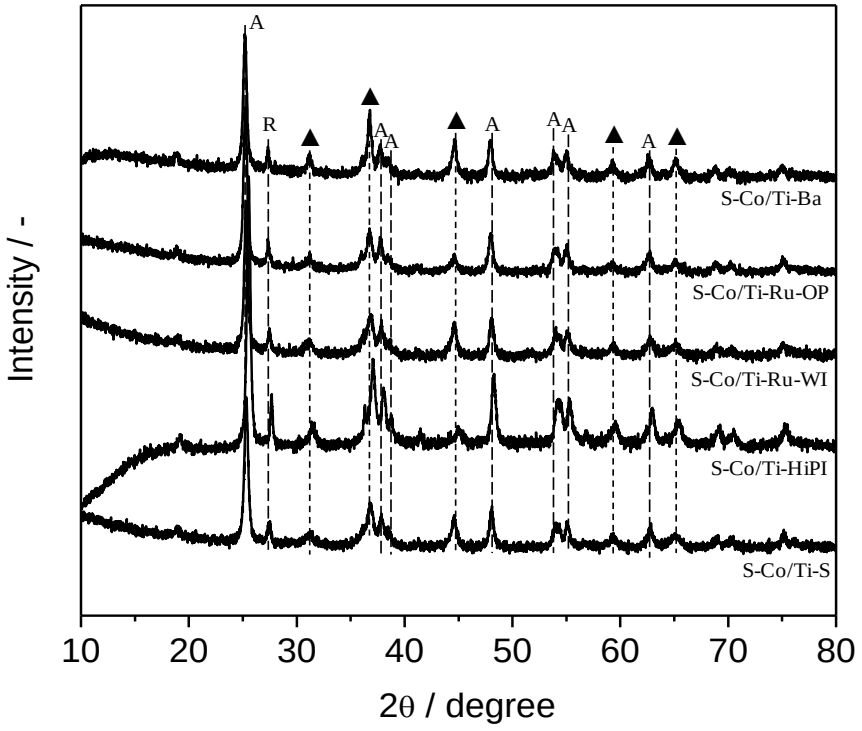

Figure 4.11. XRD patterns of catalysts synthesised in *Separex* . equipment. A = antase phase TiO_2; R = rutile TiO_2 phase and ▲ spinel Co_3O_4.

phases) and spinel Co_3O_4 were seen. The $Ba(NO_3)_2$ has been reported to form highly dispersed BaO after calcination which is not observable by XRD [19]. The $Ru(C_5H_7O_2)_3$ decomposes to RuO_2 but the small proportion of this phase is most likely below the detection limit of XRD.

4.5.2.2 Temperature programmed reduction.

TPR analysis was performed on the catalysts listed in Table 4.12 and the results are shown in Table 4.12.

It is worth noting that TPR showed two reduction peaks, as opposed to the three peaks seen previously for GAS Co/TiO_2 catalysts. The introduction of the stirrer and the baffle improved the contact between the support and the active phases during precipitation and consequently gave a non-segregated cobalt acetate precipitation. The stirrer also might improve the particle size distribution as a consequence of improving the contact between CO_2 and the slurry [39]. With reference to the standard GAS precipitated catalyst, S-Co/Ti-S, the two reduction steps were assigned to the reduction of supported Co_3O_4 to CoO and then CoO to Co. The values were close to those observed for Co/Ti-S, see Table 4.9, suggesting that the scaled-up catalyst reduced at similar temperatures to the catalysts made in the *Jerguson* equipment.

The catalyst synthesized using the HiPI equipment, S-Co/Ti-HiPI, reduced at lower temperature than S-Co/Ti-S. The low temperature reduction can be attributed to the poor contact between cobalt precursor and support.

Table 4.12. EDX, TPR and Co surface area results of scaled-up catalysts.

Catalyst	Ru wt%	Ba wt%	Co wt%	T_{R1}	T_{R2}	Co surface area $m^2 g_{Co}^{-1}$
S-Co/Ti-Ba	-	0.9	22	318	450	5.0
S-Co/Ti-Ru-OP	0.05	-	23	243	354	20.0
Co/Ti-Ru-WI	0.08	-	24	186	303	16
S-Co/Ti-HiPI	-	-	38	305	358	-
S-Co/Ti-S	-	-	22	330	444	8.0

Note: suffix –Ba stands for the sample prepared with the barium modified support, -OP refers to the GAS co-precipitation of cobalt, ruthenium precursors on TiO_2. WI stands for the S-Co/Ti-S impregnated with $Ru(NO)(NO_3)_2$. –HiPI refers to sample synthesised using the HiPI device, see *Chapter 2* and –S for GAS standard precipitation.

The addition of ruthenium to the Co/TiO_2 catalysts resulted in low reduction temperatures. The enhancement in cobalt reduction by ruthenium is well known in FT catalysts and is attributed to a decrease in activation energy for the metal phase formation as a consequence of H_2 activation on the ruthenium [34, 40].

With regard to the barium modified support, the temperature of reduction was slightly reduced compared to the standard catalyst, S-Co/Ti-S, as observed in *Jerguson* processed catalysts, and agrees with the previous reports by Luo [18].

4.5.2.3 Energy dispersive X-ray spectroscopy.

EDX analyses were performed to determine the chemical composition of the catalysts. Analysis was performed on three spots, values were averaged and were found to be within a 7% error, see Table 4.12.

Overall the cobalt content was in agreement with expected values within the observed error. The ruthenium content in S-Co/Ti-Ru-WI agrees with the analysis of Co/Ti-Ru-IW made in the *Jerguson* equipment and both are close to

the expected value. In the case of S-Co/Ti-Ru-OP, the observed ruthenium loading was below the target loading. This low loading can be attributed to the high $Ru(C_5H_7O_2)_3$ solubility in the system (*i.e.* dense CO_2 and methanol). This experiment shows that ruthenium and cobalt can be successfully co-precipitated and further investigation of synthesis parameters (adjust the total amount of $Ru(C_5H_7O_2)_3$ preloaded to the aimed ruthenium loading) may be needed to refine the ruthenium loading. The agreement between the expected and observed cobalt loading suggests that $Ru(C_5H_7O_2)_3$ did not modify the solubility of $Co(CH_3COO)_2{\cdot}4\,H_2O$ in dense CO_2.

For the barium modified support experimental values are in agreement with expected loadings and *Section 4.4.2.3*.

4.5.2.4 H_2 chemisorption.

The H_2 chemisorption was performed at *Johnson Matthey* as described in *Section 2.4.10*, and the cobalt surface area was calculated, as shown in Table 4.12.

The ruthenium containing catalysts presented a larger cobalt surface area compared to both the standard and barium doped titania supported catalyst. The increase in available cobalt on the surface was previously observed by several authors and was assigned to the cobalt nucleation points that ruthenium provides yielding small cobalt crystallites that lead to a high cobalt surface area [41]. The cobalt surface areas obtained are similar those previously reported in the literature for Co/TiO_2 catalysts, 9.6 $m^2\ g_{Co}^{-1}$ in 10% Co/TiO_2 and 11 $m^2\ g_{Co}^{-1}$ in 20% Co/TiO_2 [41, 42]. Likewise, similar values were obtained in the present work to

those reported in the literature for similar catalysts, such as 24 m^2 g_{Co}^{-1} for 10% Co - 0.5% Ru/TiO_2 [41].

4.5.2.5 Fischer-Tropsch reaction.

The catalysts listed in Table 4.11 were tested for Fisher-Tropsch activity at *Johnson Matthey*, see *Section 2.3.2*. The CO turnover is plotted in Figure 4.12 and the selectivity towards C_{5+} products in Figure 4.13.

The S-Co/Ti-S catalyst presented an initial activity deactivation. It was observed that the initial catalyst deactivation (drop of CO turnover during initial reaction time), attributed to a decrease in the density of cobalt sites was due to the formation of carbonaceous species on the cobalt surface. Also, the decrease

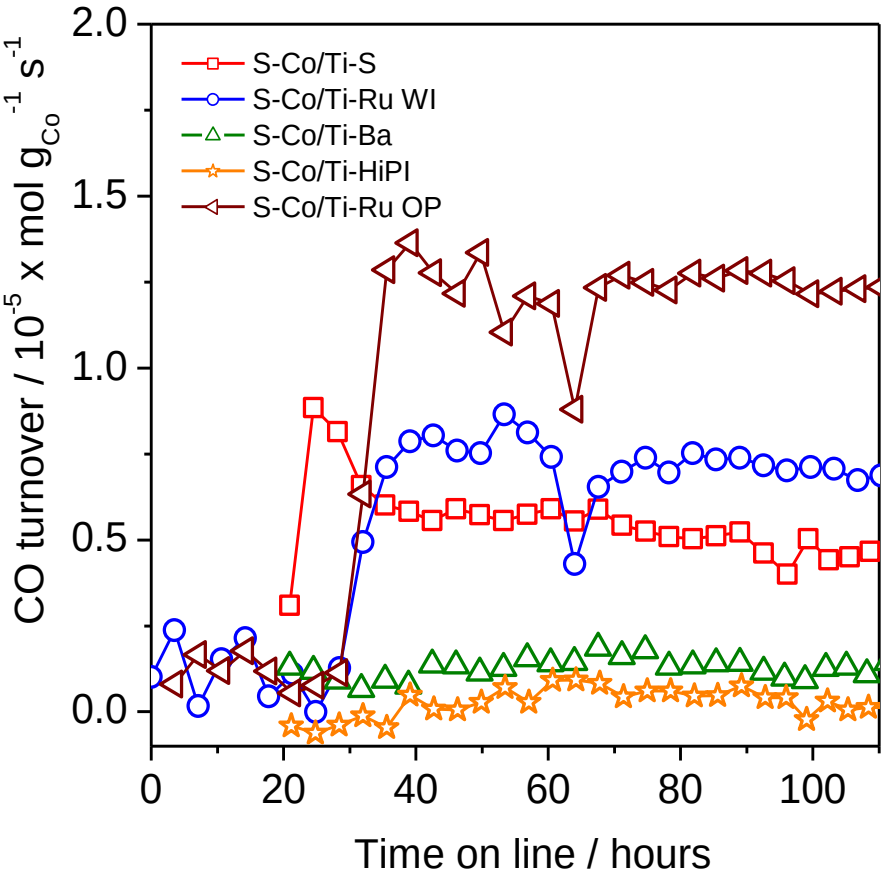

Figure 4.12. CO turnover under FT conditions of catalysts listed in Table 5.11. Reaction conditions: 210 °C, 20 bar and syn-gas mixture used was Ar:CO:H_2 = 0.1:2:1.

in available cobalt sites weakens the product readsorption, which drives the product chain growth, that ultimately decreases the C_{5+} yield [17].

The barium promoted GAS catalyst, S-Co/Ti-Ba, showed poor catalytic performance and had unstable selectivity towards C_{5+}. It has been reported that small barium loadings increase cobalt reducibility, yielding an increase in Co exposed sites and eventually an increase of CO turnover compared to a non-promoted catalyst [19]. This enhancement of cobalt reducibility for the barium doped catalysts was observed, but it did not provide improvements compared to the non-promoted catalyst for either CO turnover or C_{5+} selectivity. It is worth noting that activity did not correlate with cobalt surface area, with the barium promoted and the non-promoted catalysts presenting high surface areas (5 and 8 m^2 g_{Co}^{-1}, respectively) but significantly different activities. It was observed that the addition of barium to the support also increased the formation of water under

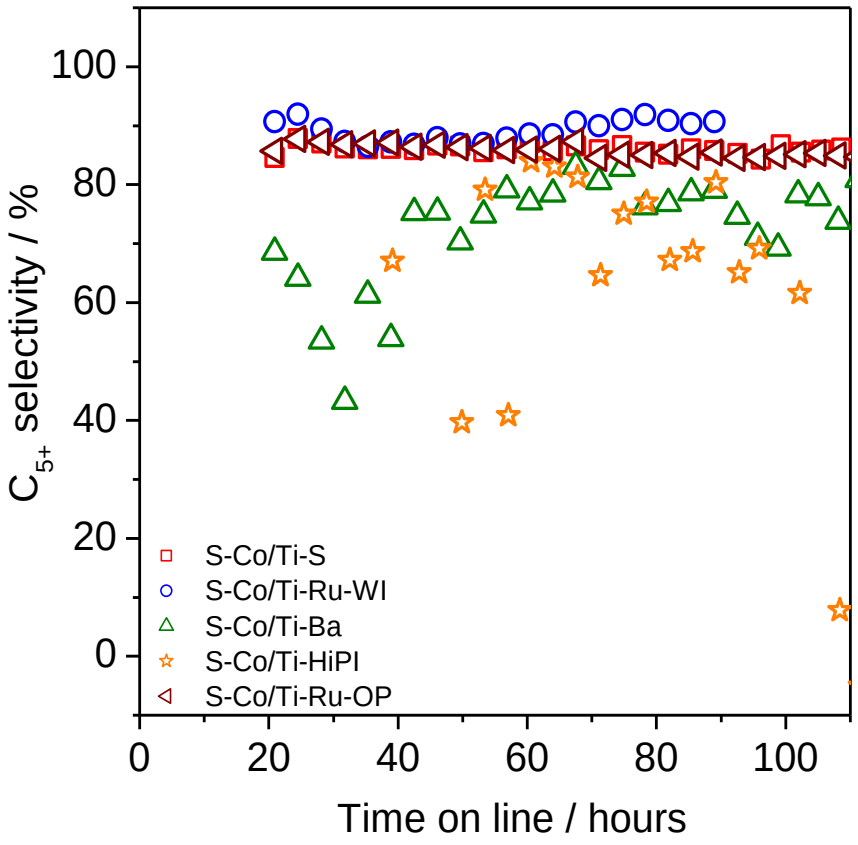

Figure 4.13. Selectivity towards C_{5+} of catalysts listed in Table 5.11.

FT conditions. Hence, the increase in water partial pressure could restrict the S-Co/Ti-Ba activity for the FT reaction [18].

For the ruthenium promoted catalysts, the conversion was found substantially higher than the barium promoted or the non-promoted catalysts and the activity was remarkably stable after 60 h under the reaction conditions. This enhancement in activity is in agreement with previous observations [14, 15, 17, 24]. Iglesia [15, 17] observed a synergic effect for Co-Ru supported catalysts with a high CO turnover and high C_{5+} selectivity. The authors suggested ruthenium protected against cobalt deactivation, due to cobalt reoxidation during FT synthesis. Kodakov [33] observed hexagonal packed-centred cobalt particles with a stable particle size using *in situ* XRD analysis during the initial 8 h of FT reaction at 220 °C, 20 bar and $H_2/CO = 2$. It is suggested that cobalt acetate precipitated by dense CO_2 on TiO_2 may preferentially form hexagonal packed-centred cobalt particles stable under FT conditions.

It is also worth noting that the ruthenium doped catalysts prepared in different ways, S-Co/Ti-Ru-OP and S-Co/Ti-Ru-WI, showed differences in CO activity. The amount of ruthenium in S-Co/Ti-Ru-WI is higher than in S-Co/Ti-Ru-OP, 0.08 and 0.05 wt% respectively, with activity of S-Co/Ti-Ru-OP larger than S-Co/Ti-Ru-WI. Thus, it should be highlighted that incorporation of ruthenium was different, co-precipitated under dense CO_2 and wet impregnated, respectively. The dense CO_2 can improve the miscibility during the co-precipitation of two metals, as observed by Tang *et al.* [35]. Iglesia [17] observed the formation of bimetallic entities, Co-Ru which were formed by an intimate contact of the metals, which increased the CO activity and the C_{5+} selectivity. Hence, it is suggested that dense CO_2 co-precipitation induced an intimate mixing between

cobalt and ruthenium precursors that ultimately formed a bimetallic Co-Ru catalyst, S-Co/Ti-OP, with high activity and selectivity towards C_{5+}.

The cobalt surface area shows good agreement with the catalysts activity, where the higher the surface area, the higher the activity. This has been observed by several authors and has been attributed to the number of active cobalt sites [42].

The catalyst prepared using the HiPI semi-continuous methodology, S-Co/Ti-HiPI, was virtually inactive under FT conditions. This poor performance might be expected from the low cobalt surface area observed. The low cobalt surface area and consequent low FT activity might arise from an inefficient cobalt acetate precipitation on the TiO_2, due to poor contact between the slurry and dense CO_2 that may evolve in poor mass transfer. Nevertheless, the results obtained using the GAS methodology encourages carrying out more experiments to improve catalyst performance.

4.5.3 Comments about GAS promoted catalysts activity.

A comparison between the GAS processed catalysts and the *Johnson Matthey* standard catalyst (JM standard) can be seen in Figure 4.14 and 4.15. The JM standard catalyst is based on highly dispersed cobalt on alumina (30 wt%) promoted with ruthenium.

It is worth noting that both JM standard and S-Co/Ti-Ru-IW presented a similar initial decrease in activity and non-stable activity with time-on-line, whereas S-Co/Ti-Ru-OP showed greater stability. Differences in activity are clear, with the JM standard being more active than the GAS impregnated materials at low temperatures between 210-230 °C. At a higher reaction temperature of 240 °C, S-Co/Ti-Ru-OP showed better performance than the JM standard deactivating to

a lesser degree. It should be noted that the GAS prepared catalysts and the JM standard were supported on different metal oxides, TiO_2 and Al_2O_3, respectively. The support plays a role in the cobalt dispersion, gives stability to cobalt particles, dissipates the reaction heat and can influence the electronic properties of cobalt favouring the CO adsorption [13]. Reuel [43] observed the following catalytic activity for 3 wt% cobalt supported catalyst: $Co/TiO_2>Co/Al_2O_3>Co/SiO_2$ at 1 bar and 225 °C. On the other hand, Iglesia [17] observed negligible effect of the support in the CH_4 and C_{5+} selectivity in reactions above 5 bar but there was a dependence on the cobalt dispersion. However, in the present work the JM standard was not characterized; thus, the catalyst properties were unknown and impossible to compare to the GAS precipitated catalysts.

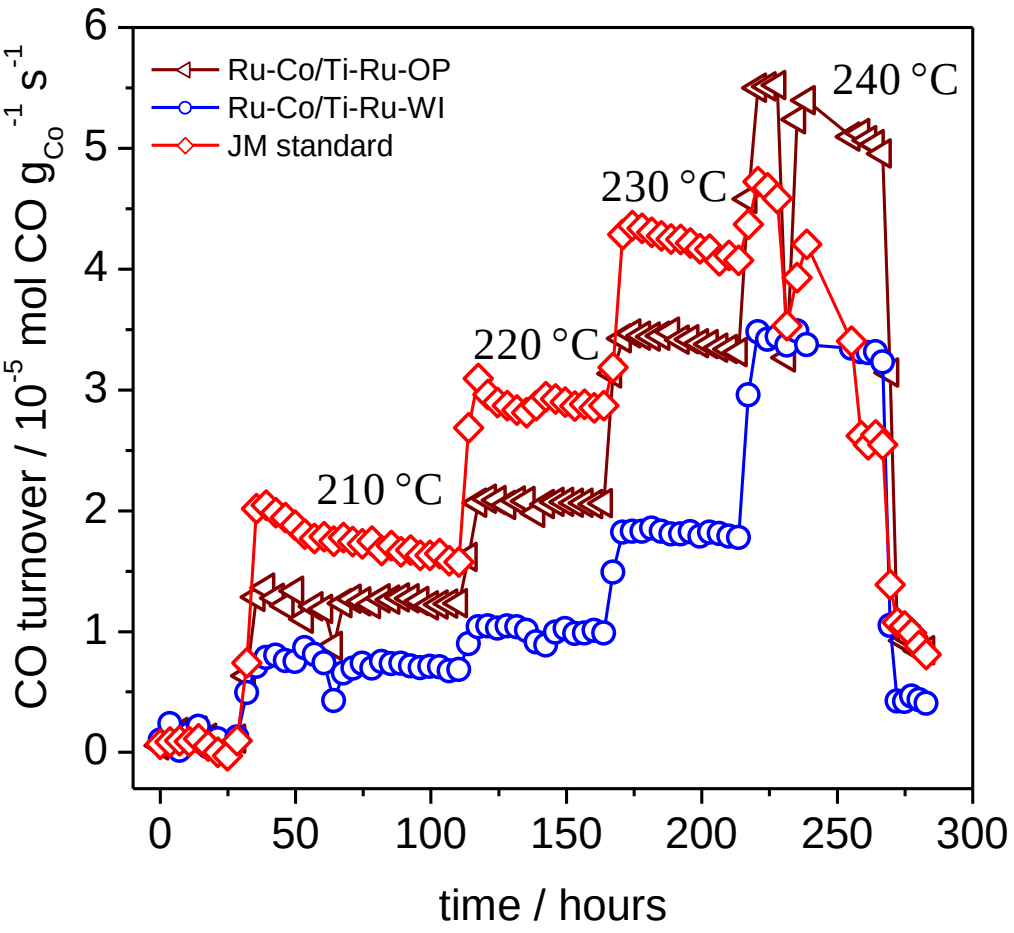

Figure 4.14. CO turnover under FT conditions of GAS processed catalysts and JM standard. Reaction conditions: 210 °C, 20 bar and syn-gas mixture used was $Ar:CO:H_2$ = 0.1:2:1.

With reference to the C_{5+} yield, it is evident that the GAS precipitated catalysts, Co/Ti-Ru-OP and Co/Ti-Ru-WI, besides showing stable CO turnover, also increased the C_{5+} selectivity at high temperatures (240 °C), whereas the selectivity of JM standard dramatically decreased at high temperatures. The decrease in C_{5+}, as well as in CO turnover, for the JM standard at high temperature can be attributed to the cobalt particle sintering. The formation of cobalt hexagonal closed-packed crystallites might explain the stability of GAS catalysts, as this phase is known to be fairly stable under FT conditions [17, 33].

4.5.4 Conclusions.

It has been shown that cobalt and promoter metals can be deposited onto a support using the GAS process. In addition, it has been demonstrated that they can be successfully scaled-up from 100 ml to 1000 ml equipment.

The XRD showed spinel Co_3O_4 and TiO_2, rutile and anatase phases, although neither ruthenium nor barium species were detected. The TPR showed two

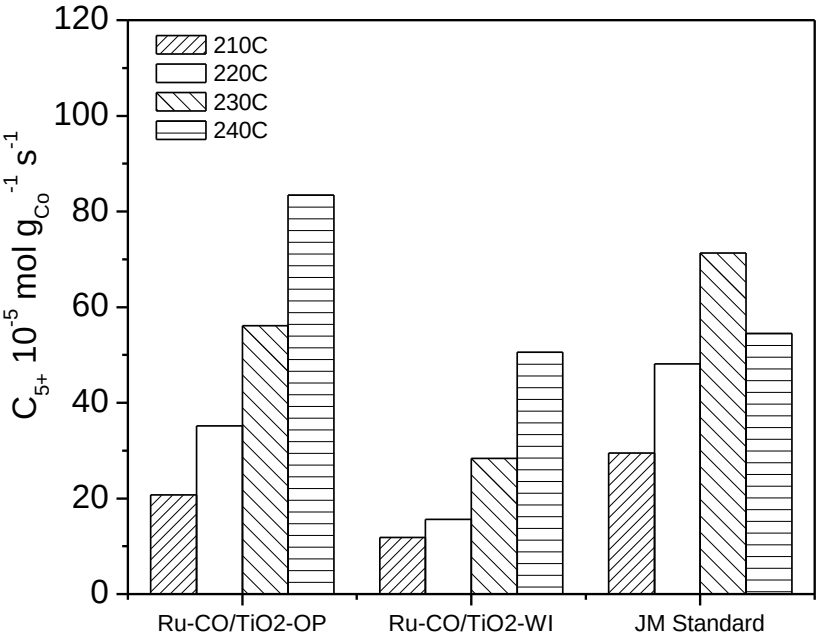

Figure 4.15. C_{5+} yield of GAS precipitated catalysts, S-Co/Ti-Ru-OP and Co/Ti-Ru-IW, and JM standard.

reduction peaks instead of the three observed in *Jerguson* experiments, suggesting better contact between the cobalt precursor and the support with the incorporation of a stirrer and the baffle. The ruthenium and barium containing catalysts reduced at lower temperature than non-promoted catalysts. EDX showed good agreement between the targeted and observed cobalt and barium loadings. Ruthenium showed poor loading compared to the targeted values, especially in Co/Ti-Ru-OP which was attributed to the high ruthenium precursor solubility in dense CO_2. The cobalt surface area was found to be larger for ruthenium promoted materials than non-promoted catalysts, due to the role ruthenium plays in the nucleation. The metal surface area was correlated with the catalysts activity with higher Co surface area materials giving higher activity.

The catalysts were tested under FT conditions and the non-promoted GAS catalyst showed stable performance, although CO turnover was lower than for the promoted catalysts. It is worth noting that GAS prepared catalysts were more stable than the industrial standard and it was assigned to the formation of cobalt hexagonal closed-packed crystallites. The catalytic performance of GAS processed catalysts, in terms of CO turnover and C_{5+} yield, were close to JM standard catalyst at temperatures of 210-230 °C, and better than the standard in terms of C_{5+} yield at high temperature (240 °C). The barium promoted catalyst showed good reducibility, a cobalt surface area similar to the non-promoted catalyst but poor catalytic performance, likely due to the high partial water pressure.

The S-Co/Ti-HiPI catalyst, prepared using the new high pressure impregnation methodology had catalytic performance that was poorer than its counterpart prepared using the GAS process, S-Co/Ti-S. However, more work should be

done to improve this attractive synthesis process, such as adjust the right ruthenium loading (0.1 wt%) under experimental conditions.

4.6 Acknowledgments.

The author thanks the research group of Professor Rosseinsky for syn-gas stability tests. Also, to Dr Dan Enache at *Johnson Matthey* is acknowledged for the Fischer-Tropsch testing.

4.7 References.

1. Fischer, F.; Tropsch, H., *Brennstoff Chemie* **1923,** *4*, 276-285.

2. Fischer, F.; Tropsch, H., *Brennstoff Chemie* **1926,** *7*, 97-104.

3. Anderson, R. B.; Storch, H.; Golumbic, N. G., *The Fischer-Tropsch and related synthesis*. J.Wiley and sons: New York, 1956.

4. Bezemer, G. L.; Radstake, P. B.; Falke, U.; Oosterbeek, H.; Kuipers, H. P. C. E.; van Dillen, A. J.; de Jong, K. P., *Journal of Catalysis* **2006,** *237* (1), 152-161.

5. Henrichi-Olive, G.; Olive, S., *Angewandte Chemie International Edition* **1976,** *15* (3), 136-141.

6. Satterfield, C. N.; Huff, G. A.; Stenger, H. G.; Madon, R. J., *Industrial & Engineering Chemistry Fundamentals* **1985,** *24* (4), 450-454.

7. Hindermann, J. P.; Hutchings, G. J.; Kiennemann, A., *Catalysis Reviews: Science and Engineering* **1993,** *35* (1), 1-127.

8. Pichler, H.; Schulz, H., *Chemical Ingineering & Technology* **1970,** *42*, 1162.

9. Anderson, R. B., *Catalysts for the Fischer-Tropsch synthesis*. Van Nostrand Reinhold: New York, 1956.

10. King, D. L.; Cusumano, J. A.; Garten, R. L., *Catalysis Reviews - Science and Engineering* **1981,** *23* (2), 233-263.

11. Jacobs, G.; Chaney, J. A.; Patterson, P. M.; Das, T. K.; Maillot, J. C.; Davis, B. H., *Journal of Synchrotron Radiation* **2004,** *11* (5), 414-422.

12. Iglesia, E., *Applied Catalysis A: General* **1997,** *161* (1-2), 59-78.

13. Khodakov, A. Y.; Chu, W.; Fongarland, P., *Chemical Reviews* **2007,** *107* (5), 1692-1744.

14. Iglesia, E.; Soled, S. L.; Fiato, R. A., *Journal of Catalysis* **1992,** *137* (1), 212-224.

15. Iglesia, E., *Applied Catalysis A: General* **1997,** *161,* 59.

16. Girardon, J.-S.; Lermontov, A. S.; Gengembre, L.; Chernavskii, P. A.; Griboval-Constant, A.; Khodakov, A. Y., *Journal of Catalysis* **2005,** *230* (2), 339-352.

17. Iglesia, E.; Soled, S. L.; Fiato, R. A.; Via, G. H., *Journal of Catalysis* **1993,** *143* (2), 345-368.

18. Luo, M.; Davis, B. H., *Applied Catalysis A: General* **2003,** *246* (1), 171-181.

19. Bao, A.; Li, J.; Zhang, Y., *Journal of Natural Gas Chemistry* **2010,** *19* (6), 622-627.

20. Bezemer, G. L.; Bitter, J. H.; Kuipers, H. P. C. E.; Oosterbeek, H.; Holewijn, J. E.; Xu, X.; Kapteijn, F.; van Dillen, A. J.; de Jong, K. P., *Journal of the American Chemical Society* **2006,** *128* (12), 3956-3964.

21. Borg, Ø.; Sigrid, E.; Edd, A. B.; Solvi, S.; Hanne, W.; Erling, R.; Anders, H., *Journal of Catalysis* **2007,** *248* (1), 89-100.

22. Borg, Ø.; Dietzel, D. C. P.; Aud, I. S.; Erik, Z. T.; John, C. W.; Spyridon, D.; Sigrid, E.; Anders, H.; Erling, R., *Journal of Catalysis* **2008,** *259* (2), 161-164.

23. Lucien, F. P.; Foster, N. R., *The Journal of Supercritical Fluids* **2000,** *17* (2), 111-134.

24. Sun, S.; Fujimoto, K.; Yoneyama, Y.; Tsubaki, N., *Fuel* **2002,** *81* (11-12), 1583-1591.

25. Belambe, A. R.; Oukaci, R.; Goodwin Jr, J. G., *Journal of Catalysis* **1997,** *166* (1), 8-15.

26. Warwick, B.; Dehghani, F.; Foster, N. R.; Biffin, J. R.; Regtop, H. L., *Industrial & Engineering Chemistry Research* **2002,** *41* (8), 1993-2004.

27. Adami, R.; Osséo, L. S.; Huopalahti, R.; Reverchon, E., *The Journal of Supercritical Fluids* **2007,** *42* (2), 288-298.

28. Adami, R.; Reverchon, E.; Järvenpää, E.; Huopalahti, R., *Powder Technology* **2008,** *182* (1), 105-112.

29. Pessey, V.; Garriga, R.; Weill, F.; Chevalier, B.; Etourneau, J.; Cansell, F., *Journal of Materials Chemistry* **2002,** *12* (4), 958-965.

30. Jongsomjit, B.; Sakdamnuson, C.; Goodwin, J. G.; Praserthdam, P., *Catalysis Letters* **2004,** *94* (3), 209-215.

31. Rønning, M.; Tsakoumis, N. E.; Voronov, A.; Johnsen, R. E.; Norby, P.; van Beek, W.; Borg, Ø.; Rytter, E.; Holmen, A., *Catalysis Today* **2010,** *155* (3-4), 289-295.

32. Tsakoumis, N. E.; Rønning, M.; Borg, Ø.; Rytter, E.; Holmen, A., *Catalysis Today* **2010,** *154* (3-4), 162-182.

33. Karaca, H.; Hong, J.; Fongarland, P.; Roussel, P.; Griboval-Constant, A.; Lacroix, M.; Hortmann, K.; Safonova, O. V.; Khodakov, A. Y., *Chemical Communications* **2010,** *46* (5), 788-790.

34. Diehl, F.; Khodakov, A. Y., *Oil & Gas Science and Technology - Rev. IFP* **2009,** *64* (1), 11-24.

35. Tang, Z.-R.; Jones, C.; Aldridge, J. W.; Davies, T. E.; Bartley, J. K.; Carley, A. F.; Taylor, S. H.; Allix, M.; Dickinson, C.; Rosseinsky, M. J.; Claridge, J. B.; Xu, Z.; Crudace, M. J.; Hutchings, G. J., *ChemCatChem* **2009,** *1* (2), 247-251.

36. Yoda, S.; Mizuno, Y.; Furuya, T.; Takebayashi, Y.; Otake, K.; Tsuji, T.; Hiaki, T., *The Journal of Supercritical Fluids* **2008,** *44* (2), 139-147.

37. De Gioannis, B.; Gonzalez, A. V.; Subra, P., *The Journal of Supercritical Fluids* **2004,** *29* (1-2), 49-57.

38. Ting, S. S. T.; Tomasko, D. L.; Foster, N. R.; Macnaughton, S. J., *Industrial & Engineering Chemistry Research* **1993,** *32* (7), 1471-1481.

39. Berends, M. E.; Bruinsma, S. L.; de Graauw, J.; van Rosmalen, M. G., *AIChE* **1996,** *42* (2), 431-439.

40. Chu, W.; Chernavskii, P. A.; Gengembre, L.; Pankina, G. A.; Fongarland, P.; Khodakov, A. Y., *Journal of Catalysis* **2007,** *252* (2), 215-230.

41. Michalak, A.; Nowosielska, M.; Jóźwiak, W., *Topics in Catalysis* **2009,** *52* (8), 1044-1050.

42. Oh, J.-H.; Bae, J.; Park, S.-J.; Khanna, P.; Jun, K.-W., *Catalysis Letters* **2009,** *130* (3), 403-409.

43. Reuel, R. C.; Bartholomew, C. H., *Journal of Catalysis* **1984,** *85* (1), 78-88.

44. Nakashima T.; Yoshimura K.; Waki H., *Talanta* **1990,** *37* (7), 735-739.

Appendix II.

4.II.1 Solubility of cobalt precursors in organic solvents.

The equilibrium solubility of cobalt, acetate and cobalt nitrate precursors, was measured in two solvents: methanol and ethanol at different temperatures (24, 30, 40 and 50 °C). This was achieved by saturating the solvent using the cobalt salt and then analyzing the solution by UV-Vis spectroscopy.

The experimental procedure is summarized below:

- Place a vial containing 10 ml of organic solvent into a water thermal bath at the desired temperature (the thermal bath was placed on a hot plate to control temperature and stirring).
- ~50 mg of cobalt salt was added stepwise every 10 minutes, until crystallites did not dissolve.
- The saturated solution was then diluted 50 times and analyzed by UV-Vis at 521 nm [44].

Results

The equilibrium concentration was found to be much higher for cobalt nitrate regardless of the solvent used, as seen in Figure II.1 and might be correlated to the contribution of coordinated water in the salt, as seen in Figure II.2. It is worth noting that as solvent polarity decreases, salt solubility decreases for both the cobalt precursors. Hence, as coordinated water may increase solvent polarity, it

may ultimately enhance the solubility of the salt. Experiments with different water incorporation into the solvent could help understanding the water effect in the equilibrium concentration.

As previously noted in *Chapter 1*, water present in the system may result in a change in system behaviour. Hence, the water salt contribution to the system was estimated based on equilibrium salt solubility, as follows:

$$H_2O\ mol = \frac{c_0\ con.}{10\ x\ MW_{cobalt\ salt}} xCW \qquad \text{Equation 4.II.1}$$

where c_0 *con.* stands for equilibrium cobalt salt concentration, from Figure II.1, $MW_{cobalt\ salt}$ for the molecular weight of the specific cobalt salt and *CW* for the number of moles of coordinated water in the salt, 4 for acetate and 6 for nitrate.

In Figure II.2 it is observed that if the nitrate precursor is used, the nature of solvent could dramatically change, as water can be up to 50% of the solvent composition. This may change the precipitation environment and ultimately the catalysts properties.

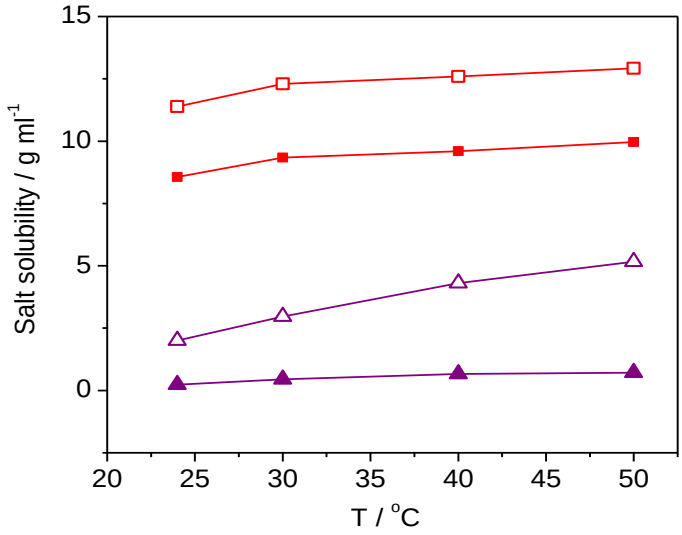

Figure II.1. Solubility of salts in organic solvents. 7 $Co(CH_3COO)_2{\cdot}4\,H_2O$ in methanol; 8 $Co(CH_3COO)_2{\cdot}4\,H_2O$ in ethanol; ! $Co(NO_3)_2{\cdot}6\,H_2O$ in methanol; ∀ $Co(NO_3)_2{\cdot}6\,H_2O$ in ethanol.

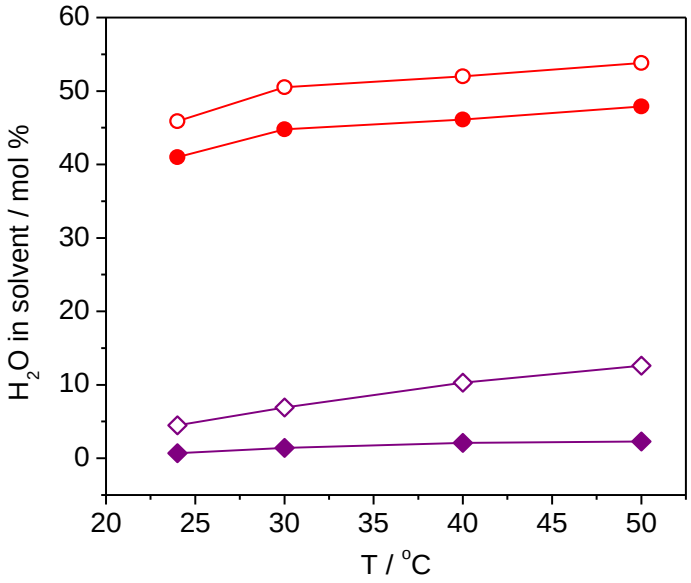

Figure II.2. Water content in the solution. M $Co(CH_3COO)_2 \cdot 4\ H_2O$ in methanol; Λ $Co(CH_3COO)_2 \cdot 4\ H_2O$ in ethanol; – $Co(NO_3)_2 \cdot 6\ H_2O$ in methanol; , $Co(NO_3)_2 \cdot 6\ H_2O$ in ethanol.

5

SAS co-precipitated catalysts for Fischer-Tropsch reaction

5.1 Introduction.

Traditionally, cobalt based catalysts for Fischer-Tropsch (FT) have been prepared by impregnation of cobalt nitrate on an oxide metal support, normally TiO_2, Al_2O_3 or SiO_2 [1-3], and several patents have been issued using this approach since the FT process was launched in the early 20th century [4, 5]. In the early 21st century, *Hegelhard Corporation* [6], and later *British Petroleum Exploration Operating Company Limited*, identified co-precipitated cobalt-zinc as a potential catalyst for FT synthesis, however in the open literature, co-precipitated systems are scarcely reported.

Khassin [7] observed a positive relationship between small cobalt particles and FT activity and selectivity in cobalt-zinc co-precipitated catalysts under reaction conditions of 210 °C, atmospheric pressure and H_2:CO = 2:1. Madikizela and co-workers [8-11] incorporated zinc into TiO_2 catalysts by co-precipitation and impregnation for FT reaction (220 °C, 8 bar, H_2:CO = 2:1, and 400 h^{-1}). It was found that the cobalt reduced at lower temperature as zinc was incorporated;

temperatures decreased from 379-472 °C to 299-362 °C with the incorporation of 5 wt% of zinc. The authors observed that zinc decreased the cobalt titania interaction, promoting the cobalt reducibility, however zinc increased the selectivity towards methane [9]. The addition of cobalt acetate onto TiO_2 impregnated with zinc nitrate further increased the cobalt dispersion compared to catalysts made with other precursor combinations (*i.e.* acetates or nitrates only or the combination of cobalt nitrate and zinc acetate) and ultimately improved catalyst performance. Li *et al*. [12] found an enhancement of FT activity using sol-gel Co/Zn/Mn catalysts dried by supercritical fluids compared to traditional thermal drying methods (heat treatment at 60 °C). C_{5+} selectivities of 64% were obtained compared to selectivities of *ca.* 50% in traditional drying methods (240 °C, 30 bar, H_2:CO = 2:1, during 300 minutes). The authors attributed the enhancement of FT to the formation of nanoparticles during the supercritical drying step. In this paper the FT reaction was performed under supercritical *n*-hexane (critical point: 234 °C and 30 bar) in a slurry reactor, and 90% CO conversion was achieved (conversion in liquid phase was 57%). The increased activity was assigned to the enhancement of mass transfer and the efficient removal of products from pores during reaction under supercritical conditions [12]. Bukur *et al.* [13] impregnated ZnO with an aqueous solution of $Co(NO_3)_2 \cdot 6\,H_2O$, 10 wt% loading, and studied the catalyst activation under H_2 and CO. Activation under H_2 yielded better FT performance than CO activation, with CO conversion increasing from 23% for the CO activated catalyst to 29% for the H_2 activated catalyst at 215 °C, 25 bar and H_2:CO = 2:1.

Based upon these interesting findings, in the current *Chapter* the SAS process was used to co-precipitate cobalt and zinc acetates from water in methanol solutions to obtain an optimum catalyst for FT reaction.

5.2 Preparation.

The initial solutions were prepared as follows: 0.7 g of $Co(CH_3COO)_2 \cdot 4\ H_2O$ and 3.5 g of $Zn(CH_3COO)_2 \cdot 2\ H_2O$ were dissolved in 100 ml of methanol and then kept under stirring for 1 h (chemicals listed in Table 5.1). Water was added as co-solvent: 0, 5, and 15 vol%. Solutions were adjusted to precipitate loadings of Co/ZnO of 15 at.%.

The experiments were performed using the *Jerguso*n equipment, as described in *Section 2.1.1* and following the process described in *Section 2.2.1*. The experimental conditions were as follows: 120 bar and 40 °C, 250 µm inner nozzle diameter and a CO_2:methanol molar ratio of 40:1 (CO_2 = 2.5 kg h^{-1} and methanol solution = 0.046 kg h^{-1}). SAS processed catalysts were labelled as CZ-*X*-P where *X* stands for % of water in the starting solution. The samples were calcined at 350 °C and 500 °C (2.5 °C min^{-1}) under static air for 5 h. Calcined samples were labelled as CZ-*X*-350 and CZ-*X*-500. For comparison, solutions of $Co(CH_3COO)_2 \cdot 4\ H_2O$ and $Zn(CH_3COO)_2 \cdot 2\ H_2O$ in methanol were prepared and processed under the conditions described above. The single metal precursors

Table 5.1. Chemicals used to prepare SAS cobalt-zinc catalysts.

Chemical	Company	Grade / purity
$Co(CH_3COO)_2 \cdot 4\ H_2O$	Sigma Aldrich	ACS reagent, ≥ 98.0%
$Zn(CH_3COO)_2 \cdot 2\ H_2O$	Sigma Aldrich	ACS reagent, ≥ 98.0%
methanol	Fisher-Scientific	Laboratory reagent grade

were calcined at 350 °C and 500 °C for 5 h and labelled as Co-350, Co-500, Zn-350 and Zn-500, respectively.

For comparison, 7 wt% Co/ZnO was made using traditional co-precipitation at *Johnson Matthey* facilities. The initial nitrate metal solutions ($Co(NO_3)_2 \cdot 6\ H_2O$ = 10 g L^{-1} and $Zn(NO_3)_2 \cdot 6\ H_2O$ = 72 g L^{-1}) were pumped by peristaltic pumps at 1000 L h^{-1} and the aqueous solution of NH_4CO_3 (NH_4CO_3 = 154 g L^{-1}) was delivered at the same flow rate. Both solutions were mixed inside a stirred vessel (300 r.p.m.). The pH was kept at 5.8 and the temperature was set at 60 °C. The as-made material was washed with 1500 ml of deionised water five times. Then material was dried at 120 °C overnight (labelled as JM-7-P) and further calcined at 350 °C and 500 °C as previously described. The materials were labelled as JM-7-350 and JM-7-500, respectively.

5.3 Results and discussion.

5.3.1 Fourier transform infra-red spectroscopy.

Infra-red spectra of the precipitated cobalt-zinc catalysts are depicted in Figure 5.1. After SAS precipitation COO^- asymmetric and symmetric stretching bands at 1560 and 1415 cm^{-1} were assigned to acetate ligands [14]. Likewise, the band at 1500 cm^{-1} was assigned to stretching vibrations mode of CO_2^{3-} [15] and was also present in JM-7-P. The strong, broad band at 1390 cm^{-1}, observed only in JM-7-P, was indicative of zinc carbonate-hydroxide [16]. The sharp band at 830 cm^{-1} was assigned to CO_2^{3-} [15], and may indicate some degree of crystallinity in cobalt-zinc carbonate. The band at 1680 cm^{-1} was attributed to OH bending mode [17]. The region between 3750-3250 cm^{-1} was also attributed to OH groups, and it was

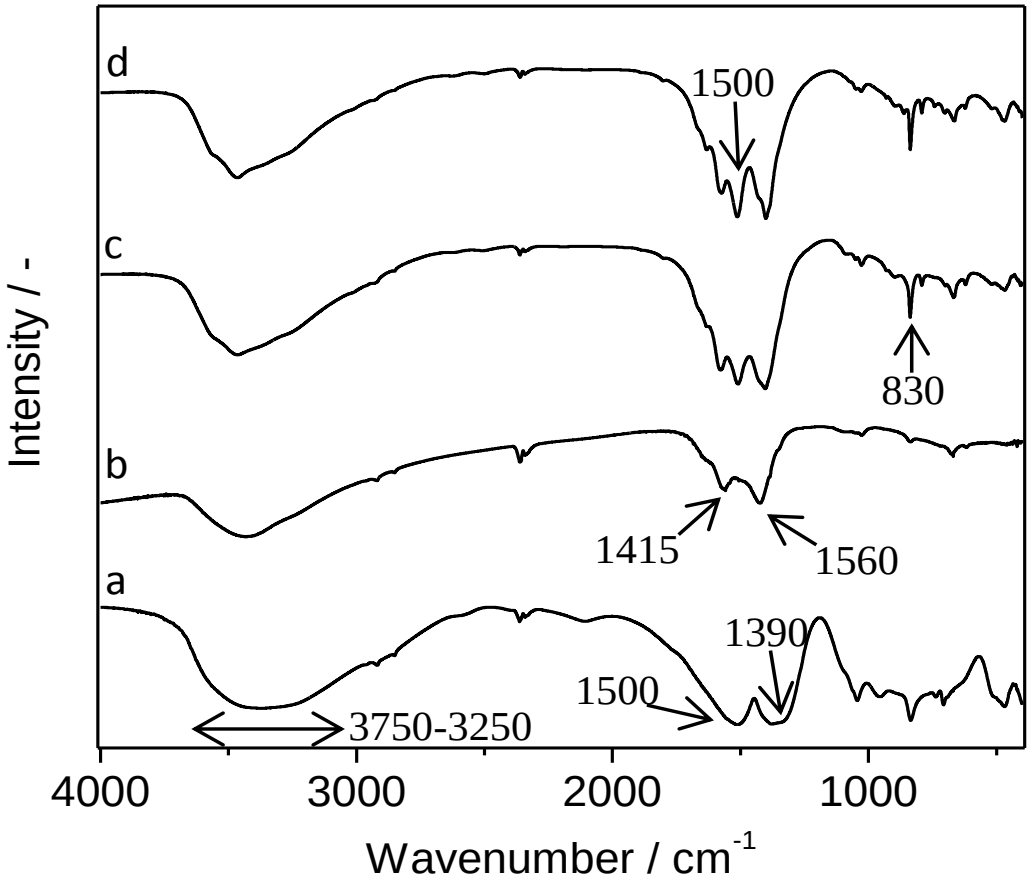

Figure 5.1. Infra-red analysis of SAS cobalt-zinc processed materials. a) JM-7-P; b) CZ-0-P; c) CZ-5-P; d) CZ-15-P.

observed that the band became sharper as water was incorporated suggesting OH groups, either -OH or H_2O, were crystallizing.

Infra-red suggests that water plays an important role as co-solvent, modifying the nature of the precipitated material. When just coordinate water was considered, *i.e.* CZ-0-P without additional water, typical SAS acetate spectra were observed. As water was added, clear carbonate/hydroxycarbonate bands were visible. It is suggested that in the cobalt-zinc system carbonates are easily formed; for instance, in *Chapter 3*, the Co-5-P showed weaker carbonate/hydroxycarbonate bands compared to CZ-5-P, although the same amount of water was introduced in the starting solution. Hence, the zinc cation

may play a nucleation role during the carbonate/hydroxycarbonate formation [18] in SAS process.

5.3.2 Thermogravimetric analysis.

The material decomposition was studied by means of TGA, as seen in Figure 5.2. In general, weight losses between 50 °C and 120 °C were attributed to desorption of water. The weight losses observed between 150 °C and 215 °C were endothermic in nature, as seen in Figure 5.3, and can be assigned to low temperature carbonate/hydroxycarbonates decomposition [18]. These steps shifted towards higher temperatures as water was incorporated, with the temperature shift attributed to the formation of crystalline species that may need high thermal energy to decompose. The increase in crystallinity upon water incorporation was further confirmed by XRD analysis, as discussed later in *Section 5.3.3*. The

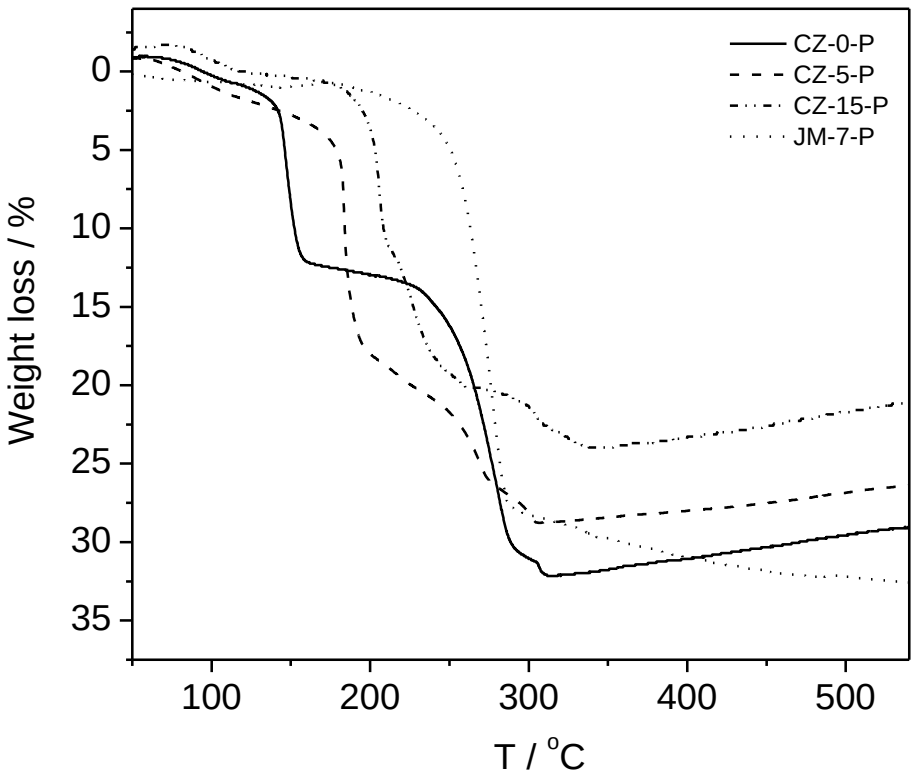

Figure 5.2. TGA of cobalt-zinc precursors.

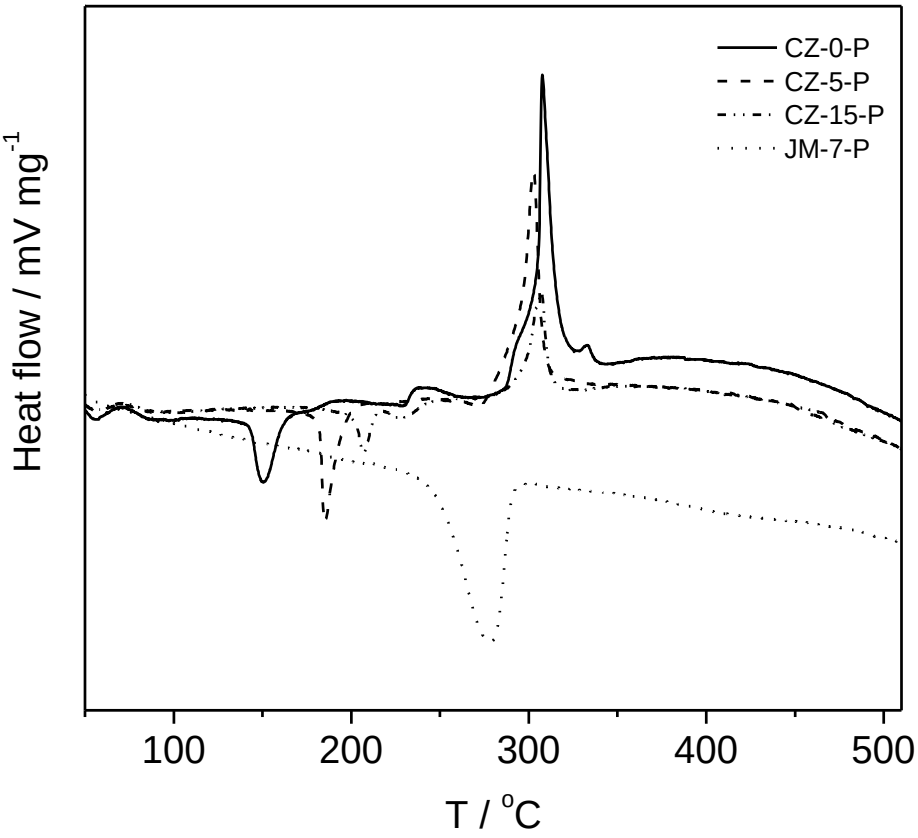

Figure 5.3. Differential thermal analysis of cobalt-zinc precursor catalysts.

weight loss associated with this decomposition, excluding adsorbed water, also increased as water was added: 11% weight loss in CZ-0-P, 16% in CZ-5-P and 21% in CZ-15-P suggesting that carbonates/hydroxycarbonates increased as water was introduced. The weight loss at *ca.* 250 °C was found to be dependent on water incorporation: 17% in CZ-0-P, 6% in CZ-5-P and hardly visible in CZ-15-P. These steps were slightly exothermic, as observed in Figure 5.3, and were assigned to the decomposition of acetates. Thus, the water incorporation concurrently promotes the formation of carbonates/hydroxycarbonates and decreases the presence of acetates. Finally, a small but highly exothermic shoulder was observed at 325 °C. Exothermic decomposition indicates acetates as the main ligand. Baird [18] observed a shoulder in co-precipitated cobalt-zinc and attributed it to the presence of different Co/Zn ratios. Thus, the observed shoulder was most likely due to decomposition of Co/Zn with a different ratio to

the bulk precipitate, it is suggested that cobalt acetate was the predominant ligand.

Hence, TGA analysis suggests materials were carbonates/hydroxycarbonates containing acetates (as observed in infra-red analysis) and the ratio of acetate/carbonate formed was water dependent, as follows:

CZ-0-P>CZ-5-P>CZ-15-P

Likewise, decomposition temperature-shifts suggested an increase in carbonate crystallinity, as follows:

CZ-15-P>CZ-5-P>CZ-0-P

This was also observed in XRD analysis, as discussed later in *Section 5.3.3.*

The co-precipitated catalysts, JM-7-P, showed an endothermic one-step decomposition (26% weight loss) suggesting zinc carbonate hydroxide hydrate (hydrozincite), theoretical weight loss 26% [18], as the main compound.

5.3.3 Powder X-ray diffraction.

The CZ-0-P precursor was amorphous, as seen in Figure 5.4, whereas CZ-5-P and CZ-15-P were crystalline precursors, although the species could not be identified. The JM-7-P showed hydrozincite with cobalt likely incorporated in the structure, as suggested by Baird [18].

Calcination of the catalysts at 350 °C, shown in Figure 5.5, resulted in the formation of ZnO in agreement with previous observations [18] for Co/Zn ratios of 0.1. Baird observed a spinel form, assigned to either Co_3O_4 or $ZnCo_2O_4$, after calcination at 350 °C for 16 h, at low Co/Zn ratios, *ca.* 0.2. However, the spinel was not observed in CZ-5-350 likely due to those spinel species requiring either long calcination times or high temperatures to crystallize[18, 19].

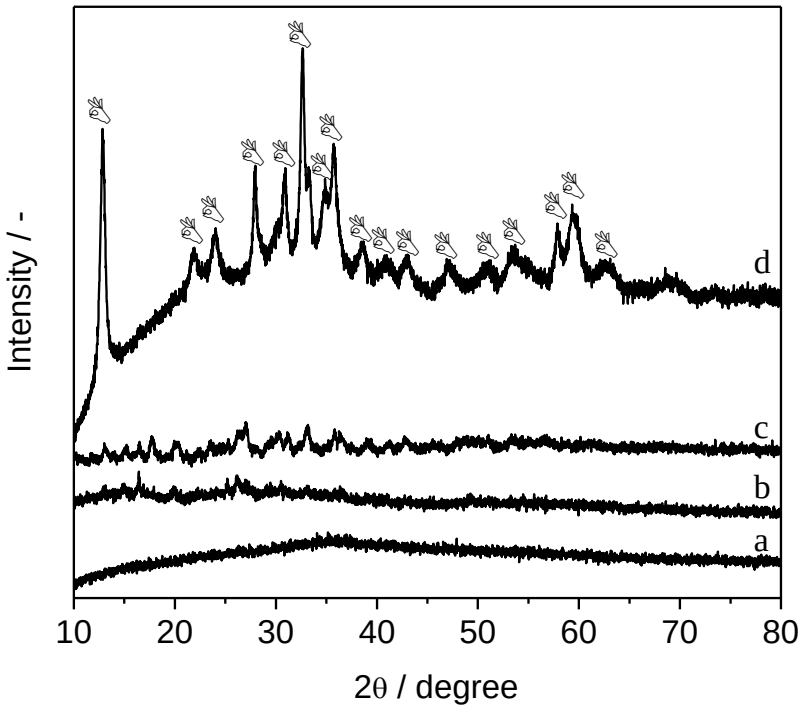

Figure 5.4. XRD patterns of precipitated cobalt-zinc precursors. a: CZ-0-P; b) CZ-5-P; c) CZ-15-P and d) JM-7-P.

Calcination at 500 °C, shown in Figure 5.6, resulted in no new phase formation with the exception of CZ-5-500 which also showed the presence of a cubic spinel phase, however significant overlap made assignment of the reflections to either Co_3O_4 or $ZnCo_2O_4$ difficult. The increase in calcination temperature could promote the crystallization and growth of spinel structures such as Co_3O_4 or $ZnCo_2O_4$. Hence, in the particular case of CZ-5-500 spinel structures were observed likely due to the increase in calcination temperature and large Co/Zn ratio (*ca.* 0.2). The XRD of co-precipitated JM-7, calcined either at 350 °C or 500 °C, showed only ZnO diffractions, as observed by Baird at low cobalt loadings [18].

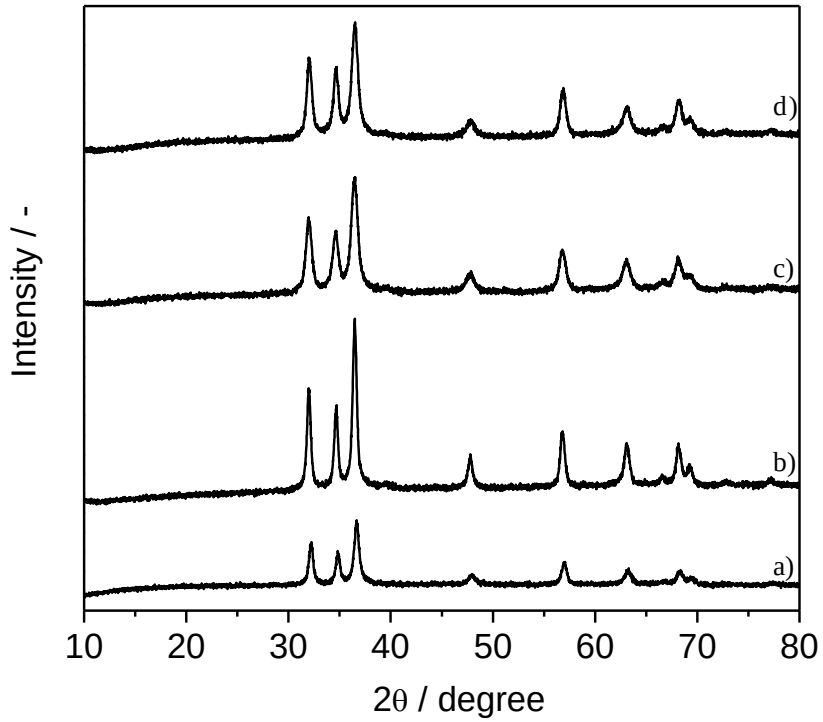

Figure 5.5. XRD diffraction of cobalt-zinc catalysts calcined at 350 °C for 5 h. a) JM-7-350; b) CZ-0-350; c) CZ-5-350; d) CZ-15-350.

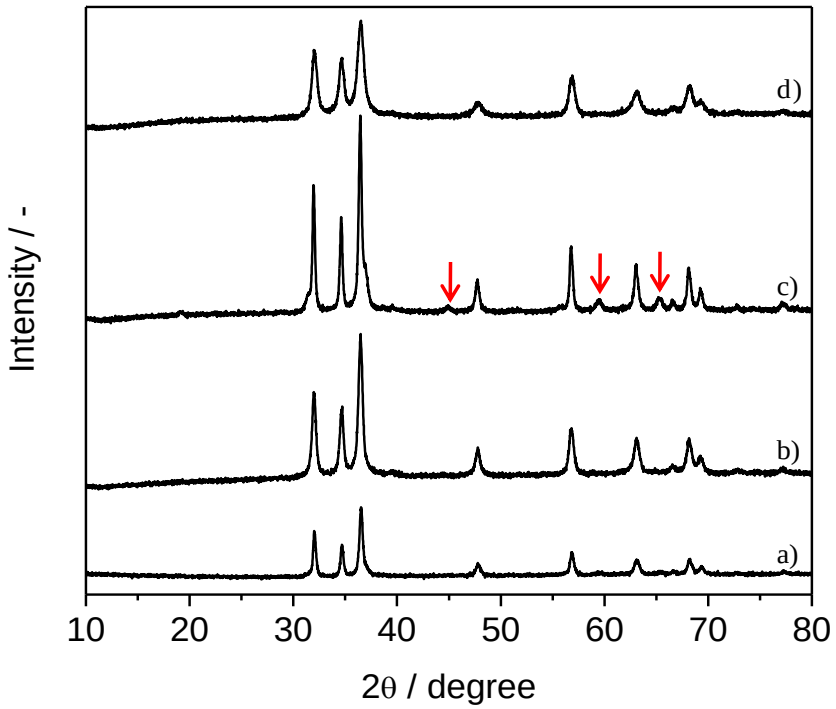

Figure 5.6. XRD diffraction of cobalt-zinc catalysts calcined at 500 °C for 5 h. a) JM-7-500; b) CZ-0-500; c) CZ-5-500; d) CZ-15-500. Arrows point spinel reflections, either Co_3O_4 or $ZnCo_2O_4$.

Table 5.2. BET surface area of SAS processed cobalt-zinc.

Catalyst	precipitated/m^2 g^{-1}	350 °C/m^2 g^{-1}	500 °C/m^2 g^{-1}
CZ-0	28	44	17
CZ-5	101	46	18
CZ-15	37	47	18
JM-7	17	44	19

5.3.4 N_2 physisorption.

The physical surface area was calculated using the B.E.T. method; values are listed in Table 5.2. In the binary cobalt-zinc system, surface area showed a strong dependence on water incorporation, as observed in cobalt precipitates (see *Chapter 3*). Hence, it is suggested that the same mechanism described in *Chapter 3* can be applied to this binary cobalt-zinc system. It should be noted that the co-precipitated cobalt-zinc precursor, JM-7-P, yielded a similar surface area to both reported catalysts precursor (22 m^2 g^{-1}) [6] and CZ-0-P. Hence, the advantage of making high surface area metal carbonates/hydroxycarbonates by SAS process can clearly be seen.

After calcination at 350 °C and 500 °C low surface area catalysts were obtained, regardless of the synthesis process. This was attributed to the formation of low surface area ZnO (Zn-350 41 m^2 g^{-1} and Zn-500 15 m^2 g^{-1}).

5.3.5 Temperature programmed reduction.

The reduction peak temperatures of cobalt-zinc catalysts are tabulated in Table 5.3. The samples calcined at 350 °C showed two reduction peaks between 210-280 °C that can be associated with the reduction of Co_3O_4 to CoO (low temperature) and the reduction of $ZnCo_2O_4$ (2 $ZnCo_2O_4$ to 2 CoO + 2 ZnO) (high temperature). Thus, TPR conveys the presence of two different cobalt species,

Table 5.3. Temperature reductions of cobalt-zinc precursors calcined at 350 °C and 500 °C.

Catalyst	350 °C			500 °C	
	T_{R1}	T_{R2}	T_{R3}	T_{R1}	T_{R2}
CZ-0	218	271	419	303	435
CZ-5	230	279	469	293	414
CZ-15	223	265	452	308	426
JM-7	210	258	456	351	441

which could be written in the generic form of $Zn_xCo_{3-x}O$ where *x* lies between 0 and 1 [20] conveying the presence of species such as Co_3O_4, $ZnCo_2O_4$ and intermediates. The peak at 419-469 °C was assigned to the reduction of CoO to Co metal. It should be noted that ZnO and $Zn_xCo_{1-x}O$ species, which may form due to diffusion of cobalt into the ZnO matrix, could contribute to the peak at high temperature, as the reduction of these species were observed above 440 °C [21].

Calcination at 500 °C changed the reduction profile as samples were reduced in two steps suggesting more homogeneous distribution of cobalt species, likely to be $ZnCo_2O_4$ as this was the only phase observed in Raman analysis, discussed later in *Section 5.3.9*. The first reduction peak (290-310 °C) was attributed to the reduction of $ZnCo_2O_4$ to CoO and the high temperature peak (410-450 °C) to the reduction of CoO to Co. As mentioned before, ZnO and $Zn_xCo_{1-x}O$ reduction could contribute to the high temperature reduction peak.

5.3.6 Scanning electron microscopy.

The SEM images of SAS processed catalysts clearly showed differences upon water incorporation, as seen in Figure 5.7. The CZ-0-P morphology was similar

to reported SAS precipitates, *i.e.* aggregated nanoparticles [22]. The addition of 5% water to the initial solution (Figure 5.7) changed the morphology of particles and large spheres (*ca.* 10-15 μm) and aggregated nanoparticles were observed. It suggests that in the presence of 5% water, two precipitations mechanisms were taking place (*i.e.* single phase and 2-phases with droplet formation). Further incorporation of water to 15% (Figure 5.8) yielded regular shapes (*i.e.* rhombohedral particles) but also aggregated needle-like particles grouped in lobe-like formations. This was previously observed in ZnO precursors [23, 24], although aggregated nanoparticles were not seen. Hence, the mechanism proposed in *Chapter 3* could be applied; and in the case of CZ-15-P growth times were sufficient to crystallize particles due to the slow CO_2 diffusion into solution. The co-precipitated JM-7-P showed lobe-like particles (Figure 5.8), as previously seen [6].

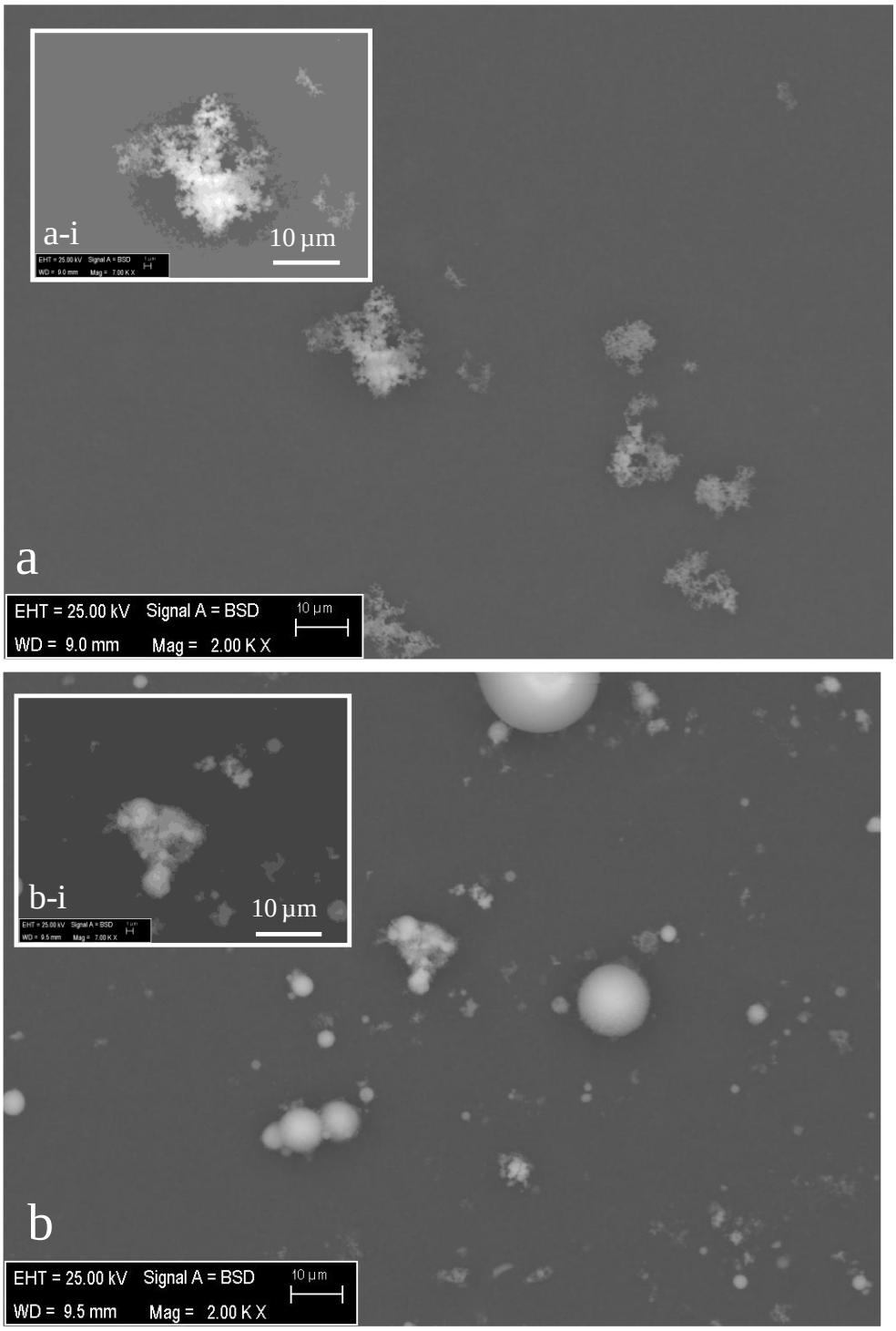

Figure 5.7. SEM of precipitated cobalt-zinc: a) CZ-0-P; b) CZ-5-P. Magnified images are depicted in the insets.

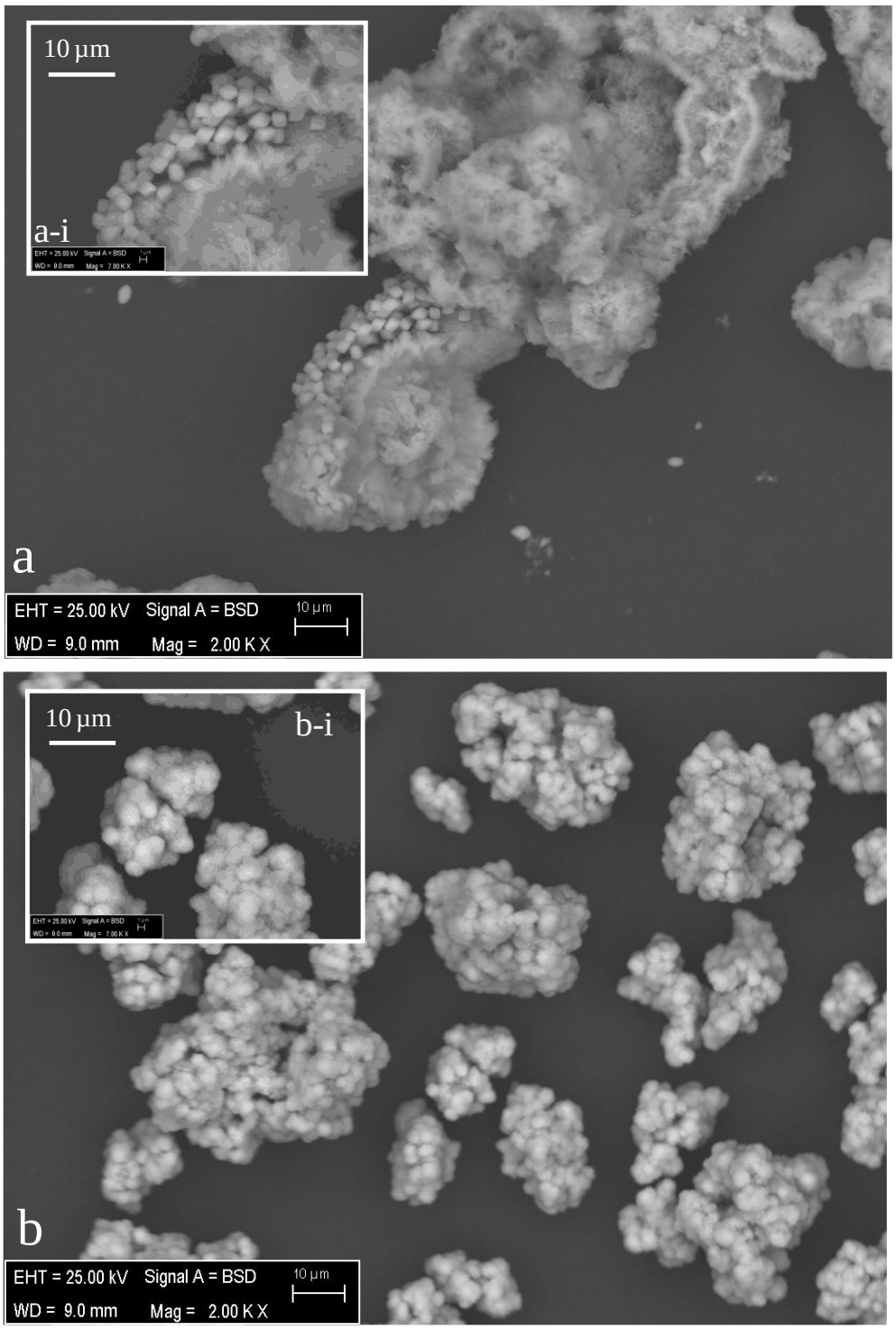

Figure 5.8. SEM of precipitated cobalt-zinc a) CZ-15-P and b) JM-7-P. Magnified images are depicted in the insets.

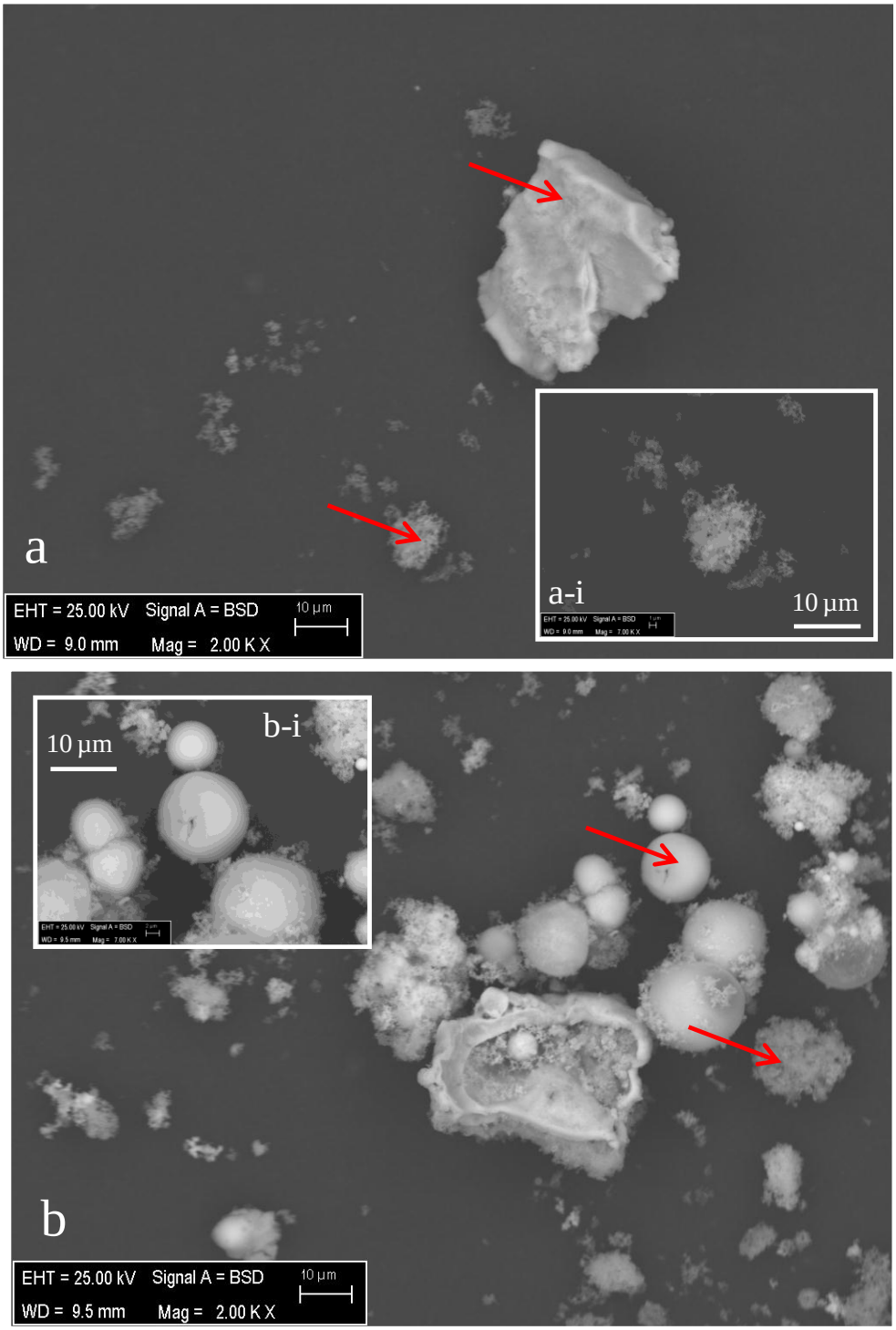

Figure 5.9. SEM of cobalt-zinc catalysts calcined at 350 °C: a) CZ-0-350; b) CZ-5-350. Arrows indicate where EDX analysis was performed.

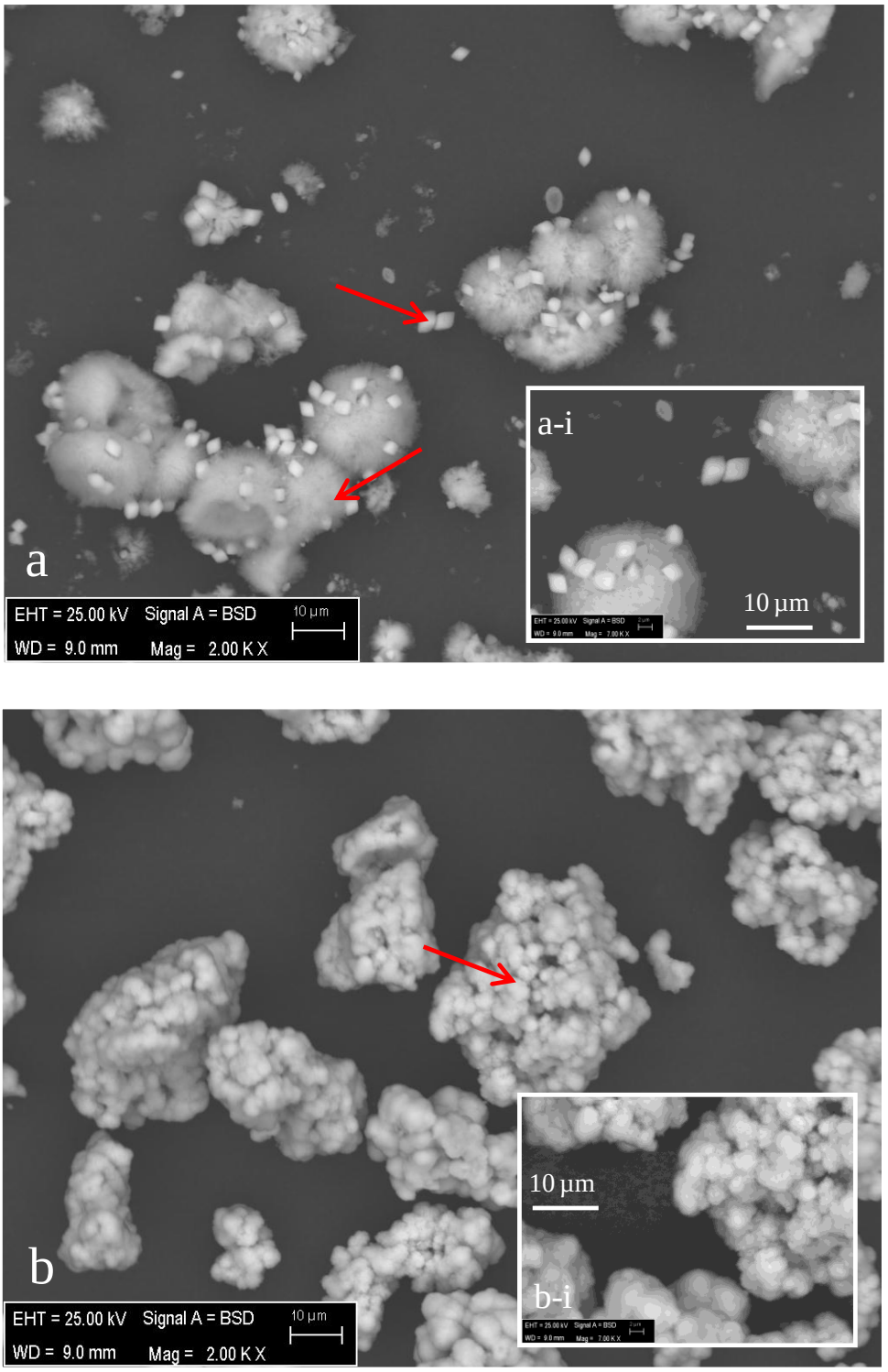

Figure 5.10. SEM of cobalt-zinc catalysts calcined at 350 °C: a) CZ-15-350 and b) JM-7-350. Magnified images are depicted in the insets. Arrows indicate where EDX analysis was performed.

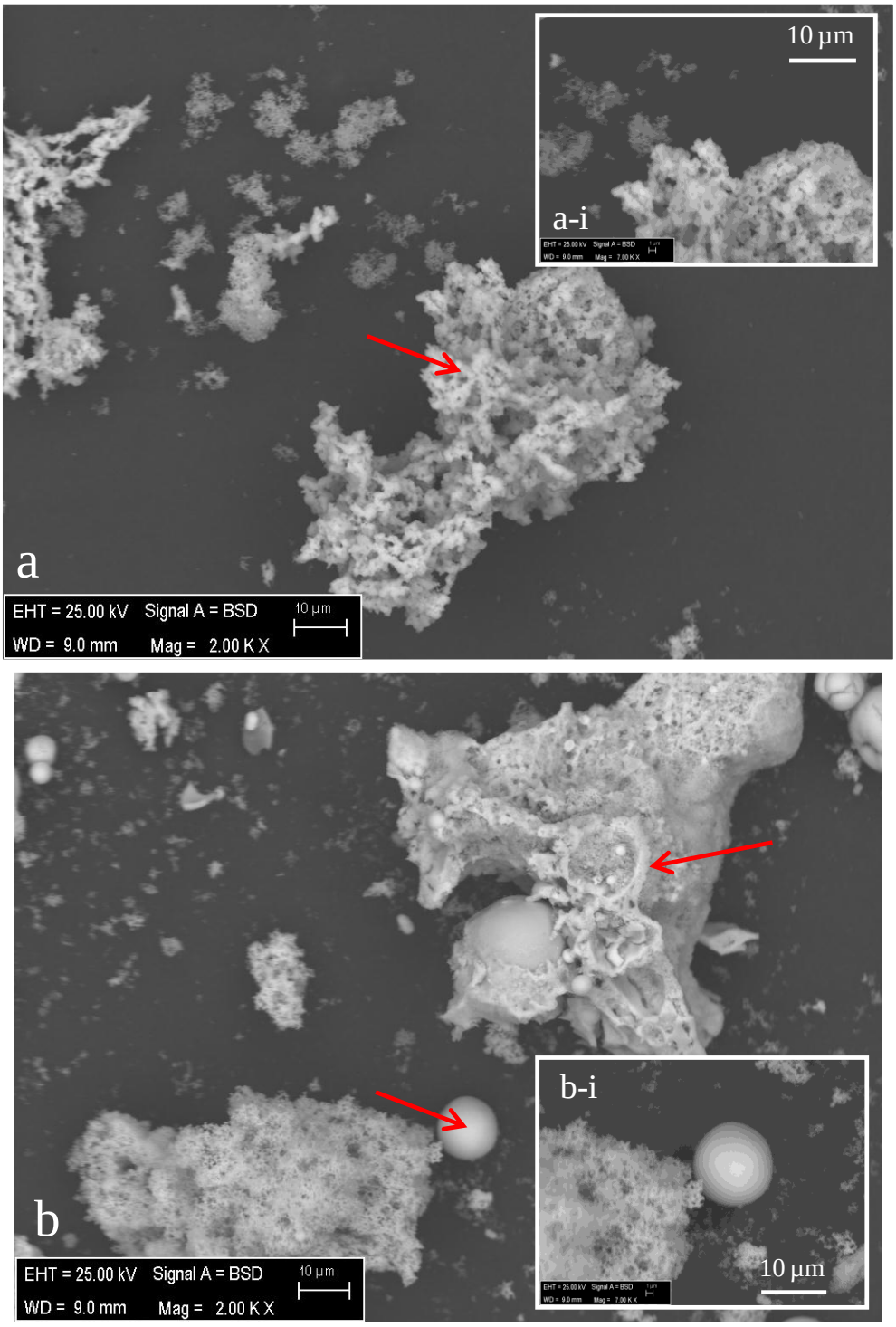

Figure 5.11. SEM of cobalt-zinc catalysts calcined at 500 °C: a) CZ-0-500; b) CZ-5-500. Arrows indicate where EDX analysis was performed.

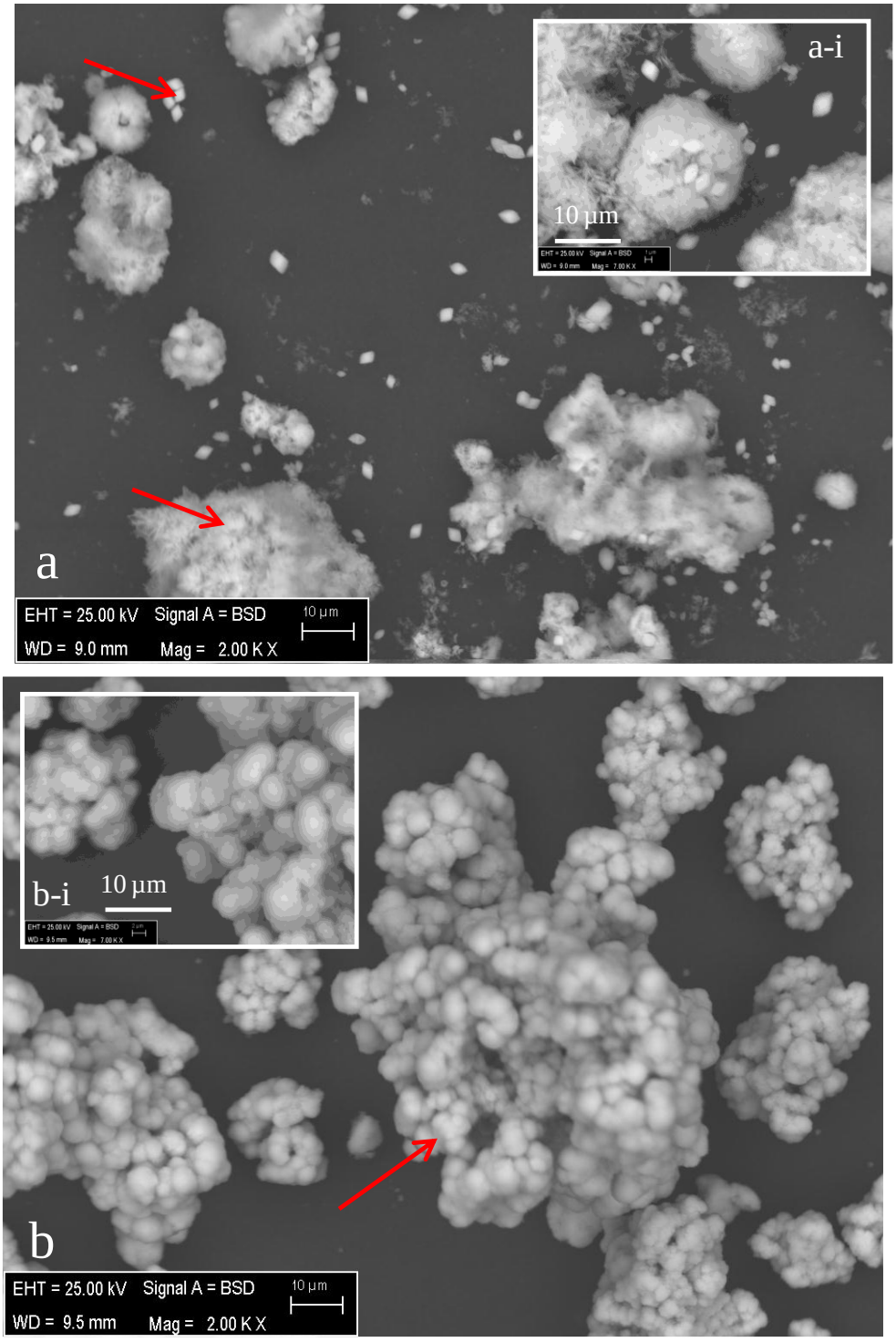

Figure 5.12. SEM of cobalt-zinc catalysts calcined at 500 °C: a) CZ-15-500; b) JM-7-500. Arrows indicates where EDX analysis was performed.

The CZ-0-350 produced particle aggregation as rock-like material (Figure 5.9), although the nanoparticulated materials were still visible, as seen in the inset in Figure 5.9. The morphology did not significantly change for CZ-5-350 compared to precipitated material and large spheres and nanoparticles were still visible, as seen in Figure 5.9. With regard to CZ-15-350, shown in Figure 5.10, thermal treatment aggregated the needle-like particles into spherical particles, and rhombohedral particles were also visible. For JM-7-350, similar material to the as-made precursor was observed (Figure 5.10).

Calcination at 500 °C, as seen in Figure 5.11, resulted in the aggregation of nanoparticles in rock-like material in CZ-0-500. For CZ-5-500 (Figure 5.12) rock-like material was observed, likely due to sintering of nanoparticulates; however, large spheres and nanoparticulates were still present. The CZ-15-500, as seen in Figure 5.12, showed rhombohedral morphologies together with needle-like particles some of which were aggregated in spheres. JM-7-500 (Figure 5.12), showed similar morphology as observed in precipitated and calcined catalysts at 350 °C.

5.3.7 Energy dispersive X-ray spectroscopy.

EDX was performed to analyse the composition of representative areas, marked with arrows in Figures 5.9 to 5.12. Nanoparticulated material of CZ-0 showed a higher Co/Zn ratio than the rock-like particles, 0.17 and 0.12 respectively, both for the samples calcined at 350 °C and 500°C. Homogeneous Co/Zn ratios were observed in CZ-5 in spheres and nanoparticles, 0.15 and 0.16 respectively, at 350 °C and 500 °C. The CZ-15 showed low cobalt content in rhombohedral particles

and cobalt rich needle-like particles grouped in lobe-like structures, 0.11 and 0.15 respectively, at 350 °C and 500 °C.

The JM-7 showed homogeneous Co/Zn ratio close to 0.12 at 350 °C and 500 °C.

5.3.8 Effluent analysis.

The metal content in SAS produced catalysts was measured by atomic absorption spectroscopy, as seen in Table 5.4. It is worth noting that CZ-5-P showed high Co/Zn ratios, suggesting that under these conditions, solubility of cobalt acetate was lower than zinc acetate. Low cobalt acetate solubility was also observed and discussed in *Chapter 3*, where the lowest cobalt concentration in the effluent was obtained using a solution of 5 vol% H_2O/methanol. Similar Co/Zn ratios in CZ-0-P and CZ-15-P were observed. Baird [18] correlated the species formed during precipitation and after calcination to Co/Zn ratios: hydrozincite (as precipitated) and ZnO phases (after calcination at 350 °C for 16 h) were observed for nominal ratios of 0.1. In contrast, hydrozincite and sphaerocobalite (as precipitated) were observed in ratios of 0.2 and above and

Table 5.4. Atomic absorption analysis of SAS catalysts and process effluents. Errors *ca.* 10% upon 3 repetitions. pH was measured by pH-meter.

Catalysts	Bulk catalysts		Effluent		
	Co/ZnO at%	Co/Zn ratio	Co / ppm	Zn / ppm	pH
CZ-0-P	14	0.15	9.72	11.7	6
CZ-5-P	18	0.20	2.2	5.7	5
CZ-15-P	15	0.16	118.04	66.1	5
JM-7-P	12	0.12	-	-	-

Note: Co/Zn ratio calculated on weight bases (wt/wt).

ZnO and a cobalt spinel species (either Co_3O_4 or $ZnCo_2O_4$) after calcination (350 °C for 16 h). Thus, the Co/Zn ratio obtained in CZ-0-P and CZ-15-P (0.15) may convey hydrozincite as the main precipitate; whereas the ratio obtained in CZ-5-P (0.2) suggests sphaerocobaltie and hydrozincite precipitates.

The effluent was also used to balance the mass of the metals in the process and precipitation yields were close to 100% for CZ-5 and slightly lower for CZ-0 and CZ-15: 98% and 96%, respectively. Slightly acidic effluents were recovered and the pH was lower in the water-added experiments; thus, the discussion in *Chapter 3* could be applied in these experiments

5.3.9 Raman spectroscopy.

Raman analysis of the calcined samples is shown in Figures 5.13 and 5.14 along with single metal oxides prepared by SAS. Zn-350 showed the typical Raman modes of ZnO of E_2 (high) at 439 cm^{-1}, A_1(TO) at 382 cm^{-1}, E_2 (high)-E_2(low) at 332 cm^{-1}. The Co-350 displayed the theoretical Raman modes for a metal oxide spinel: E_g at 484 cm^{-1}, F_{2g} at 523 cm^{-1}, F_{2g} at 622 cm^{-1} and A_{1g} at 693 cm^{-1} [25]. The band at 714 cm^{-1} in catalysts calcined both at 350 °C and 500 °C was attributed to the formation of $ZnCo_2O_4$ species, as observed by Rubio-Marcos *et al.* [26]. The authors assigned the formation of $ZnCo_2O_4$ to the diffusion of Zn into Co_3O_4. Rubio-Marcos obtained the spinel $ZnCo_2O_3$ by grinding the metal oxides (Co_3O_4 and ZnO) and calcining for long time (36 h) at 500 °C. In this work, the spinel phase was achieved at a lower temperature (350 °C) and shorter calcination time (5 h) most likely due to the intimate mixing of the cobalt and zinc precursors

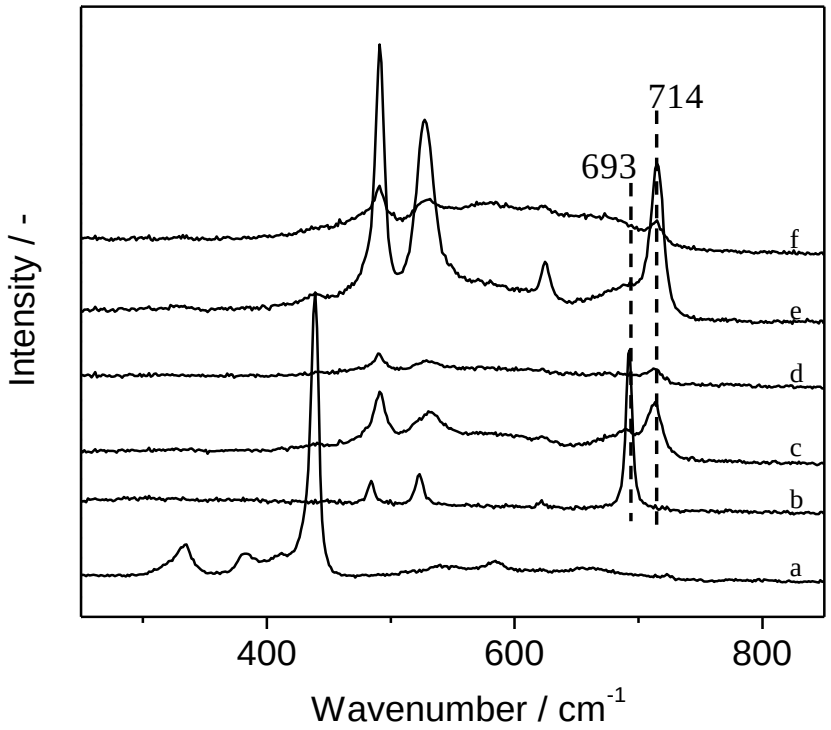

Figure 5.13. Raman spectra of catalysts calcined at 350 °C. a) Zn-350; b) Co-350; c) JM-7-350; d) CZ-0-350; e) CZ-5-350; f) CZ-15-350.

during the precipitation. It is worth noting that JM-7-350 and CZ-5-350 showed a shoulder at 693 cm^{-1}, indicating the presence of Co_3O_4.

In contrast to results from XRD analysis, the calcined cobalt-zinc SAS precipitates show only a weak band from the ZnO component, at 439 cm^{-1}, with the main vibrations attributed to strongly scattering $ZnCo_2O_4$. This is in good agreement with the literature which finds a significant blueshift in the Raman bands when Zn^{2+} is incorporated into the Co_3O_4 lattice [26, 27].

5.3.10 H_2 chemisorption.

H_2 chemisorption was used to estimate the cobalt metal surface area of cobalt-zinc catalysts, as seen in Figures 5.15 and 5.16. The cobalt surface area showed

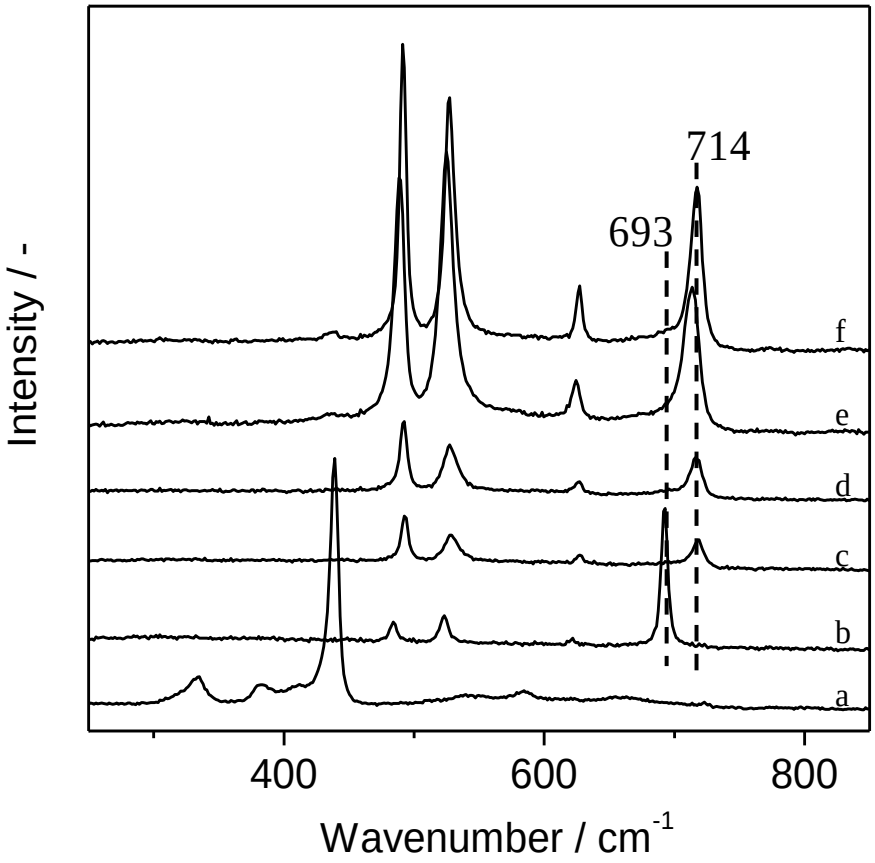

Figure 5.14. Raman spectra of catalysts calcined at 500 °C. a) SAS ZnO; b) SAS Co_3O_4; c) JM-7; d) CZ-0; e) CZ-5; f) CZ-15.

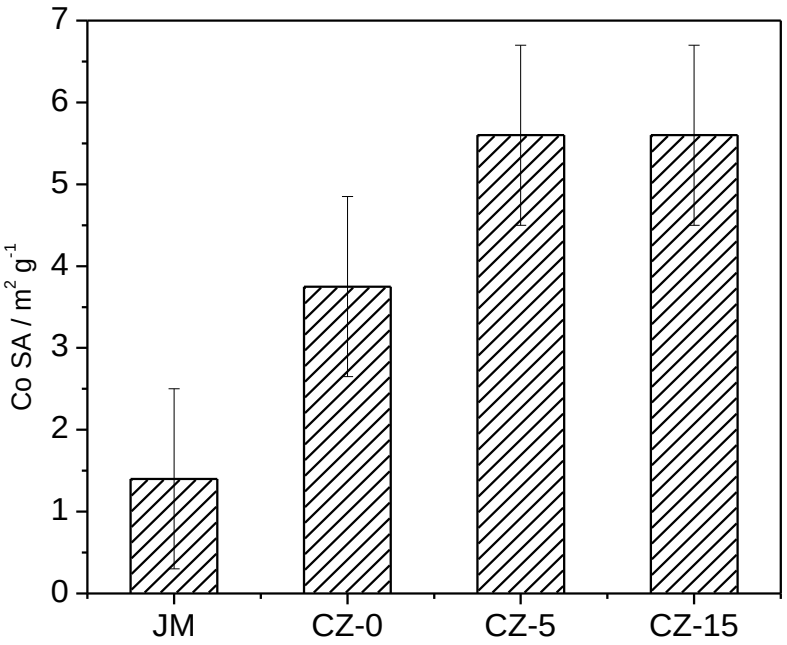

Figure 5.15. Cobalt metal surface area of cobalt-zinc catalysts calcined at 350 °C. Error of ±1.1 m^2 g^{-1} calculated upon repetitions.

significant dependence upon calcination temperature and values halved as calcination temperature was increased from 350 °C to 500 °C.

Calcination at 350 °C yielded metal surface area of 3.8 m^2 g^{-1} for CZ-0-350; this values is significantly higher than both traditional co-precipitated catalyst JM-7-350 (1.5 m^2 g^{-1}) and supported Co-Zn-TiO_2 (0.9-1.7 m^2 g^{-1}) [8]. The CZ-0-350 presented higher values than co-precipitated or impregnated catalysts, although lower than the water incorporated SAS catalysts (5.5 m^2 g^{-1} in CZ-5-350 and CZ-15-350). The advantage of using SAS to obtain high cobalt surface area catalysts can clearly be seen. The metal surface area was increased by the addition of water to the starting solution, likely due to the thermal stability of carbonated/hydroxycarbonates during the calcinations, which most likely restricted the cobalt sintering.

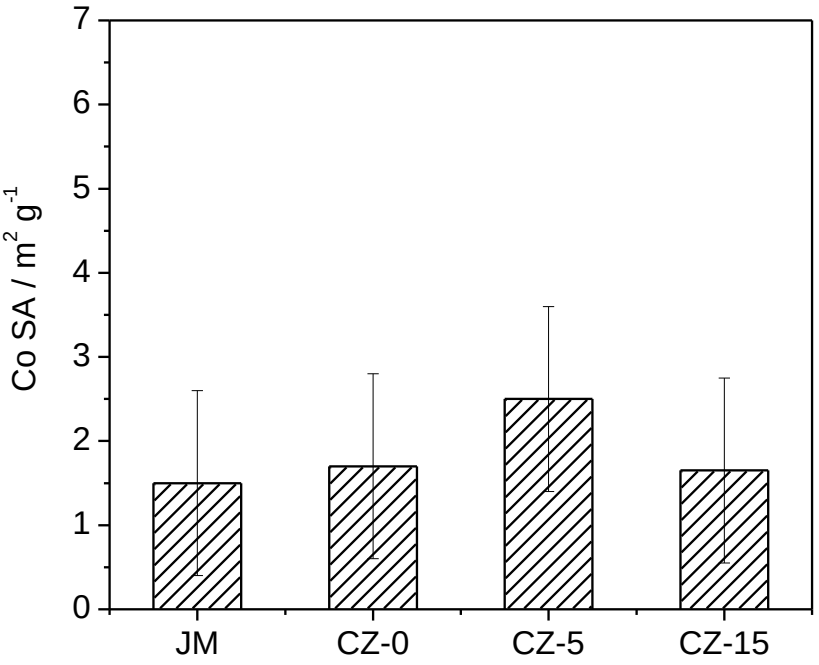

Figure 5.16. Cobalt metal surface area of cobalt-zinc catalysts calcined at 500 °C. Error of ±1.1 m^2 g^{-1} calculated upon repetitions.

Calcination at high temperatures (500 °C) drastically decreased the metal surface area of SAS catalysts. However, values were higher than those of the co-precipitated catalyst. Interestingly, CZ-5-500 yielded a relatively high metal surface area suggesting that a thermally stable catalyst was obtained. The decrease of available cobalt on the surface was also observed under XPS as discussed in *Section 5.3.11*: Co/Zn ratios were observed to decrease, except in the case of CZ-5-P which showed no changes in surface concentration with increasing calcinations temperature (0.152 and 0.153 at 350 °C and 500 °C). The reduction in surface area might be caused by the sintering of cobalt oxide crystallites or due to the formation of poorly reducible species at 500 °C, such as $ZnCo_2O_4$.

5.3.11 X-ray photoelectron spectroscopy.

XPS analysis was performed as detailed in *Section 2.4.5*. Results are shown in Table 5.5. The Co/Zn atomic ratio was calculated by integrating the area below the peak of Co $2p_{3/2}$ (780 eV) and the peak of Zn $p_{3/2}$ (1018 eV).

The Co/Zn ratios of SAS precipitates were close to the expected value (Co/Zn = 0.176), however the Co/Zn ratio increased upon water addition. It was observed that zinc formed a hydroxypolymer in the methanolic solution with the addition of water [23], as described in *Section 5.3.12*. Thus, the progressive incorporation of water into the starting solution could promote formation of the hydroxypolymer, whereby the larger the amount of water, the larger the amount of zinc hydroxypolymers. Thus, during the precipitation under SAS conditions, the cobalt acetate and the unpolymerised zinc acetate had a nucleation point to precipitate. Hence, it is suggested that by increasing the proportion of water in the starting solution, the zinc polymerization was promoted, providing a nucleation point for cobalt acetate and zinc acetate precipitation.

Table 5.5. Co/Zn atomic ratios obtained by XPS analysis. Error of 5% is the standard error of quantitative analysis in XPS.

Material	Precipitated	350 °C	500 °C
CZ-0	0.165	0.153	0.107
CZ-5	0.186	0.153	0.152
CZ-15	0.193	0.145	0.112
JM-7	0.179	0.163	0.165

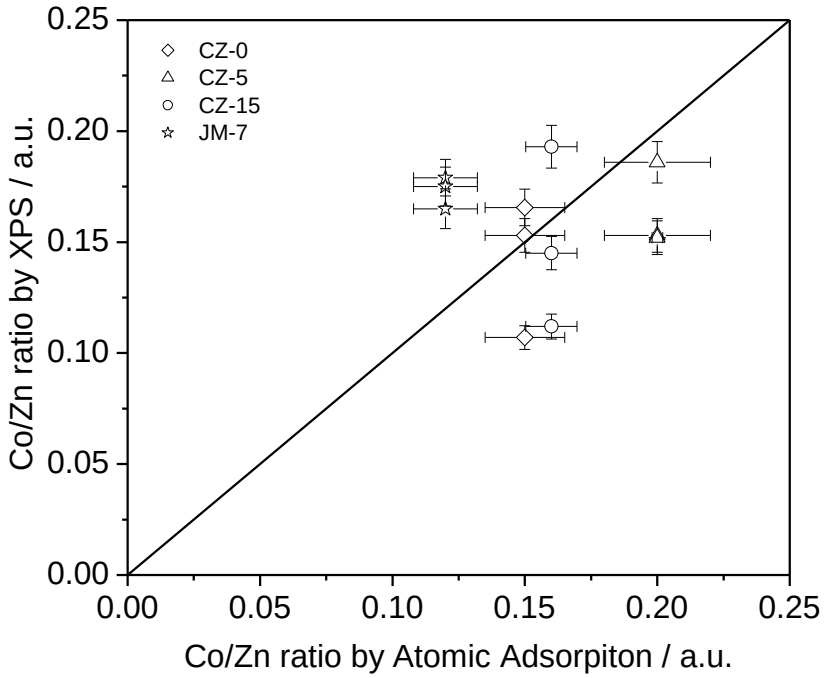

Figure 5.17. Co/Zn ratios calculated by atomic absorption spectroscopy and XPS. Theoretical Co/Zn ratio based on the salts dissolved is 0.172. Pr stands for precipitated material, arrows indicate the calcination temperature applied to the catalyst. Error of 5% is the standard value in quantitative XPS analysis. In atomic absorption error of *ca*. 10% was calculated upon repetitions.

Also, it should be noted that in SAS precipitates the Co/Zn ratio decreases as calcination temperature increases, except in CZ-5 where the ratio initially decreased after calcination at 350 °C, as for CZ-0 and CZ-15, but remained constant after calcination at 500 °C. The decrease in Co/Zn ratio, as seen in Figure 5.17, was attributed to the diffusion of cobalt into the ZnO matrix, most likely forming $Zn_{1-x}Co_xO$. This process is activated thermally and without significant changes of the crystal structure of wurtzite ZnO as the Co^{2+} radii is close to Zn^{2+} (0.058 nm and 0.06 nm, respectively) [28]. However, as the same Co/Zn ratio was observed for CZ-5-500 and CZ-5-350, it is suggested that, as in the case of the other materials, cobalt ion diffusion into the ZnO matrix does

occur but the higher initial concentration of surface cobalt results in residual cobalt left on the surface post calcinations.

For JM-7-350 and JM-7-500 a constant Co/Zn ratio was observed and this was attributed to the different precipitation mechanism (likely Zn hydroxylpolymers were not formed), as experimental procedure, solvents and reactants were different.

The XPS spectra of Co $2p_{2/3}$ in cobalt-zinc oxide catalysts calcined at 350 °C and 500 °C are shown in Figure 5.18. The SAS precipitated catalysts calcined at 350 °C all showed similar spectra, suggesting the presence of Co^{3+}/Co^{2+}. Upon calcination at higher temperature, the binding energy shifted towards lower energy (779 eV), indicating a decrease of the overall cobalt oxidation state. This shift might arise from the formation of $Zn_xCo_{1-x}O$ species.

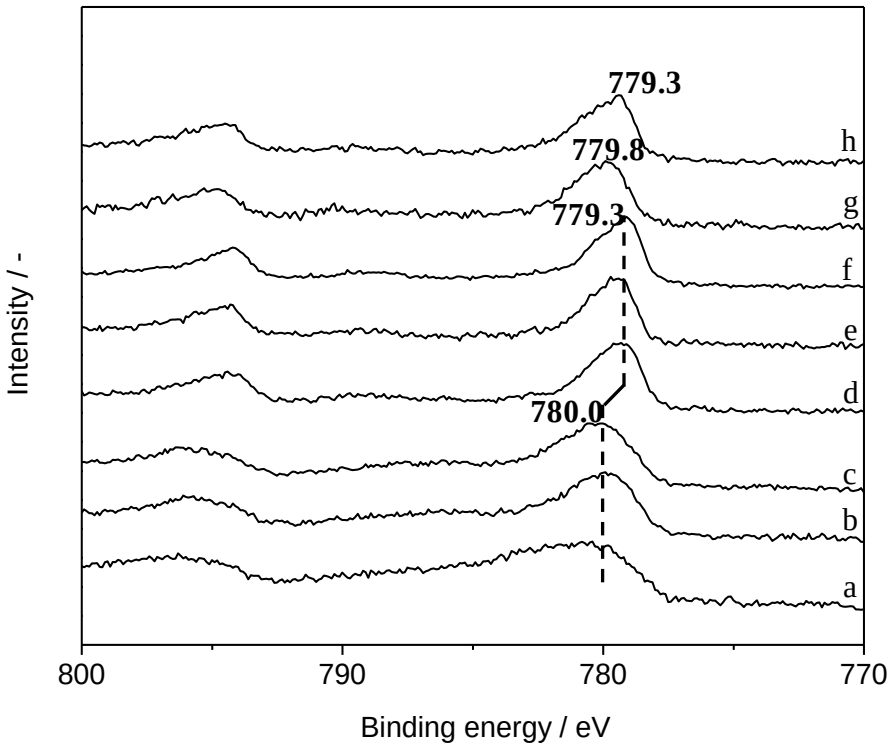

Figure 5.18. XPS spectra of calcined catalysts. a) CZ-0-350; b) CZ-5-350; c) CZ-15-350; d) CZ-0-500; e) CZ-5-500; f) CZ-15-500; g) JM-7-350 and h) JM-7-50.

5.3.12 Comments on the co-precipitation of Co/ZnO catalysts.

The traditional co-precipitation of JM-7, using cobalt and zinc nitrate salts and a base as precipitating agent, resulted in a Co/Zn ratio on the outer layer close to the expected value, 0.179 and 0.176, respectively. The Co/Zn ratio decreased upon calcination at 350 °C, possible due to the diffusion of zinc into the Co_3O_4, with the subsequent formation of $Zn_xCo_{3-x}O_4$ (where x can take any value between 0 and 1), as Raman and TPR suggest. The zinc, which was not incorporated as $Zn_xCo_{3-x}O_4$, formed ZnO as observed in Figure 5.5. Calcination at 500 °C likely completed the incorporation of zinc into Co_3O_4 yielding $ZnCo_2O_4$, as Raman and TPR suggest in Figure 5.13. The surplus zinc formed ZnO, as observed in Figure 5.6.

The SAS co-precipitated precursor catalysts can be classified in two groups depending on the amount of water added to the starting solution. The first group, where water was not added, *i.e.* CZ-0-P, the Co/Zn ratio on the outer layer of is below of expected value (0.165 and 0.176 respectively) likely due to the low solubility of zinc acetate in the system (methanol/CO_2), as the high zinc concentration observed in Table 5.4 conveys. In the second group, CZ-5-P and CZ-15-P, the addition of water could partially hydrolyze the zinc acetate yielding zinc hydroxypolimers, and possibly increased the solubility of the remaining zinc acetate in the methanol/CO_2 system. Therefore, if the polymer was formed, the cobalt and zinc acetates predominantly precipitated on the zinc hyrdroxypolimer as discussed in Section 5.3.11, due to the seeding effect of the polymers, leaving a Co/Zn ratio on the outer layer above expected values (0.186 and 0.193 for CZ-5-P and CZ-15-P respectively). The calcination at 350 °C most likely formed $Zn_xCo_{3-x}O_4$, due to zinc incorporation into the Co_3O_4, as above explained, in all

three SAS materials as Raman and TPR suggest. The surplus zinc formed ZnO, as seen in Figure 5.5. The calcination at 500 °C probably formed $ZnCo_2O_4$ in CZ-15-500 and CZ-0-500, as observed in Raman and TPR. Hence the drop in Co/Zn ratio on the outer layer observed in both CZ-0-500 and CZ-15-500. Controversially, the Co/Zn ratio on the outer layer of CZ-5-500 is very close to the one observed in CZ-5-350, 0.152 and 0.153 respectively. It is suggested that due to the high cobalt content in CZ-5 the calcination at 500 °C was not long enough to the complete formation of $ZnCo_2O_4$; consequently there was still cobalt present as Co_3O_4 or $Zn_xCo_{3-x}O_4$, as the little Raman shift towards low wavenumbers, the large cobalt surface area and low reduction temperature observed convey. It is worth noting that the high cobalt concentration in CZ-5, and then low cobalt solubility in the methanol/H_2O/SC-CO_2, agrees with the low cobalt acetate solubility observed in *Chapter 3* in systems with H_2O 5 vol%, see Figure 3.24.

5.3.13 Fischer-Tropsch reaction.

The catalysts calcined at 350 °C and 500 °C were tested for FT synthesis and results are shown in Figures 5.20 and 5.21 and Table 5.6.

Overall, during the first 150 h the catalysts were not stable, regardless of the synthesis process.

The CZ-5-350 showed relatively high CO turnover rate at medium temperatures (225 °C and 235 °C); however, at 245 °C the CO turnover decreased to similar values to those of CZ-0-350 and CZ-15-350, most likely due to carbon formation on the cobalt or to the sintering of cobalt particles. The JM-7-350 performance was similar to CZ-0-350 and CZ-15-350 at 225-235 °C but at 245 °C the CO turnover increased; blockage of the reactor prevented further testing. Similarly, blockage in CZ-15-350 was observed. There was not a clear relationship between

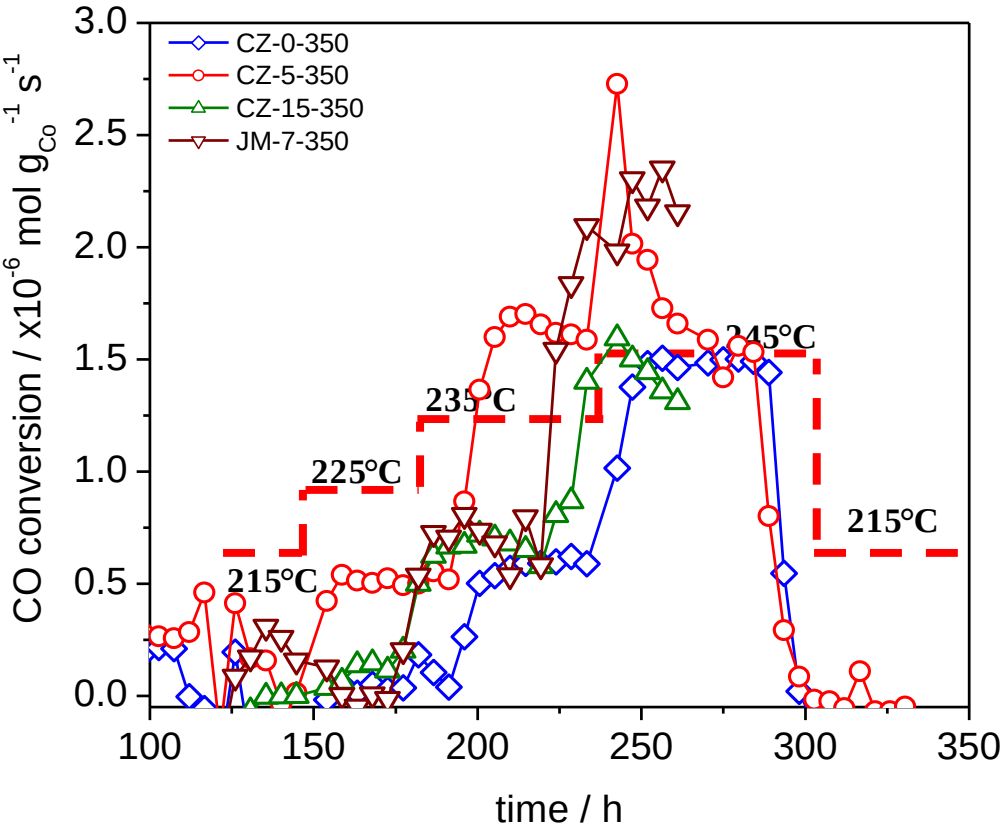

Figure 5.20. CO turnover in FT reactions for cobalt-zinc catalysts calcined at 350 °C.

metal surface area and CO turnover as CZ-5-350 and CZ-15-350 presented similar metal areas but significantly different FT activity. The lack of stability may be the cause of the mismatch between cobalt surface area and FT activity. It is suggested that the structure of the SAS cobalt-zinc catalysts was modified during the initial stage of reaction (first 150 h): modifications such as cobalt sintering or carbon formation on the catalyst surface could take place, as observed by Pan [13] in Co/ZnO catalyst.

Calcination at high temperatures (500 °C) hampered the activity of catalysts, especially for the SAS made catalysts. The co-precipitated catalyst, JM-7-500, presented stable performance and only CZ-5-500 showed similar performance. The decrease of FT activity in SAS prepared catalysts can be explained in terms of Co/Zn ratio. The XPS suggests that by increasing the calcination temperature,

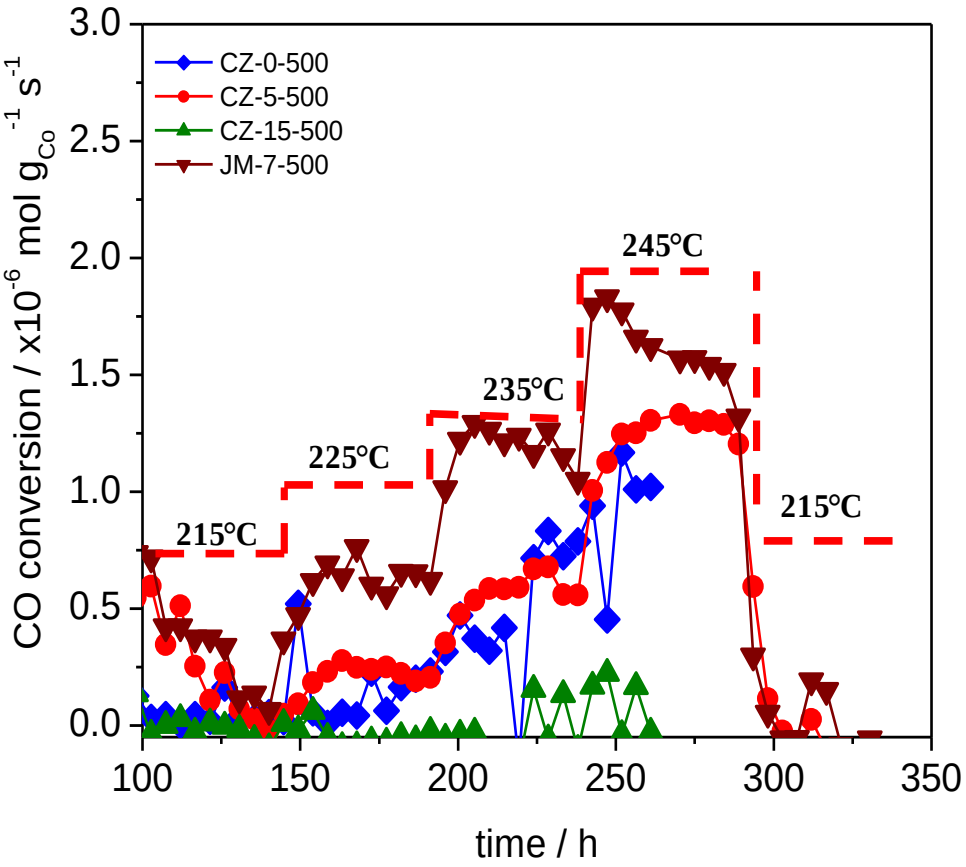

Figure 5.21. CO turnover in FT reaction for cobalt-zinc catalysts calcined at 500 °C.

cobalt diffuses towards the core of the catalysts, likely dissolving into the ZnO structure and then decreasing the available cobalt on the surface; this was also confirmed by the cobalt surface area. The amount of cobalt on the outer layers remained constant for CZ-5-500, as seen in XPS, and the cobalt surface area reduced to a lesser degree compared to CZ-0-500 and CZ-15-500, as discussed previously, which explains the better CO turnover observed in CZ-5-500. The remarkable activity shown by JM-7-500 was likely due to high stability, as evidenced by XPS Co/Zn ratios and surface areas that were constant at both calcination temperatures. The Co/Zn ratios observed by XPS in JM-7-500 and CZ-5-500 were similar (0.165 and 0.152, respectively) and the cobalt area was higher in CZ-5-500 than in JM-7-500 (1.5 and 2.5 m^2 g^{-1}, respectively). Hence, it is suggested that the stability of the traditionally co-precipitated catalyst was greater than the SAS made, likely due to the predominant hydroxycarbonate precursors, *i.e.* no residual acetates. The greater stability resulted in better CO turnovers in calcinations at 500 °C.

The selectivity towards C_{5+} and CH_4 are shown in Table 5.6. Reaction at 225 °C for catalysts calcined at 350 °C yielded selectivities of 62-70% for SAS catalysts,whereas a relatively high selectivity (81%) was obtained in the co-

Table 5.6. C_{5+}/CH_4 selectivities of cobalt-zinc catalysts at different reaction temperatures

Catalyst	C_{5+}/CH_4 selectivity (%) at 225 °C	C_{5+}/CH_4 selectivity (%) at 235 °C	C_{5+}/CH_4 selectivity (%) at 245 °C
CZ-0-350	62/22	61/22	69/27
CZ-5-350	62/14	76/26	54/36
CZ-15-350	70/21	74/15	63/22
JM-7-350	81/15	70/21	74/21
CZ-0-500	78/12	0/0	45/35
CZ-5-500	15/22	34/29	47/41
CZ-15-500	0/0	0/0	0/0
JM-7-500	65/15	74/15	70/21

precipitated catalyst, JM-7-350. Selectivity in JM-7-350 decreased as thereaction temperature was increased to 235 °C, but remained fairly constant in SAS catalysts. Further increase in temperature reaction (245 °C) restricted the formation of C_{5+} products, as selectivities were between 54-71%. Pan *et. al.* [13] observed a decrease in C_{5+} products in Co/ZnO catalysts upon increasing the reaction temperature (205 °C to 215 °C) under similar conditions (25 bar and H_2:CO = 2:1), and this decrease was attributed to carbon formation on the surface that ultimately increased CH_4 formation whilst decreasing C_{5+} formation, as observed in Table 5.6. Coville *et. al.* [9] attributed the high CH_4 selectivity to the exposure of zinc to the FT atmosphere. In the present work, it is suggested that the presence of zinc increased the selectivity towards CH_4, with the concomitant decrease of C_{5+} selectivity, compared to cobalt catalysts supported on non-zinc elements, for instance 20 wt% cobalt supported on Al_2O_3, TiO_2 and SiO_2 yielded CH_4 selectivity of 4.3%, 1.7% and 2.1% at 220 °C and 7.5%, 5.5% and 6.9% at 240 °C, respectively (20 bar and H_2:CO = 2:1) [3]. Furthermore, the increase in temperature may promote carbon formation on the cobalt species, restricting C_{5+} selectivity, regardless of the synthesis used. The calcination of catalysts at 500 °C drastically reduced the selectivity towards C_{5+} in SAS made materials at all reaction temperatures, as observed in CO turnovers. The selectivities were fairly stable in JM-7-350 and JM-7-500 suggesting the greater stability, as previously discussed.

5.4 Conclusions.

In this *Chapter* the capabilities of SAS for producing co-precipitated cobalt-zinc were surveyed and compared to a traditional co-precipitated catalyst. Also, the

addition of water during catalyst synthesis was investigated as a method of improving the catalyst performance.

The SAS process incorporated carbonates/hydroxycarbonates into the precipitated materials, although acetates were also observed. The ratio between acetate/carbonate changed as water was progressively incorporated. Water addition modified the physical surface area, as observed in *Chapter 3*, however after thermal treatments, similar surface areas were observed regardless of the synthesis process, likely due to predominant presence of low surface area ZnO. Bulk analysis of precursors showed a slightly higher Co/Zn ratio as 5% water was added. The relative increase in cobalt concentration in CZ-5 was correlated to the cubic spinel reflections observed by XRD after calcination at 500 °C, attributed either to Co_3O_4 or $ZnCo_2O_4$. Raman spectroscopy suggested the incorporation of Zn into Co_3O_4, forming $ZnCo_2O_4$. H_2 chemisorption highlighted how the SAS method can be used to synthesise materials with high metal surface areas although retention of that high surface area was very sensitive to calcinations at high temperatures. The XPS Co/Zn ratio suggested incorporation of cobalt into ZnO matrix as annealing temperature were increased. In contrast, this was not observed in the traditionally co-precipitated cobalt-zinc, suggesting a higher stability compared to the SAS precipitated material. It was suggested that zinc hydroxypolymers were formed during the initial solution preparation, which further acted as nucleation seeds where cobalt and zinc precursors precipitated. It was also conveyed that the formation of the zinc polymers was water dependent, increasing as water was incorporated. The CZ-5-350 was significantly active under FT conditions at 225-235 °C, and the mismatch between the cobalt surface area and the FT activity was attributed to the

instabilities observed during the first 150 h under reaction that most likely modified the catalysts. Catalytic activity dropped significantly as annealing temperature was increased to 500 °C. Nevertheless, the outstanding cobalt metal surface areas obtained in these experiments encourages us to seek alternatives stabilizing the catalysts made by SAS for the FT reaction.

5.6 Acknowledgments.

The author thanks Dr Dan Enache and Sharon Bale at *Johnson Matthey* for the Fischer-Tropsch testing and catalysts preparation. Dr Albert Carley is also acknowledged for the XPS data interpretation.

5.7 References.

1. Sun, S.; Fujimoto, K.; Yoneyama, Y.; Tsubaki, N., *Fuel* **2002,** *81* (11-12), 1583-1591.

2. Iglesia, E., *Applied Catalysis A: General* **1997,** *161* (1-2), 59-78.

3. Oh, J.-H.; Bae, J.; Park, S.-J.; Khanna, P.; Jun, K.-W., *Catalysis Letters* **2009,** *130* (3), 403-409.

4. Fischer, F.; Tropsch, H., *Brennstoff Chemie* **1926,** *7*, 97-104.

5. Fischer, F.; Tropsch, H., *Brennstoff Chemie* **1923,** *4*, 276-285.

6. Baijense, C.; Rekker, T. Fischer Tropsch catalysts comprising cobalt and zinc oxides. 2003.

7. Khassin, A.; Yurieva, T.; Parmon, V., *Reaction Kinetics and Catalysis Letters* **1998,** *64* (1), 55-62.

8. Madikizela-Mnqanqeni, N. N.; Coville, N. J., *Applied Catalysis A: General* **2007,** *317* (2), 195-203.

9. Madikizela-Mnqanqeni, N. N.; Coville, N. J., *Applied Catalysis A: General* **2004,** *272* (1-2), 339-346.

10. Madikizela-Mnqanqeni, N. N.; Coville, N. J., *Journal of Molecular Catalysis A: Chemical* **2002,** *181* (1-2), 129-136.

11. Madikizela-Mnqanqeni, N. N.; Coville, N. J., *Applied Catalysis A: General* **2008,** *340* (1), 7-15.

12. Li, J.; Zhang, J.; Zhang, R.; Cao, W., *Journal of Natural Gas Chemistry* **2009,** *18* (3), 325-330.

13. Pan, Z.; Bukur, D. B., *Applied Catalysis A: General* **2011,** *404* (1-2), 74-80.

14. Edwards, D. A.; Hayward, R. N., *Canadian Journal of Chemistry* **1968,** *46*, 3443-3446.

15. Nickolov, Z.; Georgiev, G.; Stoilova, D.; Ivanov, I., *Journal of Molecular Structure* **1995,** *354* (2), 119-125.

16. Wahab, R.; Ansari, S. G.; Kim, Y. S.; Dar, M. A.; Shin, H.-S., *Journal of Alloys and Compounds* **2008,** *461* (1-2), 66-71.

17. Wang, S. L.; Qian, L. Q.; Xu, H.; Lü, G. L.; Dong, W. J.; Tang, W. H., *Journal of Alloys and Compounds* **2009,** *476* (1-2), 739-743.

18. Baird, T.; Campbell, K. C.; Holliman, P. J.; W. Hoyle, R.; Stirling, D.; Williams, B. P.; Morris, M., *Journal of Materials Chemistry* **1997,** *7* (2), 319-330.

19. Baird, T.; C. Campbell, K.; J. Holliman, P.; W. Hoyle, R.; Huxam, M.; Stirling, D.; Peter Williams, B.; Morris, M., *Journal of Materials Chemistry* **1999,** *9* (2), 599-605.

20. Klissurski, D.; Uzunova, E., *Journal of Materials Science* **1994,** *29* (2), 285-293.

21. Liang, M.; Kang, W.; Xie, K., *Journal of Natural Gas Chemistry* **2009,** *18* (1), 110-113.

22. Reverchon, E.; De Marco, I.; Torino, E., *The Journal of Supercritical Fluids* **2007,** *43* (1), 126-138.

23. Hosono, E.; Fujihara, S.; Kimura, T.; Imai, H., *Journal of Colloid and Interface Science* **2004,** *272* (2), 391-398.

24. Cho, S.; Jang, J.-W.; Jung, S.-H.; Lee, B. R.; Oh, E.; Lee, K.-H., *Langmuir* **2009,** *25* (6), 3825-3831.

25. Hadjiev, V. G.; et al., *Journal of Physics C: Solid State Physics* **1988,** *21* (7), L199.

26. Rubio-Marcos, F.; Calvino-Casilda, V.; Bañares, M. A.; Fernandez, J. F., *Journal of Catalysis* **2010,** *275* (2), 288-293.

27. Samanta, K.; Bhattacharya, P.; Katiyar, R. S.; Iwamoto, W.; Pagliuso, P. G.; Rettori, C., *Physical Review B* **2006,** *73* (24), 245213-1 245213-5.

28. Yang, H.; Nie, S., *Materials Chemistry and Physics* **2009,** *114* (1), 279-282.

29. Hyeon-Jun, L.; Se-Young, J.; Chae Ryong, C.; Chul Hong, P., *Applied Physics Letters* **2002,** *81* (21), 4020-4022.

6

Conclusions and future work

6.1 Conclusions.

Dense CO_2 technology has been widely used for pharmaceutical drugs precipitation, extractions and powder production. Also, the catalytic science has used these techniques with good results. Nevertheless, up to date a comprehensive study to understand the impact of dense CO_2 technology, *e.g.* SAS and GAS techniques, in catalyst synthesis has not yet been performed. The SAS was used as a precipitation technique, similar to traditional co-precipitation; whereas GAS was approached as an alternative route for impregnations. In the present work, Fischer-Tropsch (FT) reaction and propane total oxidation were targeted as potential reactions where dense CO_2 processed catalysts can be applied. The investigation of catalyst production by dense CO_2 found the following:

- SAS was used to precipitate a variety of transition metal acetates, ranging from manganese to copper. The precipitated materials comprised mainly

acetates, although carbonate/hydroxycarbonates were also precipitated. The formation of the latter was attributed to the water of crystallization associated with the precursor compounds. The processed materials were calcined at 400 °C and then tested as bulk catalysts for propane total oxidation; amongst all the tested materials, the spinel Co_3O_4 was the most active metal oxide.

- The effect of water as a co-solvent and the consequent formation of carbonates were investigated during the course of SAS precipitation. It is suggested that carbonates/hydroxycarbonates are formed due to ligand exchange between acetates and CO_3^{2-}, the later was formed as a consequence of the dissociation of CO_2 in water. The ligand exchange was determined to primarily occur during the aging step after the material was precipitated. Experiments showed how as-received acetates (those not prepared by SAS) placed directly into the precipitation vessel could be converted to the carbonate form by treatment with a H_2O/methanol solution under high pressure CO_2. However, the formation of cobalt carbonates by ligand exchange during the precipitation stage cannot be ruled out.
- Based on previous findings, water was progressively incorporated as co-solvent into the methanol solutions to form thermally stable carbonate/hydroxocarbonate species upon precipitation. It was found that incorporation of 15% water yielded relatively high surface area cobalt oxide (35 m^2 g^{-1}) after calcinations, with small crystallites (24 nm) compared to 0% or 5% and similar to 10%. Although, the incorporation of 10% water yielded the most active catalysts.

- A precipitation mechanism was proposed: when water was not incorporated the precipitation of a single phase occurred; whereas when water was added the mechanism shifted towards droplet formation *i.e.* 2-phases. It was also proposed that the addition of low concentrations of water (5%) decreased the cobalt acetate solubility but further water incorporation (>5%) restricted the CO_2 diffusion into the droplet ultimately decreasing the precipitation yield.
- The cobalt oxide catalysts were prepared by thermal treatment of the SAS cobalt precipitated under different conditions, under static air and also under inert conditions (flowing N_2). So far, calcination in static air at 250 °C yielded the best catalyst in terms of light-off and low temperature activity. Materials made at 120 bar, 40 °C, 40:1 molar ratio, 120 µm inner nozzle diameter and calcined under static air at 250 °C (5 °C min^{-1}) during 5 h showed the lowest temperature activity and was stable with time-on-line reaction.
- Interestingly, the most developed Co_3O_4 catalyst was compared against 5 wt% Pt/Al_2O_3 in terms of light-off temperature. The Co_3O_4 SAS catalyst showed lower temperature activity than 5 wt% Pt/Al_2O_3 catalyst (at 10% conversion temperatures were 109 °C and 199 °C, respectively) supporting the case for SAS prepared cobalt oxide catalyst as an attractive material for low temperature propane total oxidation.

- Initial GAS studies focused on finding a suitable cobalt precursor to impregnate TiO_2, the study focussed on the solvent removal process and the capabilities of loading cobalt onto TiO_2. Cobalt acetate was found to

be the most suitable precursor, permitting high weight loadings of 30 wt%. An optimum solvent removal process (after precipitation) of 30 min at 25 °C by 12 L min^{-1} (STP) of CO_2 was found.

- Thereafter, GAS experimental parameters, such as temperature, volumetric expansion rate and the solvent used were surveyed and validated under severe FT conditions probing the stability of cobalt crystallites. The slow volumetric expansions at 25 °C using methanol as solvent yielded small cobalt metal crystallites (*ca*. 12 nm); although, their small size resulted in a higher reduction temperature. Also, investigations performed on this catalyst elucidated that hardly reducible compounds ($CoTiO_3$) were not found.
- Ruthenium and barium were incorporated into the GAS synthesis to improve the reducibility and stability of small cobalt particles. The impregnation of ruthenium on calcined GAS catalyst and the impregnation of barium on TiO_2 prior to GAS synthesis were found to increase the cobalt reducibility and in the case of ruthenium reduced the final cobalt metal crystallites size.
- Hence, ruthenium and barium cobalt based catalyst were scaled-up from a 100 ml to 1000 ml precipitation vessel to produce catalysts to be tested for FT and to analyze the cobalt metal surface area. The ruthenium was incorporated in two ways: by impregnating the calcined GAS catalyst and co-precipitating ruthenium and cobalt on TiO_2 simultaneously; whereas barium was incorporated before the GAS expansion.
- The cobalt metal surface area was similar in both ruthenium promoted catalysts (20 and 16 m^2 g_{Co}^{-1}). Although in the barium promoted catalyst

the metal area was as low as in non-promoted catalyst (5 and 8 $m^2 g_{Co}^{-1}$, respectively).

- The ruthenium promoted GAS catalysts showed similar CO turnovers and C_{5+} and CH_4 selectivity to the industrial standard catalyst. Interestingly, the ruthenium GAS catalysts were far more stable and did not deactivate within the testing period. The increase in reaction temperature drastically deactivated the industrial standard but ruthenium GAS catalysts deactivated to a lesser degree. It was suggested that hexagonal close-packed cobalt species could be behind the relevant stability of the GAS catalysts.

- Cobalt and zinc acetates were also co-precipitated and tested for the FT reaction. Similarities between single and binary systems in terms of acetate/carbonates formation and surface areas were found as water was incorporated; thus, the same precipitation mechanism was suggested. It was observed that 5% water incorporation increased the Co/Zn ratio and this was also correlated to the cubic cobalt species observed by XRD. It is suggested that 15% water addition promoted the growth time during the precipitation leading to the formation of crystalline precursors.
- The SAS process significantly increased the cobalt metal surface area compared to traditional co-precipitation; further water incorporation promoted the metal surface area in SAS catalysts, both with 5% and 15% water. Nevertheless, the metal surface area was sensitive to temperature and calcination at 500 °C reduced the metal area, most likely due to

cobalt sintering or the formation of $ZnCo_2O_4$ species, albeit that SAS processed catalysts still showed the highest metal surface area.

- The FT reaction showed unstable activity for the cobalt-zinc catalysts, albeit after 150 h under reaction stabilized the catalysts and relevant activity was observed for the 5% water catalyst calcined at 350 °C. The catalysts calcined at 500 °C showed poor catalytic activities regardless of the synthesis process and this agrees with the drop in metal surface area.

6.2 Future work.

- In this work the feasibility of using dense CO_2 to precipitate organo-metalic compounds has been shown, both for transition metals oxides and PGMs. Hence, it is proposed to conduct experiments to co-precipitate binary compounds as bulk catalysts for propane total oxidation, *i.e.* cobalt-manganese oxides, nickel-manganese oxides or cobalt-iron oxides. Also, Mn_2O_3 was observed as very active catalysts; thus, a study of water effect on the SAS precipitation of manganese acetate could be interesting.
- It has been mentioned that propane oxidation is a model reaction to study exhaust after-treatment catalysts. However, after-treatment technology uses supported catalysts. Thus, it is suggested to investigate the GAS or HiPI process to make supported catalysts (initially on TiO_2 and then Al_2O_3) for low temperature propane total oxidation.
- A study to understand the carbonate formation under SAS conditions was carried out. However, difficulties were found to determine whether carbonates are formed directly on precipitation. Hence, *operando* studies

using infra-red or Raman spectroscopy may help to understand the nature of precipitates.

- The effect of the pH in the starting solution may have an impact on the SAS precipitate. Therefore, the study of a matrix of solutions with different pH and also buffered solutions (such as acetate buffers) may help to understand the impact of this parameter during the precipitation and ultimately on the precipitated material.
- The investigation of the characteristics of the Co_3O_4 that correlates the structural and chemical features of catalysts with the activity of propane total oxidation is an attractive topic. The determination of the pore volume and pore size distribution may help to understanding the mass transfer limitations taking place in the catalyst. Oxygen temperature programmed desorption can elucidate the interaction of the Co_3O_4 with the O_2, which has been suggested as one of the oxygen source during the oxidation. Also, the interaction between propane and the Co_3O_4 can improve the understanding of the reaction; in this sense, DRIFT experiments are suggested.
- The high pressure injection equipment (HiPI) developed during this work can be used in a semi-continuous GAS mode. This process may further improve the initial GAS results due to the crystallization being more uniform compared to GAS process ultimately yielding more homogeneous catalysts. It is thought that the co-introduction of slurry and SC-CO_2 *via* coaxial nozzle could benefit the process.
- The ruthenium promoted GAS catalysts stability under FT reaction is the major discovery of this work. This could be further investigated under the

perspective of the ruthenium effect in terms of support-cobalt interaction or ruthenium-cobalt interaction (alloy formation). The investigation of the stable phases during FT reaction obtained in the GAS prepared catalyst is an interesting study that can be investigated by *in situ* XRD.

- The cobalt-zinc SAS made catalyst with 5% water added showed high metal surface area; although, the lack of stability under FT reaction conditions is a drawback. As previously mentioned, several patents were issued claiming that Co-Zn catalysts precipitated by traditional routes and then promoted by PGM that may stabilize the catalysts and improve the C_{5+} selectivity. Hence, the precipitation of a ternary system, such as Pt-Co-Zn, Re-Co-Zn or Ru-Co-Zn, could be an interesting step forward in dense CO_2 precipitation for catalyst technology. Also, feasibility of precipitating metals normally used as supports, such as zirconium, was observed during the course of this work. The co-introduction of this element can stabilize the catalyst performance.